Title	Fermi Surface Properties of Rare Earth and Uranium Compounds Grown by the Self-Flux and Chemical Transport Methods
Author(s)	Aoki, Dai
Citation	大阪大学, 2000, 博士論文
Version Type	VoR
URL	https://doi.org/10.11501/3169102
rights	
Note	

Doctoral Thesis

Fermi Surface Properties of
Rare Earth and Uranium Compounds
Grown by the Self-Flux and
Chemical Transport Methods

by

DAI AOKI

Department of Physics
Graduate School of Science
Osaka University

January, 2000

Abstract

The f electrons in the rare earth and uranium compounds indicate variety of physical properties including magnetic ordering, quadrupolar ordering, metamagnetism, a large mass of the conduction electron and superconductivity. In the present paper, we grew high-quality single crystals of RPb_3 (R = Pr, Sm, Eu, Gd, Yb), $YbIn_3$, UAl_3, UGa_3, UX_2 (X = P, As, Sb, Bi) and UCd_{11}, which are in the best quality as far as we know.

In $PrPb_3$, we found a mass enhancement of the conduction electron named branch γ, from 1.6 to $4.0 \, m_0$ with decreasing temperature below 1 K. This is caused by the antiferroquadrupolar ordering which occurs at 0.4 K. The mass enhancement based on the antiferroquadrupolar ordering is the first observation. Below 0.6 K, we found metamagnetic transitions at 70 kOe, which corresponds to the phase transition from the antiferroquadrupolar phase to the paramagnetic one.

A valence change is also an interesting phenomenon in the rare earth compounds. $YbPb_3$, $EuPb_3$ and $YbIn_3$ are divalent, whereas the valence is usually trivalent. These Fermi surfaces are therefore found to be highly different from the corresponding trivalent ones.

We also studied the electronic nature of $5f$ electrons in uranium compounds of UAl_3, UGa_3, UCd_{11} and UX_2 (X = P, As, Sb, Bi). We succeeded in observing the dHvA oscillations in UAl_3, UGa_3 and UX_2 (X = As, Sb, Bi).

In UX_2, we found for the first time the two-dimensional Fermi surfaces, namely, cylindrical ones. Fermi surfaces of UBi_2 is found to consist of a spherical Fermi surface and a cylindrical one. These Fermi surfaces in UBi_2 change into cylindrical ones in USb_2 and UAs_2. This change of the Fermi surfaces is well explained by a flattened magnetic Brillouin zone. The two-dimensional character of the Fermi surfaces on these compounds is mainly due to the conduction electrons in the U-plane, including the $5f$ electrons. The itinerant nature of $5f$ electrons is reflected to the large cyclotron masses. The magnetic breakthrough (breakdown) phenomenon is also discussed on USb_2.

Contents

Chapter 1 Introduction

The rare earth compounds are usually treated in magnetism by a f-localized model, but show various interesting phenomena such as valence fluctuations, gap states, Kondo lattice, quadrupolar ordering and heavy Fermions (heavy electrons).[1] These originate from the $4f$ electrons in the rare earth compounds, which are either bound to the lanthanide atoms or delocalized, indicating an itinerant nature. As shown in Fig. 1.1 (b),[2] the $4f$ electrons in the atom are pushed deep into the interior of the closed $5s$ and $5p$ shells because of the strong centrifugal potential $l(l+1)/r^2$, where $l = 3$ holds for the f electrons. This is the reason why the $4f$ electrons possess an atomic-like character in the crystal. On the other hand, the tail of their wave function spreads to the outside of the closed $5s$ and $5p$ shells, which is highly influenced by the potential energy, the relativistic effect and the distance between the lanthanide atoms. These enhance the hybridization effect of the $4f$ electrons with the conduction electrons, resulting in the various phenomena mentioned above.

Magnetism in the rare earth compounds is based on the $4f$ electrons with a local moment. An indirect interaction, mediated by a conduction electron with spin polarization, causes a magnetic order. This indirect interaction is called the Ruderman–Kittel–Kasuya–Yosida (RKKY) interaction.[3-5] The RKKY interaction is a fundamental theory in f-electron magnetism.

On the other hand, some Ce compounds such as $CeCu_6$[6] indicate the Kondo effect. In these compounds, the Kondo effect seems to overcome the above RKKY interaction. In a purely periodic system, the ground state cannot be a scattering state but becomes a coherent Kondo lattice state. Namely, the localized $4f$ electrons become itinerant because the $4f$ electrons hybridize with the conduction electrons. This hybridization yields a large density of states at the Fermi level, and thus an effective mass of the conduction electrons becomes quite large. Such a system is called the heavy Fermion (heavy electron) system. The heavy Fermion system can be described in terms of a Fermi liquid, following a T^2-dependent electrical resistivity contribution arising from electron–electron scattering varying as $\rho \sim AT^2$, the electronic specific heat coefficient varying as $C = \gamma T$ with γ independent of T in the limit $T \to 0$, and the enhanced Pauli spin susceptibility $\chi \simeq \chi(0)$ independent of T. These values of A, γ and χ in the heavy Fermion system, holding a relation of $\sqrt{A} \sim \gamma \sim \chi$, are huge compared to those of the conventional metal.

The $5f$ electrons in the uranium compounds have a characteristic nature between the itinerant like $3d$ electrons and the localized $4f$ electrons.[1,7] Figure 1.1 (c) shows the effective radial charge density of the U atom, which is compared to those of Ni or Ce atoms. For example, $5f$ electrons of UGe_3, USi_3, URu_3, UIr_3 and URh_3 show an itinerant electron character from the results of the dHvA experiment and the energy band calculation. On the other hand, UPd_3, UPb_3 and UTl_3 show a localized electron one.

Some uranium compounds such as UPt_3, UBe_{13}, UPd_2Al_3 are interesting, showing not

only the heavy Fermion nature but also superconductivity. These compounds are called unconventional or anisotropic superconductors because they do not follow thermally an exponential law expected from the BCS theory but a power law.

To elucidate the f electron nature of these compounds, the Fermi surface study is essentially important. The dHvA experiment is a useful method to clarify the Fermi surface and the character of the conduction electrons. It is, however, difficult to carry out the dHvA experiment, because the heavy effective mass and/or large impurity scattering suppress the dHvA oscillation. Therefore, the dHvA experiment requires the high magnetic fields, extremely low temperatures and high-quality single crystals. These criterions for the usual rare earth compounds are, for example, low temperatures less than 1 K, high fields more than 100 kOe and the residual resistivity ratio (ρ_{RT}/ρ_0) of the sample larger than 40. In the case of heavy electrons with an effective mass of 100 m_0, much more severe experimental conditions such as a low temperature of 20 mK, a high field of 150 kOe and a sample with $\rho_{RT}/\rho_0 = 500$ are needed to detect the dHvA oscillation.

In spite of these experimental difficulties, many rare earth compounds were investigated by the dHvA experiments, especially devoting a lot of efforts to growing high-quality single crystals. Nevertheless, the dHvA experiments were scarcely proceeded for the compounds whose high-quality samples are hardly available. In particular, the compounds with incongruent melt is difficult to obtain the high-quality sample, because unexpected compounds with different compositions are included as impurities.

In the present study, we grew high-quality single crystals of rare earth and uranium compounds by using a self-flux method and a chemical transport one, overcoming difficulties as mentioned above. On the Fermi surface study, it is important to carry out the dHvA experiments for a lot of compounds and classify the results into typical examples. The samples which we grew are RPb_3 (R = Pr, Sm, Eu, Gd, Yb), $YbIn_3$, UAl_3, UGa_3, UX_2 (X = P, As, Sb, Bi) and UCd_{11}. The dHvA experiments were done for all these compounds except UP_2 and UCd_{11} and their Fermi surface properties were clarified.

In this paper, we will give a review including more detail background of this study in Chap. 2 and summarize the characteristic properties of the present compounds in Chap. 3. Next we will present the single crystal growth and experimental method in Chap. 4. In Chap. 5, we will give the results and discussion. Finally, we will summarize the present study in Chap. 6.
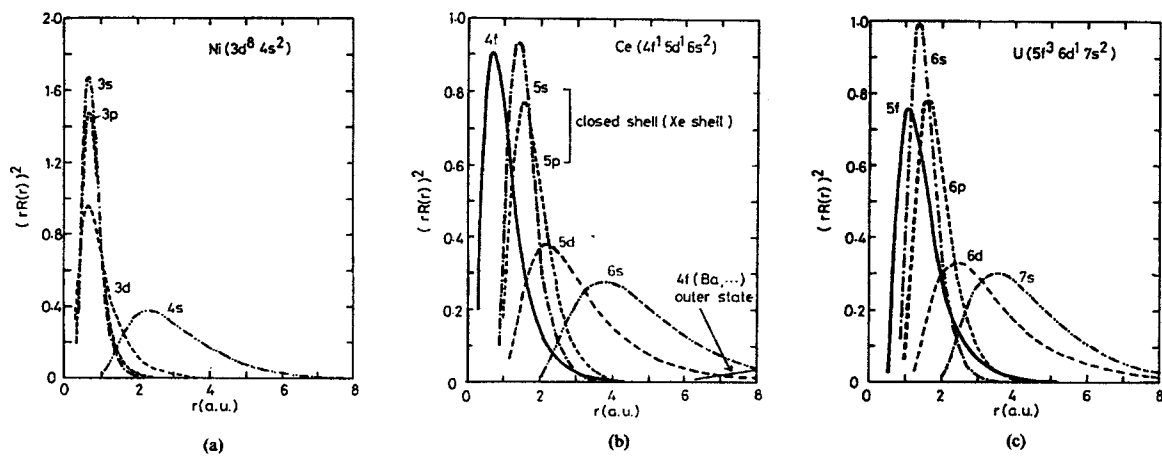
Fig. 1.1 Effective radial charge densities of (a) Ni, (b) Ce and (c) U atoms, cited from ref. (2).

Chapter 2   Introduction to Relevant Physics

2.1 $3d$ itinerant system

2.1.1   Hubbard model

The $3d$ electron system is often described as following the Hubbard model,

$$\mathcal{H} = \sum_{ij\sigma} t_{ij} c_{i\sigma}^{\dagger} c_{j\sigma} + U \sum_{j} n_{j\uparrow} n_{j\downarrow}, \qquad (2.1)$$

where t_{ij} is a transfer integral, U is a Coulomb energy, $c_{i\sigma}^{\dagger}$ and $c_{j\sigma}$ are annihilation and creation operators of the $3d$ electron, respectively and n_j is a number operator denoted as $n_j = c_j^{\dagger} c_j$. The first term means a kinetic energy when the electron moves into the neighbor site, which is proportional to a band width. The second term is a Coulomb repulsive energy when the two electrons set on one site. A relative difference between two terms provides the different character of the $3d$ electron. For example, the $3d$ electron is localized on the lattice and shows ferro- or antiferromagnetism when U is extremely large. The limit of $U/t \gg 1$ provides the Heisenberg Hamiltonian $\mathcal{H} = -\sum_{ij} J_{ij} \boldsymbol{S}_i \cdot \boldsymbol{S}_j$, which is useful model for magnetism of an insulator, where $\boldsymbol{S}$ is spin of a localized electron and J_{ij} is an exchange interaction between i and j sites.

From the band theory and the dHvA experiment, however, the $3d$ electron in Fe and Ni can be described as a one-body band picture in the ground state, that is, the $3d$ electrons are clarified to be itinerant. Here, the one-body band picture means the theory which treats the correlated electron under the mean field approximation. This contradiction was explained by Stoner as given next.

2.1.2   Stoner's theory

The itinerant $3d$ electron system such as Fe or Ni shows Curie–Weiss behavior at higher temperatures, just like a localized moment system, whereas the $3d$ electron system is described by an itinerant band picture, as mentioned above. Stoner added the molecular field theory into Pauli paramagnetism and introduced a spontaneous magnetization.

$$M = \chi_{\mathrm{P}}(H + \alpha M) \qquad (2.2)$$

This is transformed into

$$\chi = \frac{M}{H} = \frac{\chi_{\mathrm{P}}}{1 - \alpha \chi_{\mathrm{P}}}, \qquad (2.3)$$

where M is the magnetization, χ_{P} is the Pauli susceptibility and H is a magnetic field. The susceptibility is enhanced by the molecular field. The Ferromagnetism appears when

a denominator $1 - \alpha\chi_P < 0$, namely:

$$2\alpha\mu_B{}^2 D(\varepsilon_F) > 1, \tag{2.4}$$

where μ_B is Bohr magneton and $D(\varepsilon_F)$ is the density of states at the Fermi energy. This is called the Stoner's condition, and a large value of α or $D(\varepsilon_F)$ is a condition of ferromagnetism.

Difficulty of this theory is that it cannot explain the Curie–Weiss law at higher temperatures and it gives a large Curie temperature.

2.1.3 SCR theory

Difficulty in the Stoner model was removed by Moriya on the basis of SCR (self consistent renormalization) theory, which treats the spin fluctuation in the band electron.[8]

We show the spatial distribution of the spin density $\rho_s(r)$ in Fig. 2.1.[9] The ρ_s value can be expressed as a deviation between the wave functions with up-spin and down-spin, namely, $\rho_s(r) = |\psi_\uparrow(r)|^2 - |\psi_\downarrow(r)|^2$. In the Stoner model, there is no difference between the density of states with up- and down-spins above a Curie temperature T_C, and thus $\rho_s = 0$ (Fig. 2.1 (a)). On the other hand, in the localized spin model, the magnitude of each moment is constant, but the spin takes any directions by the thermal motion above T_C (Fig. 2.1 (b)). Considering the spin fluctuation effect, the spin at the finite temperature varies not only the direction but also its amplitude, as seen in Fig. 2.1 (c).

2.2 General property of the f electron system

2.2.1 RKKY interaction

The $4f$ electrons in the Ce atom are pushed into the interior of the closed $5s$ and $5p$ shells because of the strong centrifugal potential $l(l + 1)/r^2$, where $l = 3$ holds for the f electrons.[1] This is a reason why the $4f$ electrons possess an atomic-like character in the crystal. On the other hand, the tail of their wave function spreads to the outside of the closed $5s$ and $5p$ shells, which is highly influenced by the potential energy, the relativistic effect and the distance between the Ce atoms. This results in the hybridization of the $4f$ electrons with the conduction electrons. These cause various phenomena such as valence fluctuations, Kondo lattice, heavy Fermion, Kondo insulator, quadrupolar ordering and unconventional superconductivity.

The Coulomb potential repulsive force of the $4f$ electron U at the same atomic site is so strong, for example $U \approx 5\,\mathrm{eV}$ in Ce compounds (see Fig. 2.2[10]). In the Ce compounds the tail of the $4f$ partial density of states extends to the Fermi level even at room temperature, and thus the $4f$ level approaches the Fermi level in energy and the $4f$ electrons hybridize strongly with the conduction electron. This $4f$-hybridization coupling constant is denoted by V. When U is strong and/or V is ignored, the freedom of the charge in the $4f$ electron

(a) Stoner model

(b) localized spin model

(c) spin fluctuation model
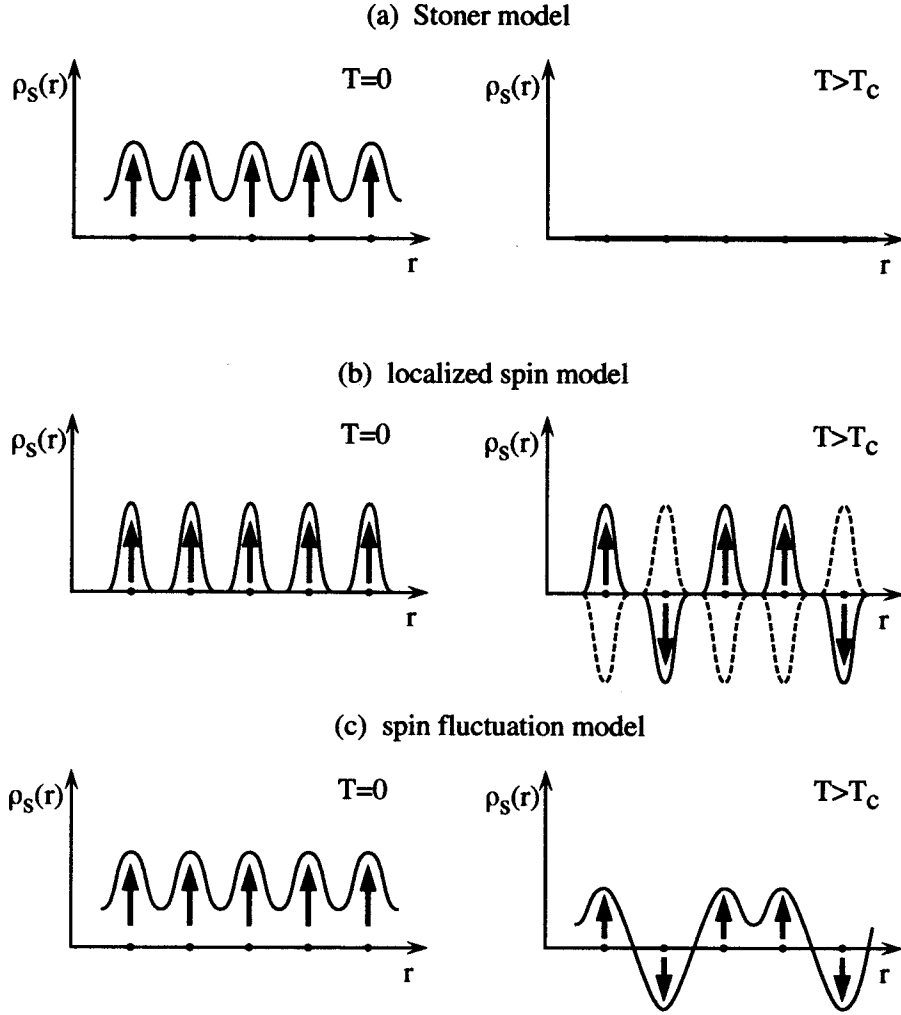
Fig. 2.1 Spatial distribution of the spin density $\rho_s(r)$ for (a) Stoner model, (b) localized spin model and (c) spin fluctuation model. The left-hand side is at $T = 0$, the right-hand side is $T > T_C$. In (a), $\rho_s(r)$ vanishes. In (b), $\rho_s(r)$ is unchanged. In (c), the local density of spin is slightly diminished at $T > T_C$. Cited from ref. (9).

is suppressed, while the freedom of the spin is retained, representing the $4f$-localized state. Naturally, the degree of localization depends on the level of the $4f$ electrons E_f, where larger E_f helps to increase the localization. This situation is applied to most of the lanthanide compounds in which the Ruderman–Kittel–Kasuya–Yosida (RKKY) interaction play a predominant role in magnetism. The mutual magnetic interaction between the $4f$ electrons occupying different atomic sites cannot be of a direct type, such as $3d$ metal magnetism, but should be indirect, which occurs only through the conduction electrons.

In the RKKY interaction, a localized spin S_i interacts with a conduction electron with spin s, which leads to a spin polarization of the conduction electron. This polarization interacts with another spin S_j localized on an ion j and therefore creates an indirect

Fig. 2.2 Density of states of the $4f$ electron in the Ce compound (Ce^{3+}), cited from ref. (10).
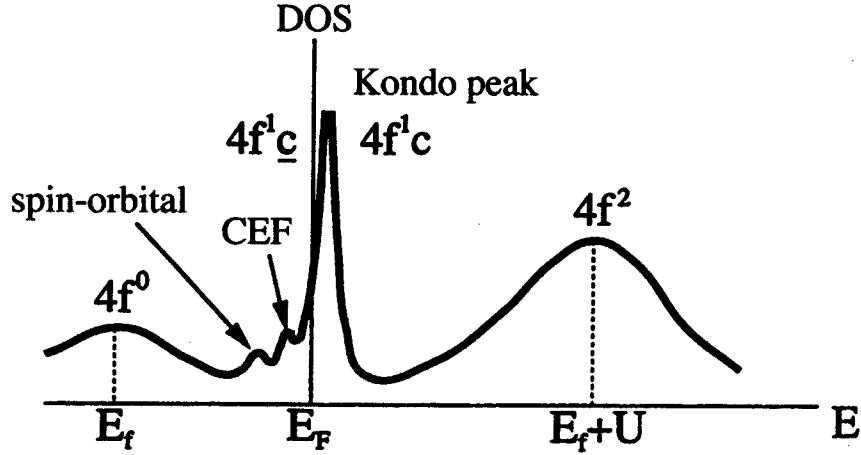
interaction between the spins S_i and S_j. This indirect interaction extends to the far distance and damps with a sinusoidal $2k_F$ oscillation, where k_F is half of the caliper dimension of the Fermi surface. When the number of $4f$ electrons increases in such a way that the lanthanide element changes from Ce to Gd or reversely from Yb to Gd in the compound, the magnetic moment becomes larger and the RKKY interaction stronger, leading to magnetic order of which the ordering temperature roughly follows the de Gennes relation, $(g_J - 1)^2 J(J + 1)$. Here g_J and J are the Landé g factor and the total angular momentum, respectively.

2.2.2 Quadrupolar interaction

The quadrupolar interaction is of basic importance in the f electron magnetism as well as the magnetic interactions such as the RKKY interaction and many-body Kondo effect. A localized f electron possesses the anisotropic charge distribution due to the orbital degrees of freedom, which yields the quadrupole moment. Therefore, the quadrupole moment is obtained from the electrostatic energy:

$$\mathcal{H} = \int \rho(r) V(r) \, d^3 r$$

$$= ZeV(0) + \sum_j P_j \left(\frac{\partial V}{\partial x_j} \right)_0 + \frac{1}{2} \sum_{j,k} Q_{jk} \left(\frac{\partial^2 V}{\partial x_j \partial x_k} \right)_0 + \ldots, \tag{2.5}$$

$$Ze = \int \rho(r) \, d^3 r, \tag{2.6}$$

$$P_j = \int \rho(r) x_j \, d^3 r, \tag{2.7}$$

$$Q_{jk} = \int \rho(r) x_j x_k \, d^3 r, \tag{2.8}$$

where $\rho(r)$ is the change distribution of f electrons in the rare earth and uranium compounds, $V(r)$ is the electrostatic potential, Ze is the charge of f electrons, P_j is the dipole term and Q_{jk} is the quadrupole term. The independent terms in $x_j x_k$ of eq. (2.8) are the following five ones: $2z^2 - x^2 - y^2$, $x^2 - y^2$, xy, yz and zx. They are converted into the following quadrupole moments of $(2J_z{}^2 - J_x{}^2 - J_y{}^2)/\sqrt{3} = O_2^0$, $J_x{}^2 - J_y{}^2 = O_2^2$, $J_x J_y + J_y J_x = O_{xy}$, $J_y J_z + J_z J_y = O_{yz}$ and $J_z J_x + J_x J_z = O_{zx}$, respectively, which are shown in Fig. 2.3.
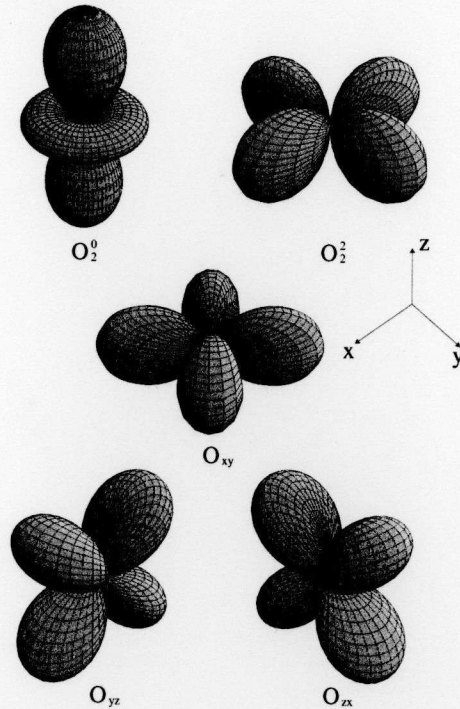
Fig. 2.3 Charge distribution of the quadrupole moments.

The quadrupole moment O_{Γ_γ} couples to the strain $\varepsilon_{\Gamma_\gamma}$ and distorts the crystal. For example, the cubic structure in CeAg is changed into the tetragonal one when O_2^0 becomes the order parameter below 16 K. PrCu$_2$ is a typical example where the quadrupole moment plays an essential role for the metamagnetic transition accompanying with the conversion between the hard and easy axes magnetization.[11]

In a form analogous to the bilinear exchange coupling between magnetic moments, a two-ion coupling between the quadrupole moment is possible.[12] This coupling between two-ions (i and j) can be written as

$$\mathcal{H}_Q = -K(ij)O_{\Gamma_\gamma}(i)O_{\Gamma_\gamma}(j). \tag{2.9}$$

A ferroquadrupolar (antiferroquadrupolar) coupling, i. e. $K(ij) > 0$ (< 0), favours electronic distributions on sites i and j such that their quadrupole moments are parallel (perpendicular) to the local z axes. A schematic picture is shown in Fig. 2.4. The primary

source of this coupling is indirect Coulomb and exchange interaction via the conduction electrons, which is analogous to the RKKY interaction.

(a) Ferroquadrupolar ordering (K > 0)

(b) Antiferroquadrupolar ordering (K < 0)

Fig. 2.4 Schematic representations of (a) ferroquadrupolar and (b) antiferroquadrupolar orderings.
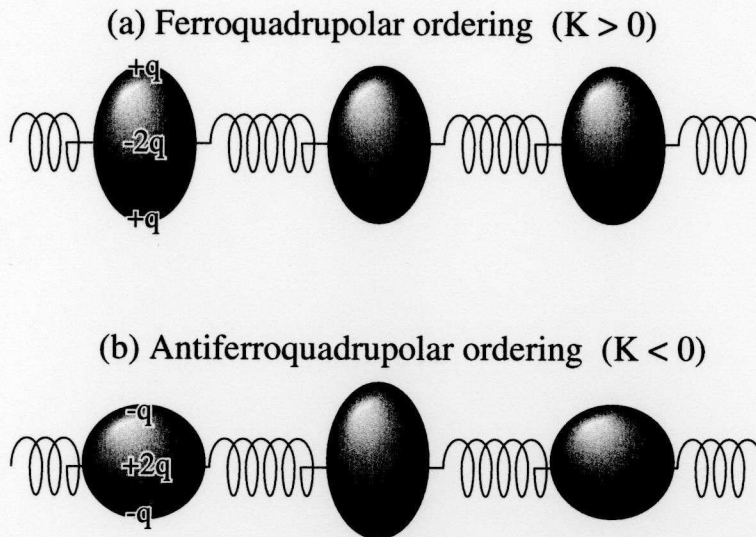
In particular, antiferroquadrupolar compounds such as CeB_6,[13] $TmTe$[14] and $PrPb_3$[15] show an interesting H–T phase diagram (see Fig. 2.5). Namely, the antiferroquadrupolar transition temperature T_Q increases by applying the magnetic field. This behavior is not trivial, and has brought about various arguments.[16–22]

2.2.3   Dense Kondo effect

Higher V tends to enhance the hybridization of the $4f$ electrons with conduction electrons, thus accelerating the delocalization of the $4f$ electrons.[23] The delocalization of $4f$ electrons tends to make the $4f$ band wide. When $E_f > V$, we have still better localization and expect the Kondo regime in the Ce (or Yb) compounds.

The Kondo effect was studied for the first time in a dilute alloy where a ppm range of the $3d$ transition metal is dissolved in a pure metal of copper. Kondo showed the transition impurity diverges logarithmically with decreasing temperature, and clarified the origin of the long standing problem of the resistivity minimum. This became the start of the Kondo problem, and it took ten years for theorists to solve this divergence problem at the Fermi energy.

The many-body Kondo bound state is now understood as follows. For the simplest case of no orbital degeneracy, the localized spin $S(\uparrow)$ is coupled antiferromagnetically with the spin of the conduction electron $s(\downarrow)$. Consequently the singlet state $\{S(\uparrow)\cdot s(\downarrow)\pm S(\downarrow)\cdot s(\uparrow)\}$ is formed with the binding energy $k_B T_K$. Here the Kondo temperature T_K is the single energy scale. In other words, disappearance of the localized moment is thought to be
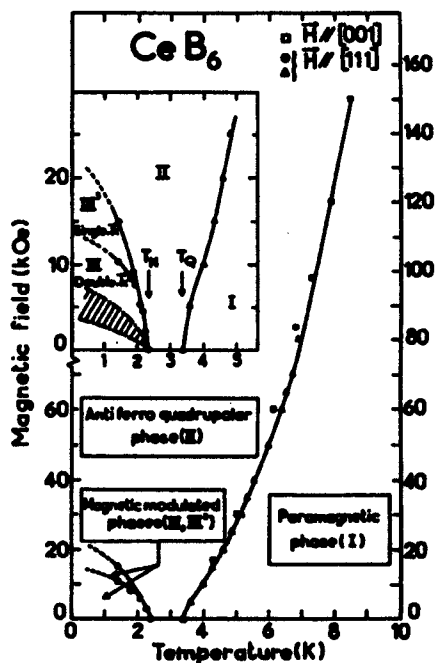
9

Ce B$_6$ □ H∥[001] ●| H∥[11̄1]

Fig. 2.5 H–T phase diagram in CeB$_6$, cited from ref. (13).

due to the formation of a spin-compensating cloud of the electron around the impurity moment.

Kondo-like behavior was observed in the lanthanide compounds, typically in Ce and Yb compounds.[24-26] For example, the electrical resistivity in Ce$_x$La$_{1-x}$Cu$_6$ increases logarithmically with decreasing temperature for all x-values,[6] as shown in Fig. 2.6. The Kondo effect occurs independently at each Ce site even in a dense system. Therefore, this phenomenon was called the dense Kondo effect.

The Kondo temperature in the Ce (or Yb) compound is large compared to the magnetic ordering temperature based on the RKKY interaction. For example, the Ce ion is trivalent ($J = 5/2$), and the $4f$ energy level is split into the three doublets by the crystalline electric field, namely possessing the splitting energies of Δ_1 and Δ_2 (see Fig. 2.7[10]). The Kondo temperature is given as follows:[27]

$$T_K^h = D \exp\left(-\frac{1}{3|J_{ex}|D(E_F)}\right) \qquad \text{when } T > \Delta_1, \Delta_2 \qquad (2.10)$$

and

$$T_K = \frac{D^2}{\Delta_1 \Delta_2} D \exp\left(-\frac{1}{|J_{ex}|D(E_F)}\right) \qquad \text{when } T < \Delta_1, \Delta_2. \qquad (2.11)$$

Here D, $|J_{ex}|$ and $D(E_F)$ are the band width, exchange energy and density of states, respectively. If we postulate $T_K \approx 5\,\text{K}$, for $D = 10^4\,\text{K}$, $\Delta_1 = 100\,\text{K}$ and $\Delta_2 = 200\,\text{K}$, the value of $T_K^h \approx 50\,\text{K}$ is obtained, which is compared to the $S = \frac{1}{2}$-Kondo temperature
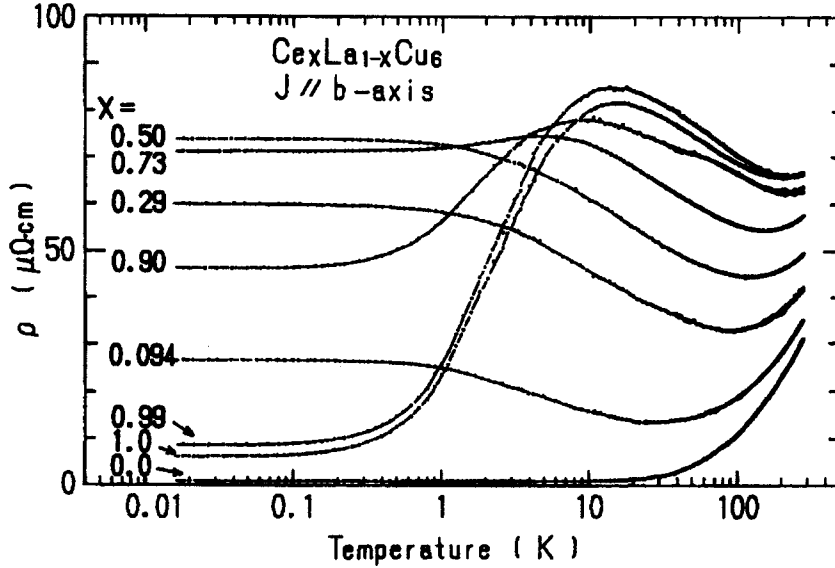
10

Fig. 2.6 Temperature dependence of the electrical resistivity of $La_{1-x}Ce_xCu_6$, cited from ref. (6).

of 10^{-3} K defined as $T_K^0 = D\exp(-1/|J_{ex}|D(E_F))$. Theses large values of the Kondo temperature shown in eqs. (2.10) and (2.11) are due to the orbital degeneracy of the $4f$ levels. Therefore, even at low temperatures the Kondo temperature is not T_K^0 but T_K shown in eq. (2.11).

On the other hand, the magnetic ordering temperature is about 5 K in the Ce (or Yb) compounds, which can be simply estimated from the de Gennes relation under the consideration of the Curie temperature of about 300 K in Gd. Therefore, it depends on the compound whether or not magnetic ordering occurs at low temperatures.

2.2.4 Heavy Fermion system

The ground state properties of the dense Kondo system are interesting in magnetism, which is highly different from the dilute Kondo effect. In the Ce intermetallic compounds such as $CeCu_6$, Ce ions are periodically aligned whose ground state cannot be a scattering state but becomes a coherent Kondo-lattice state. The electrical resistivity ρ decreases steeply with decreasing temperature, following $\rho \approx AT^2$ with a large value of the coefficient A.[28] The $\sqrt{A}$-value is proportional to the effective mass of the carrier and thus inversely proportional to the Kondo temperature. Correspondingly, the electronic specific heat coefficient γ roughly follows the simple relation $\gamma \approx 10^4/T_K$ (mJ/K^{2}mol) because

11
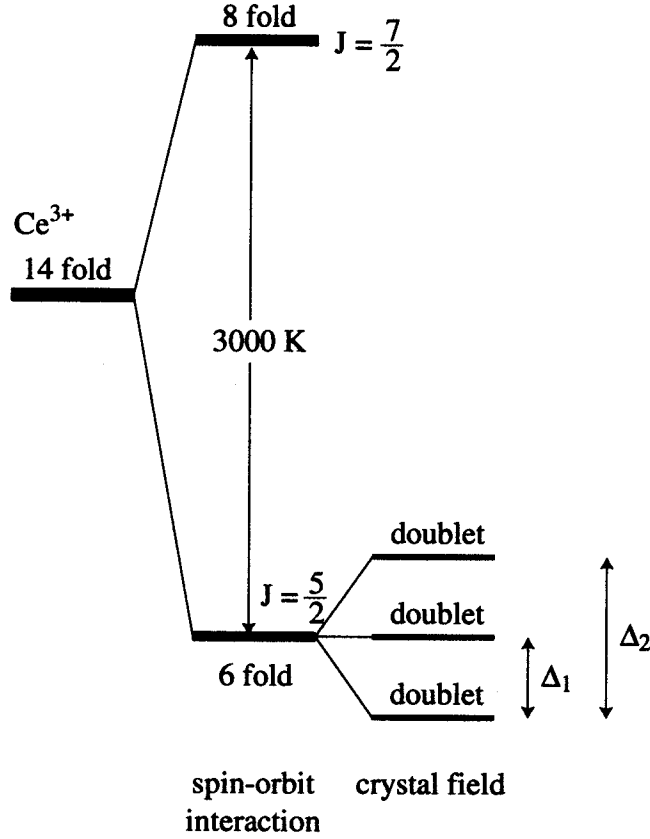
Fig. 2.7 Level scheme of the $4f$ electron in Ce^{3+}, cited from ref. (10).

the Kramers doublet of the $4f$ levels is changed into the γ-value in the Ce compound:

$$R\ln 2 = \int_0^{T_K} \frac{C}{T}\,dT \tag{2.12}$$

$$C = \gamma T \tag{2.13}$$

Thus

$$\gamma = \frac{R\ln 2}{T_K} = \frac{5.8 \times 10^3}{T_K} \quad (\text{mJ/K}^2\text{mol}). \tag{2.14}$$

It reaches $1600\,\text{mJ/K}^2\text{mol}$ for $CeCu_6$ because of a small Kondo temperature of 4 K. The conduction electrons possess large effective masses and thus move slowly in the crystal. Actually in $CeRu_2Si_2$ an extremely heavy electron of $120\,m_0$ is detected from the de Haas–van Alphen (dHvA) effect measurements. Therefore the Kondo-lattice system is called a heavy electron or heavy Fermion system. The Ce Kondo-lattice compound with magnetic ordering also possesses a large γ-value even if the RKKY interaction overcomes the Kondo effect at low temperatures. For example, the γ-value of CeB_6 is $250\,\text{mJ/K}^2\text{mol}$, which is roughly one hundred times larger than that of LaB_6, $2.6\,\text{mJ/K}^2\text{mol}$.

When $E_f < V$, the $4f$ electrons may tend to be delocalized, manifesting the valence fluctuation regime. CeSn$_3$ and CeNi were once called valence fluctuation compounds or mixed valent compounds. The magnetic susceptibility in these compounds follows the Curie–Weiss law at higher temperatures than room temperature, possessing the magnetic moment near Ce^{3+}, while it becomes approximately temperature-independent with decreasing temperature, showing a broad maximum around 150–200 K.[29] Thus the valence of Ce atoms seems to change from Ce^{3+} to Ce^{4+} (non-magnetic state) with decreasing temperature.

A significant correlation factor is thought to be the ratio of the measured magnetic susceptibility $\chi(0)$ to the observed γ-value:[30]

$$R_{\mathrm{W}} \equiv \left(\frac{\pi^2 k_{\mathrm{B}}{}^2}{\gamma} \right) \left(\frac{\chi(0)}{\mu_{\mathrm{B}}{}^2 g_J{}^2 J(J+1)} \right). \tag{2.15}$$

This ratio R_{W} is called Wilson–Sommerfeld ratio. Stewart evaluated R_{W} for the heavy Fermion system, as shown in Fig. 2.8.[31] He suggested that in the f electron system R_{W} is not 1 but roughly 2. A deviation from $R_{\mathrm{W}} = 1$ depends on the strength of the many-body effect. Kadowaki and Woods stressed the importance of a universal relationship between A and γ as shown in Fig. 2.9.[32] They noted that the ratio A/γ^2 has a common value of $1.0 \times 10^{-5} \, \mu\Omega \cdot \mathrm{cm} \, \mathrm{K}^2 \mathrm{mol}^2/\mathrm{mJ}^2$.
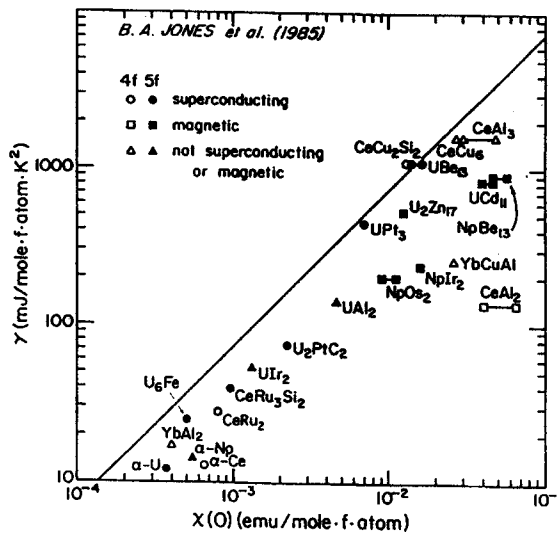

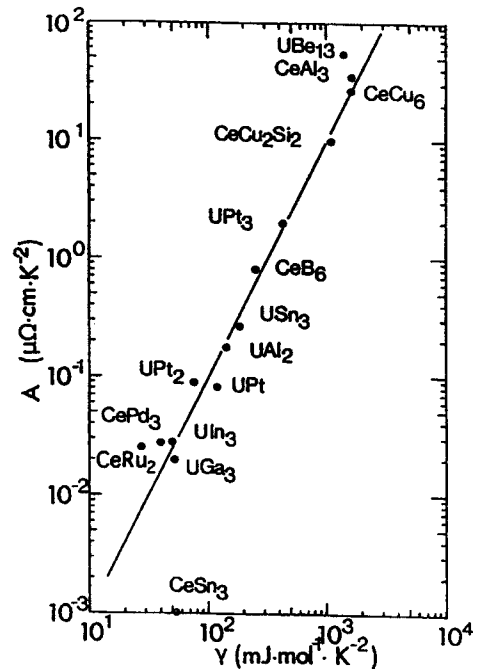Fig. 2.8 γ versus χ plot, cited from ref. (33).

Fig. 2.9 Kadowaki–Woods plot, cited from ref. (32).

13

2.2.5 Fermi surface study

Fermi surface studies are very important to know the ground-state properties of the various magnetic compounds.[34,35] Even in the localized system, the presence of $4f$ electrons alters the Fermi surface through the $4f$-electron contribution to the crystal potential and through the introduction of new Brillouin zone boundaries and magnetic energy gaps which occur when $4f$ electron moments order. The latter effect may be approximated by a band-folding procedure where the paramagnetic Fermi surface, which is roughly similar to the Fermi surface of the corresponding La compound, is folded into a smaller Brillouin zone based on the magnetic unit cell, which is larger than the chemical unit cell.

If the magnetic energy gaps associated with the magnetic structure are small enough, conduction electrons undergoing cyclotron motion in the presence of magnetic field can tunnel through these gaps and circulate the orbit on the paramagnetic Fermi surface. If this magnetic breakthrough (breakdown) effect occurs, the paramagnetic Fermi surface may be observed in the de Haas–van Alphen (dHvA) effect even in the presence of magnetic order.

For Kondo lattice compounds with magnetic ordering, the Kondo effect is expected to have minor influence on the topology of the Fermi surface, representing that the Fermi surfaces of the Ce compounds are roughly similar to those of the corresponding La compounds, but are altered by the magnetic Brillouin zone boundaries mentioned above. Nevertheless the effective masses of the conduction carriers are extremely large compared to those of La compounds. In this system a small amount of $4f$ electron most likely contributes to make a sharp density of states at the Fermi energy. Thus the energy band becomes flat around the Fermi energy, which brings about the large mass.

In some Ce compounds such as $CeCu_6$, $CeRu_2Si_2$, $CeNi$ and $CeSn_3$, the magnetic susceptibility follows the Curie–Weiss law with a moment of Ce^{3+}, $2.54\,\mu_B/Ce$, has a maximum at a characteristic temperature $T_{\chi_{max}}$, and becomes constant at lower temperatures. This characteristic temperature $T_{\chi_{max}}$ corresponds to the Kondo temperature T_K. A characteristic peak in the susceptibility is a crossover from the localized $4f$ electron to the itinerant one. The Fermi surface is thus highly different from that of the corresponding La compound. The cyclotron mass is also extremely large, reflecting a large γ-value of $\gamma \simeq 10^4/T_K$ (mJ/K^2mol).

2.2.6 General property of uranium compounds

The $5f$ electron system, including U compounds, are particularly interesting in the sense that they bridge the gap between the $3d$ and the $4f$ electron systems. The $5f$ electrons in the U atom have a character between the $3d$ and $4f$ electrons, located slightly inside the closed $6s$ and $6p$ shells. Therefore, they may possess both band-like and atomic-like characters, even in the crystal. The properties of some U compounds thus have been understood on the basis of the $5f$ band model, similar to the $3d$ transition metals and their

intermetallic compounds. The dHvA effect was measured in some of these U compounds. The $5f$ band model can explain the observed dHvA results very well.

The discovery of heavy Fermions in rare earth compounds encouraged the search and study of the heavy Fermion states in the actinide compounds and actually some heavy Fermion systems are found in the U compound too. In particular, UPt_3, UBe_{13}, URu_2Si_2, UPd_2Al_3 and UNi_2Al_3 show unconventional superconductivity with magnetic ordering. Coexistence of superconductivity and magnetism accelerated, furthermore, the study of heavy Fermion U compounds. In many respects, however, the heavy Fermions in the U compounds are different from those in the rare earth compounds, and thus Fermi surface studies are interesting and very important. Such studies have actually been done in some of these materials and they offer interesting information.

We will summarize the characteristic features in the U compounds:

(1) The magnetic ordering temperature is in a wide temperature range from close to 0 to 300 K, which is compared to 0–20 K in the Pr compounds.

(2) The magnetic moment is also in a wide range from close to 0 ($0.02\,\mu_B/U$) to $3\,\mu_B/U$, which is compared to about $3\,\mu_B/Pr$.

15

Chapter 3 Review

3.1 RPb$_3$ (R = La, Pr, Nd, Sm, Eu, Gd and Yb)

Many RX$_3$ and UX$_3$ compounds possess the AuCu$_3$-type cubic crystal structure, which belongs to the space group $Pm/3m$. Figure 3.1 shows the crystal structure of AuCu$_3$-type where the corner-sites are occupied by the R or U atoms and the face centered site are occupied by the X atoms.
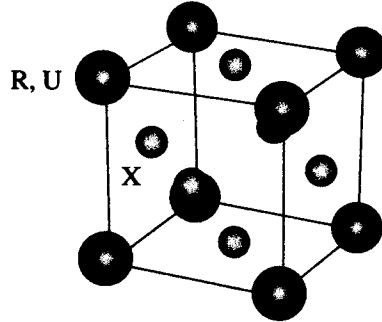
Fig. 3.1 AuCu$_3$-type cubic crystal structure.

RPb$_3$ (R = La, Ce, Pr, Nd, Sm, Eu, Gd and Yb) compounds also crystallize the AuCu$_3$-type cubic crystal structure. Characteristic properties of RPb$_3$ are listed in Table 3.1

Table 3.1 Characteristic properties of RPb$_3$ compounds with the AuCu$_3$-type cubic crystal structure. AF: antiferromagnetic. AFQ: antiferroquadrupolar.

	Lattice const. (Å)	T_N (K)	μ_{eff} (μ_B/R)	Remarks
LaPb$_3$	4.603	Pauli Para.		
CePb$_3$	4.874	1.1	2.3	AF, heavy Fermion ($\gamma = 1.5\,\mathrm{J/K^2 mol}$)
PrPb$_3$	4.860	$T_Q = 0.4$	3.63	AFQ, Γ_3 ground state
NdPb$_3$	4.852	2.7	3.61	
SmPb$_3$	4.835	5.5		
EuPb$_3$	4.915	20	7.5	Eu^{2+}
GdPb$_3$	4.826	16	7.6	
TbPb$_3$	4.810	15	9.21	
DyPb$_3$	4.806	11	10.20	
HoPb$_3$	4.800	3.7	10.0	
ErPb$_3$	4.797	5		
YbPb$_3$	4.862	Pauli Para.	Yb^{2+}	

1) PrPb₃

PrPb$_3$ is the most interesting compound in RPb$_3$, which was studied from a view point of quadrupolar ordering.[36] The magnetic susceptibility shows Van Vleck paramagnetic at low temperatures, as shown in Fig. 3.2.[37] The specific data exhibit, in Fig. 3.3, a large anomaly at 0.35 K, at which the entropy is close to $R \ln 2$.[38] This anomaly is due to the quadrupolar ordering, leading to a non-Kramers doublet Γ_3 as the CEF ground state. The Γ_3 ground state is characterized by possessing no magnetic moment but quadrupole moment. The $4f$ level scheme of the CEF was determined by an inelastic neutron scattering experiment.[39] Γ_3 is the ground state, as expected from the specific heat data, and excited levels are Γ_4, Γ_5 and Γ_1, which are separated by 19, 29, 47 K, respectively from Γ_3, as shown in Fig. 3.4. The analyses of the parastriction and the third-order magnetic susceptibility indicated negative quadrupolar parameters.[40] An antiferroquadrupolar ordering is therefore realized, and $\langle O_2^0 \rangle$ is the order parameter for the field along $\langle 100 \rangle$ direction in the present cubic system.

There are only a few examples known as antiferroquadrupolar compounds in literature, namely CeB$_6$, TmTe, Ce$_3$Pd$_{20}$Ge$_6$ and TmGa$_3$.[13,14,41,42] The antiferroquadrupolar ordering phases for these compounds are very narrow in the temperature range because the successive antiferromagnetic ordering occurs at a lower temperature. On the other hand, PrPb$_3$ is a good candidate to study the antiferroquadrupolar ordering state because of no magnetic ordering.
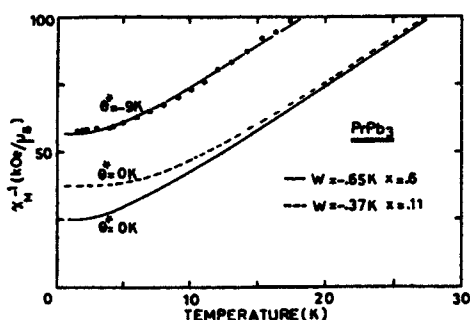
Fig. 3.2 Inverse magnetic susceptibility of PrPb$_3$, cited from ref. (40). Closed circles are the experimental data. Solid and broken lines are results of the CEF calculation.

2) Other RPb₃ compounds

LaPb$_3$ is a Pauli paramagnetic compound without $4f$ electrons, so that it would be a good reference compound for the other RPb$_3$.

CePb$_3$ undergoes an antiferromagnetic transition at 1 K. Extensive studies have been carried out in CePb$_3$, because the competition between the Kondo effect and the antiferromagnetism is realized. The electronic specific heat coefficient is about 1500 mJ/K^{2}mol

17

Fig. 3.3 Specific heat at low temperature in PrPb₃, cited from ref. (38).

Fig. 3.4 CEF level scheme in PrPb₃ determined by the inelastic neutron scattering experiment, cited from ref. (39).
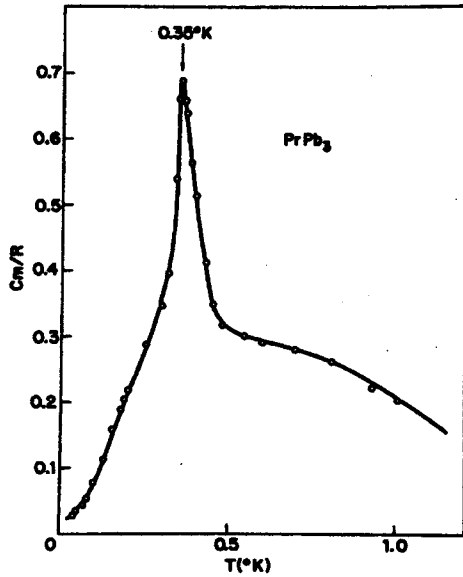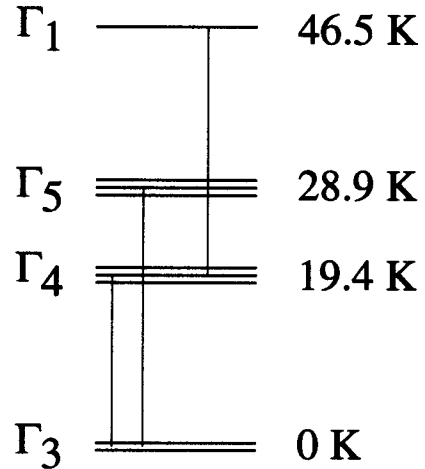
and this compound is recognized as the typical heavy Fermion compound. Moreover, $CePb_3$ was once studied from the viewpoint of field-induced superconductivity, which was denied but characterized by a large negative magnetoresistance,[43] most likely based on the Kondo effect.

$NdPb_3$ is an antiferromagnet with the Néel temperature of 2.7 K.[44] The magnetization of the polycrystalline sample in $NdPb_3$ increases monotonously with increasing field up to 270 kOe, indicating no metamagnetic transitions. Ebihara et al. carried out the de Haas–van Alphen experiments in $NdPb_3$ and determined the Fermi surfaces.[45] Figure 3.5 shows the angular dependence of the dHvA frequency in $NdPb_3$. Main Fermi surfaces consist of four closed ones, which were well explained by the FLAPW band calculations. Reflecting the magnetic Brillouin zone which is smaller than the paramagnetic one, small pocket Fermi surfaces are observed. The cyclotron effective masses are in the range from 0.4 to $3\,m_0$.

Considering the same value of $J = 5/2$ in Ce^{3+} and Sm^{3+} ion, the Kondo effect would be expected in Sm-compounds. Actually, there are some reports which claims the existence of Kondo effect in SmX_3 ($X = Pb$, In, Sn, Tl, Pd).[46-48] $SmPb_3$ undergoes an antiferromagnetic transition at 5 K. The specific heat at low temperature shows the Fermi liquid-like T-linear feature with a large γ-value of about 100 mJ/K²mol.[46] In magnetic susceptibility and ultrasonic measurements of $SmPb_3$, it was clarified that the ground state multiplet splits into Γ_8 quartet and Γ_7 doublet which are the ground state and excited state at $\Delta = 60$ K, respectively. The ultrasonic measurements indicated that
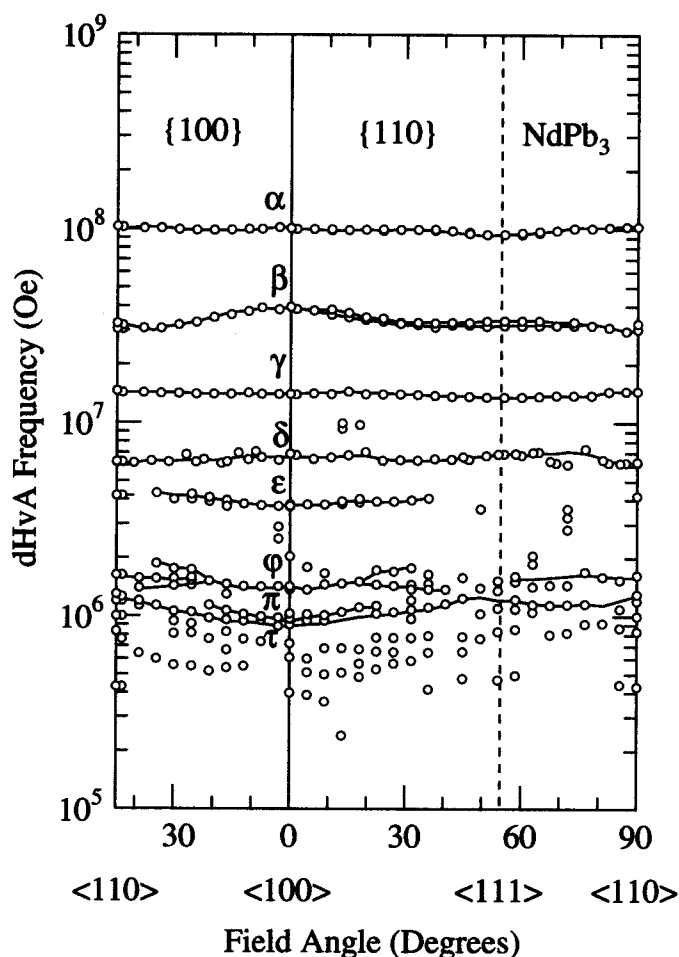
18

Fig. 3.5 Angular dependence of the dHvA frequency in NdPb₃, cited from ref. (45).

Sm³⁺ of SmPb₃ shows no valence fluctuation, and quadrupolar interactions are relatively strong.[47]

EuPb₃ is a divalent metal possessing the magnetic moment.[49,50] Namely, the spin angular momentum number is $S = 7/2$, although the orbital angular momentum number L is zero. In fact, an antiferromagnetic ordering occurs below 20 K. The valence electrons, where the conduction electrons are formed from Eu $(6s^2)$ and Pb $(6s^2 6p^2)$, are in principle the same as in YbPb₃. The Fermi surface of EuPb₃ is therefore expected to be similar to that of YbPb₃, although it would be modified by the magnetic Brillouin zone boundary.

GdPb₃ becomes an antiferromagnet below 17 K.

YbPb₃ is known to be a Pauli-paramagnetic compound with Yb²⁺ $(4f^{14})$. The electrical resistivity shows a usual T-linear dependence.[51] From the specific heat measurements, the γ-value and the Debye temperature are estimated at 1.9 mJ/K²mol and 122 K, respectively.[51] The conduction electrons are formed from the valence electrons of Yb $(6s^2)$ and

19

Pb ($6s^2 6p^2$). YbPb$_3$ is thus a compensated metal with equal numbers of electrons and holes, which is highly different from an uncompensated metal of La($5d^1 6s^2$)Pb$_3$.

3.2 RIn$_3$ (R = Ce, La, Yb)

RIn$_3$ (R = Ce, Pr, Nd, Sm, Gd, Tb, Dy, Ho, Er, Tm, Yb, Lu) compounds also crystallize in the AuCu$_3$-type cubic structure, as shown in Fig. 3.1.

Among RIn$_3$, CeIn$_3$ is a well known Kondo-lattice compound, showing antiferromagnetic ordering at 10 K. Recently, a superconducting transition was observed below 200 mK under pressure of 25 kbar.[52] Fermi surface properties was once studied by the dHvA experiments.[53-55]

The dHvA measurements were done in a non-f reference compound LaIn$_3$.[56-59] Figures 3.6 shows the angular dependence of the dHvA frequency in LaIn$_3$. Branch a originates from the band 7-electron Fermi surface, while the others originate from the band 6-hole Fermi surface, as shown in Fig. 3.7. The latter Fermi surface consists of three kinds of major parts, which are centered at the Γ, R and X points. Among them, a Fermi surface centered at Γ, denoted by d, is electron in dispersion and is spherical in topology, bulges slightly along the $\langle 100 \rangle$ direction and connects with another part of the Fermi surface centered at R by the slender arm elongated along the $\langle 111 \rangle$ direction. The arm is denoted by j. The topology of Fermi surface is similar to that of Cu, although the volume is small compared to that of Cu.

YbIn$_3$ also crystallizes the AuCu$_3$-type cubic structure with a lattice constant of 4.620 Å. This lattice constant is considerably larger than those of the adjacent compound TmIn$_3$ and LuIn$_3$ in the periodic table. Therefore the Yb ion is expected to be divalent, forming $4f^{14}$ closed shell structure. From the Mössbauer spectroscopy measurement, it was confirmed that Yb ion is divalent.[60]

3.3 UX$_3$ (X = Al, Ga)

The uranium compounds UX$_3$, where X is a IIIA or IVA element, Ru or Rh, crystallize in the cubic AuCu$_3$-type structure with a U-U separation $d_{U\text{-}U}$ between 4.0–4.8 Å.[61,62] This value of $d_{U\text{-}U}$ is much larger than the Hill limit for uranium compounds,[63] and using the Hill criterion, one might naively expect magnetic ordering in all of the mentioned UX$_3$ compounds. Instead, they display a wide range of behavior: Pauli enhanced paramagnetism (UAl$_3$, USi$_3$, UGe$_3$ and URh$_3$), antiferromagnetism (UPb$_3$, UGa$_3$, UTl$_3$ and UIn$_3$), Kondo lattice system (USn$_3$) and superconductivity (URu$_3$).[23,62,64] The different behavior can be explained by the great variation in the f-electron hybridization with the X atoms s, p and d orbitals.[23] The effect of the different hybridization strengths becomes apparent in the electronic specific heat coefficient γ which varies from 12 mJ/K^{2}mol in
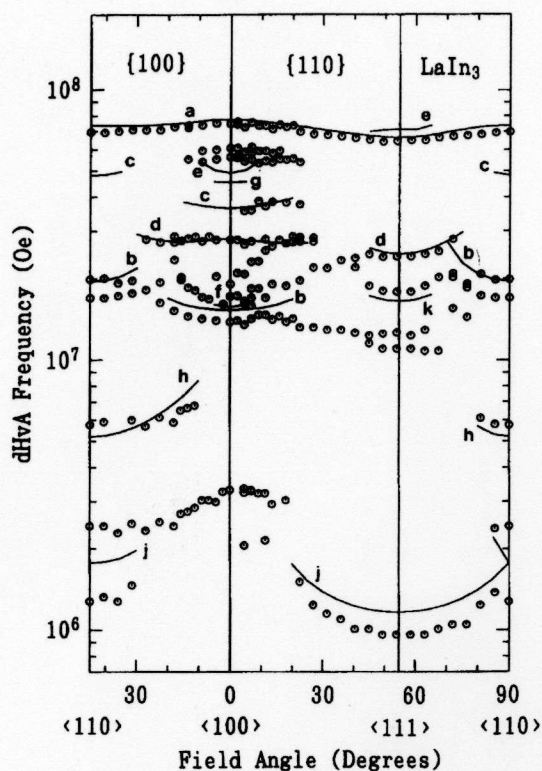
Fig. 3.6 Angular dependence of the dHvA frequency in LaIn$_3$.[56] The solid lines represent the results of band calculations.[57-59]
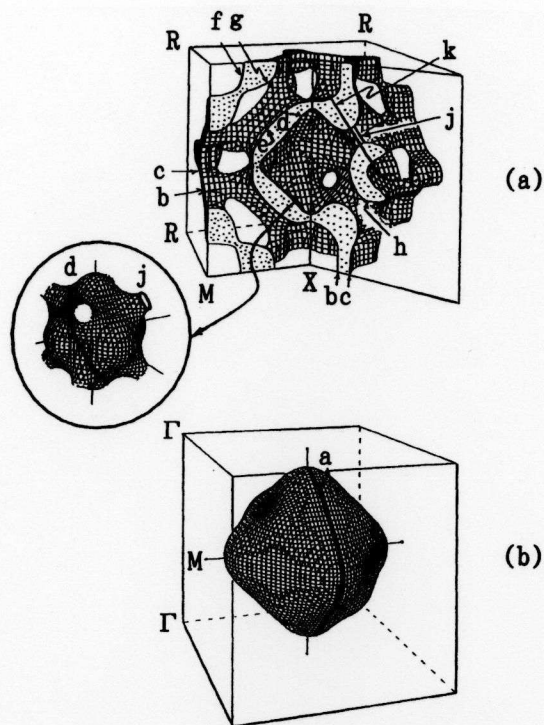
Fig. 3.7 (a) Hole and (b) electron Fermi surfaces in LaIn$_3$.[57-59] The stippled regions indicate the cross sections of the hole Fermi surfaces in (100) and (110) planes.

URu$_3$ to 170 mJ/K^{2}mol in USn$_3$.[62,65,66] Characteristic properties of UX$_3$ are summarized in Table 3.2

1) UAl$_3$

Figure 3.8 shows the electrical resistivity of UAl$_3$ (including USn$_3$ and UGa$_3$).[61] At low temperature, the resistivity is proportional to AT^2 with a value of A that is much larger than for typical Fermi liquids. This large value of A indicates that UAl$_3$ is a spin fluctuator.[32,67]

The inverse magnetic susceptibility in UAl$_3$ displays a weak temperature dependence as shown in Fig. 3.9 (including USn$_3$ and UGa$_3$).[61] No magnetic ordering is observed down to 1.5 K, indicating a Pauli paramagnetic compound. In the other report, Curie–Weiss behavior is seen from 240 to 800 K.[68]

The electronic specific heat coefficient γ of UAl$_3$ is 43 mJ/K^{2}mol,[61] which is considerably large and shows that the hybridization of 5f is strong. The γ-value is constant against the magnetic field.

The dHvA signal was observed in UAl$_3$ from the pulse-field magnetization,[61] although

Table 3.2 Characteristic properties of UX_3 compounds

|	Lattice const. (Å)	T_N (K)	γ (mJ/K^{2}mol)	μ_{ord} (μ_B/U)	μ_{eff} (μ_B/U)	Remarks
UAl$_3$	4.264	Para.	43			
UGa$_3$	4.248	67	52	~ 0.9		$5f$-itinerant, $k = (1/2,1/2,1/2)$
UIn$_3$	4.601	~ 100?	50	1	3.6	
UTl$_3$	4.674	~ 90		1.6		$5f$-localized, $k = (1/2,1/2,1/2)$
USi$_3$	4.035	Pauli Para.	14			
UGe$_3$	4.206	Pauli Para.	20			
USn$_3$	4.626	Para.	170		2.65	Kondo lattice
UPb$_3$	4.793	30	110	~ 1.6	3.2	$5f$-localized, $k = (0,0,1/2)$
URu$_3$	3.977	Pauli Para.	12.4			superconductivity: $T_c = 0.145\,$K
URh$_3$	3.991	Pauli Para.				
UIr$_3$	4.023	Pauli Para.				
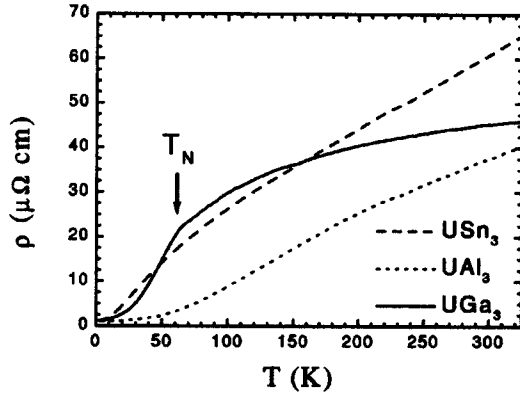
Fig. 3.8 Electrical resistivity of UAl$_3$, cited from ref. (61).
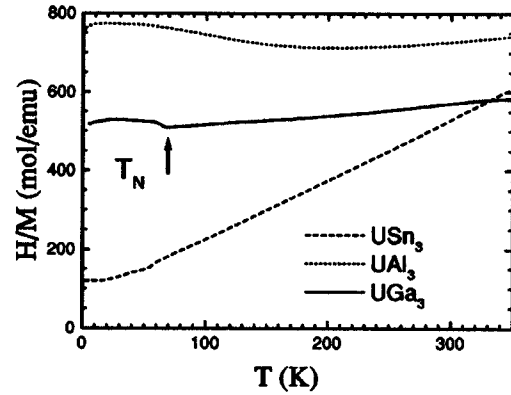
Fig. 3.9 Inverse magnetic susceptibility of UAl$_3$, cited from ref. (61).

a single weak peak appeared at 2.5×10^7 Oe along $\langle 100 \rangle$ in the fast Fourier transform (FFT) spectrum. The cyclotron mass was estimated as $1 < m_c^*/m_0 < 4$.

Figure 3.10 shows the magnetoresistance of UAl$_3$ (including USn$_3$ and UGa$_3$).[61] The data are fitted to a function of $(\rho(H) - \rho(0))/\rho(0) \equiv \Delta\rho/\rho \propto H^n$. In the range from 30 to 100 kOe, n is determined as 1.83.

Cornelius *et al.* calculated the band structure of UAl$_3$ on the basis of the $5f$ itinerant model, as shown in Fig. 3.11.[61] In their calculation there is altogether only one open Fermi surface. On the symmetry axis R–Γ there is one band that is close to, but does not cross ε_F. On this Fermi surface there is one extremal orbit centered at the Γ-point, and also a large "dogs bone" type in the extended zone scheme, centered at the R-point. The calculated electronic specific heat coefficient is $16\,$mJ/K^{2}mol, which is a factor of 2.5 smaller than the experimental value.
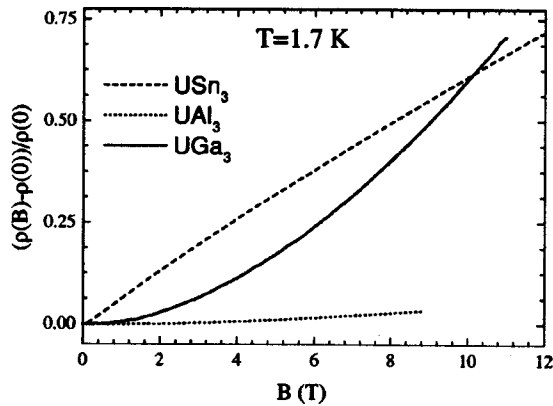
22

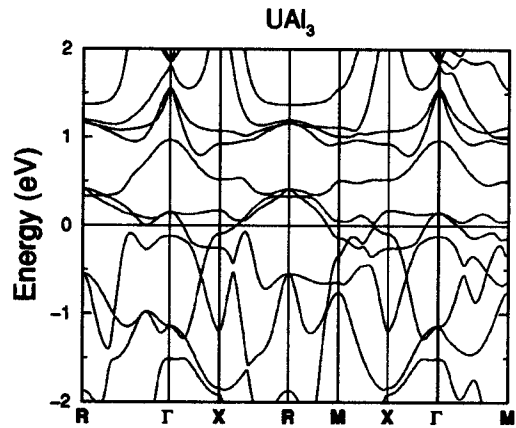**Fig. 3.10** Magnetoresistance of UAl₃, cited from ref. (61).

Fig. 3.11 Calculated band structure of UAl₃, cited from ref. (61).

2) UGa₃

UGa₃ attracts special interests because of its anomalous magnetism. Figure 3.12 shows the lattice constants of UX_3 compounds, where X is a IIIA or IVA element. It is worth noting that the lattice constant of UGa₃ is less than that of UAl₃. It would be expected the lattice would expand as one moves down a column in the periodic table as seen in the IVA series, where a large parameter of UGe₃ is by 0.17 Å larger than that of USi₃. This anomalous behavior of the lattice parameter in UGa₃ relative to UAl₃ is attributed to the much larger hybridization in UGa₃, causing the formation of $5f$ bands which lower the U-U spacing.

Kaczorowski *et al.* measured the electrical resistivity, as shown in Fig 3.13.[69] The kink at 65 K, which corresponds to the antiferromagnetic ordering, is observed. In the early literature, this kink was not detected due to the difficult availability of the high-quality sample. A T^2-dependence of the resistivity is observed below 20 K.

The specific heat was measured by the Kaczorowski *et al.*, as shown in Fig. 3.14. As is apparent from this figure, the phonon contribution to the specific heat is dominant and the magnetic one is extremely small. The estimated magnetic entropy is $0.14R\ln 2$ at the Néel temperature. From this reduced magnetic entropy and weak-temperature dependent magnetic susceptibility (mentioned below), they concluded that the basis of the magnetism in UGa₃ is $5f$-itinerant. The electronic specific heat coefficient γ possesses a considerably large value of $52\,\mathrm{mJ/K^2mol}$.[61]

The magnetic susceptibility in UGa₃ shows the weak-temperature dependence. There is no evidence for Curie–Weiss behavior up to 1000 K,[70] which has been explained by the itinerant nature of the $5f$ electrons. This itinerant view of the $5f$ electron is also supported by the pressure dependence of the Néel temperature[71,72] and the reduced magnetic entropy as mentioned above. Figure 3.15 shows the magnetic susceptibility
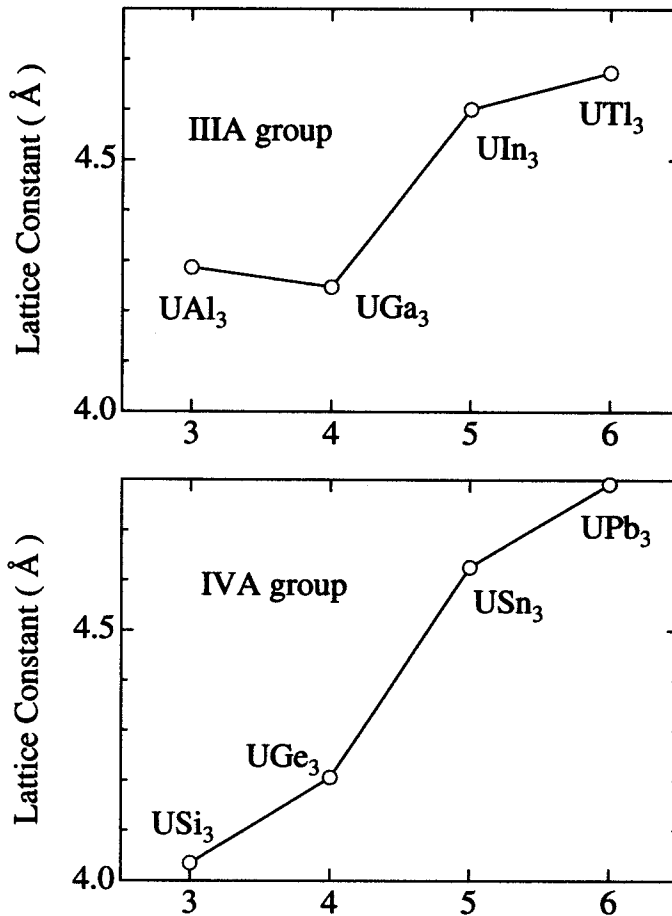
23

Fig. 3.12 Lattice constant of UX_3 compounds. Bottom axis is the number of a column in the periodic table.

measured by Kaczorowski *et al.*[73] The pronounced maximum at 65 K corresponds to an onset of antiferromagnetic ordering. The other two singularities at 40 and 8 K, which were also observed by the thermal conductivities,[73] are unknown in origin.

From the neutron scattering experiments, it was confirmed that the transition at 65 K is antiferromagnetic.[74,75] The ordered magnetic moment of uranium was about $1\,\mu_B/U$. The magnetic structure consists of spins that are ferromagnetically aligned in (111) planes with adjacent (111) planes, being antiferromagnetically coupled. The direction of the magnetic moments is, however, unknown. Very recently, Dervenagas *et al.* carried out the neutron diffraction measurements on a single crystal.[76] The ordered moment is $0.74(8)\,\mu_B/U$ at 5 K. They claim that the moments are most likely along the [111] direction. As shown in Fig. 3.16, at about 40 K a rapid change in the intensity of the strong nuclear reflections are observed, resulting from a change in the mosaic spread of the crystal. This may be due to either a small crystallographic distortion or it can
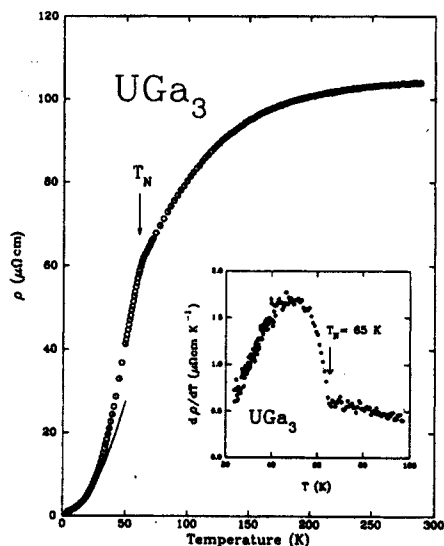
24

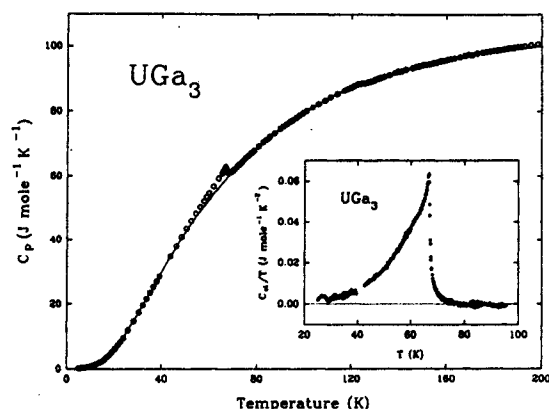Fig. 3.13 Electrical resistivity of UGa₃, cited from ref. (69).

Fig. 3.14 Specific heat of UGa₃, cited from ref. (69).

be of magnetic origin (moment reorientation). The latter possibility is supported by the anomaly of the susceptibility at 40 K, as mentioned above.

Cornelius *et al.* observed the dHvA oscillations by the pulse-field magnetization.[61] The measurement was done only for a field along ⟨100⟩ direction. Figure 3.17 shows the dHvA oscillation and the FFT spectrum. Cornelius *et al.* insisted that there is a metamagnetic transition at 120 kOe and the dHvA frequencies are different between above and below metamagnetic transition, indicating a major reconstruction of the Fermi surface. The existence of the metamagnetic transition is, however, less reliable, because the anomaly of the transition is very small.

The band structure calculation was done by Cornelius *et al.*[61] In their calculation, the total energy with the moment along [100] direction is lower than that along [111] direction. Thus they assumed that the moment is aligned along [100] and calculated the band structure, as shown in Fig. 3.18. Here, the magnetic unit cell is the fcc structure so that the magnetic Brillouin zone is half of the volume of the paramagnetic one. This is always true even if the moment is aligned along other directions, because there is an evidence from neutron experiment that adjacent (111) planes are antiferromagnetically coupled. The calculated Fermi surfaces and its parameters in antiferromagnetic state are shown in Fig. 3.19 and Table 3.3.

As found in alloying experiments on the pseudobinary $U(Ga_{1-x}Ge_x)_3$ system,[77] where UGe_3 is a Pauli paramagnet, the antiferromagnetic state of UGa_3 is very sensitive to any disorder in the metalloid sublattice. Upon substitution of Ge for Ga, a rapid decrease in the Néel temperature was observed, and for $x \geq 0.18$ the magnetic order was found to disappear. Similar properties were also found for another isomorphous alloy system,
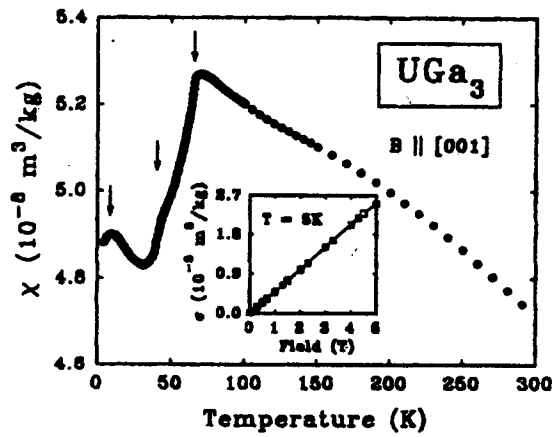
Fig. 3.15 Magnetic susceptibility of UGa₃, cited from ref. (73).
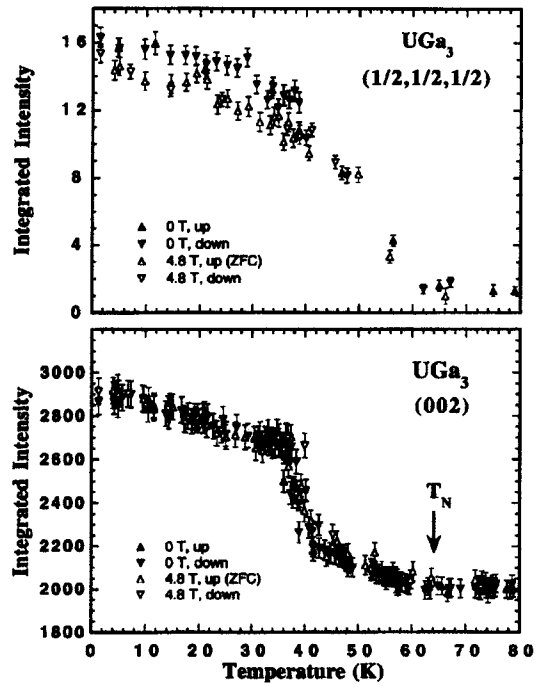
Fig. 3.16 Temperature dependence of the integrated intensities of the (002) strong nuclear and the (1/2, 1/2, 1/2) magnetic reflection in UGa₃, cited from ref. (76).
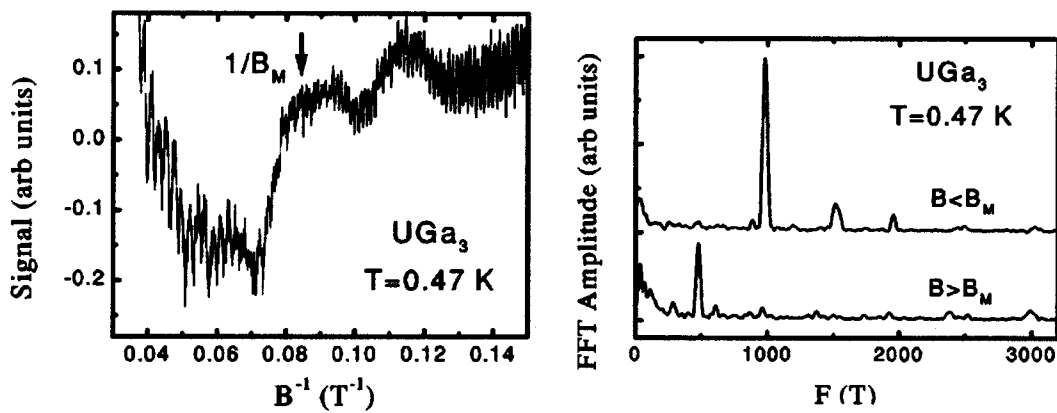
Fig. 3.17 dHvA oscillation and its FFT spectra by pulse-field magnetization in UGa₃, cited from ref. (61).

26

(a)

(b)

UGa$_3$ (AF)
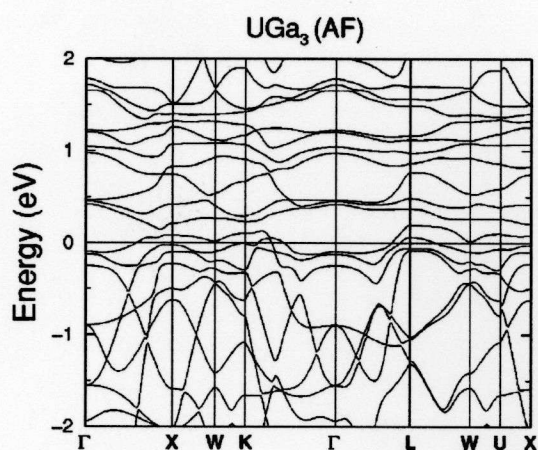
Fig. 3.18 Calculated band structure of UGa$_3$ in the antiferromagnetic state, cited from ref. (61).
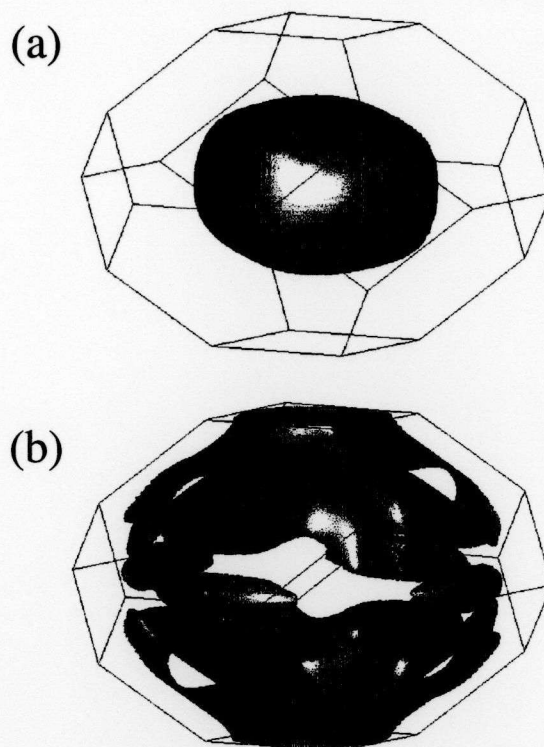
Fig. 3.19 Calculated Fermi surfaces of UGa$_3$ in the antiferromagnetic state, cited from ref. (61).

Orbit center	Fermi surface area (kT)	Band mass (m_e)
Γ	6.28	1.83
Z	2.11	1.21
	0.52	0.65

Table 3.3 Calculated Fermi surface parameters of UGa$_3$ in the antiferromagnetic state, cited from ref. (61).

U(Ga$_{1-x}$Al$_x$)$_3$, where antiferromagnetic order disappears at $x \simeq 0.2$.[78] On the other hand, in the pseudobinary alloy U(Ga$_{1-x}$Sn$_x$)$_3$, where USn$_3$ is a Kondo lattice compound, the Néel temperature initially strongly rises with increasing x, reaches a maximum value of 102 K at $x = 0.2$ and finally decreases to zero at $x \simeq 0.5$.[69]

3.4 UX$_2$ (X = P, As, Sb and Bi)

Uranium dipnictides UX$_2$ (X = P, As, Sb and Bi) crystallize in the tetragonal structure of anti-Cu$_2$Sb (D_{4h}^7 or $P4/nmm$). They order antiferromagnetically below relatively high Néel temperatures.[79-81] Magnetic moments of uranium ions are aligned ferromagnetically in the (001) planes, which are stacked along the [001] direction in an antiferromagnetic

($\uparrow\downarrow\downarrow\uparrow$) sequence in UP_2, UAs_2 and USb_2, as shown in Fig. 3.20 (a).[82–84] In the case of UBi_2, this sequence is ($\uparrow\downarrow\uparrow\downarrow$), as shown in Fig. 3.20 (b).[84] It is worth mentioning here that the magnetic unit cells of UP_2, UAs_2 and USb_2 are doubled with respect to the chemical unit cells along [001], which bring about flat magnetic Brillouin zones. The ratio of the length in the magnetic Brillouin zone is $k_c/k_a = 0.243$–0.245. On the other hand, the magnetic unit cell of UBi_2 is not elongated but the same as the chemical one, so that the magnetic Brillouin zone is not fattened, although the ratio k_c/k_a is fairly a small value of 0.499.

The characteristic properties of UX_2 (X = P, As, Sb and Bi) are summarized in Table 3.4.
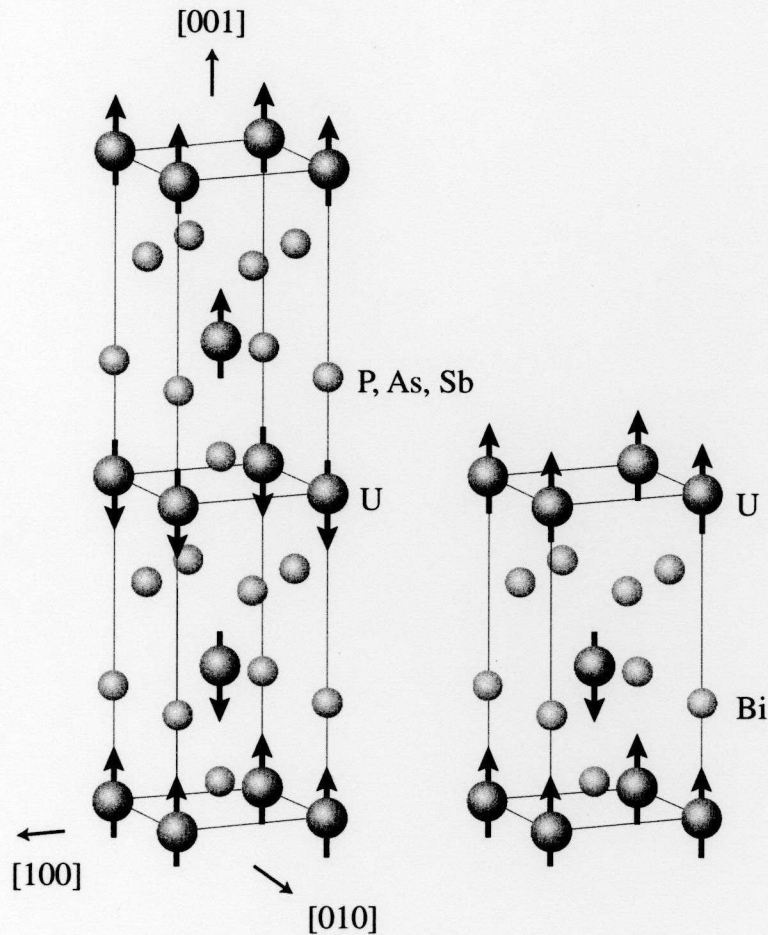

Fig. 3.20 (a) Tetragonal magnetic unit cell of UP_2, UAs_2 and USb_2. (b) Tetragonal magnetic unit cell of UBi_2

1) USb_2

USb_2 orders antiferromagnetically below $T_N = 203$ K. The ordered moment is $1.88\,\mu_B/U$.[84] A strong anisotropy of the resistivity appears in USb_2, as shown in Fig. 3.21.[85] This

Table 3.4 Characteristic properties of uranium dipnictides UX_2 (X = P, As, Sb and Bi).

	Lattice Const.		k_c/k_a	U–U dist.	T_N	γ	μ_{ord}	μ_{eff}
	c(Å)	a(Å)		(Å)	(K)	(mJ/K^{2}mol)	(μ_B/U)	(μ_B/U)
UP_2	7.76	3.80	0.245	3.81	204 (↑↓↓↑)	27	2	2.29
UAs_2	8.12	3.95	0.243	3.95	274 (↑↓↓↑)	11.7	1.61	2.94
USb_2	8.75	4.27	0.244	4.27	203 (↑↓↓↑)	26	1.88	3.04
UBi_2	8.91	4.45	0.499	4.45	181 (↑↓↑↓)	20	2.1	3.4

measurement along [001] (c-axis) was done by the Montgomery's method,[86] which is often applied to the layered sample. A large hump below T_N along [001] (c-axis) suggests the reconstruction of the Fermi surfaces due to the magnetic Brillouin zone.
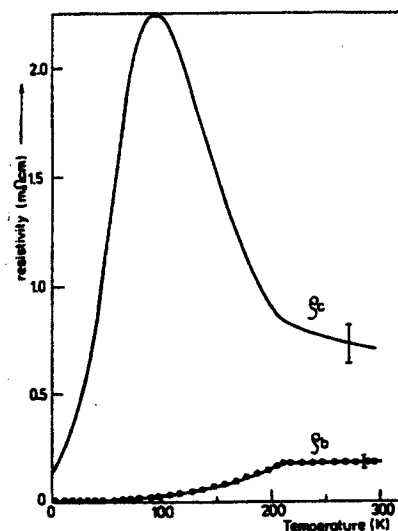
Fig. 3.21 Electrical resistivity of USb_2, cited from ref. (85).

The number of carrier is estimated at $6.2 \times 10^{21}\,\text{cm}^{-3}$ from the Hall coefficient.[85]

Most of the magnetic and thermal properties were clarified and discussed on the basis of the crystalline electric field (CEF) model and molecular field approximations.[80,87,88] In many aspects, however, the uranium compounds are different from the rare earth compounds with the localized $4f$ electrons. The $5f$ electrons in the uranium ions have an intermediate character between the localized $4f$ electrons and the itinerant $3d$ electrons in the transition metal compounds.

3.5 UCd_{11}

UCd_{11} is a heavy Fermion compound with the cubic $BaHg_{11}$-type structure, as shown in Fig. 3.22. The lattice constant is 9.29 Å and the distance between uranium ions is

$d_{\text{U-U}} = 6.56$ Å, which is much larger than the Hill limit ($d_{\text{U-U}} \simeq 3.5$ Å).[63]

The specific heat C in the form of C/T is proportional to T^2 in the temperature range from 7 to 13 K, indicating a large electronic specific coefficient γ of 840 mJ/K^{2}mol.[89] UCd$_{11}$ undergoes an antiferromagnetic transition below $T_\text{N} = 5$ K. It is noted that there appears a shoulder at 3–4 K in the specific heat. Interestingly, this shoulder is most likely changed into a small but clear peak in higher fields than 140 kOe as shown in Fig. 3.23, suggesting the second phase transition below T_N.[90]

As shown in Fig. 3.24, the magnetic susceptibility exhibits Curie–Weiss behavior above 80 K with $\mu_{\text{eff}} = 3.45\,\mu_\text{B}/\text{U}$ and $\Theta_\text{p} = -20$ K.

When external pressure is applied to UCd$_{11}$, two further transitions are inferred from anomalies in the resistivities.[91] While the exact nature of these transitions is unclear, it has been proposed that at least one of them corresponds simply to a spin reorientation of the complicated magnetic structure.

The antiferromagnetic structure is little known mainly because Cd is a neutron absorber. The previous elastic neutron scattering experiments only suggested that an ordered moment is less than $1.5\,\mu_\text{B}/\text{U}$.[92] The magnetic structure is unknown.
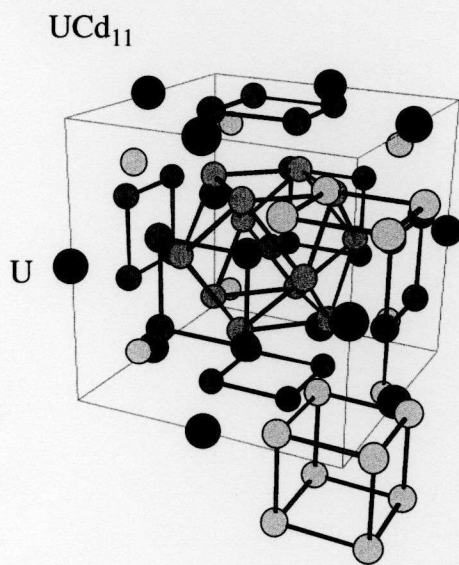

Fig. 3.22 Cubic BaHg$_{11}$-type structure of UCd$_{11}$.
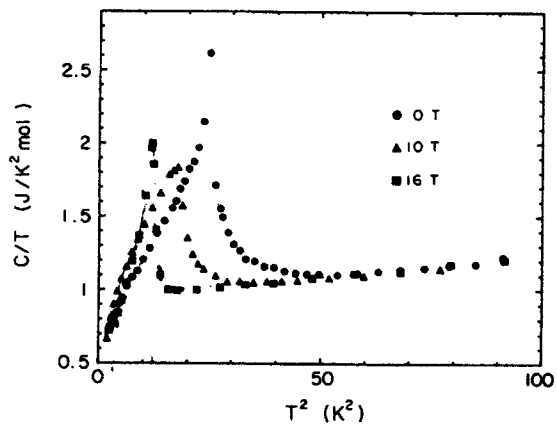
Fig. 3.23 C/T versus T^2 of UCd_{11} in $H = 0$, 10 and 16 T, cited from ref. (90).
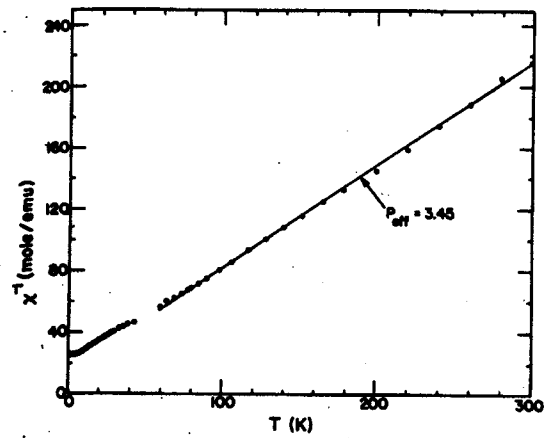

Fig. 3.24 Magnetic susceptibility of UCd_{11}, cited from ref. (89).

Chapter 4 Experimental

4.1 Single crystal growth

4.1.1 Self-flux method

The self-flux method used for the growth of single crystals corresponds to a slow cooling process of the premelted components, taken in non-stoichiometric amounts. This method is applied for obtaining single crystals of magnetic oxides and high-T_c cuprates. The advantages of this technique are:[93,94]

(1) Single crystals can be grown often well below their melting points, and this often produces single crystals with fewer defects and much less thermal strain.

(2) Flux metals offer a clean environment for growth, since the flux getters impurities which do not subsequently appear in the crystal.

(3) There are no stoichiometric problems caused, for instance, by oxidation or evaporation of one of the components. Single crystal stoichiometry "control" itself.

(4) This technique can be applied to the compounds with high evaporation pressure, since the crucible is sealed in the ampoule.

(5) No special technique is required during crystal growth and it can be done with the simple and inexpensive equipment. This is why the flux method is sometimes called "poor man's" technique.[93]

There are, to be sure, a number of disadvantages to the technique. The first and foremost is that it is no always an applicable method: an appropriate metal flux from which the desired compound will crystallize may not be found. In addition, difficulties are encountered with some flux choices, when the flux enters the crystal as an impurity. The excessive nucleation causes small crystals, which takes place either due to a too fast cooling rate, or supercooling of the melt by subsequent multiple nucleation and fast growth of large but imperfect crystals usually containing inclusion. The contamination from the crucible cannot be ignored, when reactions with materials occur at high temperatures. And finally, the ability to separate crystals from the flux at the end of growth needs special consideration.

1) Example

RPb_3 (R = Pr, Sm, Eu, Gd, Yb), $YbIn_3$, UX_3 (X = Al, Ga, In, Sn, Pb), UX_2 (X = Sb, Bi) and UCd_{11} were grown by the self-flux method. Here, we mention the process in USb_2 as an actual example. The other examples are summarized in Appendix.

We used the high-quality alumina crucible (Al_2O_3: 99.9 %) as a container with outer diameter of 15.5 mm, inner diameter of 11.5 mm and length of 60 mm. Since the crucible usually contains impurities, we clean the crucible in alcohol, and bake it up to 1070 °C under high-vacuum (less than 1×10^{-6} torr), as shown in Fig. 4.1.
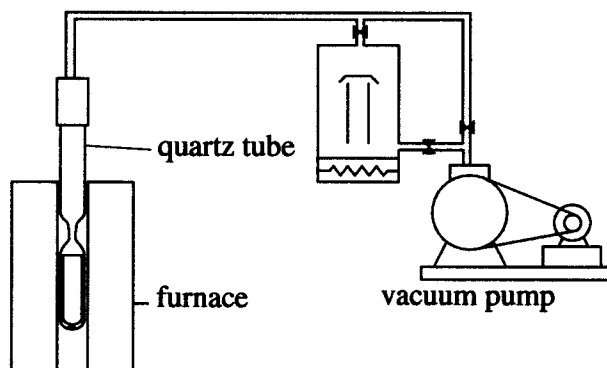

Fig. 4.1 Baking of an alumina crucible.

Figure 4.2 shows the U–Sb phase diagram. The off-stoichiometric atomic ratio of U and Sb is determined as 6.5 and 93.5 %. The melting point of this composition is 1050 °C. Generally, large crystals in size and much amount of crystals are obtained, when the ratio of the starting materials is close to the stoichiometry. However, it raises up the melting point and is prolonged for the total procedure of the growth. Contamination from the crucible may not be negligible. Furthermore, we should retain the melting point less than 1070 °C, which corresponds to just below the temperature softening quartz ampoule and the limit of the electronic furnace.

The starting material of U (purity: 99.97 %) is etched by HNO_3, and that of Sb (purity: 99.9999 %) is cleaned in alcohol by a ultrasonic washer. We put these materials into the alumina crucible and sealed in a quartz ampoule with 170 mmHg Ar pressure, which is adjusted to reach at 1 atm at the highest temperature.

Next we set the sealed ampoule in the electronic furnace, as shown in Fig. 4.3. The furnace possesses the temperature gradient naturally. As we know from our own experience, the better results is obtained when we put the ampoule where the temperature is more homogeneous. Therefore, we placed the ampoule at the highest- and the flat-temperature gradient position. Nevertheless, the temperature gradient is useful for growing some compounds. There are some reports of growing crystals by temperature gradient method (ex. GdB_6).[93]

The furnace is controlled by the PID temperature controller with Pt-PtRh13% (type-R) thermocouple. Figure 4.4 shows the block diagram of the furnace control system. In this system, we obtain the temperature stability less than 0.1 °C.

A growing process of USb_2 is presented in Fig. 4.5. Since the evaporation pressure of Sb is high, we increased the temperature with a rather low rate of 9.8 °C/hr from 600 to

33
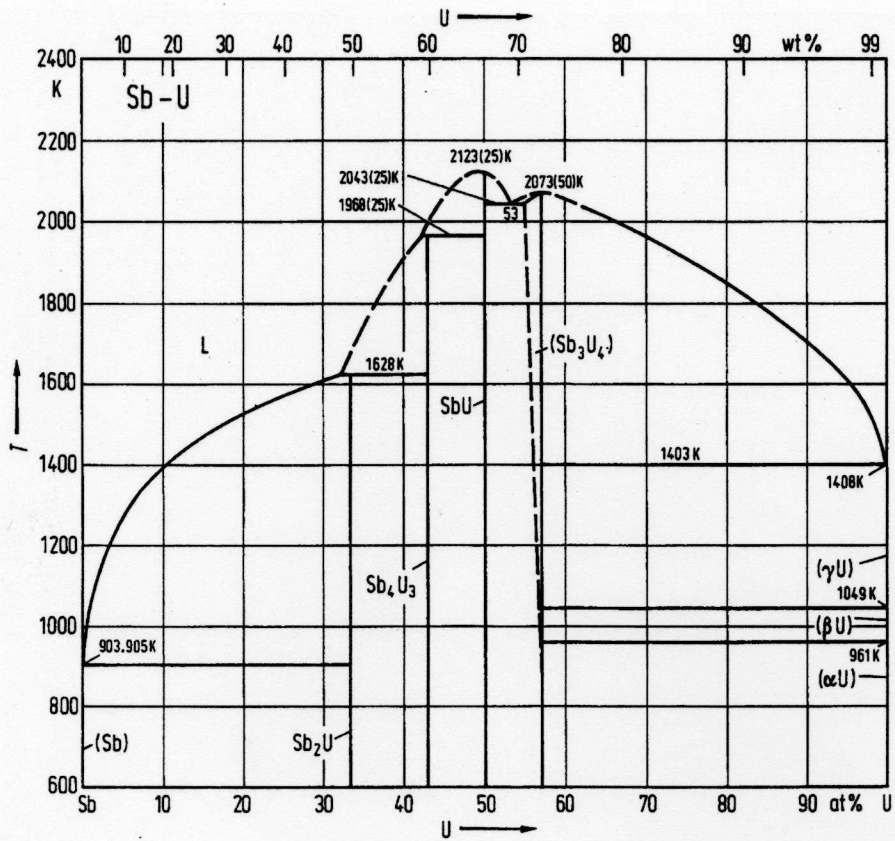
Fig. 4.2 Phase diagram of U–Sb system.
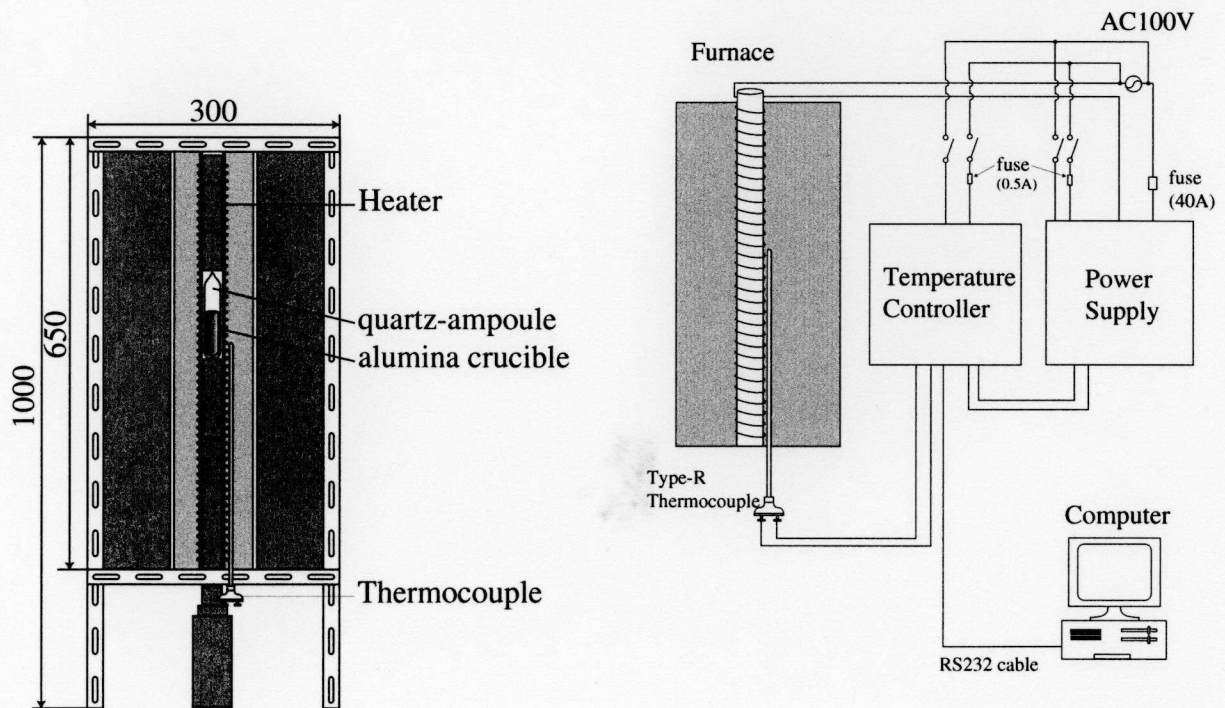
Fig. 4.3 Illustration of the electric furnace.

Fig. 4.4 Block diagram of the furnace control system.

1070 °C. Then we retained 1070 °C for 48 hours and started to decrease the temperature with 0.4 °C/h. The cooling rate was gradually increased with decreasing the temperature and the furnace was switched off at 100 °C. Here we note that the quick cooling rate might induce thermal strains of the crystal or cracks of the crucible. Total time for this process was 38 days.
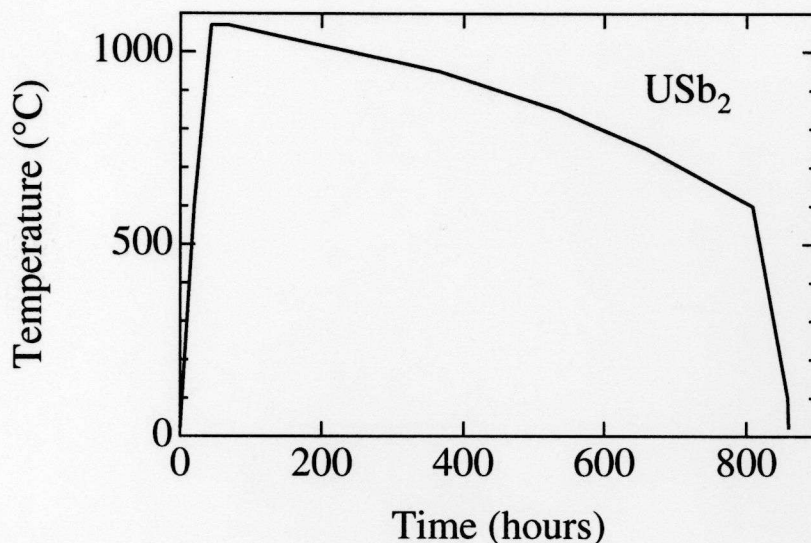
Fig. 4.5 Time dependence of the temperature during the self-flux growth of USb$_2$.

After taking out the ampoule from the furnace, we opened the ampoule and sealed it again in a quartz ampoule under high vacuum, as shown in Fig. 4.6. The ampoule was heated above the melting point of the flux (680 °C for Sb) in the muffle furnace. Next the ampoule was taken out quickly from the furnace and was set into the centrifuge. Then we removed the flux from the crystals by spinning the ampoule in the centrifuge.
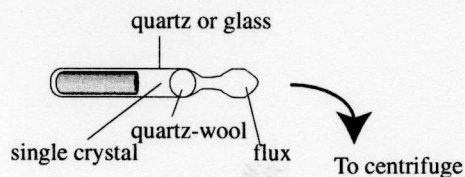
Fig. 4.6 Separation of flux and crystals by spinning the ampoule in the centrifuge.

Figure 4.7 shows the photograph of the obtained single crystal. The typical dimensions were 10 mm and 5 mm in cross-section along [100] and [001], respectively. It was easily cleaved at the (001) plane, reflecting the layered crystal structure, as mentioned in Sec. 3.4.
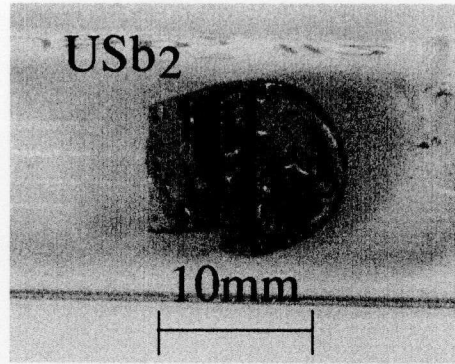
Fig. 4.7 Photograph of the USb$_2$ ingot.

4.1.2 Chemical transport method

Both UP$_2$ and UAs$_2$ were grown by the chemical transport method in a closed quartz ampoule.

Figure 4.8 schematically shows this method. In our example, transporting agent was iodine. At the lower temperature zone the feed substance decomposes forming iodine containing the gaseous components. Under the influence of the temperature gradient these components are transported into a higher temperature zone. At the higher temperature zone, iodine decomposes and the starting compound is again present. The result of crystal growth depends mainly on the choice of the temperature.

The stoichiometric amounts of U and As (P) were sealed together with $3\,\mathrm{mg/cm^3}$ iodine in an evacuated quartz ampoule. The ampoule was gradually heated up and was retained at 750 °C (800 °C) without temperature gradient. It took 4 or 5 days for pre-reaction with U and As (P). Then we set up the ampoule in the temperature gradient of 900 / 750 °C (900 / 800 °C) for 20 days. Numerous whisker-like single crystals have grown on the wall of the ampoule. In Fig. 4.9, we show a typical single crystal with dimensions of $4 \times 0.2 \times 0.05\,\mathrm{mm^3}$ along [100], [010] and [001] axes, respectively.

4.2 Electrical resistivity

4.2.1 Introduction to the electrical resistivity

An electrical resistivity consists of four contributions: the electron scattering due to impurities or defects ρ_0, the electron-phonon scattering ρ_{ph}, the electron-electron scattering $\rho_{\mathrm{e-e}}$ and the electron-magnon scattering ρ_{mag}:

$$\rho = \rho_0 + \rho_{\mathrm{ph}} + \rho_{\mathrm{e-e}} + \rho_{\mathrm{mag}}. \tag{4.1}$$

This relation is called a Matthiessen's rule.

The ρ_0-value, which originates from the electron scattering due to impurities and defects, is constant for a variation of the temperature. This value is important to know

Fig. 4.8 Schematic picture of the chemical transport method.

Fig. 4.9 Photograph of UAs$_2$ whisker-like crystals.

the quality of an obtained sample. If ρ_0 is large, the sample contains many impurities or defects. A quality of a sample can be estimated by determining a so-called residual resistivity ratio (RRR $= \rho_{RT}/\rho_0$), where ρ_{RT} is the resistivity at room temperature. Of course, a large value of RRR indicates that the quality of the sample is good.

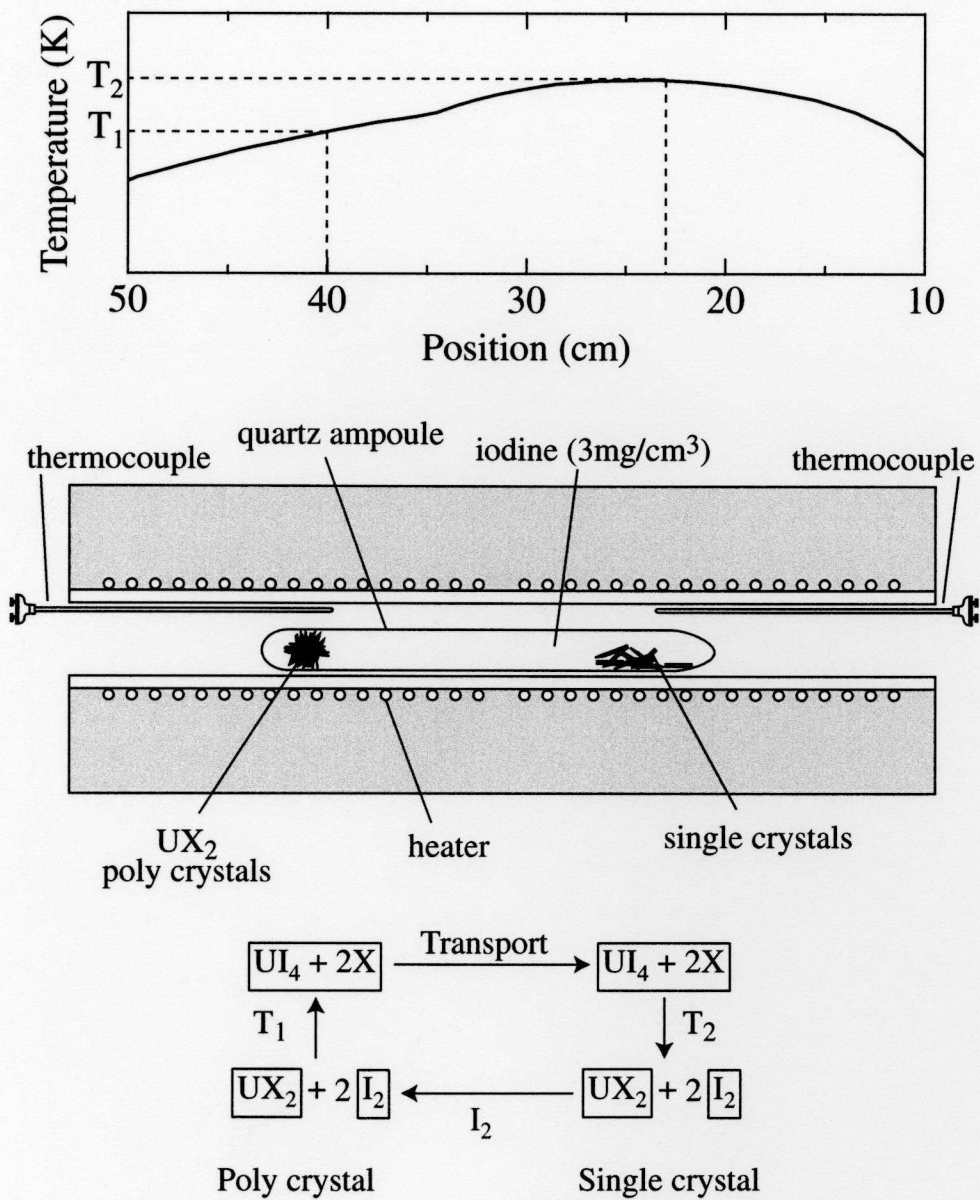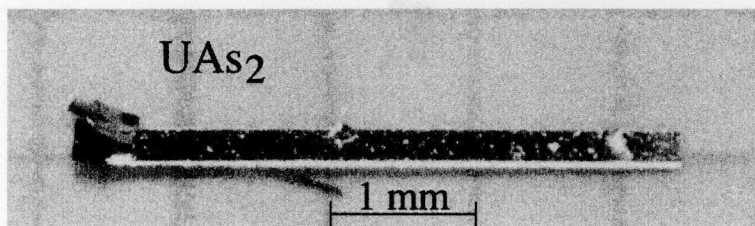Let us introduce a scattering lifetime τ_0 and a mean free path l_0 from the resistivity. The residual resistivity ρ_0 can be written as

$$\rho_0 = \frac{m^*}{ne} \cdot \frac{1}{\tau_0}, \tag{4.2}$$

where n is a density of carrier and e is an electric charge. Then τ_0 and l_0 values are

$$\tau_0 = \frac{m^*}{ne\rho_0}, \tag{4.3}$$

$$l_0 = v_F\tau_0 = \frac{\hbar k_F}{ne\rho_0}. \tag{4.4}$$

The temperature dependence of ρ_{ph}, which originates from the electron scattering by phonon, changes monotonously. ρ_{ph} is proportional to T above the Debye temperature, while it is proportional to T^5 far below the Debye temperature, and ρ_{ph} will be zero at $T = 0$.

In the strongly correlated electron system, the contribution of ρ_{e-e}, which can be expressed in terms of the reduction factor of the quasiparticle and the Umklapp process, is dominant at low temperature. Therefore, we can regard the total resistivity in non-magnetic compounds at low temperatures as follows:

$$\rho(T) = \rho_0 + \rho_{e-e}(T), \tag{4.5}$$

$$= \rho_0 + AT^2, \tag{4.6}$$

where the coefficient $\sqrt{A}$ is proportional to the effective mass. Yamada and Yosida obtained the rigorous expression of ρ_{e-e} in the strongly correlated electron system on the basis of the Fermi liquid theory.[28] According to their theory, ρ_{e-e} is proportional to the imaginary part of the f electron self-energy Δk, and Δk is written as

$$\rho_{e-e} \propto \Delta k \simeq \frac{4}{3}(\pi T)^2 \sum_{k',q} \pi D^f_{k-q}(0) \, D^f_{k'}(0) \, D^f_{k'+q}(0)$$

$$\times \left\{ \Gamma_{\uparrow\downarrow}{}^2(k, k'; k' + q, k - q) + \frac{1}{2}\Gamma_{\uparrow\uparrow}{}^{A^2}(k, k'; k' + q, k - q) \right\}, \tag{4.7}$$

where $\Gamma_{\sigma\sigma}$ is the four-point vertex, which means the renormalized scattering interaction process of $k(\sigma)k'(\sigma) \rightarrow k' + q(\sigma)k - q(\sigma)$, $\Gamma^A_{\uparrow\uparrow}$ is denoted as $\Gamma_{\uparrow\uparrow}(k_1, k_2; k_3, k_4) - \Gamma_{\uparrow\uparrow}(k_1, k_2; k_4, k_3)$, and $D^f_k(0)$ is the true (perturbed) density of states of f electrons with mutual interaction in the Fermi level. This Δk is proportional to the square of the enhancement factor and gives a large T^2-resistivity to the heavy Fermion system.

In a magnetic compound, an additional contribution to the resistivity must be taken into consideration, namely ρ_{mag}. This contribution describes scattering processes of conduction electrons due to disorder in the arrangement of the magnetic moments. In general, above the ordering temperature T_{ord}, ρ_{mag} is given by

$$\rho_{\mathrm{mag}} = \frac{3\pi N m^*}{2\hbar e^2 \varepsilon_{\mathrm{F}}} |J_{\mathrm{ex}}|^2 (g_J - 1)^2 J(J + 1), \tag{4.8}$$

where J_{ex} is the exchange integral for the direct interaction between the local moments and conduction electrons. When $T = T_{\mathrm{ord}}$, ρ_{mag} shows a pronounced kink, and when $T < T_{\mathrm{ord}}$, ρ_{mag} strongly decreases with decreasing temperature. The magnetic resistivities in the actinides, however, are ascribed to strong scattering of the conduction electrons by the spin fluctuations of $5f$ electrons. This contribution to the resistivity at low temperatures is given by the square of the temperature, namely $\rho_{\mathrm{mag}} = A'T^2$. In the heavy Fermion system, the coefficient A' is extremely large. Therefore, ρ_{mag} and $\rho_{\mathrm{e-e}}$ are inseparable and ρ_{mag} can be considered to change to $\rho_{\mathrm{e-e}}$. An analogous situation occurs to the specific heat, Namely, in the heavy Fermion system, the magnetic specific heat C_{mag} is changed into a large electronic one C_{e}.

4.2.2 Experimental method of the resistivity measurement

We have done the resistivity measurement using a standard four probe DC current method. The sample was fixed on a plastic plate by an instant glue. The gold wire with $0.025\,\mathrm{mm}$ in diameter and silver paste were used to form contacts on the sample. Spot welding method using platinum lead wire ($0.05\,\mathrm{mm}$ in diameter) were also used for small samples. The sample was mounted on a sample-holder and installed in a ^{4}He or ^{3}He cryostat. We measured the resistivity from 1.3 or $0.5\,\mathrm{K}$ to the room temperature. The thermometers are a RuO_2 registor at lower temperatures (below $20\,\mathrm{K}$) and a Au-Fe-Ag thermocouple at higher temperatures.

4.3 Specific heat

4.3.1 Introduction to the specific heat

At low temperatures, the specific heat is written as the sum of electronic, lattice, magnetic and nuclear contributions:

$$C = C_{\mathrm{e}} + C_{\mathrm{ph}} + C_{\mathrm{mag}} + C_{\mathrm{nuc}} \tag{4.9}$$

$$= \gamma T + \beta T^3 + C_{\mathrm{mag}} + \frac{A}{T^2}, \tag{4.10}$$

where A, γ and β are constants characteristic of the material.

The electronic term is linear in T and is dominant at sufficiently low temperatures. If we can neglect the magnetic and nuclear contributions, it is convenient to exhibit the experimental values of C as a plot of C/T versus T^2:

$$\frac{C}{T} = \gamma + \beta T^2. \tag{4.11}$$

Then we can estimate the electronic specific heat coefficient γ. Using the density of states, the coefficient γ can be expressed as

$$\gamma = \frac{\pi^2}{3}k_B{}^2 D(\varepsilon_F). \tag{4.12}$$

Since the the density of states based on the free electron model is proportional to the electron mass, the coefficient γ possesses an extremely large value in the heavy Fermion system.

According to the Debye T^3 law, for $T \ll \Theta_D$:

$$C_{\text{ph}} \simeq \frac{12\pi^4 N k_B}{5} \left(\frac{T}{\Theta_D}\right)^3 \equiv \beta T^3, \tag{4.13}$$

where Θ_D is the Debye temperature, N the number of atoms and R the gas constant. For the actual lattices the temperatures at which the T^3 approximation holds are quite low. It may be necessary to be below $T = \Theta_D/50$ to get a reasonably pure T^3 law.

If the f energy level splits due to the crystalline electric field (CEF) in the paramagnetic state, the inner energy per one magnetic ion is given by

$$E_{\text{CEF}} = \langle E_i \rangle = \frac{\sum\limits_i n_i E_i \exp(-E_i/k_B T)}{\sum\limits_i \exp(-E_i/k_B T)}. \tag{4.14}$$

where E_i and n_i are the energy and the degenerate degree on the level i. Thus the magnetic contribution to the specific heat is given by

$$C_{\text{Sch}} = \frac{\partial E_{\text{CEF}}}{\partial T}. \tag{4.15}$$

This contribution is called a Schottky term. Here, the entropy of the f electron S is defined as

$$S = \int_0^T \frac{C_{\text{Sch}}}{T} \, dT. \tag{4.16}$$

The entropy is also described as

$$S = R \ln W, \tag{4.17}$$

where W is a state number at temperature T. Therefore we acquire information about the CEF level.

In the magnetic ordering state C_{mag} is:

$$C_{\text{mag}} \propto T^{3/2} \qquad \text{(ferromagnetic ordering)} \qquad (4.18)$$

$$\propto T^3 \qquad \text{(antiferromagnetic ordering).} \qquad (4.19)$$

When the antiferromagnetic magnon is accompanied with the energy gap Δ_{m}, eq. (4.19) is modified to $C_{\text{mag}} \propto T^3 \exp(-\Delta_{\text{m}}/k_{\text{B}}T)$.

4.3.2 Experimental method of the specific heat

The specific heat was measured by the quasi-adiabatic heat pulse method using a dilution refrigerator, ^{3}He and ^{4}He cryostat at temperatures down to 0.2, 0.6 and 1.7 K, respectively. The sample was put on the Cu-addenda. We measured the temperature of a sample with constant heating, and the specific heat is deduced as follows:

$$C = \frac{\Delta Q}{\Delta T} = \frac{I \cdot V \cdot \Delta t}{\Delta T}. \qquad (4.20)$$

Here, ΔQ is the amount of heat, I and V are the current and the voltage flowing to the heater, respectively, Δt is the duration of heating and ΔT is the change of temperature due to heating. The temperature was measured by the RuO_2 resistor at the addenda. The specific heat of the sample is derived by subtracting the specific heat of the addenda measured.

4.4 Transverse magnetoresistance

4.4.1 Introduction to the transverse magnetoresistance

High field transverse magnetoresistance $\Delta\rho/\rho \equiv \{\rho(H) - \rho(0)\}/\rho(0)$, in which the direction of the magnetic field and the current are perpendicular to each other, provides important information on the overall topology of the Fermi surface, although the experimental technique is simple.[34] Under the high field condition of $\omega_c\tau \gg 1$, it is possible to know whether the sample under investigation is a compensated metal with an equal carrier number of electrons and holes ($n_e = n_h$), or an uncompensated metal ($n_e \neq n_h$), and whether the open orbit exists or not. Here, $\omega_c = eH/m_c^*c$ is the cyclotron frequency, τ the scattering lifetime, m_c^* the cyclotron effective mass and $\omega_c\tau/2\pi$ is the number of the cyclotron cycles performed by the carrier. The characteristic features of the high field magnetoresistance are summarized as follows for $\omega_c \gg 1$:

(1) For a given field direction, when all of the cyclotron orbits are closed orbits, (a) for the uncompensated metal the magnetoresistance saturates ($\Delta\rho/\rho \sim H^0$), and (b) for the compensated metal the magnetoresistance increases quadratically ($\Delta\rho/\rho \sim H^2$).

(2) For a given magnetic field direction, when some of the cyclotron orbits are not closed but form open orbits, the magnetoresistance increases quadratically and depends on the current direction as $\Delta\rho/\rho \sim H^2 \cos^2\alpha$, where α is the angle between the current direction and the open orbit direction in $\boldsymbol{k}$-space. This is true regardless of the state of compensation.

In Fig. 4.10 we show this transverse magnetoresistance for a metal with partially cylindrical Fermi surface whose cylinder axis is in the k_z-plane and deviates by an angle α from the k_x-axis. Here, the current $\boldsymbol{J}$ is directed along the k_x-axis and the magnetic field $\boldsymbol{H}$ rotates in the k_x-plane.

If we count the number of valence electrons of various rare earth and uranium compounds in the unit cell, most of them are even in number, meaning that they are compensated metals. In this case the transverse magnetoresistance increases as H^n ($1 < n \leq 2$) for a general direction of the field. When the magnetoresistance is saturated for a particular field direction, often a symmetrical direction, some open orbits exist whose directions are parallel to $\boldsymbol{J} \times \boldsymbol{H}$, namely $\alpha = \pi/2$ in $\boldsymbol{k}$-space. We summarize in Table 4.1 the characteristic feature of magnetoresistance in a high field at each condition.

As the magnetoresistance in the general direction is roughly equal to $(\omega_c\tau)^2$, we can estimate the $\omega_c\tau$ value. If the quality of the sample is better, the magnetoresistance becomes larger in a high field, corresponding to the longer scattering lifetime τ.

The presence of open orbits is revealed by (a) spikes against a low background for the uncompensated metal (Fig. 4.10 (c)) and (b) dips against a large background for the compensated metal (Fig. 4.10 (d)).

4.4.2 Experimental method of the magnetoresistance

The magnetoresistance experiment was carried out at temperatures down to 0.4 K (0.04 K) and fields up to 140 kOe (170 kOe) by using a superconducting magnet with a ^{3}He cryostat (dilution refrigerator). A technique of the magnetoresistance measurement is almost the same as the electrical resistivity measurement. As shown in Fig. 4.11, the current direction is fixed to a crystal symmetrical axis of the sample and the sample is rotated in a constant magnetic field which is perpendicular to the current direction.

4.5 de Haas–van Alphen effect

4.5.1 Introduction to the de Haas–van Alphen effect

Under a strong magnetic field the orbital motion of the conduction electron is quantized and forms Landau levels.[34] Therefore various physical quantities show a periodic variation with $1/H$, since increasing the field strength H causes a sharp change in the free energy of the electron system when a Landau level crosses the Fermi energy. In a three-dimensional
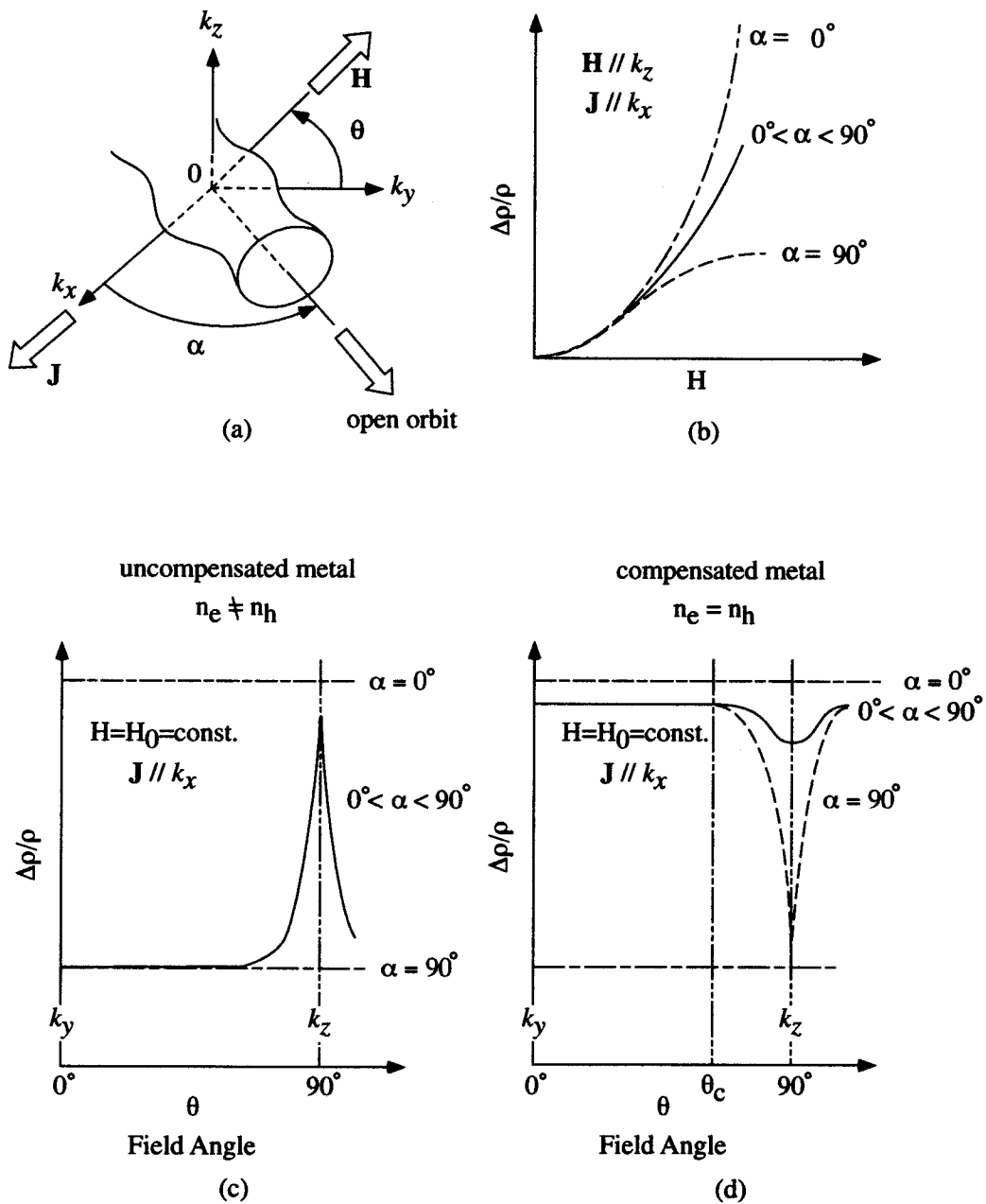
Fig. 4.10 Schematic picture of the transverse magnetoresistances in uncompensated and compensated metals when a partially cylindrical Fermi surface exists. The magnetic field H rotates in the k_x-plane.
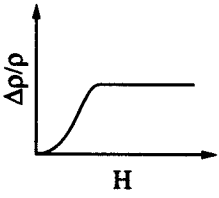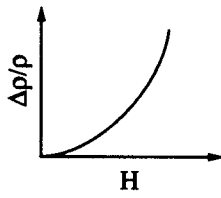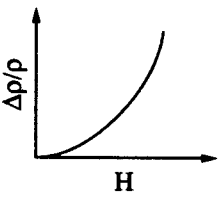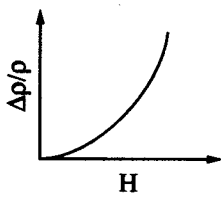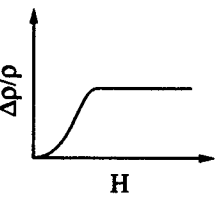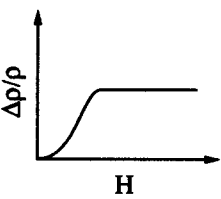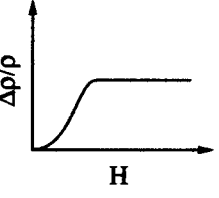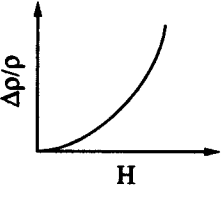
open orbit (in k-space)	uncompensated metal	compensated metal
none		
open orbit $//$ **J**		
open orbit $\perp$ **J** When an open orbit exists on the plane sliced vertical with **H**		
When no open orbit exists on the plane sliced vertical with **H**		

Table 4.1 Magnetoresistance in a high field at each condition.
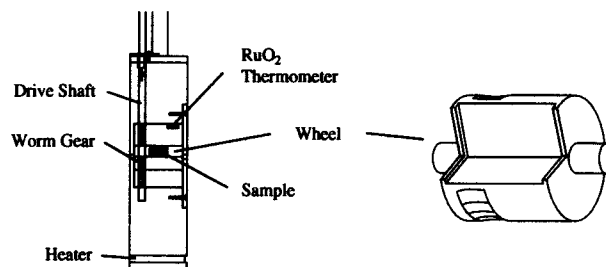
Fig. 4.11 Detailed picture of the sample holder and the inside wheel.

system this sharp structure is observed at the extremal areas in k-plane, perpendicular to the field direction and enclosed by the Fermi energy because the density of states also becomes extremal. From the field and temperature dependences of various physical quantities, we can obtain the extremal area S, the cyclotron mass m_c^* and the scattering lifetime τ for this cyclotron orbit. The magnetization or the magnetic susceptibility is the most common one of these physical quantities, and its periodic character is called the de Haas-van Alphen (dHvA) effect. It provides one of the best tools for the investigation of Fermi surfaces of metals.

The theoretical expression for the oscillatory component of magnetization M_{osc} due to the conduction electrons was given by Lifshitz and Kosevich as follows:

$$M_{\mathrm{osc}} = \sum_r \sum_i \frac{(-1)^r}{r^{3/2}} A_i \sin\left(\frac{2\pi r F_i}{H} + \beta_i\right), \tag{4.21}$$

$$A_i \propto H^{1/2} \left|\frac{\partial^2 S_i}{\partial k_H^2}\right|^{-1/2} R_{\mathrm{T}} R_{\mathrm{D}} R_{\mathrm{S}}, \tag{4.22}$$

$$R_{\mathrm{T}} = \frac{\lambda r m_{ci}^* T/H}{\sinh(\lambda r m_{ci}^* T/H)}, \tag{4.23}$$

$$R_{\mathrm{D}} = \exp(-\lambda r m_{ci}^* T_{\mathrm{D}}/H), \tag{4.24}$$

$$R_{\mathrm{S}} = \cos(\pi g_i r m_{ci}^*/2m_0), \tag{4.25}$$

$$\lambda = 2\pi^2 c k_{\mathrm{B}}/e\hbar. \tag{4.26}$$

Here the magnetization is periodic on $1/H$ and has a dHvA frequency F_i:

$$F_i = \frac{\hbar c}{2\pi e} S_i, \tag{4.27}$$

which is directly proportional to the i-th extremal (maximum or minimum) cross-sectional area S_i ($i = 1, \ldots, n$). The extremal area means a gray plane in Fig. 4.12, where there is one extremal area in a spherical Fermi surface. On the other hand, three extremal areas exist in a gourd-shaped Fermi surface.

The factor R_{T} in the amplitude A_i is related to the thermal damping at finite temperature T. The factor R_{D} is also related to the Landau level broadening $k_{\mathrm{B}} T_{\mathrm{D}}$. Here T_{D} is due to both the lifetime broadening and inhomogeneous broadening caused by impurities, crystalline imperfections and strains. T_{D} is called the Dingle temperature and is given by

$$T_{\mathrm{D}} = \frac{\hbar}{2\pi k_{\mathrm{B}}} \frac{1}{\tau}. \tag{4.28}$$

The factor R_{S} is called the spin factor, and related to the difference of phase between the Landau levels due to the Zeeman split. When $g_i = 2$ (free electron value) and $m_{ci}^* = 0.5 m_0$, this term becomes zero for $r = 1$. The fundamental oscillation vanishes for all values of the field. This is called the zero spin-splitting situation in which the up and down spin contributions to the oscillation cancel out, and this can be useful for
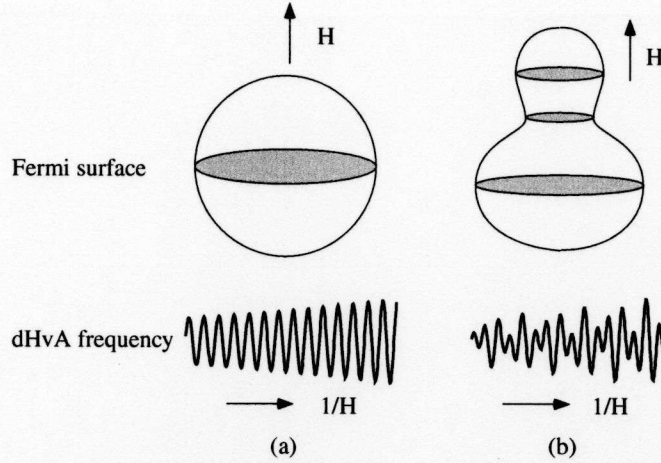
Fig. 4.12 Simulations of the cross-sectional area and its dHvA signal for a simple Fermi surface. There is one dHvA frequency in (a), while there are three different frequencies in (b)

determining the value of g_i. Note that in this situation the second harmonics for $r = 2$ should gave a full amplitude.

The quantity $|\partial^2 S/\partial k_H{}^2|^{-1/2}$ is called the curvature factor. The rapid change of the cross-sectional area around the extremal area along the field direction diminishes the dHvA amplitude for this extremal area.

The detectable conditions of dHvA effect are as follows:

(1) The distance between the Landau levels $\hbar\omega_c$ must be larger than the thermal broadening width $k_B T$: $\hbar\omega_c \gg k_B T$ (high fields and low temperatures).

(2) At least one cyclotron motion must be performed during the scattering, namely $\omega_c \tau/2\pi > 1$ (high-quality sample). In reality, however it can be observed even if a cyclotron motion is about 10 % of one cycle.

(3) The fluctuation of the static magnetic field must be smaller than the field interval of one cycle of the dHvA oscillation (homogeneity of the magnetic field).

4.5.2 Shape of the Fermi surface

The angular dependence of dHvA frequency gives very important information about a shape of the Fermi surface. As a volume of Fermi surface corresponds to a carrier number, we can also obtain the carrier number of metal directly.

We show the typical Fermi surfaces and their angular dependences of dHvA frequencies in Fig. 4.13. In a spherical Fermi surface, the dHvA frequency is constant for any field direction. On the other hand, in a cylindrical Fermi surface (Fig. 4.13 (b)) the frequency increases as a function of $1/\cos\theta$ (θ is a tilted angle from k_z to k_x or k_y). In an ellipsoidal

46

Fermi surface (Fig. 4.13 (c)) the angular dependence of the frequency is more complicated. These relatively simple shaped Fermi surfaces can be determined only by the experiment. The complicated Fermi surface, however, requires the information from an energy band calculation.
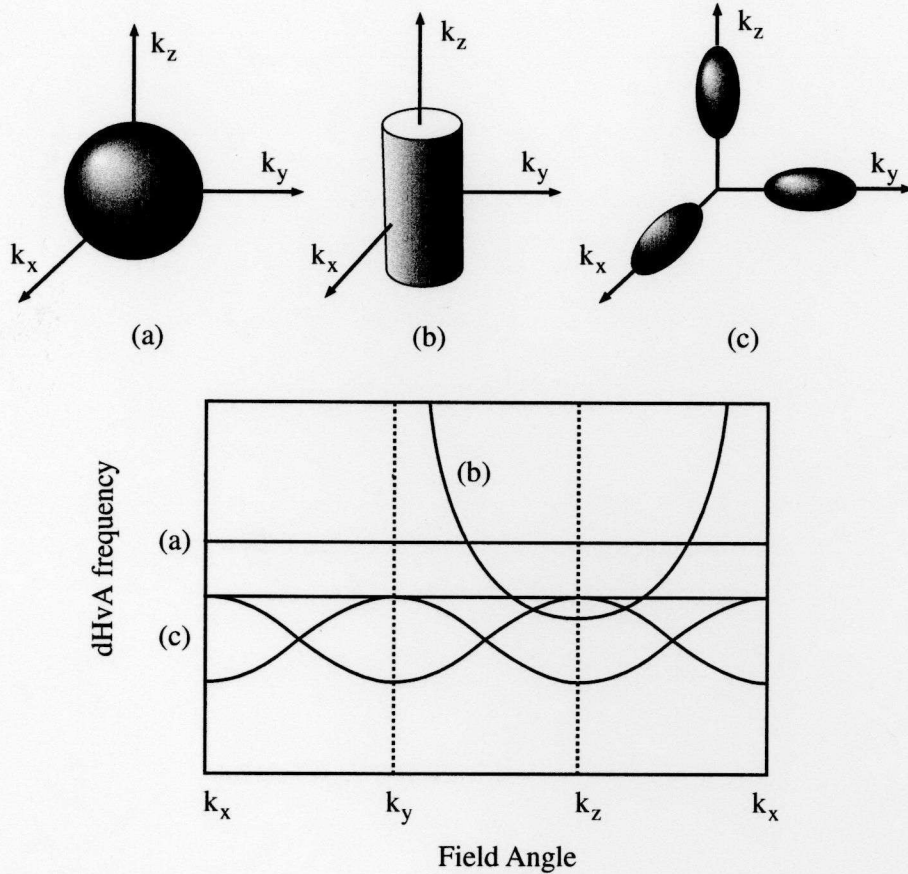
Fig. 4.13 Angular dependence of the dHvA frequency in three typical Fermi surfaces (a) sphere, (b) cylinder and (c) ellipsoid

4.5.3 Cyclotron effective mass

We can determine the cyclotron effective mass m_{ci}^* from the temperature dependence of the dHvA amplitude. Equation (4.23) is transformed into:

$$\ln\left\{\frac{A_i}{T}\left[1 - \exp\left(\frac{-2\lambda m_{ci}^* T}{H}\right)\right]\right\} = -\frac{\lambda m_{ci}^*}{H}T + \text{const.} \qquad (4.29)$$

We can obtain the cyclotron mass from the slope of a plot (so-called mass plot) of $\ln\{A_i[1-\exp(-2\lambda m_{ci}^* T/H)]/T\}$ versus T at constant field H by using a method of successive approximation.

Let us consider the relation between the cyclotron mass and the electronic specific heat coefficient γ. Using a density of states $D(\varepsilon_F)$, γ is described as

$$\gamma = \frac{\pi^2}{3} k_B{}^2 D(\varepsilon_F). \tag{4.30}$$

In the spherical Fermi surface, using $\varepsilon_F = \hbar^2 k_F^2 / 2m_c^*$ takes

$$\gamma = \frac{\pi^2}{3} k_B^2 \cdot \frac{V}{2\pi^2} \left(\frac{2m_c^*}{\hbar^2} \right)^{3/2} \varepsilon_F{}^{1/2} \tag{4.31}$$

$$= \frac{k_B{}^2 V}{3\hbar^2} m_c^* k_F, \tag{4.32}$$

where V is molar volume.

In the case of the cylindrical Fermi surface, the density of states is

$$D(\varepsilon_F) \equiv \left. \frac{\partial N}{\partial \varepsilon} \right|_{\varepsilon_F} = \frac{\partial}{\partial \varepsilon} \left[2Sk_z \left/ \left(\frac{(2\pi)^3}{V} \right) \right. \right]_{\varepsilon_F} \tag{4.33}$$

$$= \frac{k_z V}{4\pi^3} \cdot \left. \frac{\partial S}{\partial \varepsilon} \right|_{\varepsilon_F}, \tag{4.34}$$

where the Fermi wave number k_z is parallel to axial direction of the cylinder, and S is the cross-sectional area of the cylindrical Fermi surface. Since the cyclotron effective mass is written as:

$$m_c^* = \frac{\hbar^2}{2\pi} \left. \frac{\partial S}{\partial \varepsilon} \right|_{\varepsilon_F}, \tag{4.35}$$

we obtain the γ-value from eqs. (4.30), (4.34) and (4.35) as:

$$\gamma = \frac{k_B{}^2 V}{6\hbar^2} \cdot m_c^* k_z. \tag{4.36}$$

We regard the Fermi surfaces as sphere, ellipse or cylinder approximately and then can calculate the γ-values.

4.5.4   Dingle temperature

We can determine the Dingle temperature T_D from measuring the field dependence of the dHvA amplitude. Equations (4.22)-(4.24) yield

$$\ln \left[A_i H^{1/2} \sinh \left(\frac{\lambda m_{ci}^* T}{H} \right) \right] = -\lambda m_{ci}^* T_D \cdot \frac{1}{H} + \text{const.} \tag{4.37}$$

We can obtain the Dingle temperature from the slope of a plot (so-called Dingle plot) of $\ln[A_i H^{1/2} \sinh(\lambda m_{ci}^* T/H)]$ versus $1/H$ at constant T. Here, the cyclotron effective mass must have already been obtained.

We can estimate the mean free path l or the scattering lifetime τ from the Dingle temperature. The relation between the effective mass and the lifetime takes the form:

$$\hbar k_{\mathrm{F}} = m_{\mathrm{c}}^* v_{\mathrm{F}}, \tag{4.38}$$

$$l = v_{\mathrm{F}}\tau. \tag{4.39}$$

Then eq. (4.28) is transformed into

$$l = \frac{\hbar^2 k_{\mathrm{F}}}{2\pi k_{\mathrm{B}} m_{\mathrm{c}}^* T_{\mathrm{D}}}. \tag{4.40}$$

4.5.5 Field modulation method

Experiments of the dHvA effect were conducted by using the usual ac susceptibility field modulation method. Here we give an outline of the field modulation method in the present study.

A small ac field $h_0 \cos \omega t$ is varied on an external field H_0 ($H_0 \gg h_0$) in order to obtain the periodic variation of the magnetic moment. The sample is placed in a pair of balanced coils (pick up and compensation coils) as shown in Fig. 4.14. Induced e.m.f. V will be proportional to

$$V = c\frac{\mathrm{d}M}{\mathrm{d}t} \tag{4.41}$$

$$= c\frac{\mathrm{d}M}{\mathrm{d}H}\frac{\mathrm{d}H}{\mathrm{d}t} \tag{4.42}$$

$$= -ch_0\omega \sin \omega t \sum_{k=0}^{\infty} \frac{h_0{}^k}{2^{k-1}(k-1)!} \left(\frac{\mathrm{d}^k N}{\mathrm{d}H^k}\right)_{H_0} \sin k\omega t, \tag{4.43}$$

where c is the constant which is fixed by the number of turns in the coil and so on, and the higher differential terms of the coefficient of $\sin k\omega t$ are neglected. Calculating the $(\mathrm{d}^k M/\mathrm{d}H^k)$, it becomes

$$V = -c\omega A \sum_{k=1}^{\infty} \frac{1}{2^{k-1}(k-1)!} \left(\frac{2\pi h_0}{\Delta H}\right)^k \sin \left(\frac{2\pi F}{H} + \beta - \frac{k\pi}{2}\right) \cdot \sin k\omega t. \tag{4.44}$$

Here, $\Delta H = H^2/F$. Considering $h_0{}^2 \ll H_0{}^2$, the time dependence of the magnetization $M(t)$ is given by

$$M(t) = A\left[J_0(\lambda) \sin \left(\frac{2\pi F}{H_0} + \beta\right) + 2\sum_{k=1}^{\infty} kJ_k(\lambda) \cos k\omega t \cdot \sin \left(\frac{2\pi F}{H} + \beta - \frac{k\pi}{2}\right)\right], \tag{4.45}$$

where

$$\lambda = \frac{2\pi F h_0}{H_0{}^2}. \tag{4.46}$$

49

Here, J_k is the Bessel function of the first kind of order k. Finally we can obtain the output e.m.f. as follows;

$$V = c \left(\frac{dM}{dt} \right) = -2c\omega A \sum_{k=1}^{\infty} k J_k(\lambda) \sin \left(\frac{2\pi F}{H} + \beta - \frac{k\pi}{2} \right) \cdot \sin k\omega t. \tag{4.47}$$

The signal was detected at the second harmonic of the modulation frequency 2ω using a Lock-in-Amplifier, since this condition may cut off the offset magnetization and then detect the component of the quantum oscillation only. We usually choose the modulation field h_0 to make the value of $J_2(\lambda)$ maximum, namely $\lambda = 3.05$. Figure 4.15 shows the Bessel function of the first kind for the various order k. The typical values of the modulation frequency were 159 Hz for the ^{3}He cryostat and 21 Hz for the dilution refrigerator. Figure 4.16 shows a block diagram for the dHvA measurement in the present study.
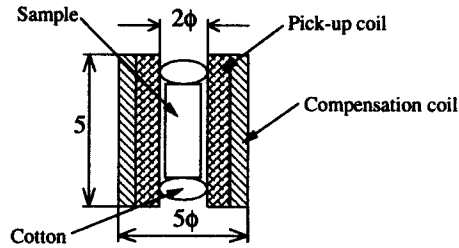
Fig. 4.14 The detecting coil and the sample location.
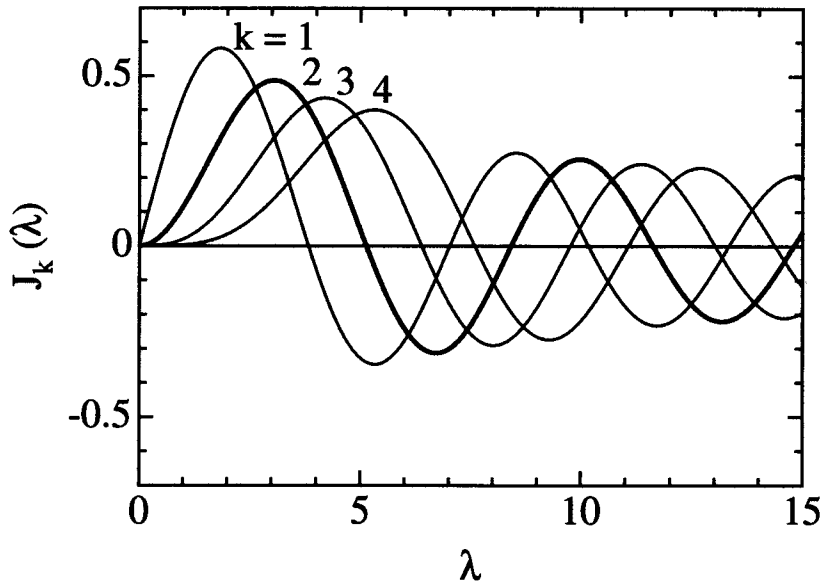
Fig. 4.15 Bessel function $J_k(\lambda)$ of the first kind.

50
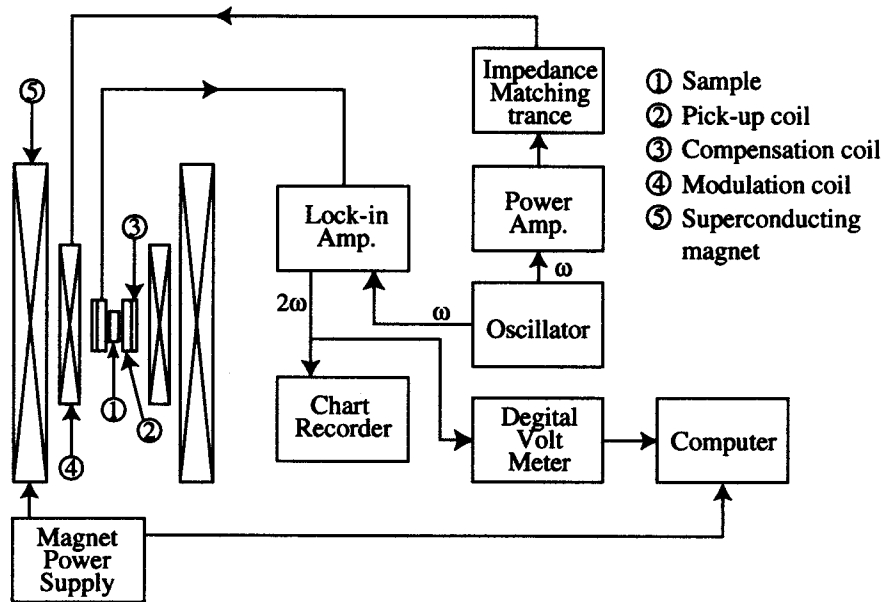
Fig. 4.16 Bock diagram for the dHvA measurement.

4.6 Shubnikov–de Haas effect

4.6.1 Introduction to the Shubnikov–de Haas effect

The Shubnikov–de Haas (SdH) effect is the dHvA oscillation reflected in the field dependence of the electrical resistivity.[95] The theory of the effect[96] is quite complicated, since it involves the detailed problem of electron scattering in a magnetic field. On the basis of the simple model,[97] however, the probability of scattering is proportional to the number of states into which the electrons can be scattered, and so this probability, which determines the scattering lifetime τ and the resistivity, will oscillate in sympathy with the oscillation of the density of states at the Fermi energy.

Actually, the observed oscillations follows the Lifshitz–Kosevich formula, as described in eqs. (4.21)-(4.26). Thus the obtained physical quantities from the SdH effect are the same as those from the dHvA effect.

The SdH measurement is also a useful method especially for tiny samples. Because the SdH amplitude depends on the electrical potential on the sample detected as the resistivity. On the other hand, the dHvA effect requires the large volume of the sample, which is proportional to the dHvA amplitude.

4.6.2 Experimental method of the Shubnikov–de Haas effect

We have done the SdH measurements using a standard four probe DC current method. The gold wire and silver paste were used to form contacts on the sample. The sample holder was set as shown in Fig. 4.17. We carried out the measurements by using a field

51

modulation method as if to observe the dHvA effect at temperature down to 0.4 K and fields up to 140 kOe. Current and modulation frequency were typically 3 mA and 159 Hz, respectively.
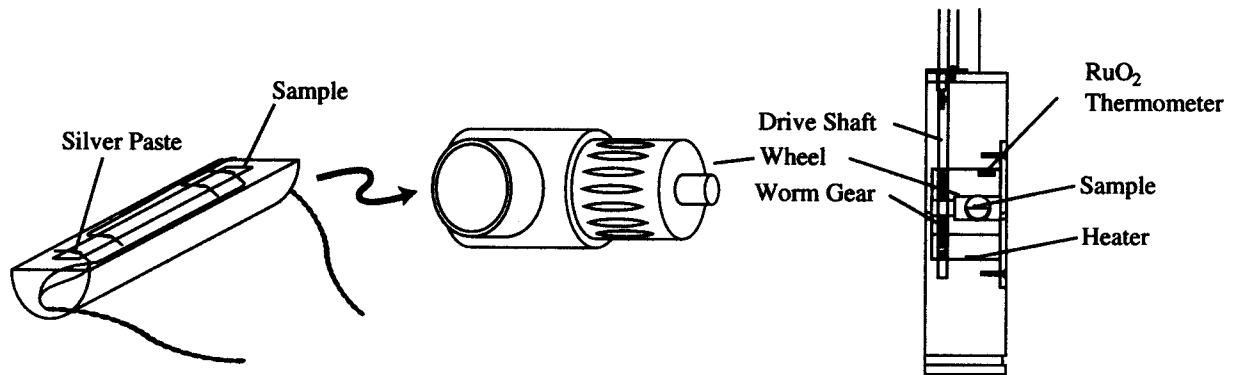
Fig. 4.17 Detailed picture of the sample holder and the inside wheel for the SdH effect.

Chapter 5   Experimental Results and Discussion

5.1   PrPb$_3$

5.1.1   Specific heat

We have measured the specific heat in the temperature range from 0.2 to 70 K.[36,98,99] In Fig. 5.1, we show the temperature dependence of the magnetic specific heat C_m in the low temperature range. The magnetic part of the specific heat was obtained by subtracting the phonon part of a non-f reference compound LaPb$_3$. The sharp λ like peak at 0.4 K corresponds to the quadrupolar ordering. This result is in good agreement with the previous specific heat data obtained by Bucher *et al.*, which displays the peak at 0.35 K, as shown in Fig 3.3.[38] A large slope from 0.4 K up to the vicinity of 1 K indicates that the short-range quadrupolar ordering starts from a higher temperature than the quadrupolar ordering temperature of 0.4 K.
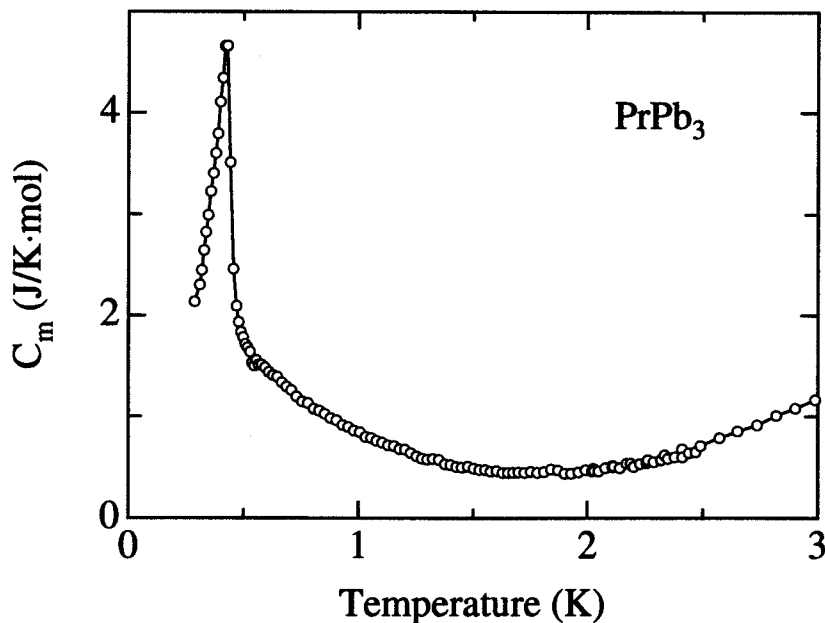
Fig. 5.1 Magnetic specific heat of PrPb$_3$.

We also show in Fig. 5.2 the temperature dependence of the magnetic entropy S_m. The magnetic entropy S_m was obtained by integrating C_m/T over T. The entropy reaches $R\ln 2$ at 5 K, $R\ln 5$ at 20 K and $R\ln 8$ at 38 K, although the data are a little scattered in the temperature range of 35 to 50 K. The present data are almost consistent with the $4f$ energy scheme shown in an inset of Fig. 5.2 with the ground state of the Γ_3 non-Kramers doublet.
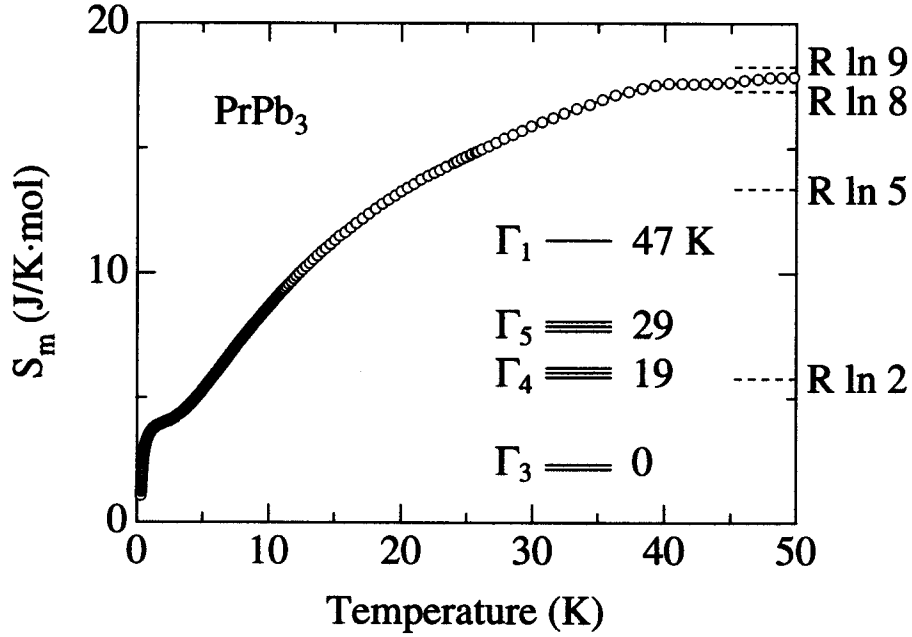
Fig. 5.2 Temperature dependence of the magnetic entropy for PrPb$_3$. The inset shows the 4f level scheme determined by the neutron experiment, cited from ref. (39).

5.1.2 dHvA effect

Figure 5.3 shows the typical dHvA oscillation and the corresponding fast Fourier transformation (FFT) spectrum for the field along the ⟨100⟩ direction in the field range from 110 to 130 kOe. Branches α, β, γ and δ correspond to main Fermi surfaces. Figure 5.4 shows the angular dependence of the dHvA frequency. Since the frequency of the main dHvA branches α, β, γ and δ are almost constant against the field angle, the main dHvA branches correspond to nearly spherical Fermi surfaces. The experimental results of PrPb$_3$ are compared to those of the non-f reference compound LaPb$_3$ shown in Fig. 5.5.

The angular dependence of the main dHvA branches in PrPb$_3$ is in good agreement with that of LaPb$_3$. Therefore we can treat the Fermi surfaces of PrPb$_3$ as those of LaPb$_3$. The theoretical angular dependence of the dHvA frequency, which has been calculated on the basis of the full potential linear augmented plane wave (FLAPW) method, is also shown in Fig. 5.6 for comparison. The experimental results of the main Fermi surfaces in LaPb$_3$ and PrPb$_3$ are in good agreement with the results of band calculations. We show in Fig. 5.7 the calculated Fermi surfaces based on the FLAPW method. The origin of the main branches is as follows:

    branch α: a band-11 hole Fermi surface centered at the R point
    branch β: a band-11 hole one centered at the Γ point
    branch γ: a band-10 hole one centered at the Γ point
    branch δ: band-11 hole ones, which are twelve in number
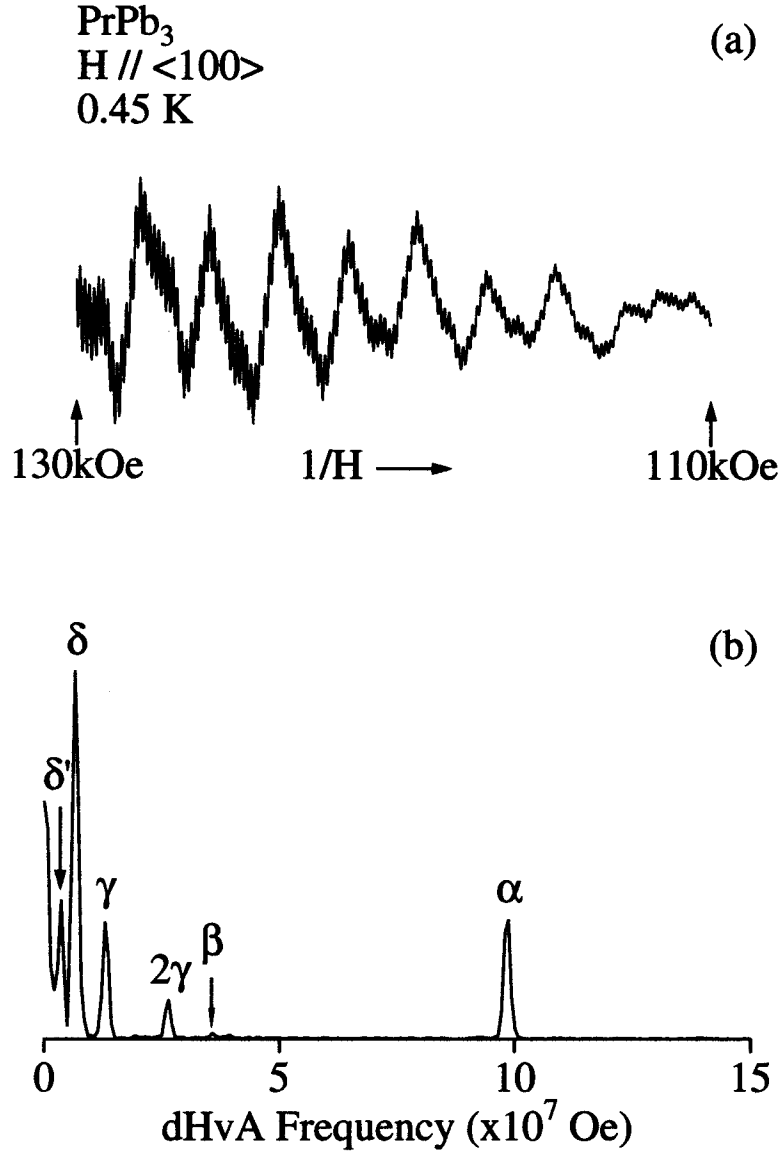
Fig. 5.3 (a) dHvA oscillation and (b) its FFT spectrum for the field along the ⟨100⟩ direction for PrPb$_3$.

The band-10 hole Fermi surface in Fig. 5.7, centered at the Γ point, is almost spherical. This corresponds to branch γ. The band-11 hole Fermi surface, centered at the Γ point, is also almost spherical, but a little distorted like a regular octahedron swelled to the ⟨100⟩ direction. This is reflected in an increase of the dHvA frequency on branch β for the field along the ⟨100⟩ direction. The band-11 hole Fermi surfaces, which is in the shape of a pillow, correspond to branches δ and δ'. The band-11 hole Fermi surface, centered at the R point, is again a nearly spherical one, which corresponds to branch α. This Fermi surface is the largest in volume.

We have determined the cyclotron effective mass m_c^* from the temperature dependence
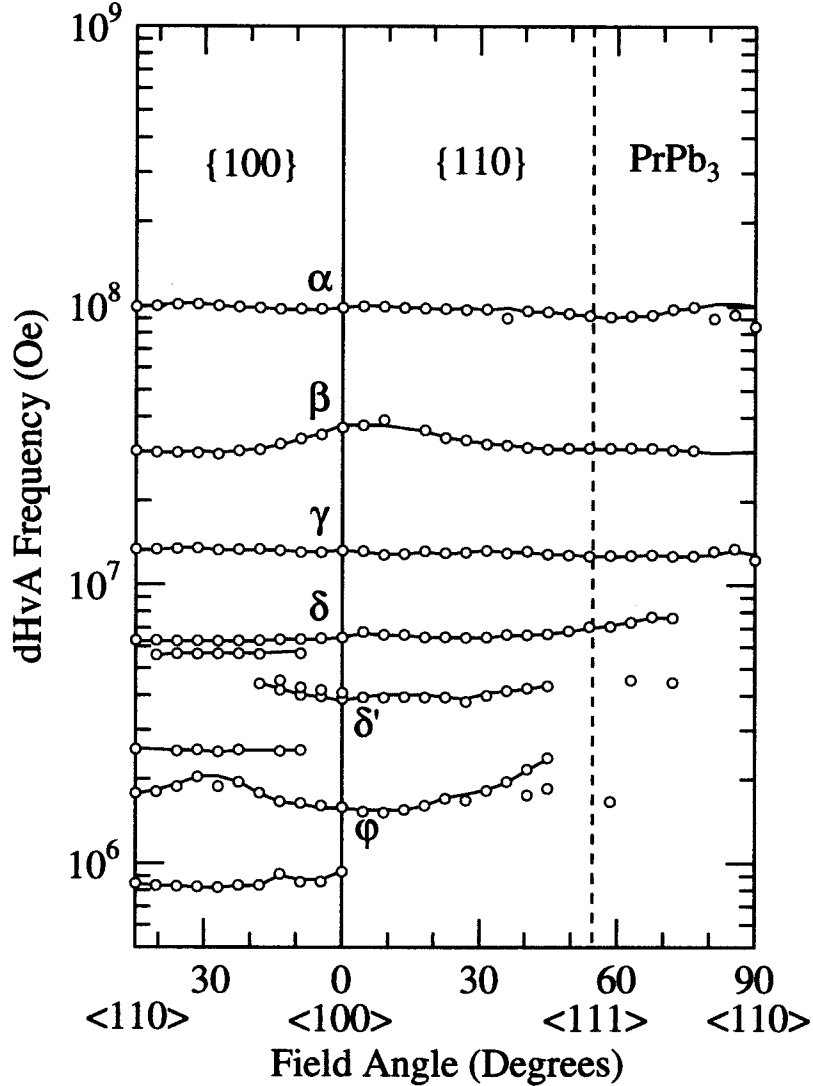
Fig. 5.4 Angular dependence of the dHvA frequency in $PrPb_3$.

of the dHvA amplitude by using eq. (4.29), as mentioned above. The cyclotron masses, which have been determined in the temperature range of 0.45 to 1.2 K, are shown in Table 5.1 for the principal field directions, where m_0 denotes the free electron mass. We also show the Dingle temperature T_D in Table 5.1, which has been determined from the field dependence of the dHvA amplitude by using eq. (4.37) under a constant temperature of 0.45 K, as mentioned above. The mass is in the range from $0.87\,m_0$ to $6.7\,m_0$. Here we note that the mass of the main branch α is heavy, ranging from $3.7\,m_0$ to $6.7\,m_0$. The cyclotron masses of $PrPb_3$, $NdPb_3$, $LaPb_3$ and the band mass of $LaPb_3$ are summarized in Table 5.2 for comparison. The cyclotron masses of $PrPb_3$ are 1 to 2.5 times larger than those of $NdPb_3$, 2 to 6 times larger than those of $LaPb_3$ and 2 to 7 times larger than the
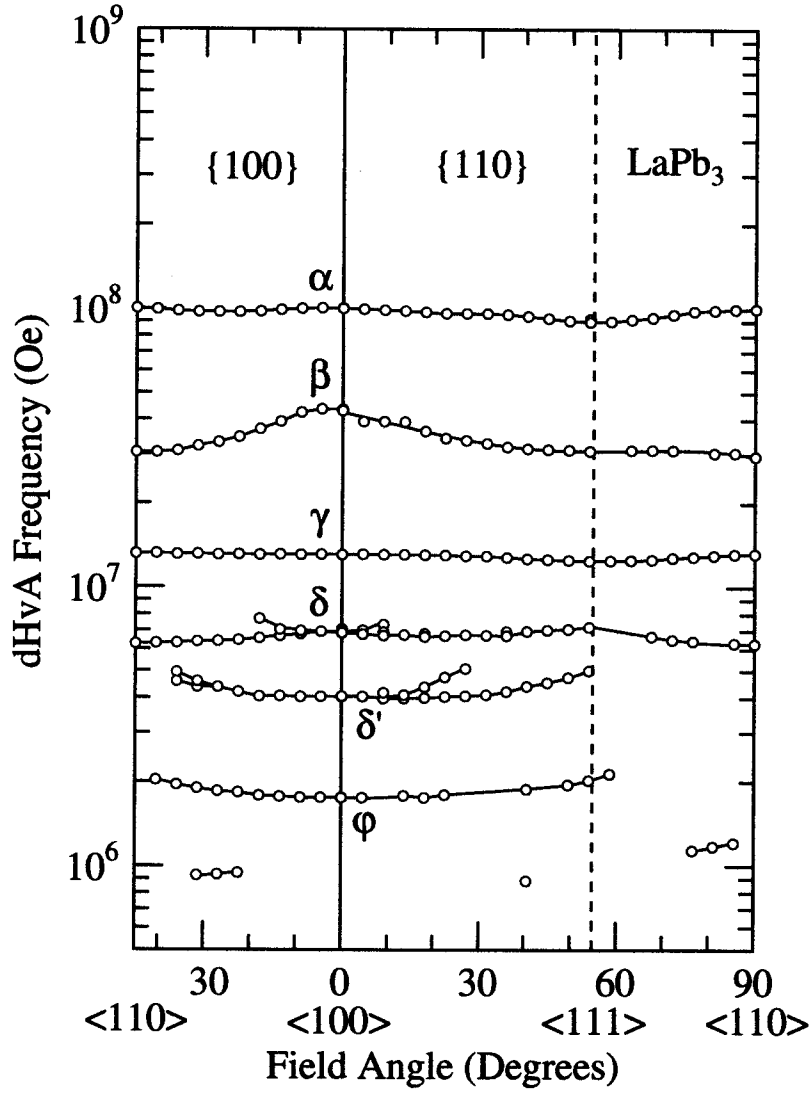
Fig. 5.5 Angular dependence of the dHvA frequency in LaPb$_3$.

Table 5.1 dHvA frequency F, cyclotron mass m_c^* and Dingle temperature T_D in PrPb$_3$.

	$H // \langle 110 \rangle$				$H // \langle 100 \rangle$				$H // \langle 111 \rangle$		
	F ($\times 10^6$ Oe)	m_c^* (m_0)	T_D (K)		F ($\times 10^6$ Oe)	m_c^* (m_0)	T_D (K)		F ($\times 10^6$ Oe)	m_c^* (m_0)	T_D (K)
α	99.1	6.7	—	α	98.5	3.7	2.2	α	93.8	4.9	—
β	30.2	3.9	—	β	36.7	—	—				
γ	13.4	2.0	1.9	γ	13.3	2.2	2.0	γ	13.0	1.9	2.8
δ	6.30	1.2	2.4	δ	6.45	2.5	1.7	δ	7.09	—	—
				δ'	3.88	1.3	—				
φ	1.78	1.1	2.2	φ	1.59	0.98	1.0				
	0.85	0.87	1.4								

57

Fig. 5.6 Theoretical angular dependence of the dHvA frequency for the non-f reference compound LaPb$_3$.

band masses.

We have also analyzed the temperature dependence of the cyclotron mass in a much wider temperature range down to 0.03 K, crossing the antiferroquadrupolar ordering. Figure 5.8 shows the so-called mass plot on branch γ for the field along the $\langle 100 \rangle$ direction. In general the mass plot mentioned above is expected to be a straight line whose slope gives the cyclotron mass. However, the slope of the mass plot shown in Fig. 5.8 increases with decreasing the temperature. This suggests an increasing of the mass below about 1 K. The straight line in Fig. 5.8 whose slope gives 1.5 m_0 is fitted only in the temperature range from 1.5 to 1.0 K. To obtain the temperature dependence of the mass in detail,

LaPb₃

band 10
hole

(a)

band 11
hole

(b)

band 11
hole

(c)
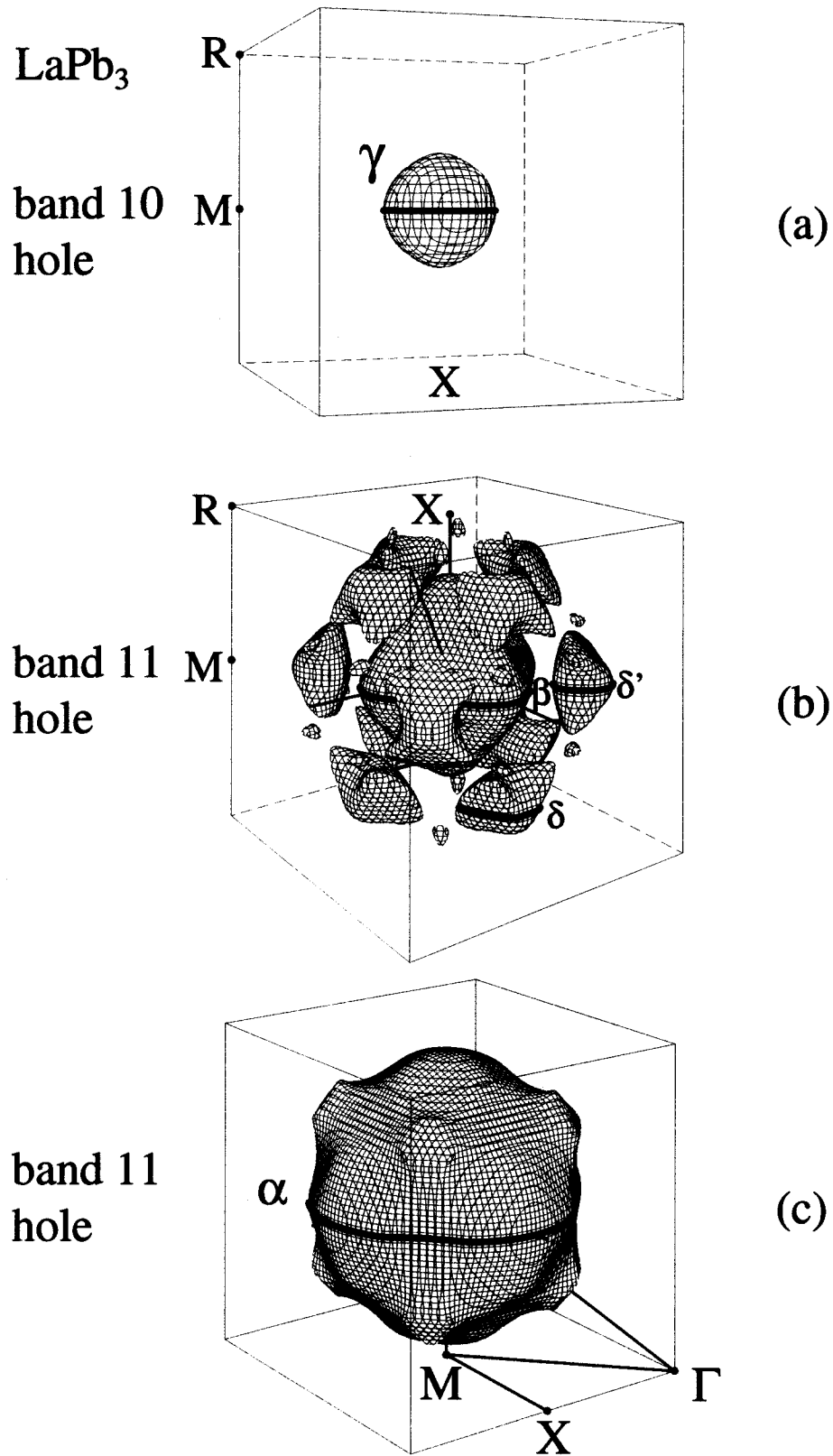
Fig. 5.7 Fermi surfaces in LaPb₃: (a) hole in band 10 centered at the Γ point, (b) hole in band 11 centered at the Γ point, (c) hole in band 11 centered at the R point.

Table 5.2 Cyclotron masses in $PrPb_3$, $NdPb_3$ and $LaPb_3$ and band mass of $LaPb_3$. The data of $NdPb_3$ were cited from ref. (45).

	$PrPb_3$ m_c^* (m_0)	$NdPb_3$ m_c^* (m_0)	$LaPb_3$ m_c^* (m_0)	Band Mass m_b (m_0)
H // $\langle 100 \rangle$				
α	3.7	2.08	1.45	0.77
β	—	—	2.29	1.07
γ	2.2	0.94	0.38	0.30
δ	2.5	1.26	0.63	0.54
H // $\langle 110 \rangle$				
α	6.7	2.67	1.46	1.17
β	3.9	2.76 3.09	1.40	0.78
γ	2.0	0.94	0.46	0.32
δ	1.2	1.31	0.60	0.64

Fig. 5.8 Mass plot between 0.03 K and 1.5 K for branch γ in $PrPb_3$. The straight line is fitted only in the temperature range from 1.5 to 1.0 K.

we have determined each cyclotron mass from seven data points in a narrow temperature range, repeating this procedure in the temperature range from 1.5 to 0.03 K. Figure 5.9 shows the temperature dependence of the mass, including the Dingle temperature and the product of the mass and the Dingle temperature for branch γ along the field $H \parallel \langle 100 \rangle$ direction. The mass of $1.6\,m_0$ around 1.2 K increases up to $4.0\,m_0$ at 0.17 K. Here we note that the mass of branch γ is cited as $2.2\,m_0$ in Table 5.1, which has been determined in the temperature range from 0.45 K to 1.2 K. The corresponding Dingle temperature in Fig. 5.9 decreases from 3.5 to 1.5 K with decreasing the temperature. The product of the mass and the Dingle temperature is approximately constant against the temperature.
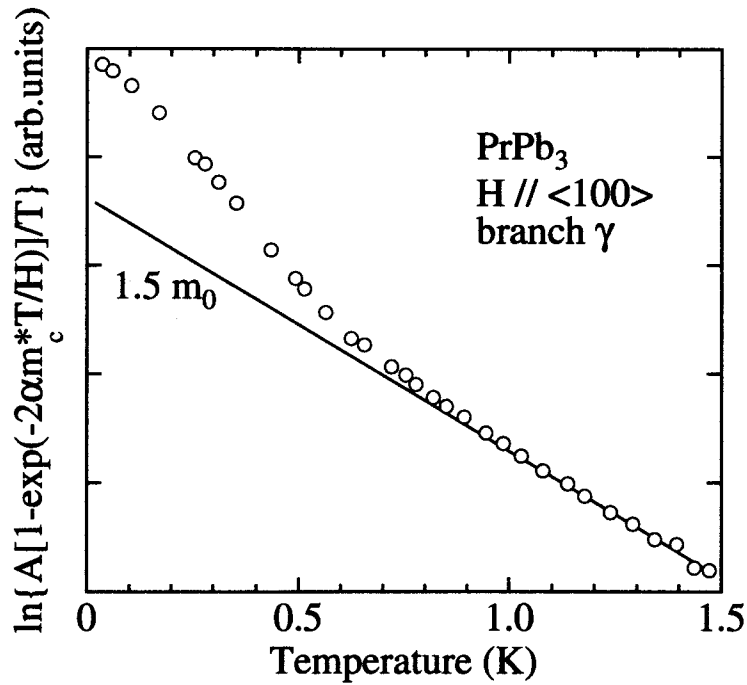
On the other hand, branch δ indicates a different behavior, as shown in Fig. 5.10. The mass is almost constant, $2\,m_0$, but decreases slightly below 0.5 K. The corresponding Dingle temperature is 0.8 K in the temperature range from 1.1 to 0.5 K and increases up to 2.8 K at the temperature of 0.03 K. The product of the mass and the Dingle temperature increases from 2 to 4 with decreasing the temperature, which is mainly due to the increase of the Dingle temperature.

The experimental cyclotron effective mass m_c^* is usually larger than the band mass m_b, as shown in Table 5.2. Therefore, the enhancement factor λ for the cyclotron effective mass can be defined as

$$m_c^* = (1 + \lambda)m_b \qquad (5.1)$$

Origins for λ are ascribed to the many-body effects which cannot be taken into account in the usual band theory. The electron-phonon interaction and the magnetic interaction are usually considered, which are denoted by λ_p and λ_m, respectively. The value of the electron-phonon term λ_p is smaller than 1. If it were large, it might cause lattice instability. The magnetic contribution or the magnon enhancement λ_m occurs in cerium and uranium compounds. Actually, a large cyclotron mass of $120\,m_0$ is detected in the dHvA experiment for the Kondo lattice compound $CeRu_2Si_2$.[100]

As for $PrPb_3$, the localized $4f$ electron does not form a Kondo lattice nor induce the magnetic ordering. Therefore, λ_m is usually small. For example, the cyclotron mass in a Van Vleck paramagnet $PrIn_3$ is only twice larger than the corresponding mass of $LaIn_3$.[101] The cyclotron mass in $PrPb_3$ is, however, considerably large, which is 2 to 6 times larger than that of $LaPb_3$. The mass enhancement mechanism in $PrPb_3$ might be ascribed to the quadrupole ordering. The primary source of the quadrupolar pair coupling is considered to be the indirect Coulomb and exchange interaction via conduction electrons, which is analogous to the RKKY interaction.[102] The present experimental results suggest that the short-range antiferroquadrupolar ordering starts roughly from 1 K at which the mass for branch γ starts to become heavy. This is consistent with the result of the specific heat.

Fig. 5.9 Temperature dependences of (a) the cyclotron effective mass m_c^*, (b) the Dingle temperature T_D and (c) the product of the mass and the Dingle temperature $m_c^* T_D$ for branch γ in PrPb$_3$.
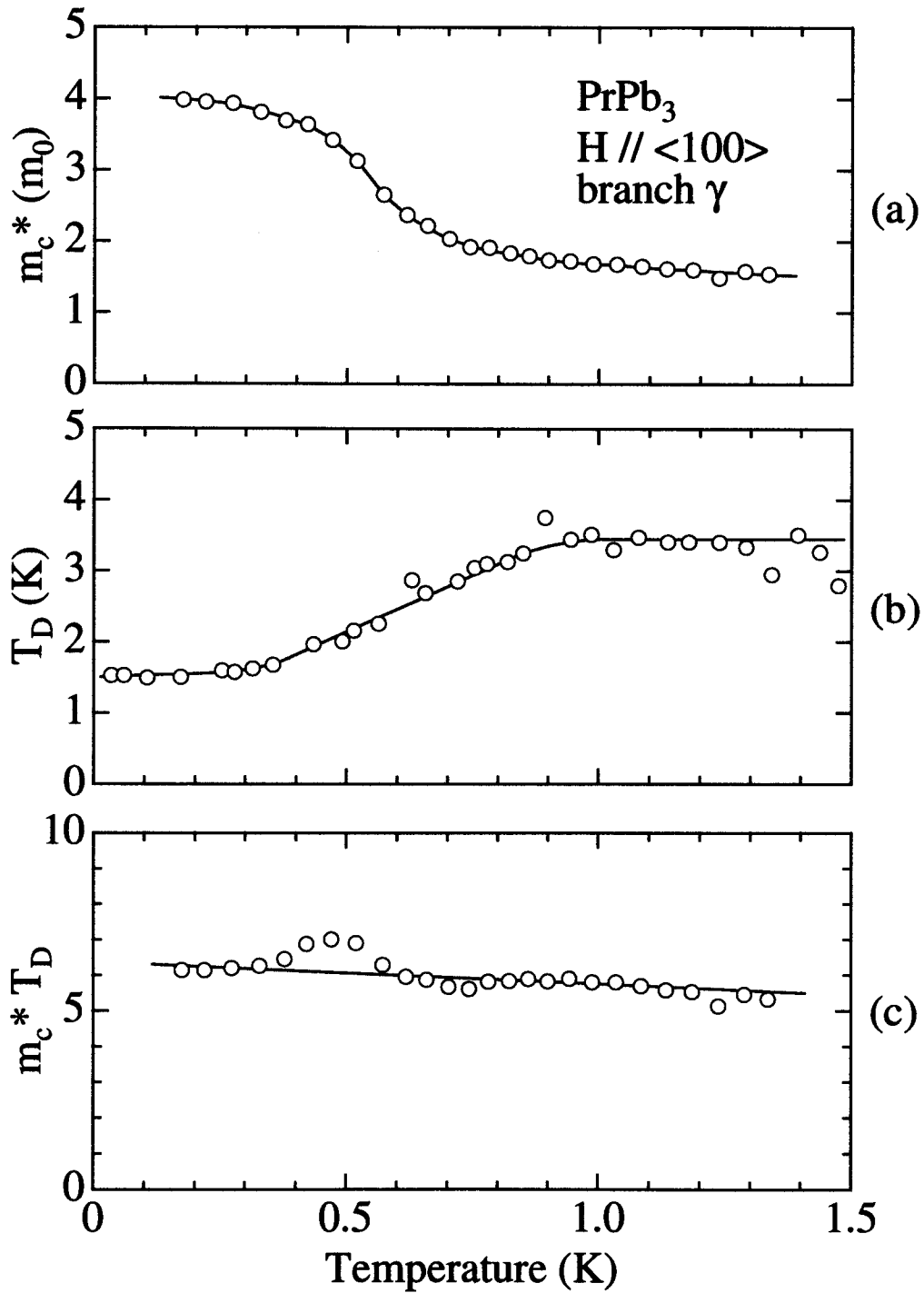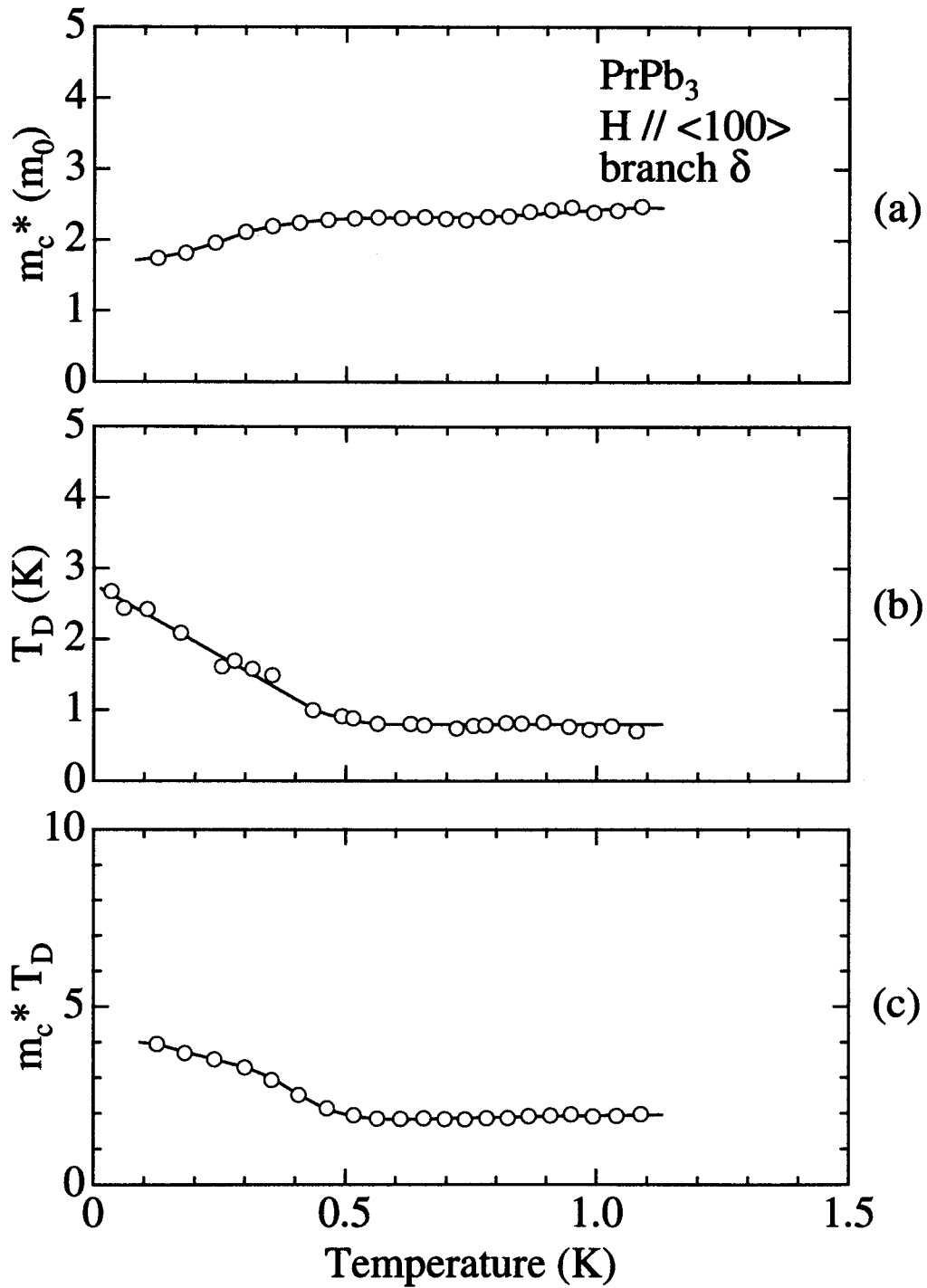
Fig. 5.10 Temperature dependences of (a) the cyclotron effective mass m_c^*, (b) the Dingle temperature T_D and (c) the product of the mass and the Dingle temperature $m_c^* T_D$ for branch δ in PrPb$_3$.

5.1.3 Metamagnetism

Figure 5.11 shows the magnetization for the field along the $\langle 100 \rangle$ direction at 0.40 K and 1.05 K. Both data have been obtained with increasing the field, although the magnetization process possesses no hysteresis. The magnetization at 1.05 K increases almost linearly. On the other hand, the magnetization curve at 0.40 K indicates a small step-like behavior shown by an arrow, which corresponds to the metamagnetic transition. Plots of differential magnetic susceptibility as a function of magnetic field, as shown in the inset of Fig. 5.11, allow us to determine the critical field of the metamagnetic transition. A large maximum in the dM/dH curve at 0.40 K is observed at 75 kOe. The maximum at 0.55 K becomes broader than that at 0.40 K, and slightly shifts to a lower field of 74 kOe. The maximum is no longer observed above 0.6 K.

We have also measured the magnetostriction for the field along the $\langle 100 \rangle$ direction, as shown in Fig. 5.12. The data at 0.42 K exhibit a large minimum at 73 kOe which we define as the critical field of the metamagnetic transition. The minimum becomes broader with increasing the temperature and finally disappears at 0.78 K. The critical field slightly shifts to a lower field with increasing the temperature, from 73 kOe at 0.42 K to 71 kOe at 0.55 K.

It is interesting to examine the metamagnetic behavior below the quadrupolar ordering temperature of 0.4 K. We show in Fig. 5.13 the results of the field dependence of the AC susceptibility at low temperatures down to 0.07 K for the field along the $\langle 100 \rangle$ direction, whose measurement was done by fundamentally the same technique as the dHvA experiment. A broad maximum in χ_{AC}, modulated by the dHvA oscillations, is observed at 70 kOe at the lowest temperature of 0.07 K, which is shown by an arrow. The critical field is almost constant in the temperature range of 0.07 K to 0.52 K, although the maximum becomes broader at 0.52 K and disappears above 0.6 K.

These experimental results of the magnetization, magnetostriction and AC susceptibility are summarized as follows:

(1) The metamagnetic transition occurs below 0.6 K. This is almost the same temperature as the short-range antiferroquadrupolar ordering starts to develop.

(2) The critical field of the metamagnetic transition has approximately no temperature dependence and is about 70 kOe.

Next we discuss the origin of the present metamagnetic transition. Since the ground state is the non-Kramers doublet possessing no magnetic moment and the susceptibility exhibits the Van Vleck behavior at low temperatures, the metamagnetic transition does not originate from the magnetic ordering. We have calculated the magnetization by considering the CEF scheme of Pr^{3+} $4f$ levels with a molecular field constant λ. The Hamiltonian which describes this system is

$$\mathcal{H} = \mathcal{H}_{\text{CEF}} + \mathcal{H}_{\text{J}}, \tag{5.2}$$
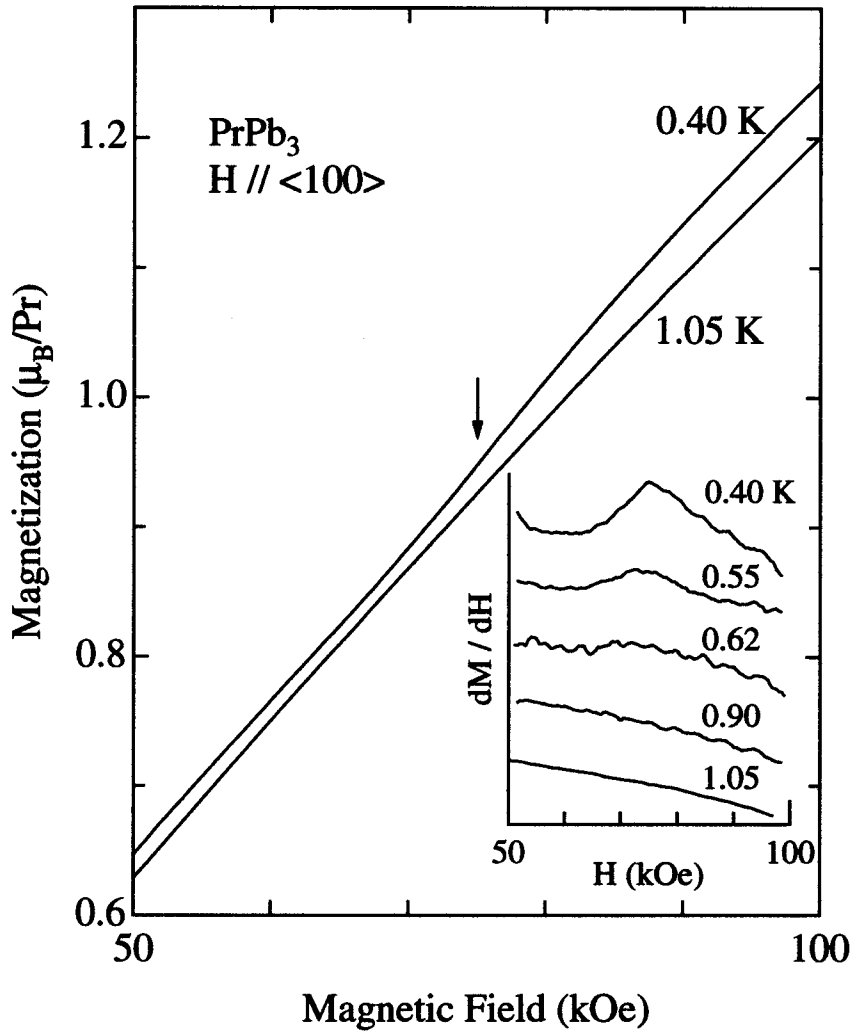
Fig. 5.11 Magnetization curves along the $\langle 100 \rangle$ direction in $PrPb_3$ at 0.40 and 1.05 K. The inset shows the differential magnetic susceptibility.

where the CEF Hamiltonian $\mathcal{H}_{\text{CEF}}$ is given by the CEF parameters B_n^m and the Stevens' operator equivalents as

$$\mathcal{H}_{\text{CEF}} = B_4^0(O_4^0 + 5O_4^4) + (O_6^0 - 21O_6^4), \tag{5.3}$$

and the magnetic dipolar term H_J including Zeeman and Heisenberg couplings can be described as

$$\mathcal{H}_J = -g_J\mu_B(\boldsymbol{H} + \lambda g_J\mu_B\langle\boldsymbol{J}\rangle) \cdot \boldsymbol{J}. \tag{5.4}$$

The CEF level scheme was determined in two ways. One scheme, which was given by Lethuillier and Chaussy, can perfectly describe the susceptibility data,[37] although it is inconsistent with the CEF level scheme determined from the inelastic neutron scattering
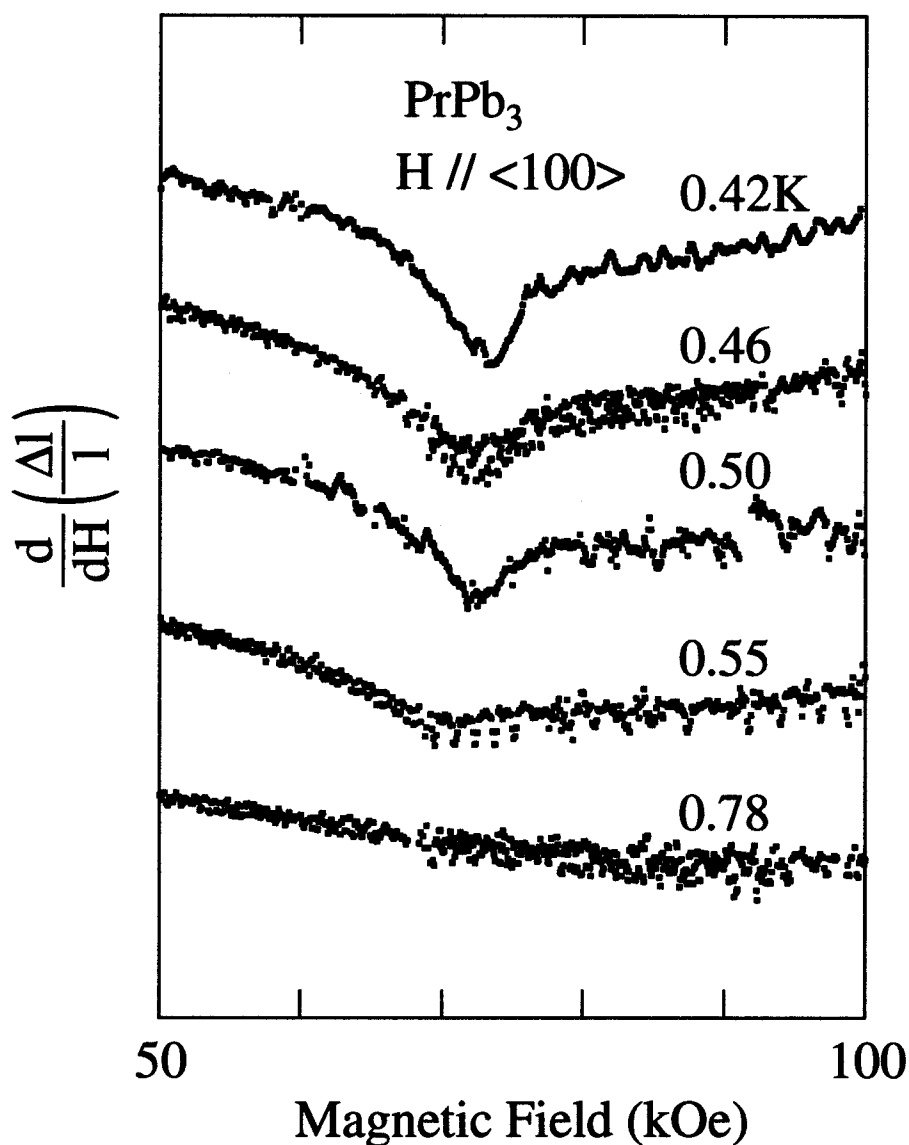
Fig. 5.12 Field dependence of the magnetostriction in PrPb$_3$.

by Gross et al.[39] Namely, the latter CEF scheme is not consistent with the temperature dependence of the susceptibility. We have calculated the magnetization on the basis of the above two cases. In both level schemes, the result of CEF calculations indicates a metamagnetic behavior in the magnetization curve. The transition field is roughly 50 kOe. These are due to the crossing of Zeeman-split energy levels. That is, the first excited state is the Γ_4 triplet in both schemes. This triplet splits into three separated levels with increasing the field. One of them increases with increasing the field up to about 30 kOe but decreases with further increasing the field. Another 4f level of Γ_4 increases monotonously with increasing the field. These two levels originated from the Γ_4 triplet cross each other at about 50 kOe. We cannot, however, consider the origin of the present metamagnetic behavior as the crossing of Zeeman-split energy levels, because the
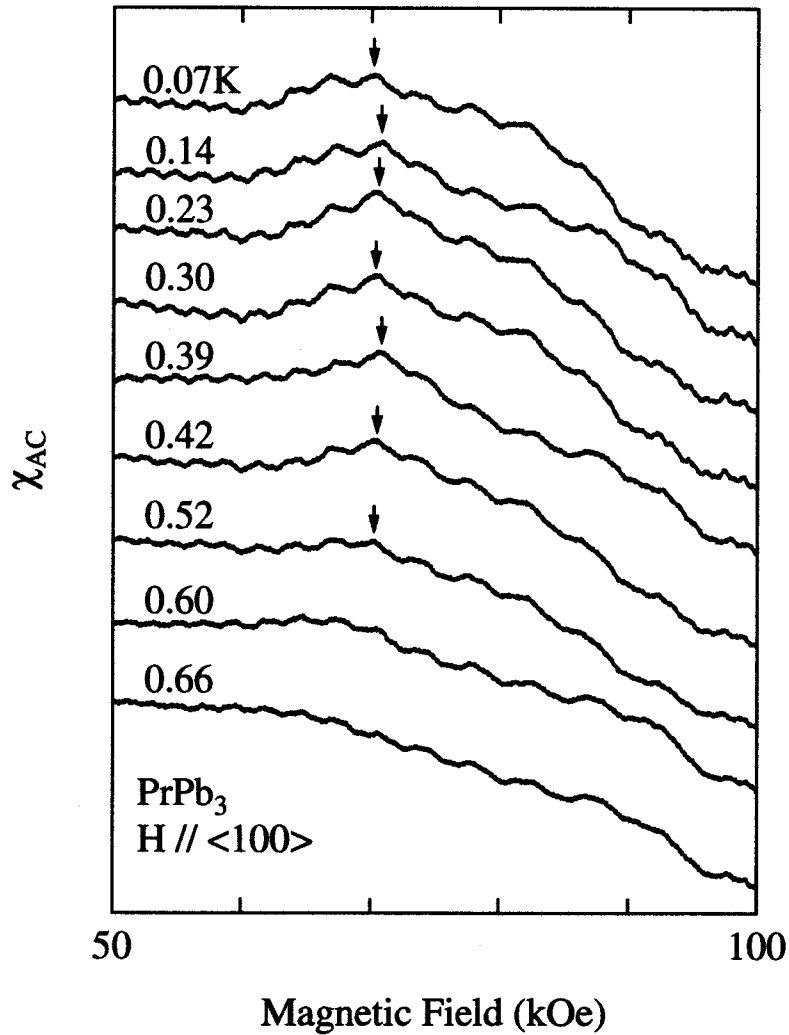
Fig. 5.13 Field dependence of the AC susceptibility in PrPb₃.

result of the CEF calculation indicates the metamagnetic behavior even at 4.2 K but the metamagnetic transition disappears above 0.6 K in experiment.

As the most probable origin, we consider the antiferroquadrupolar ordering. We can recognize from the experimental results that the short-range quadrupolar ordering starts to develop at about 1 K, well above the long-range ordering temperature of 0.4 K. The present metamagnetic transition occurs below 0.6 K, which is almost the same temperature as the antiferroquadrupolar ordering starts to develop. This is supported by the magnetization measurements which determined the H–T phase diagram (see next section).[15,98,103,104]

5.1.4 Other group's studies

Using the samples of $PrPb_3$ which we grew in the present study, the magnetization and specific heat measurements were done in Sakakibara group in Hokkaido University.[15,103,104]

Magnetic susceptibility and specific heat

Figure 5.14 shows the temperature dependence of the magnetic susceptibility M/H ($\equiv \chi$) obtained at $H = 1$ T applied parallel to the $\langle 100 \rangle$ axis. The plateau of χ below 5 K reflects the non-magnetic CEF ground state. The dashed line in the figure is the calculated result for $\chi(T)$ in the paraquadrupolar state, consisting of a single-sited contribution χ_{CEF} with the CEF level scheme $\Gamma_3(0)-\Gamma_4(15\,K)-\Gamma_5(28\,K)-\Gamma_1(35\,K)$ and an antiferromagnetic molecular field coefficient n: $\chi = \chi_{CEF}(1 - n\chi_{CEF})$. Good agreement was obtained with $n = -4.6$ mole/emu, which gives rise to a high-temperature Curie–Weiss constant of $\theta_p = -7$ K, consistent with the previous results.[37,40] Below 0.4 K, χ exhibits a small but clear increase due to the antiferroquadrupolar ordering. The inset of Fig. 5.14 shows the χ around T_Q obtained under various fields. Interestingly, $T_Q(H)$ defined by the bending point in $M(T)$ increases with H.
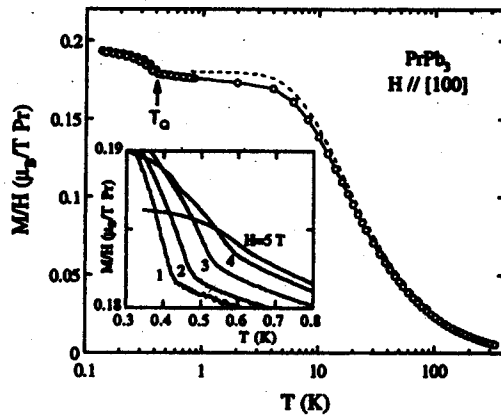
Fig. 5.14 Magnetic susceptibility of $PrPb_3$ measured in $H = 1$ T applied parallel to $\langle 100 \rangle$. Open circles are the experimental results while the dashed line is the calculated one. The inset shows M/H near T_Q obtained under various fields from 1 to 5 T, cited from ref. (104).

Figure 5.15 (a) and (b) show the results of the specific heat measurements under magnetic field applied parallel to $\langle 100 \rangle$ and $\langle 110 \rangle$ axes, respectively. By increasing H, the peaks in $C(T)$ shifts to higher temperatures, in accord with the magnetization results. For $H \parallel \langle 100 \rangle$ the peak position suddenly turns to decrease at 7 T and the structure of $C(T)$ becomes very broad, indicating the antiferroquadrupolar phase boundary is rapidly closing at higher fields. In contrast, a clear peak is still observed at 7 T for $H \parallel \langle 110 \rangle$, suggesting

68

that the critical field where the antiferroquadrupolar ordering collapses is slightly higher in this direction.
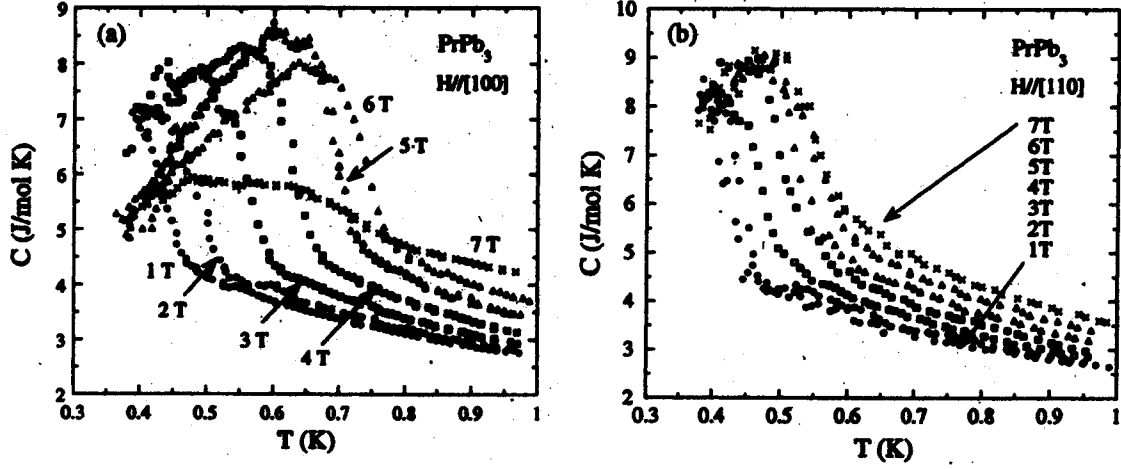
Fig. 5.15 Specific heat of PrPb$_3$ measured at various fields. (a) $H \parallel \langle 100 \rangle$; (b) $H \parallel \langle 110 \rangle$, cited from ref. (104).

The antiferroquadrupolar ordering temperature $T_Q(H)$ determined by these experiments is plotted in Fig. 5.16 for (a) $H \parallel \langle 100 \rangle$ and (b) $H \parallel \langle 110 \rangle$, where open circles and solid squares are the data points determined from $C(H)$ and $M(T)$ measurements, respectively. The solid circles in Fig. 5.16 (a) indicate the position of a small metamagnetic jump in $M(H)$ curves,[15,36] which is considered to be a transition from the antiferroquadrupolar state to a paraquadrupolar state. On the other hand, no clear anomaly was observed in the magnetization curves for $H \parallel \langle 110 \rangle$ below 8 T. For both field directions, T_Q is found to increase with H. This enhancement of $T_Q(H)$ is the largest for $H \parallel \langle 100 \rangle$.

Analysis of the phase diagram

For simplicity, a two-sublattice antiferroquadrupolar structure was assumed as schematically shown in Fig. 5.17. Here the ordered state is an array of O_2^0 quadrupolar moment. The ovals of different orientations in Fig. 5.17 represent two states of the O_2^0 moment ($\langle O_2^0 \rangle > 0$ and $\langle O_2^0 \rangle < 0$). When external field H is applied along the z ([001]) axis, a staggered magnetic moment parallel to H appears in addition to a uniform component, as shown by thick arrows in Fig. 5.17. The Van Vleck susceptibility would then take a different value for each sublattice, leading to the non-uniform paramagnetic magnetization. The appearance of the antiferromagnetic moment would stabilize the antiferroquadrupolar phase in the presence of the antiferromagnetic interactions, and may increase T_Q under magnetic field. The argument can be made more quantitative by introducing the following
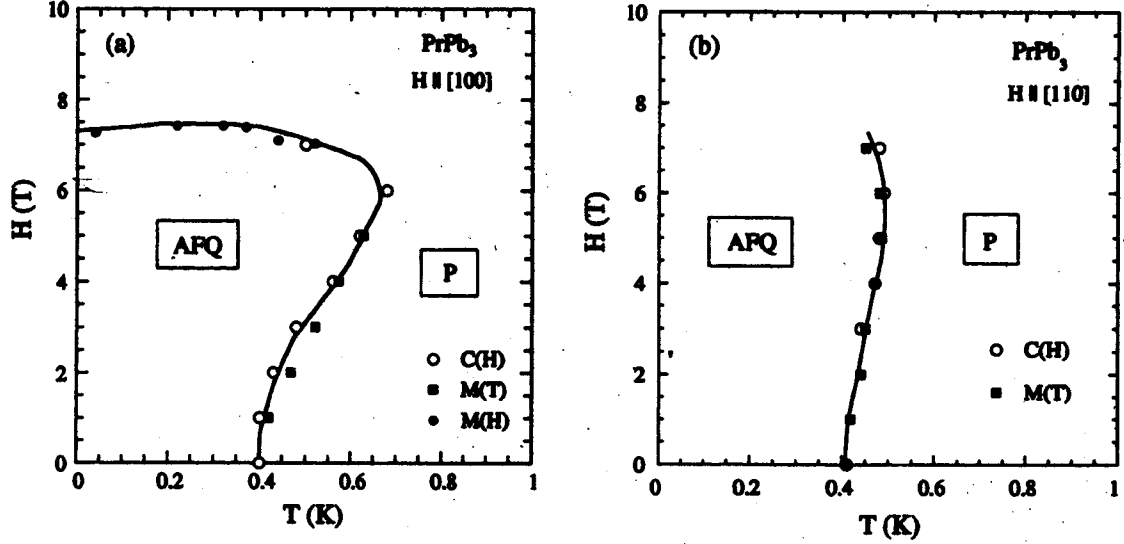
Fig. 5.16 Antiferroquadrupolar ordering temperature T_Q of PrPb$_3$ determined by magnetization and specific heat measurements. (a) $H \parallel \langle 100 \rangle$; (b) $H \parallel \langle 110 \rangle$ Solid lines are guides to the eyes, cited from ref. (104).

single-site Hamiltonian for each sublattice A, B:

$$\mathcal{H}^{I}_{A(B)} = \mathcal{H}_{CEF} - g_J \mu_B \boldsymbol{J} \cdot \boldsymbol{H} - (K_1 \langle J \rangle_{B(A)} + K_2 \langle J \rangle_{A(B)}) \cdot \boldsymbol{J}$$
$$- K_{\Gamma_3} \left[\langle O_2^0 \rangle_{B(A)} O_2^0 + \langle O_2^2 \rangle_{B(A)} O_2^2 \right]. \tag{5.5}$$

The calculated H-T phase diagram for $H \parallel [001]$ is shown in Fig. 5.18 by a solid line. This phase diagram explains the experimental result in Fig. 5.16 (a), satisfactorily. Under fields applied parallel to [001], the O_2^0 phase becomes stable.

The dot-dashed line in Fig. 5.19 shows the calculated result of $T_Q(H)$ for $H \parallel [110]$ obtained by eq. (5.5). In this field direction, O_2^2-antiferroquadrupolar phase becomes stable. The result disagrees with the experimental one in Fig. 5.16 (b). This contradiction can be removed by introducing an octupolar interaction. Namely, the following inter-sublattice octupole interaction was introduced in addition to eq. (5.5);

$$\mathcal{H}^{I}_{\beta} = -G_{\beta} \langle \boldsymbol{T}_{\beta} \rangle \cdot \boldsymbol{T}_{\beta}, \tag{5.6}$$

where $\boldsymbol{T}_{\beta} = (T_x^{\beta}, T_y^{\beta}, T_z^{\beta})$ is a octupole moment. The definition of the operator is $T_x^{\beta} \equiv \frac{\sqrt{15}}{6}(\overline{J_x J_y^2} - \overline{J_z^2 J_x})$, where the bar means the symmetrized product; one needs to sum over possible permutations of the indices x, y and z. The solid line in Fig. 5.19 is the $T_Q(H)$ calculated by using eq. (5.5) and (5.6). This is fairly in good agreement with the experimental results in Fig. 5.16 (b).

70
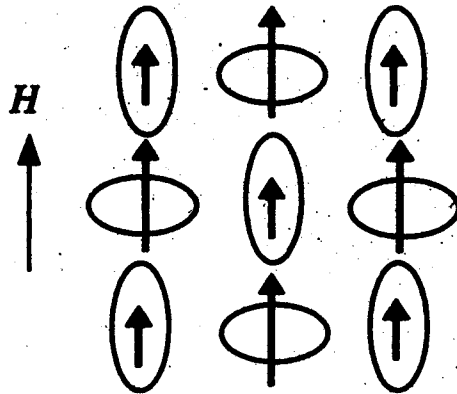
Fig. 5.17 Schematic O_2^0 antiferroquadrupolar phase. The arrows indicate the induced magnetic moment under magnetic field applied parallel to the [001] direction, cited from ref. (104).
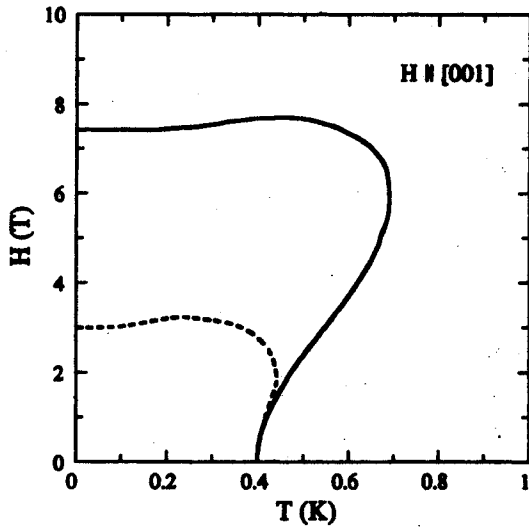
Fig. 5.18 Calculated field variation of $T_Q(H)$ for $H \parallel [100]$. The solid line is the solution of eq. (5.5). The dashed line is the result with $K_1 = K_2 = 0$ for comparison, cited from ref. (104).
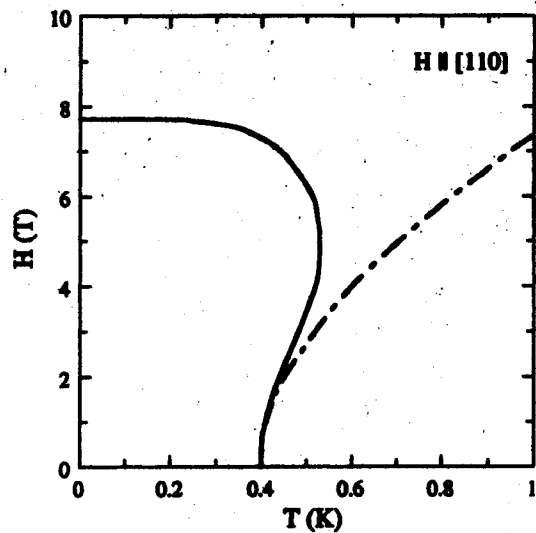
Fig. 5.19 Calculated field variation of $T_Q(H)$ for $H \parallel [110]$. The dot-dashed line is the solution of eq. (5.5), while the solid line is the result indicating the octupole interaction eq. (5.6), cited from ref. (104).

5.2 YbPb$_3$ and EuPb$_3$

5.2.1 Electrical resistivity

We measured the electrical resistivity in YbPb$_3$ and EuPb$_3$ at temperatures down to 7 K.[50] Figure 5.20 shows the temperature dependence of the electrical resistivity ρ in YbPb$_3$ and EuPb$_3$. The resistivity in YbPb$_3$ indicates a T-linear dependence above 120 K, which is similar to the previous data.[51] The resistivity at 7 K ρ_{7K} and the resistivity ratio ρ_{RT}/ρ_{7K} are 2.6 $\mu\Omega$·cm and 30, respectively. The resistivity in EuPb$_3$ also shows a T-linear dependence above 100 K. A steep decrease below 20 K is due to the antiferromagnetic ordering, which is in good agreement with the previous report.[49] The resistivity at 7 K ρ_{7K} and the resistivity ratio ρ_{RT}/ρ_{7K} are 4.4 $\mu\Omega$·cm and 21, respectively. Here we note that the residual resistivity ratio ρ_{RT}/ρ_{0K} must be much larger than $\rho_{RT}/\rho_{7K} = 21$, because the resistivity still tends to decrease at lower temperatures.
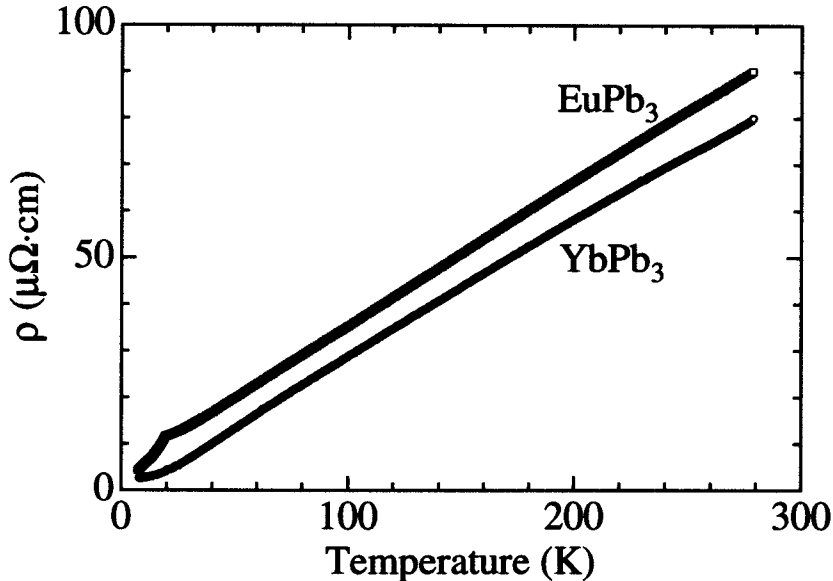
Fig. 5.20 Temperature dependence of the electrical resistivity in YbPb$_3$ and EuPb$_3$.

5.2.2 dHvA effect in YbPb$_3$

The dHvA experiments were measured in fields up to 130 kOe and at temperatures down to 0.4 K. Figures 5.21 and 5.22 show the typical dHvA oscillations and the corresponding fast Fourier transformation (FFT) spectra for the fields along the ⟨100⟩ and ⟨110⟩ directions in the field range from 20 to 60 kOe and 65 to 70 kOe, respectively. Branches α, ε and φ correspond to Fermi surfaces. The other dHvA frequencies in the FFT spectra are due to harmonics of the fundamental frequency named φ. Figure 5.23
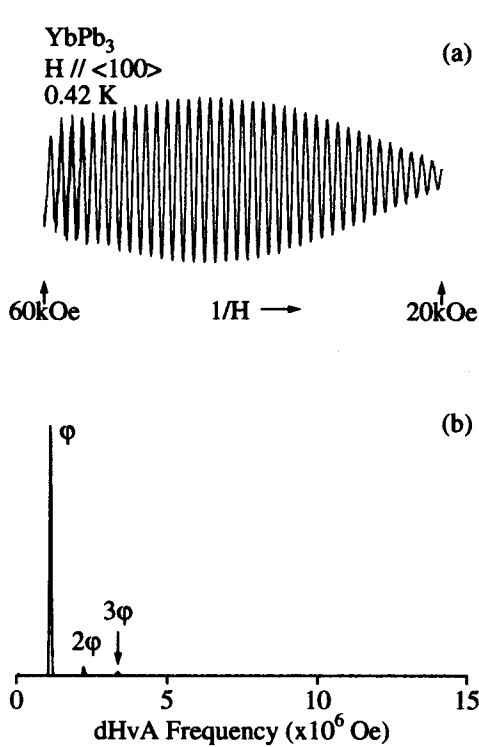
Fig. 5.21 (a) dHvA oscillation and (b) its FFT spectrum in the field range from 20 to 60 kOe for the field along ⟨100⟩ in YbPb₃.
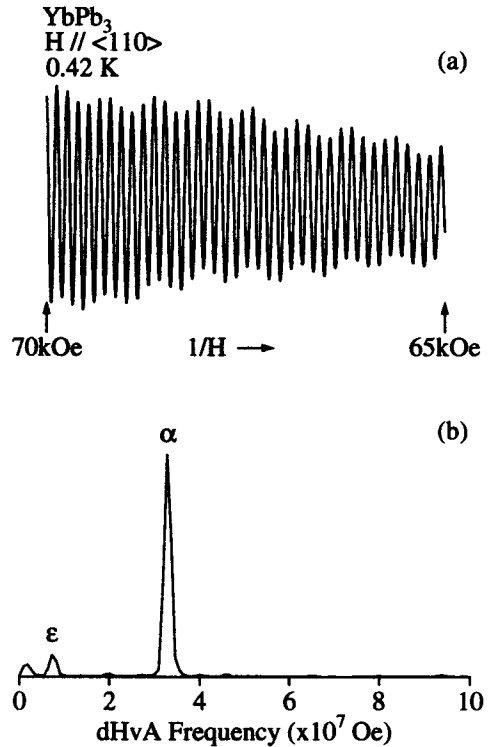
Fig. 5.22 (a) dHvA oscillation and (b) its FFT spectrum in the field range from 65 to 70 kOe for the field along ⟨110⟩ in YbPb₃.

shows the angular dependence of the dHvA frequency, which is proportional to the cross-sectional area of the Fermi surface. Since the frequencies of the main dHvA branches α and φ are almost constant against the field angle, these branches correspond to nearly spherical Fermi surfaces. The volumes of the Fermi surfaces for the branches α and φ are small and occupy 8.1 % and 0.05 % of the cubic Brillouin zone, respectively. The angular dependence of the dHvA frequency in YbPb₃ is completely different from those of LaPb₃, PrPb₃ and NdPb₃ shown in Figs. 5.5, 5.4 and 3.5.[36,45] This is because the valence state of Yb in YbPb₃ is not trivalent but divalent, as described in Sec. 3.1. YbSn₃ has the same crystal structure and the same valence state as in YbPb₃. The angular dependence of the dHvA frequency in YbSn₃[105] is approximately in agreement with the present results in YbPb₃.

The detected branches are compared to the results of the FLAPW-band calculations. Figure 5.24 shows the theoretical angular dependence of the dHvA frequency. Furthermore, the calculated Fermi surfaces are shown in Fig. 5.25. The result of experimental angular dependence of the dHvA frequency is in excellent agreement with that of theoretical one. It is easily found that the experimental branch α corresponds to the 14th hole Fermi surface in Fig. 5.25 (a). Branch ε near the ⟨110⟩ direction originates in the
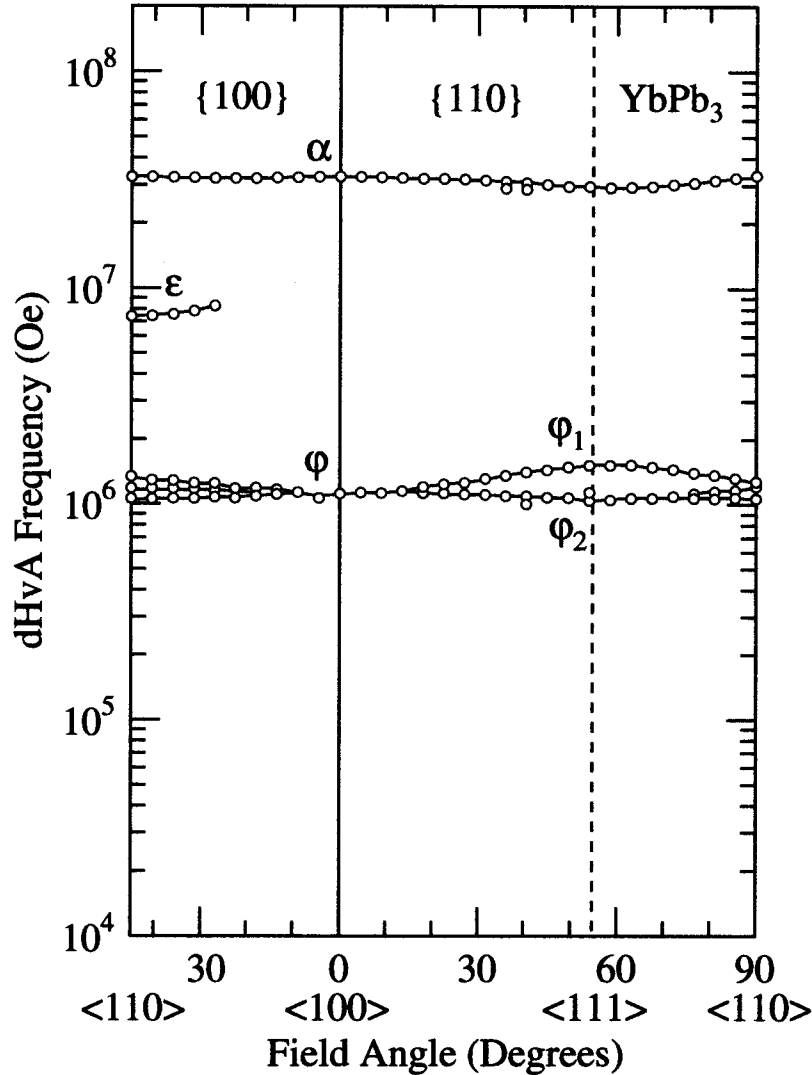
Fig. 5.23 Angular dependence of the dHvA frequency in YbPb$_3$.

cross-sectional area of the electron Fermi surface at the X points in Fig. 5.25 (b) because of the similarity of the angular dependence, althgough the experimental data appear only around $\langle 100 \rangle$. This is most likely due to the curvature factor of the Fermi surface. Branch φ should be explained by the small electron pocket Fermi surfaces on the Λ axes in Fig. 5.25 (c).

We also determined the cyclotron effective mass m_c^* from the temperature dependence of the dHvA amplitude. The cyclotron masses, which were determined in the temperature range of 0.45 to 1.2 K, are shown in Table 5.3 for the principal field directions, where m_0 denotes the free electron mass. The present Fermi surfaces possess light masses, which are in the range from 0.21 to 0.60 m_0.
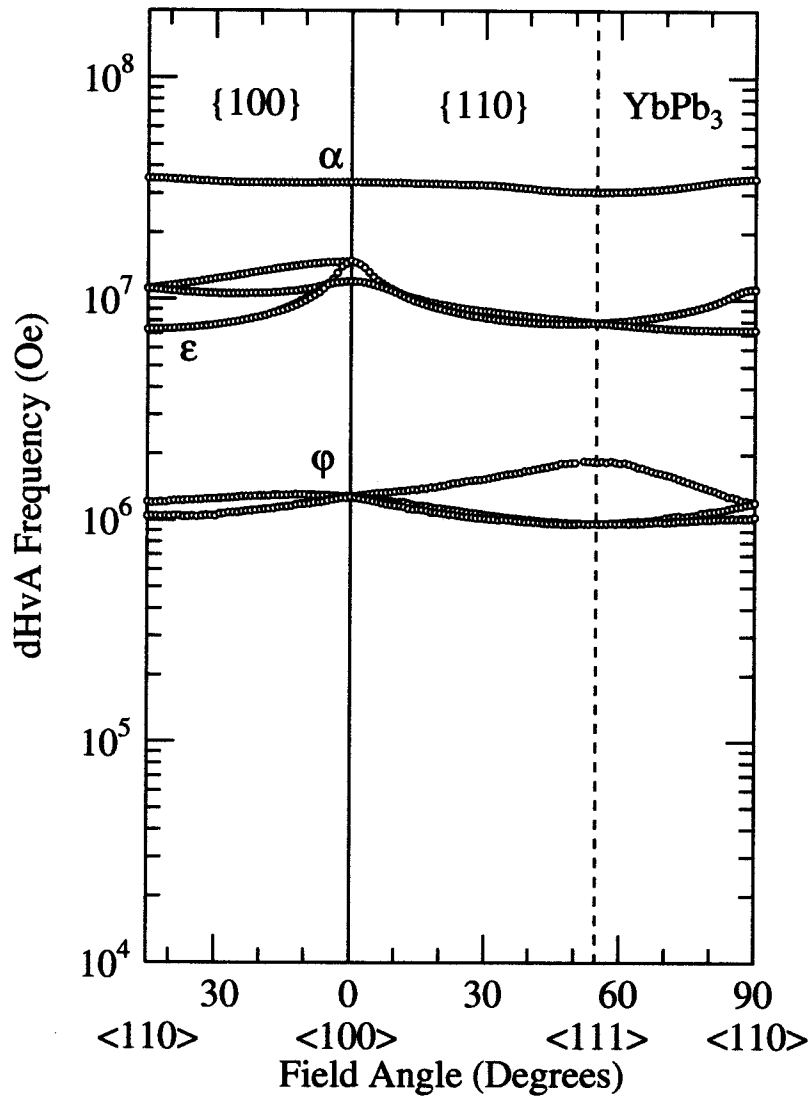
Fig. 5.24 Angular dependence of the theoretical dHvA frequency in YbPb$_3$.

We also show the Dingle temperature T_D in Table 5.3, which was determined from the field dependence of the dHvA amplitude under a constant temperature of 0.45 K. Here, $T_D = 1$ K, which is inversely proportional to the scattering lifetime, corresponds to a scattering lifetime of 1.2×10^{-12} sec. The Dingle temperature for the present sample is in the range from 1.7 to 8.0 K. Generally saying, the sample is not in high quality because the Dingle temperature is higher than 1 K.

5.2.3 dHvA effect in EuPb$_3$

We also detected the dHvA oscillation of the antiferromagnetic compound EuPb$_3$. Figures 5.26 and 5.27 show the typical dHvA oscillations and FFT spectra for the field

YbPb₃

Band 14th hole surface
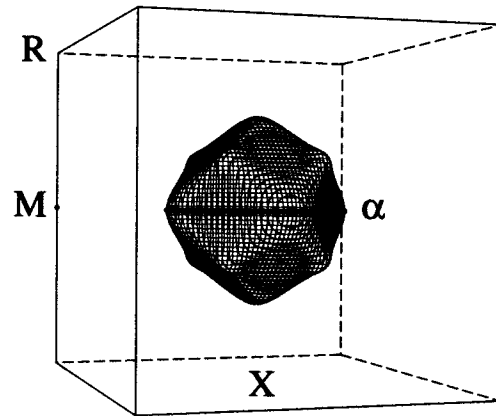
(a)

Band 15th electron surface
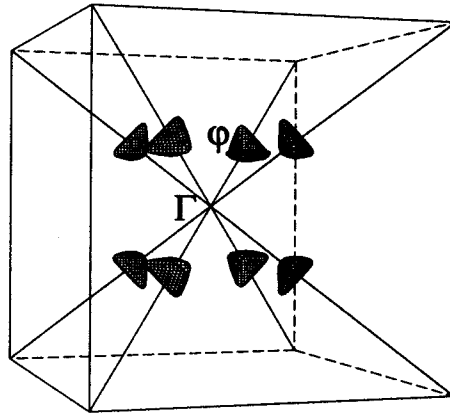
(b)

Band 15th electron surface
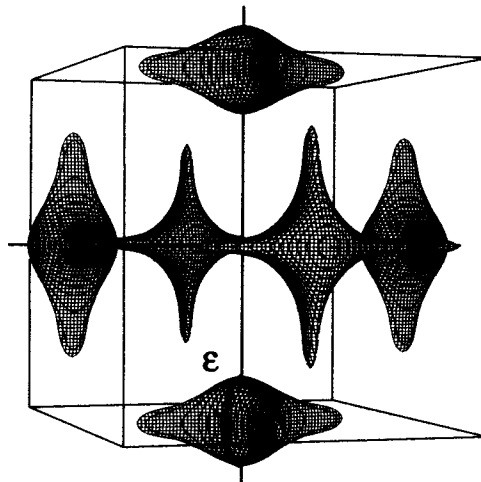
(c)

Fig. 5.25 (a) 14th hole Fermi surface centered at the Γ point, (b) 15th electron Fermi surfaces centered at the Γ point and (c) 15th electron Fermi surfaces centered at the Γ point in YbPb₃.

Table 5.3 dHvA frequency, cyclotron mass and Dingle temperature in YbPb$_3$.

	$H // \langle 110 \rangle$				$H // \langle 100 \rangle$				$H // \langle 111 \rangle$		
	F ($\times 10^6$ Oe)	m_c^* (m_0)	T_D (K)		F ($\times 10^6$ Oe)	m_c^* (m_0)	T_D (K)		F ($\times 10^6$ Oe)	m_c^* (m_0)	T_D (K)
α	32.9	0.58	3.2	α	32.9	0.60	2.8	α	29.4	0.48	8.0
ε	7.39	0.46	4.4								
φ_1	1.30	0.27		φ	1.13	0.23	3.4	φ_1	1.51	0.34	1.7
φ_2	1.19	0.24						φ_2	1.04	0.23	2.6
φ_3	1.06	0.21									

along the $\langle 100 \rangle$ direction in the field range from 3 to 40 kOe and 80 to 100 kOe, respectively. Branches η_1 and η_2 with low dHvA frequencies in Fig. 5.26 are observed in low fields. A quantum limit state is realized for branches η_1 and η_2 with extremely small Fermi surfaces. Namely, the Landau-level numbers $n = 0$ and 1 for branch η_1 with 7.0×10^4 Oe correspond to the fields of 140 and 47 kOe, respectively. On the other hand, branches δ, γ and α, which correspond to the main Fermi surfaces, are observed in higher fields, as shown in Fig. 5.27.
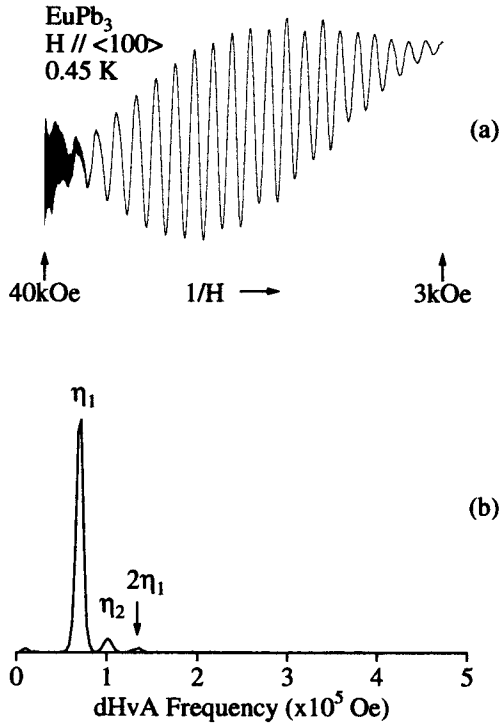
Fig. 5.26 (a) dHvA oscillation and (b) its FFT spectrum in the field range from 3 to 40 kOe for EuPb$_3$.
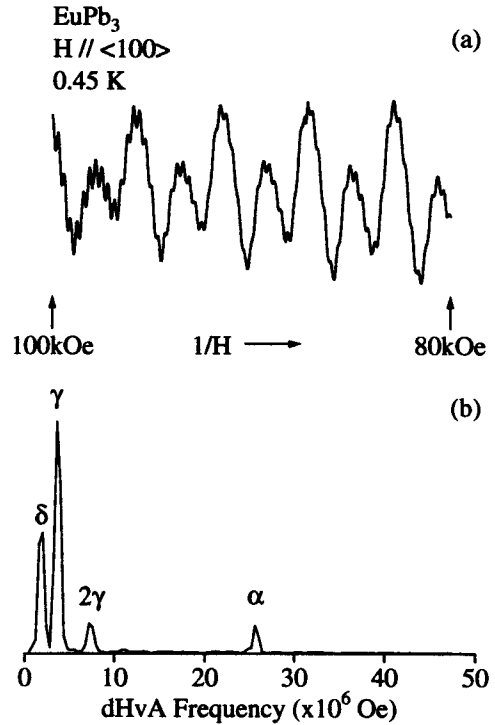
Fig. 5.27 (a) dHvA oscillation and (b) its FFT spectrum in the field range from 80 to 100 kOe for EuPb$_3$.

We show in Fig 5.28 the angular dependence of the dHvA frequency in the field range from 3 to 130 kOe, which is in the antiferromagnetic state. The Fermi surface of EuPb$_3$ is expected to be similar to that of YbPb$_3$, if the presence of $4f$ electrons is neglected. In fact, branch α is similar to the one of YbPb$_3$ in magnitude, although it disappears around

the $\langle 110 \rangle$ direction. Branch α corresponds to the spherical Fermi surface as shown in Fig. 5.25 (a). The magnetic ordering, however, influences the Fermi surface. When the magnetic order occurs, the paramagnetic Fermi surface is folded into a smaller magnetic Brillouin zone. If the magnetic energy gaps at the new zone boundaries are not too large, the paramagnetic Fermi surface can still be seen due to magnetic breakdown. This is realized in branch α in EuPb$_3$. The other branches are different from those of YbPb$_3$ in both the angular dependence and the magnitude. These are the antiferromagnetic Fermi surfaces. Branches γ and δ are almost constant against the field angle, which are also due to the nearly spherical Fermi surfaces. Branch η, which corresponds to an ellipsoidal Fermi surface, is most likely split into up (η_1) and down (η_2) spin branches due to the magnetic exchange interaction.

We determined the cyclotron effective mass m_c^* from the temperature dependence of the dHvA amplitude. The cyclotron masses are shown in Table 5.4 for the principal field directions. We also show the Dingle temperature T_D in Table 5.4 which was determined from the field dependence of the dHvA amplitude at a constant temperature of 0.45 K. The mass is in the range from 0.05 to $0.57\,m_0$, which is quite small as in YbPb$_3$. The cyclotron mass of branch α for the field along the $\langle 111 \rangle$ direction, $0.46\,m_0$, is in good agreement with $0.48\,m_0$ of YbPb$_3$. The Dingle temperature is larger than 1 K as in YbPb$_3$.

Table 5.4 dHvA frequency, cyclotron mass and Dingle temperature in EuPb$_3$.

	$H \parallel \langle 110 \rangle$				$H \parallel \langle 100 \rangle$				$H \parallel \langle 111 \rangle$		
	F ($\times 10^6$ Oe)	m_c^* (m_0)	T_D (K)		F ($\times 10^6$ Oe)	m_c^* (m_0)	T_D (K)		F ($\times 10^6$ Oe)	m_c^* (m_0)	T_D (K)
				α	25.7	—	—	α	26.9	0.46	3.2
β	11.9	0.45	4.5								
γ	3.49	0.53	2.0	γ	3.64	0.57	2.1				
	2.41	0.32	4.9						2.71	0.30	6.3
δ	1.92	0.44	1.7	δ	1.80	0.28	3.3	δ	1.59	0.20	3.5
					1.43	0.40	—				
η_1	0.15	0.07	—	η_1	0.10	0.06	—	η_1	0.14	0.08	—
η_2	0.10	0.06	—	η_2	0.07	0.05	—	η_2	0.10	0.07	—

5.2.4 Specific heat of EuPb$_3$

We measured the specific heat in the temperature range from 1.6 to 40 K. Figure 5.29 shows the temperature dependence of the specific heat. A sharp λ like peak at 20 K corresponds to the Néel temperature. This value is almost the same as the previous one of 22 K, which was determined from the magnetic susceptibility experiment.[49]

We also show in Fig. 5.30 the temperature dependence of the magnetic entropy S_m. The magnetic entropy S_m was obtained by integrating C_m/T over T, where C_m denotes the magnetic part of the specific heat. The phonon part was estimated from the Debye model with the Debye temperature of 120 K. Namely, we obtained the phonon part of the specific heat by fitting the Debye function to the data, assuming that the magnetic contribution is negligible above the Néel temperature. The electronic contribution was
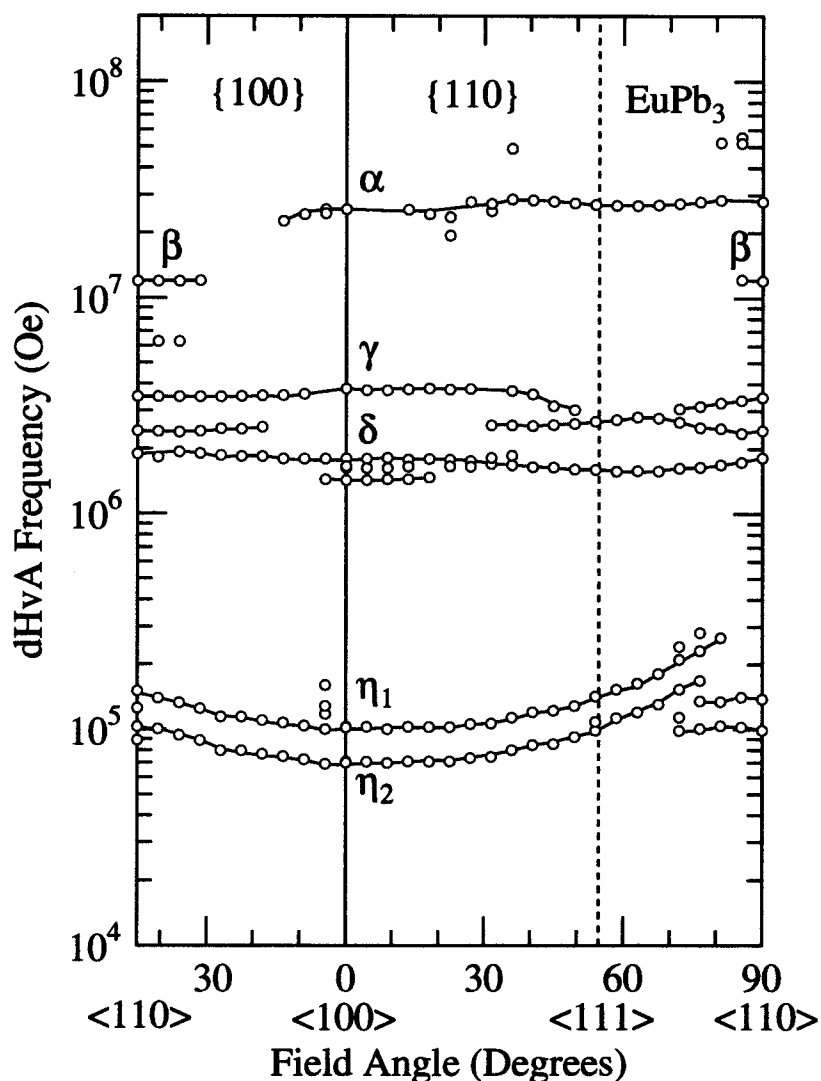
Fig. 5.28 Angular dependence of the dHvA frequency in EuPb₃.

also neglected because it is extremely small. The $R \ln 8$ value is thus obtained around 30 K, as shown in Fig. 5.30. This is approximately consistent with the present situation, where the crystalline electric field of the $4f$ levels does not exist in the divalent state of EuPb₃ ($L = 0$ and $S = 7/2$) and the relation of $2S + 1 = 8$ is realized.

5.2.5 Magnetic susceptibility and magnetization of EuPb₃

We show in Fig. 5.31 the temperature dependence of the reciprocal magnetic susceptibility $1/\chi$ for the field along the $\langle 100 \rangle$, $\langle 110 \rangle$ and $\langle 111 \rangle$ directions for EuPb₃. An inset of the Fig. 5.31 shows the susceptibility in the low temperature region. The susceptibility follows the Curie–Weiss law above 80 K. The paramagnetic Curie temperature θ_p is -55,
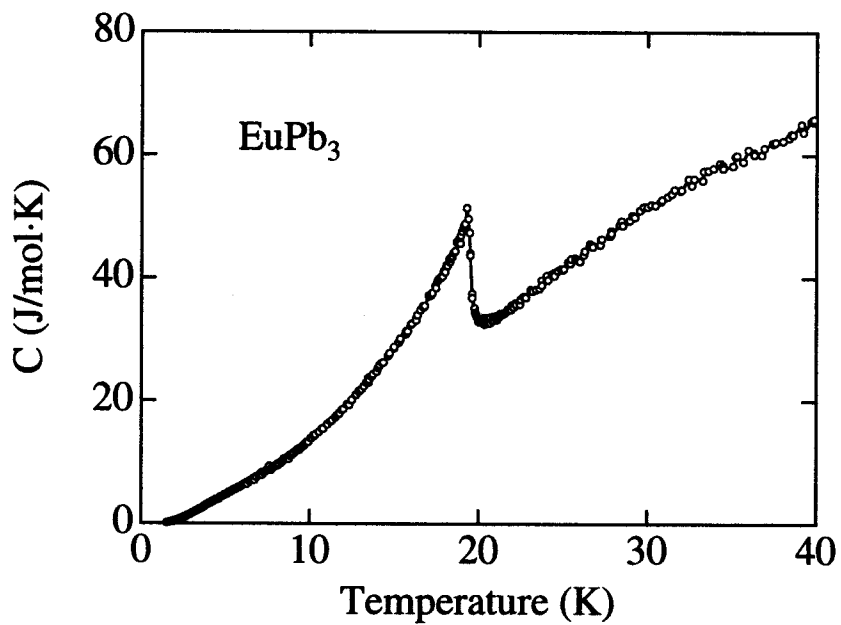
Fig. 5.29 Temperature dependence of the specific heat in EuPb₃.
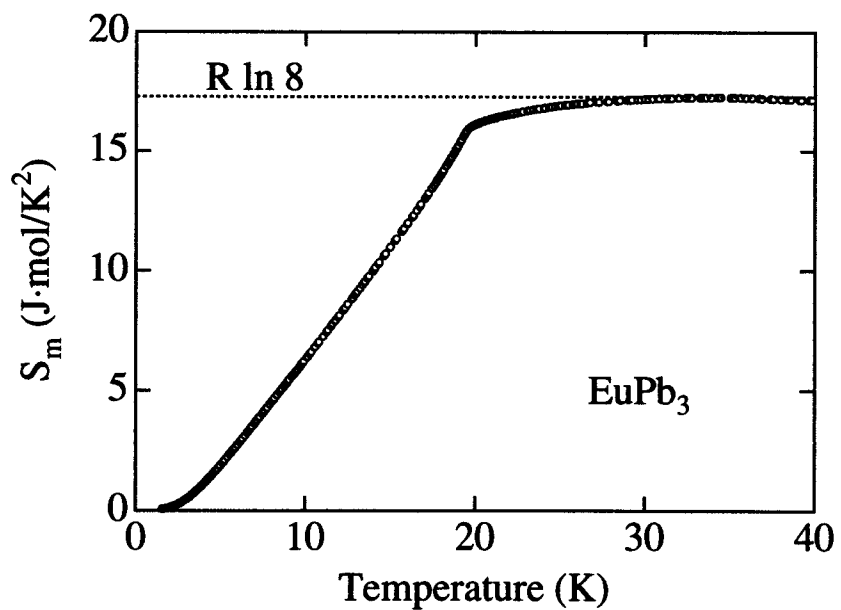
Fig. 5.30 Temperature dependence of the magnetic entropy in EuPb₃.
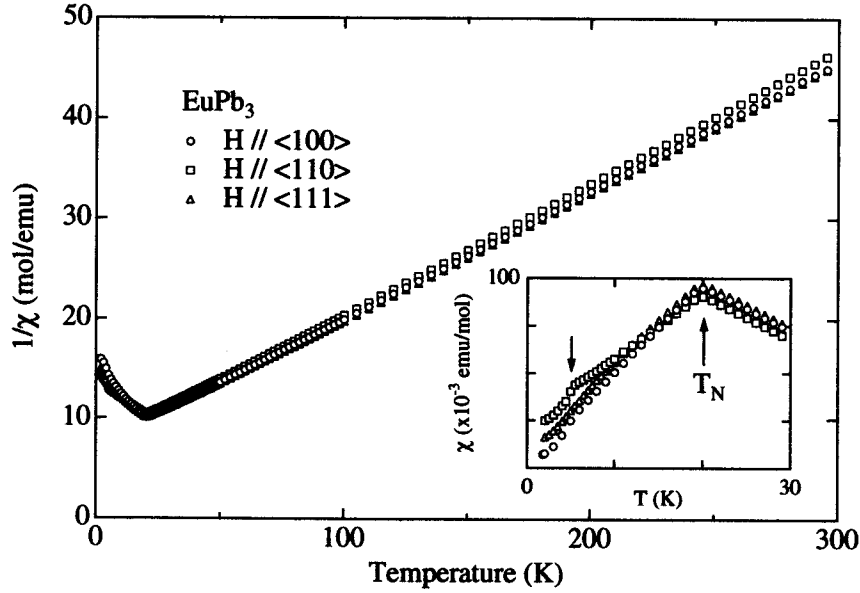
Fig. 5.31 Temperature dependence of the reciprocal magnetic susceptibility in EuPb₃. The inset shows the low temperature susceptibility.

−53 and −53 K for the $\langle 100 \rangle$, $\langle 110 \rangle$ and $\langle 111 \rangle$ directions, respectively. The effective Bohr magneton is also determined as 7.89, 7.77 and $7.89\,\mu_{\rm B}$/Eu for $\langle 100 \rangle$, $\langle 110 \rangle$ and $\langle 111 \rangle$, respectively. The anisotropies of the Curie temperature and the effective Bohr magneton are negligibly small. The experimental value of the effective Bohr magneton is almost the same as the theoretical free ion value of $\rm Eu^{2+}$, $7.94\,\mu_{\rm B}$/Eu. The Néel temperature $T_{\rm N}$ of the present sample is determined as 20 K from the kink of the susceptibility. This result is consistent with the electrical resistivity and specific heat data, as mentioned above. The inset of Fig. 5.31 indicates a small kink at 5 K for all the principal directions, as shown by an arrow. This suggests a change of the antiferromagnetic state.

We measured the magnetization with pulse and steady fields for the field along the $\langle 100 \rangle$ direction at 4.2 K, as shown in Fig. 5.32. The solid line and the open circles indicate the results in pulse and steady fields, respectively. Magnetization increases linearly up to 380 kOe and is saturated at higher fields. The saturated moment is $6.8\,\mu_{\rm B}$/Eu, which is almost the same as the theoretical free ion value of $\rm Eu^{2+}$, $7\,\mu_{\rm B}$/Eu. A linear increase of the magnetization is due to the canting process of the spin.

We simply estimated the magnetic exchange interaction on the basis of a two-sublattice model. The exchange field $H_{\rm E}$, Néel temperature $T_{\rm N}$ and paramagnetic Curie–Weiss
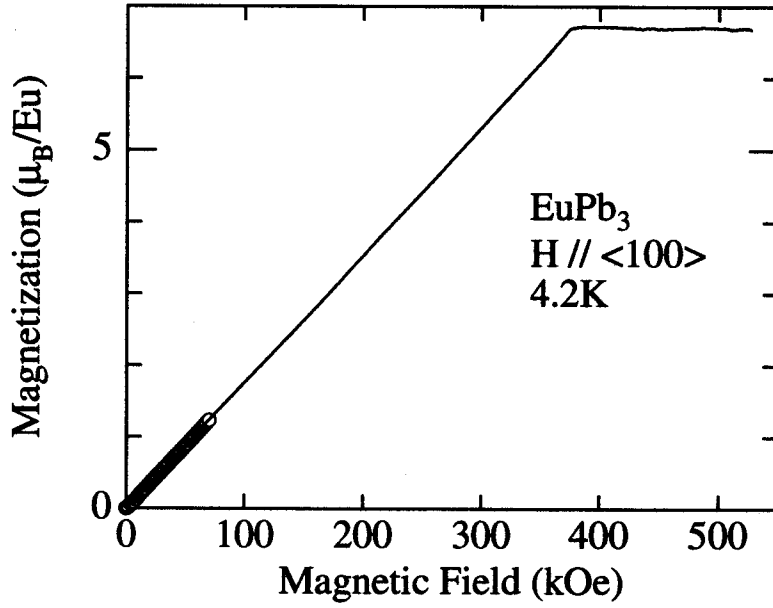
Fig. 5.32 Magnetization of EuPb₃. The solid line and the open circles show the results in pulse and steady fields, respectively.

temperature θ_p are obtained as follows:[106]

$$H_E = \frac{2S}{g\mu_B}|\alpha|,$$ (5.7)

$$T_N = \frac{2S(S+1)}{3k_B}(\beta - \alpha),$$ (5.8)

and

$$\theta_p = \frac{2S(S+1)}{3k_B}(\beta + \alpha),$$ (5.9)

where the spin angular momentum number S (= 7/2), g (= 2) is the g-factor, α and β are the magnetic exchange interaction in the inter- and intra-magnetic sublattices, respectively. A saturated magnetic field H_c corresponds to $2H_E$. From the present data of $H_c = 380\,\text{kOe}$ and $T_N = 20\,\text{K}$, we can obtain $\alpha/k_B = -3.65\,\text{K}$, $\beta/k_B = -1.74\,\text{K}$ and $\theta_p = -57\,\text{K}$. A value of $\theta_p = -57\,\text{K}$ is in good agreement with the obtained values of -53 and $-55\,\text{K}$.

5.3 SmPb₃ and GdPb₃

5.3 SmPb$_3$ and GdPb$_3$

5.3.1 Electrical resistivity

Figure 5.33 shows the electrical resistivity in SmPb$_3$ and GdPb$_3$ at temperatures down to 7 K.[107] The resistivity of LaPb$_3$ is also shown as a reference. The resistivity in SmPb$_3$ retains a fairly large value even in the low temperature range. In the previous report, this behavior was analyzed on the basis of the Kondo effect.[48] The resistivity in GdPb$_3$ decreases with decreasing the temperature, showing almost the same temperature dependence as that of LaPb$_3$. Then the resistivity in GdPb$_3$ steeply decreases below 16 K, which corresponds to the Néel temperature. This value is in good agreement with the previous result.[49] The similar temperature dependence between GdPb$_3$ and LaPb$_3$ indicates that the magnetic contribution to the resistivity in GdPb$_3$ is constant above the Néel temperature.
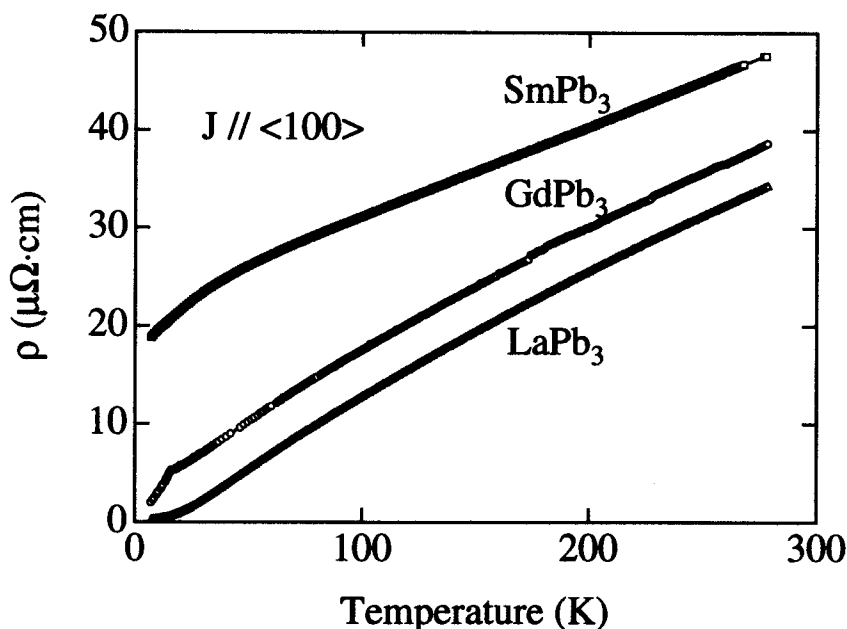
Fig. 5.33 Temperature dependence of the electrical resistivity in SmPb$_3$, GdPb$_3$ and LaPb$_3$.

5.3.2 Specific heat

We show in Fig. 5.34 the temperature dependence of the specific heat in SmPb$_3$ and GdPb$_3$. Sharp λ-like peaks are observed at 5.4 and 15.4 K for SmPb$_3$ and GdPb$_3$, which correspond to the Néel temperatures. The Néel temperature in GdPb$_3$ is in good agreement with the results of the electrical resistivity mentioned above. The specific heat in SmPb$_3$ is consistent with the previous result of the specific heat.[46]
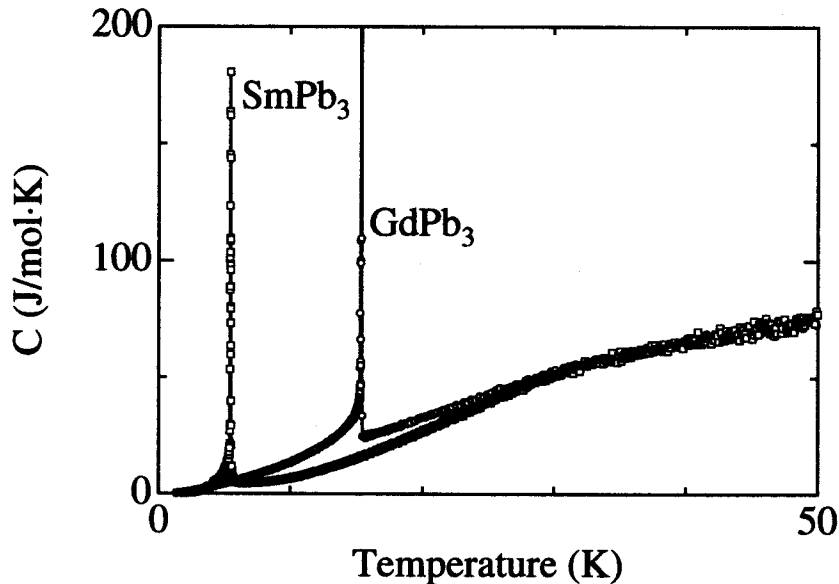
Fig. 5.34 Temperature dependence of the specific heat in SmPb$_3$ and GdPb$_3$.

5.3.3 dHvA effect

We measured the dHvA oscillations both in SmPb$_3$ and in GdPb$_3$ in fields up to 130 kOe and at temperatures down to 0.4 K. The measurements were carried out in the antiferromagnetic states for both compounds.

1) SmPb$_3$

First we show the results of SmPb$_3$. The typical dHvA oscillation and its FFT spectrum in SmPb$_3$ are shown in Fig. 5.35. There are detected three dHvA branches named β, γ and δ and its harmonics and sum. When the field is reduced or the field angle is tilted, the another branches φ and α are observed.

We show in Fig. 5.36 the angular dependence of the dHvA frequency in SmPb$_3$. Branch α is similar to branch α in LaPb$_3$ as shown in Fig. 5.5, although it is observed only around the $\langle 111 \rangle$ direction. Therefore branch α in SmPb$_3$ most likely originates from the spherical Fermi surface. However, the other branches disagree with those in LaPb$_3$. The Fermi surfaces are probably modified in topology by the magnetic Brillouin zone boundaries. Nevertheless, branch α can be seen due to breaking through the antiferromagnetic gap.

We also determined the cyclotron mass from the temperature dependence of the dHvA amplitude A by using eq. (4.29). The mass is in the range from 0.23 to 1.4 m_0. These small masses are not consistent with the γ-value of 100 mJ/K^{2}mol reported in ref. (46). The determined masses are summarized in Table 5.5.
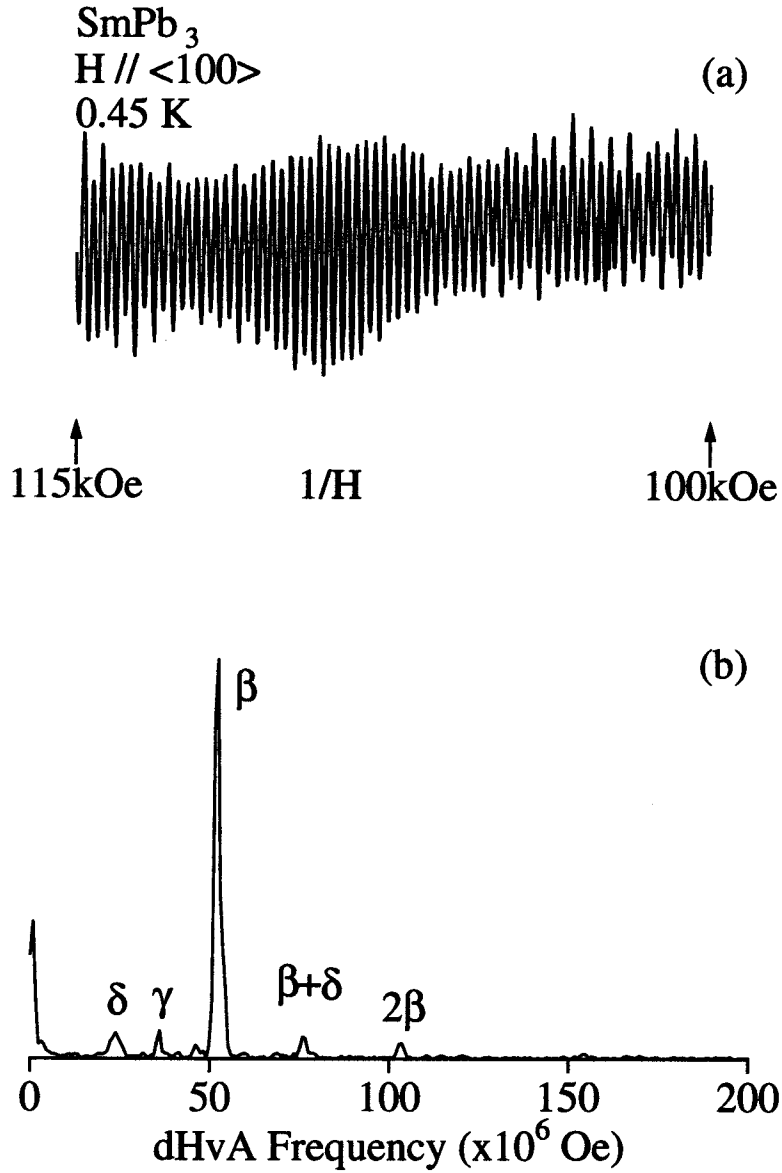
Fig. 5.35 (a) Typical dHvA oscillation and (b) its FFT spectrum for the field along ⟨100⟩ in SmPb₃.

Table 5.5 dHvA frequency F and cyclotron mass m_c^* for SmPb₃.

	H // ⟨110⟩		H // ⟨100⟩		H // ⟨111⟩	
	F ($\times 10^7$ Oe)	m_c^* (m_0)	F ($\times 10^7$ Oe)	m_c^* (m_0)	F ($\times 10^7$ Oe)	m_c^* (m_0)
α					11.0	
β			5.21	1.4		
γ			3.56			
δ	1.79	0.55	2.36		2.16	
ε	0.67	0.45	0.49	0.23	0.91	

85

Fig. 5.36 Angular dependence of the dHvA frequency in SmPb₃.

2) GdPb₃

We show in Fig. 5.37 the typical dHvA oscillation and the corresponding FFT spectrum. Fundamental branches α, β, γ, δ, ε, and ζ are observed. The second harmonics of branch γ is also observed as 2γ. Figure 5.38 shows the angular dependence of the dHvA frequency in GdPb₃. The data in GdPb₃ are not similar to those in LaPb₃ as shown in Fig. 5.5. Many branches with small dHvA frequencies are observed, which are most likely derived from the small pocket Fermi surfaces formed by the smaller magnetic Brillouin zone.

We also determined the cyclotron mass from the temperature dependence of the dHvA

GdPb$_3$
H // <100>
0.5 K   (a)

120kOe   1/H —→   110kOe

γ   (b)

ζ ε   δ   β   α   2γ

0   50   100   150
dHvA Frequency (x10^6 Oe)
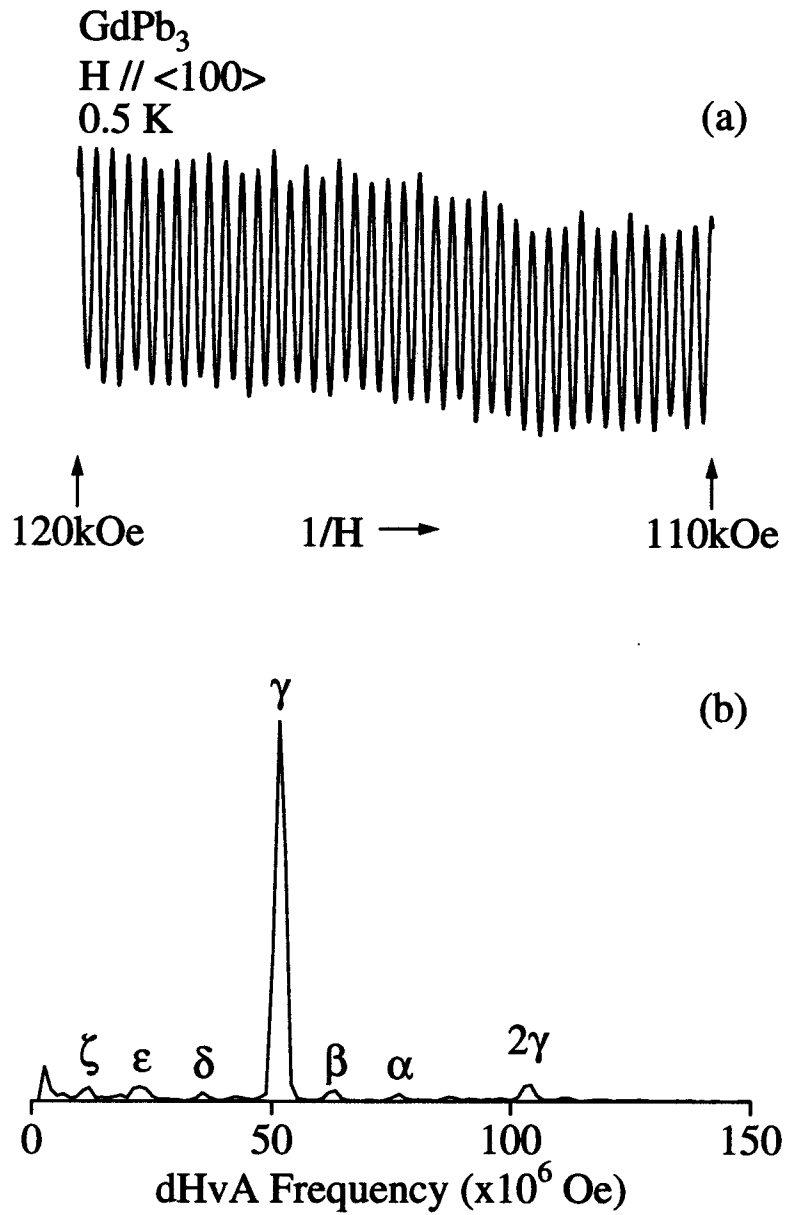
Fig. 5.37 (a) Typical dHvA oscillation and (b) its FFT spectrum for the field along ⟨100⟩
in GdPb$_3$.

amplitude A by using eq. (4.29). The detected masses are in the range from 0.61 to 1.6 m_0,
as summarized in Table 5.5.

10^9

{100}   {110}   GdPb₃

10^8

α   γ
     β
δ
ε
ζ

10^7

dHvA Frequency (Oe)

10^6

10^5

30   0   30   60   90
<110>   <100>   <111>   <110>
Field Angle (Degrees)
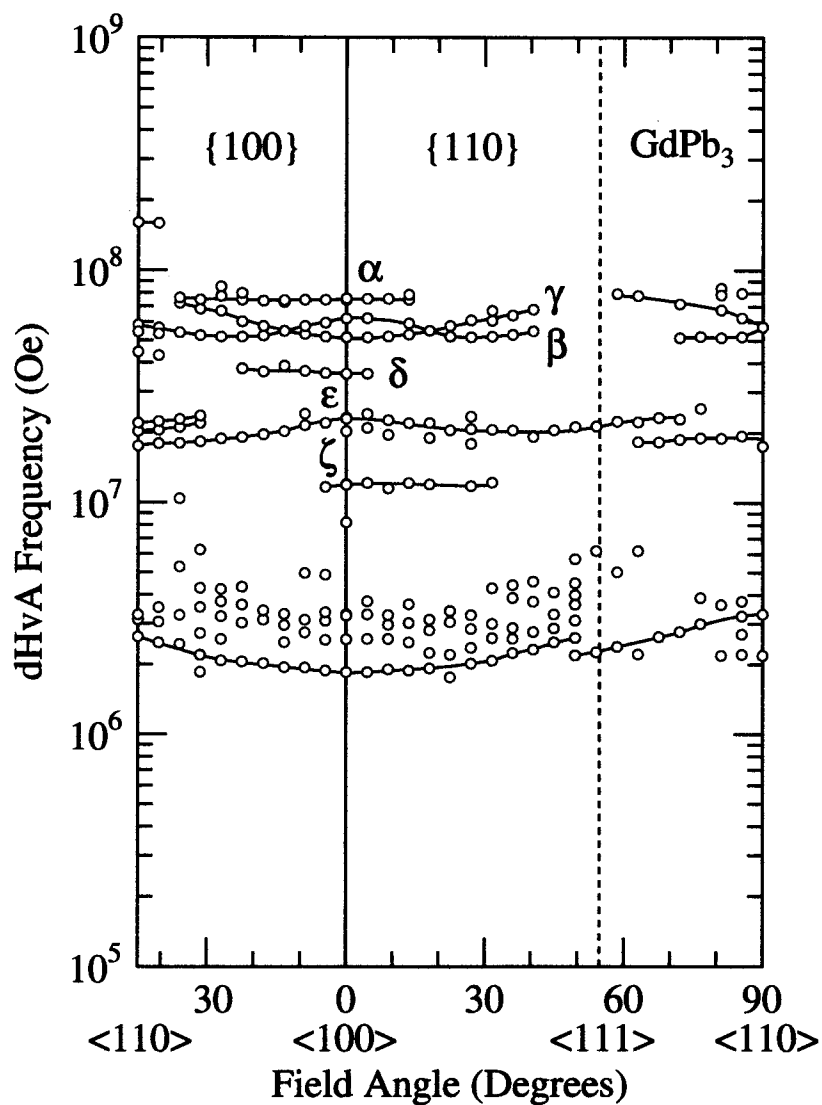
Fig. 5.38 Angular dependence of the dHvA frequency in GdPb₃.

Table 5.6 dHvA frequency F and cyclotron mass m_c^* for GdPb₃.

| $H // \langle 110 \rangle$ | | | $H // \langle 100 \rangle$ | | | $H // \langle 111 \rangle$ | | |
F ($\times 10^7$ Oe)	m_c^* (m_0)			F ($\times 10^7$ Oe)	m_c^* (m_0)		F ($\times 10^7$ Oe)	m_c^* (m_0)
		α	7.60	1.6				
β	5.83	β	6.22	1.5				
		γ	5.16	1.3				
		δ	3.60	1.2				
ε	1.75	0.61	ε	2.31	0.80	ε	2.14	0.64
		ζ	1.20	1.5				

5.4 YbIn₃

5.4.1 Electrical resistivity

We show in Fig. 5.39 the temperature dependence of the electrical resistivity in $YbIn_3$. The resistivity increases linearly above 50 K with increasing the temperature, showing no magnetic contribution to the resistivity. This is consistent with the divalent Yb ion possessing no magnetic moment. The resistivity ratio $\rho_{RT}/\rho_{4.2K}$ was 120. This value indicates a high-quality sample and is generally good enough to detect the dHvA oscillation.
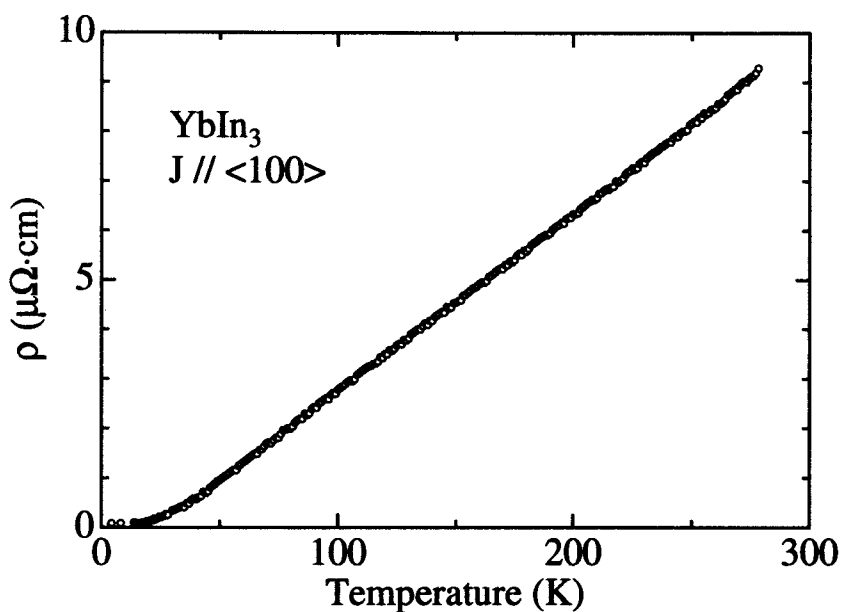
Fig. 5.39 Temperature dependence of the electrical resistivity in $YbIn_3$.

5.4.2 Specific heat

Figure 5.40 shows the specific heat in the form of C/T versus T^2 in $YbIn_3$. The determined γ-value and the Debye temperature were $4.7\,\mathrm{mJ/K^2mol}$ and 190 K, respectively. It is expected that the mass enhancement of the conduction electrons is small from this small γ-value.

5.4.3 dHvA effect

We measured the dHvA oscillations of $YbIn_3$ in fields up to 130 kOe and at temperatures down to 0.4 K. We show in Fig. 5.41 the typical dHvA oscillation and its FFT spectrum. There are detected four fundamental branches named α, β, γ and ε as well as their harmonics, sum and difference. Figure 5.42 shows the angular dependence of the
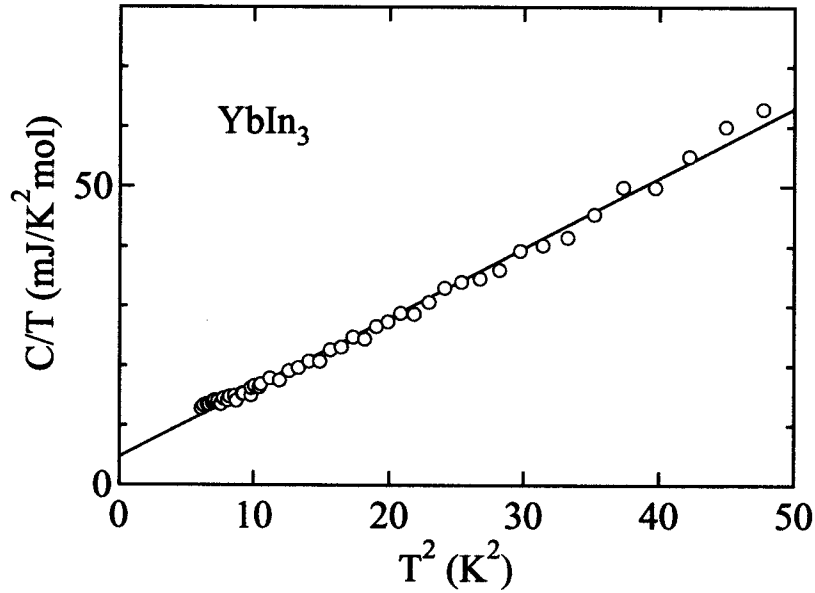
Fig. 5.40 T^2-dependence of the specific heat C in the form of C/T for YbIn$_3$.

Table 5.7 dHvA frequency F and cyclotron mass m_c^* for YbIn$_3$.

$H /\!/ \langle 100 \rangle$		$H /\!/ \langle 110 \rangle$		$H /\!/ \langle 111 \rangle$	
F ($\times 10^7$ Oe)	m_c^* (m_0)	F ($\times 10^7$ Oe)	m_c^* (m_0)	F ($\times 10^7$ Oe)	m_c^* (m_0)
α 12.3	1.1	α 12.5	1.3	α 13.8	
β 6.54	0.61	β 6.44	0.68	β 5.87	0.45
γ 1.97	0.33	γ 1.97	0.41	γ 1.77	0.59
$\delta_{2,3}$ 0.607	0.36	$\delta_{1,2}$ 0.648		δ 0.634	0.36
		δ_3 0.598	0.31		
ε 0.497	0.33	ε_1 0.538		ε_2 0.746	0.49
		ε_2 0.482		ε_1 0.473	0.28
ζ 0.340	0.22	ζ_1 0.361	0.28	ζ 0.348	0.32
		ζ_2 0.304	0.25		

dHvA frequency in YbIn$_3$. Branches α, β and γ are nearly constant against the field angle. Thus the corresponding Fermi surfaces are almost spherical. Branches δ_1 and $\delta_{2,3}$ originates from the same Fermi surface, although branch δ_1 is not observed around the $\langle 100 \rangle$ direction due to the curvature factor. The expected Fermi surface for this branch is a disk-shaped one. The Fermi surfaces for branches ε and ζ are again closed ones but are modified from a sphere.

We determined the cyclotron mass m_c^* from the temperature dependence of the dHvA amplitude A, by using eq. (4.29). The cyclotron mass is in the range from 1.3 to 0.22 m_0. These small cyclotron masses reflect the small γ-value. All determined values are summarized in Table 5.7.

90
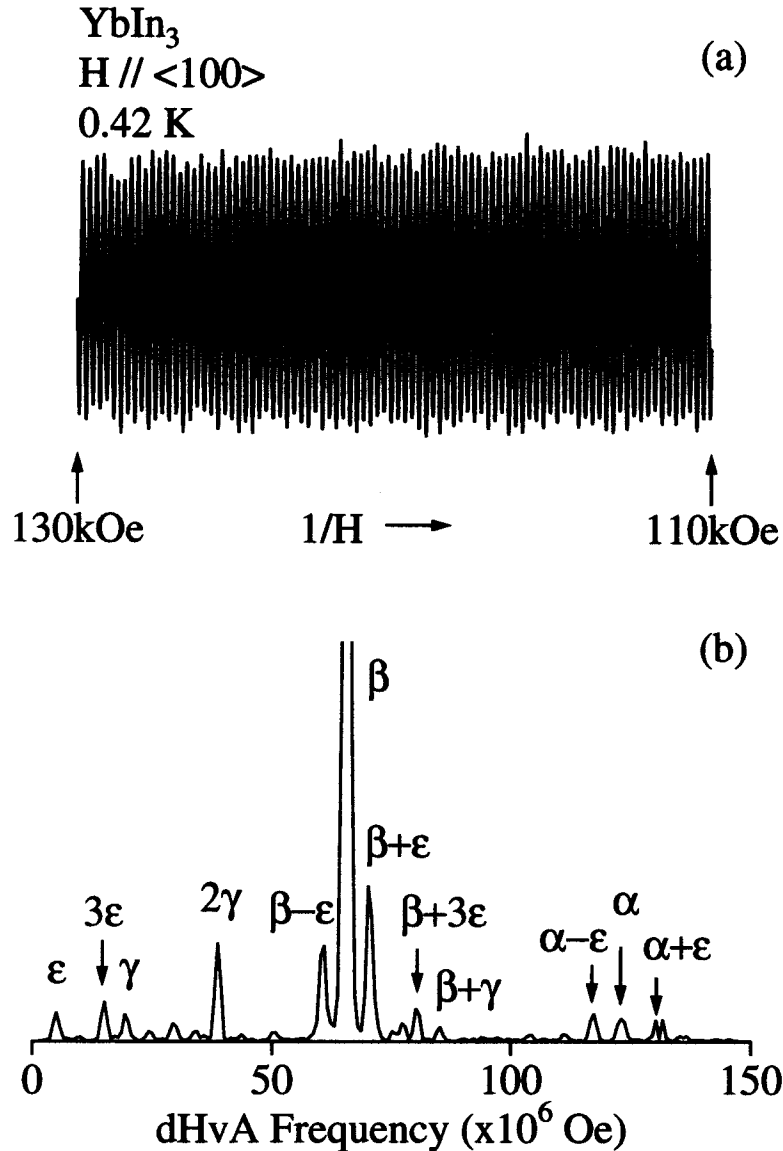
Fig. 5.41 (a) Typical dHvA oscillation and (b) its FFT spectrum in YbIn$_3$.

We will discuss the topology of the Fermi surface on the basis of the band model. If the $4f$ electrons are localized, namely, Yb^{3+} is realized, the topology of the Fermi surface in YbIn$_3$ is the same as that in LaIn$_3$ or LuIn$_3$. The angular dependence of the dHvA frequency in YbIn$_3$, however, is quite different from that in LaIn$_3$ or LuIn$_3$ (see Fig. 3.6 for LaIn$_3$). Therefore, $4f$-localized band model cannot be applied to the present case.

Next we tried to apply the $4f$-itinerant band model in the scheme of the FLAPW method, where Yb is a divalent. Figures 5.43 and 5.44 show the angular dependence of the theoretical dHvA frequency and the corresponding Fermi surfaces. All experimental branches except ζ are in excellent agreement with the theoretical ones. Moreover, if the theoretical branch ζ is slightly shifted to the lower frequency, it is also in good agreement

91
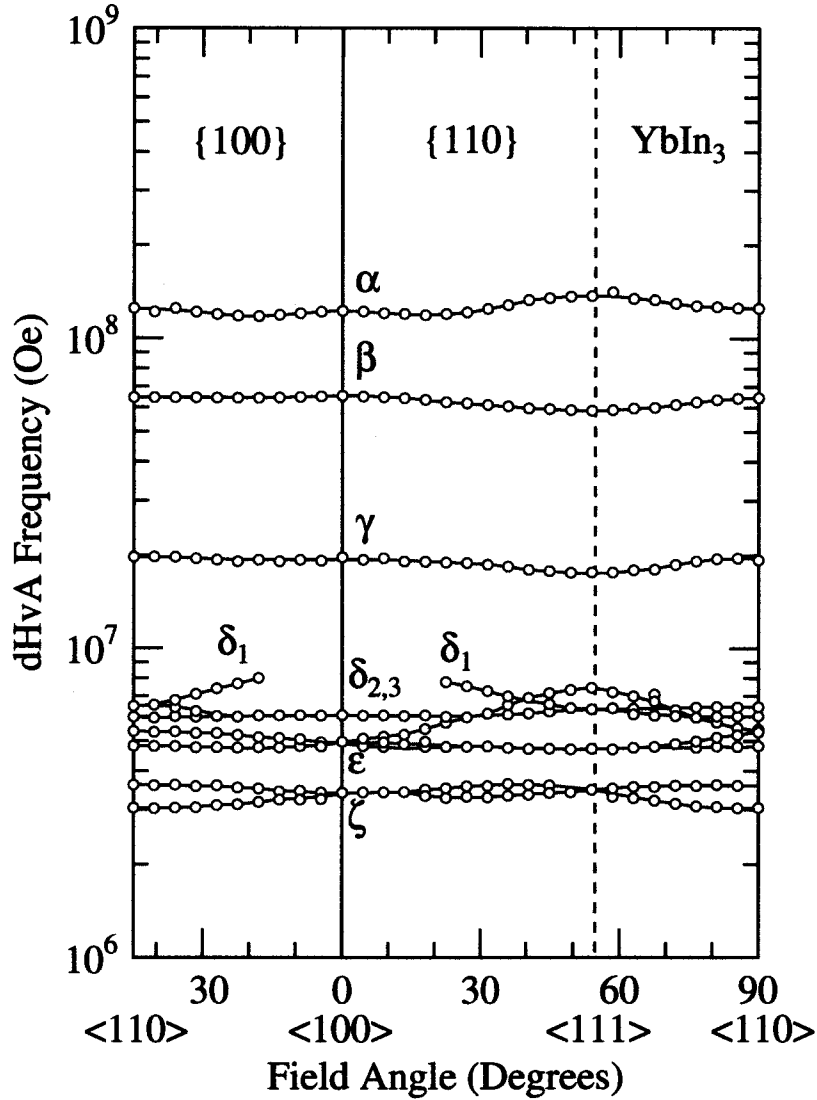
Fig. 5.42 Angular dependence of the dHvA frequency in YbIn₃.

with the experimental one in topology. Therefore, we can define the experimental branches as follows:

branch α: 13th band electron Fermi surface centered at R point,

branch β: 14th band electron Fermi surface centered at R point,

branch γ: 13th band electron Fermi surface centered at Γ point,

branch δ: 12th band hole Fermi surface centered at M point,

branch ε: 12th band hole Fermi surface on Λ axis and

branch ζ: 13th band electron Fermi surface centered at X point.

This consistency between experiments and theory is attributed to the $4f$-levels which

are far below the Fermi level. Hence, the $4f$-electrons do not affect the Fermi surface. We can give the same example of YbPb$_3$ as described in Sec. 5.2. On the other hand, a Pauli paramagnet YbAl$_3$ requires the artificial shifting of the $4f$-levels to explain the dHvA results.[108] As a result, the $4f$ electrons in YbAl$_3$ become a substantial component of the conduction band, forming heavy effective mass of the conduction electrons. Returning to our results in YbIn$_3$, the detected masses are very small, ranging from 1.3 to 0.22 m_0. This indicates that there is no modification of the Fermi surface caused by the $4f$ electrons.
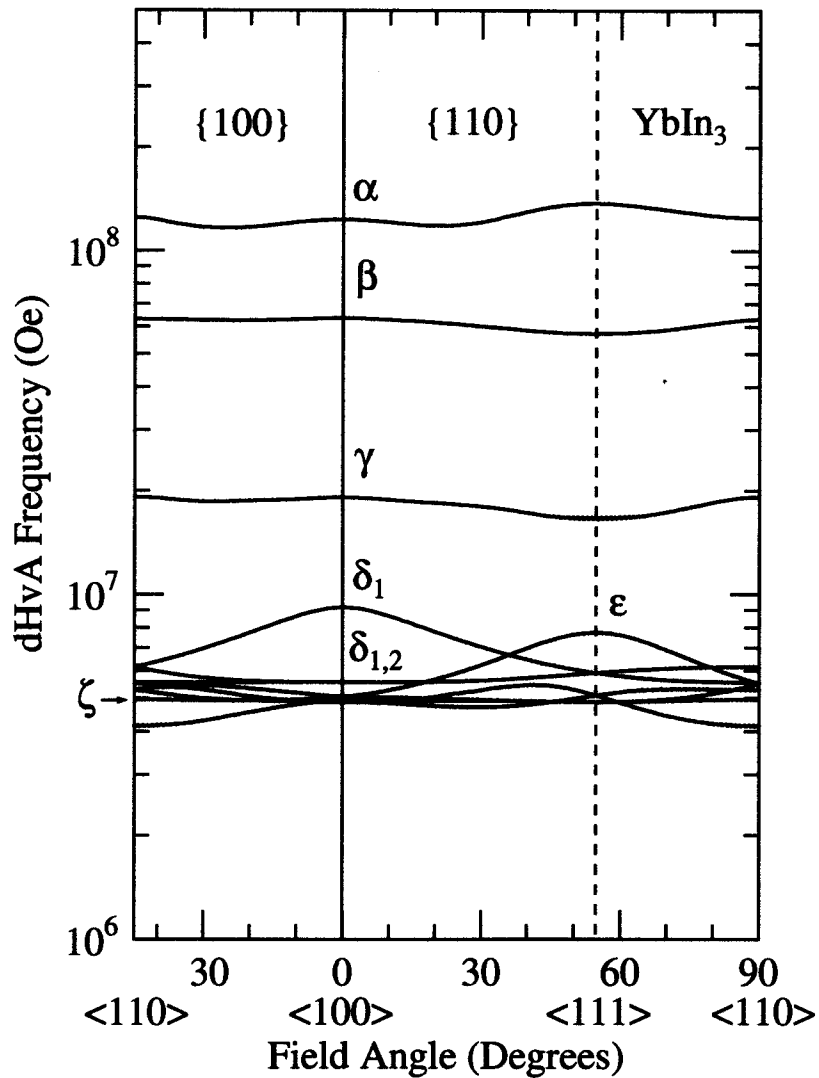
Fig. 5.43 Theoretical angular dependence of the dHvA frequency in YbIn$_3$.

YbIn₃

(a)

ε

δ₂

δ₁   δ₃

12th band hole

(b)

η   ζ₃

ζ₁

ζ₂

13th band electron

(c)

γ

13th band electron

(d)

α

13th band electron

(e)

β

14th band electron
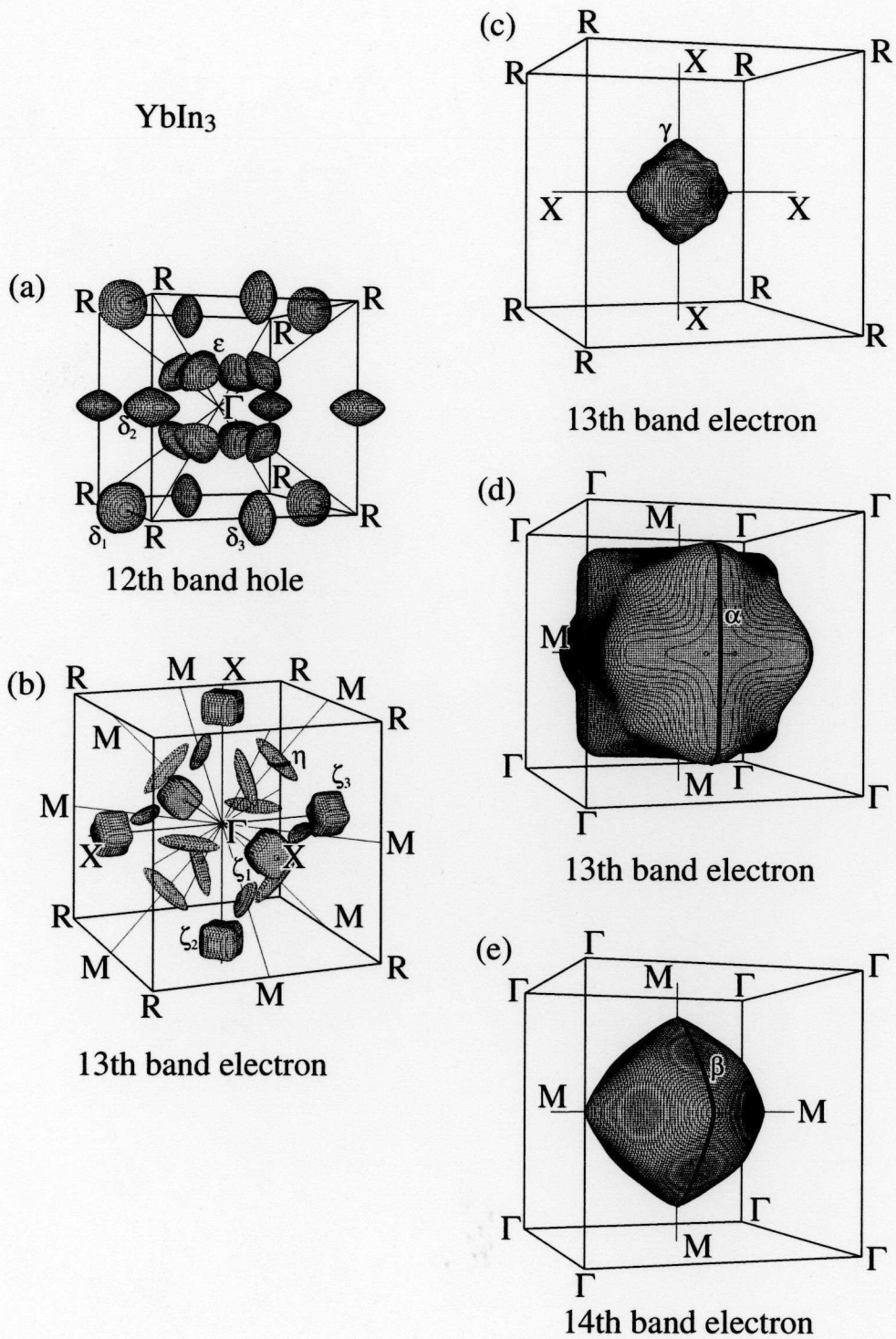
Fig. 5.44 Calculated Fermi surfaces in YbIn₃.

94

5.5 UAl₃

5.5.1 Electrical resistivity

We show in Fig. 5.45 the temperature dependence of the electrical resistivity ρ. The resistivity decreases monotoniously with decreasing the temperature, reflecting the paramagnetism. At low temperatures, the resistivity follows the Fermi liquid nature of a T^2-dependence below about 3 K: $\rho = \rho_0 + AT^2$ ($A = 1.50 \times 10^{-2}\,\mu\Omega\cdot\text{cm/K}^2$), as shown in an inset of Fig. 5.45. The positive curvature, however, appears around 200 K, indicating the spin fluctuation-like behavior. The residual resistivity ρ_0 and the residual resistivity ratio ρ_{RT}/ρ_0 are $1.04\,\mu\Omega\cdot\text{cm}$ and 88, respectively. In the previous report, ρ_{RT}/ρ_0 was 37.[61] The present single-crystal sample indicates the highest quality as far as we know.
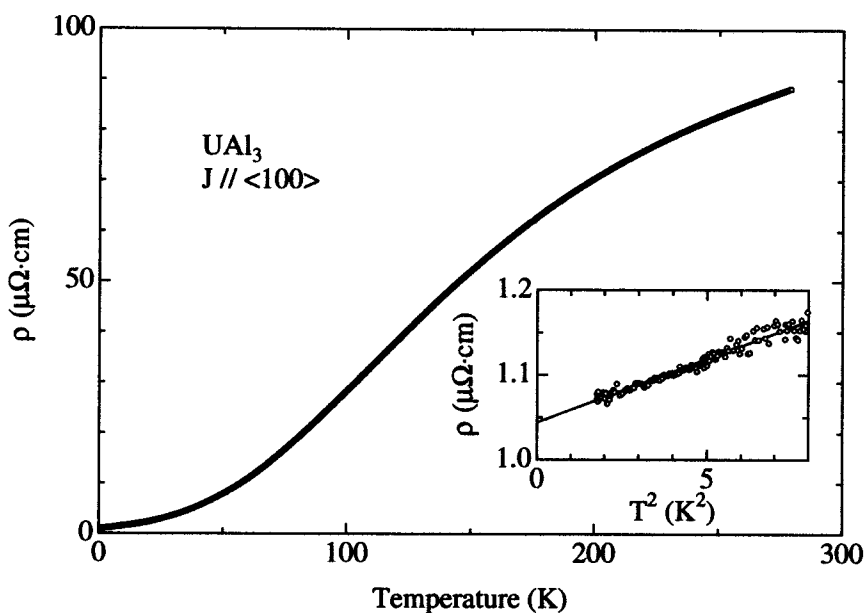
Fig. 5.45 Temperature dependence of the electrical resistivity in UAl₃.

5.5.2 dHvA effect

We measured the dHvA effect in fields up to 170 kOe and at temperatures down to 30 mK. Figure 5.46 shows the typical dHvA oscillation and the corresponding FFT spectrum for the field along $\langle 100 \rangle$ direction. There are detected three dHvA branches named β, γ and φ as well as the second harmonics of branch γ. Branch γ' might originate from the same Fermi surface of branch γ. These branches are split due to the corrugated Fermi surface, indicating maximum and minimum cross-sections. We also show in Fig. 5.47 the dHvA oscillation and its FFT spectrum at high magnetic fields. In addition to branch β and γ, branch α is clearly observed, although the dHvA amplitude for branch α is small compared to those for the other main branches.

95

Next we show in Fig. 5.48 the angular dependence of the dHvA frequency in UAl_3. The branches, indicating small dHvA amplitudes, are displayed by small circles. The solid lines are guides to eye. Branch γ is nearly constant against the field angle, indicating the spherical Fermi surface, although the signal disappears around the $\langle 110 \rangle$ direction.
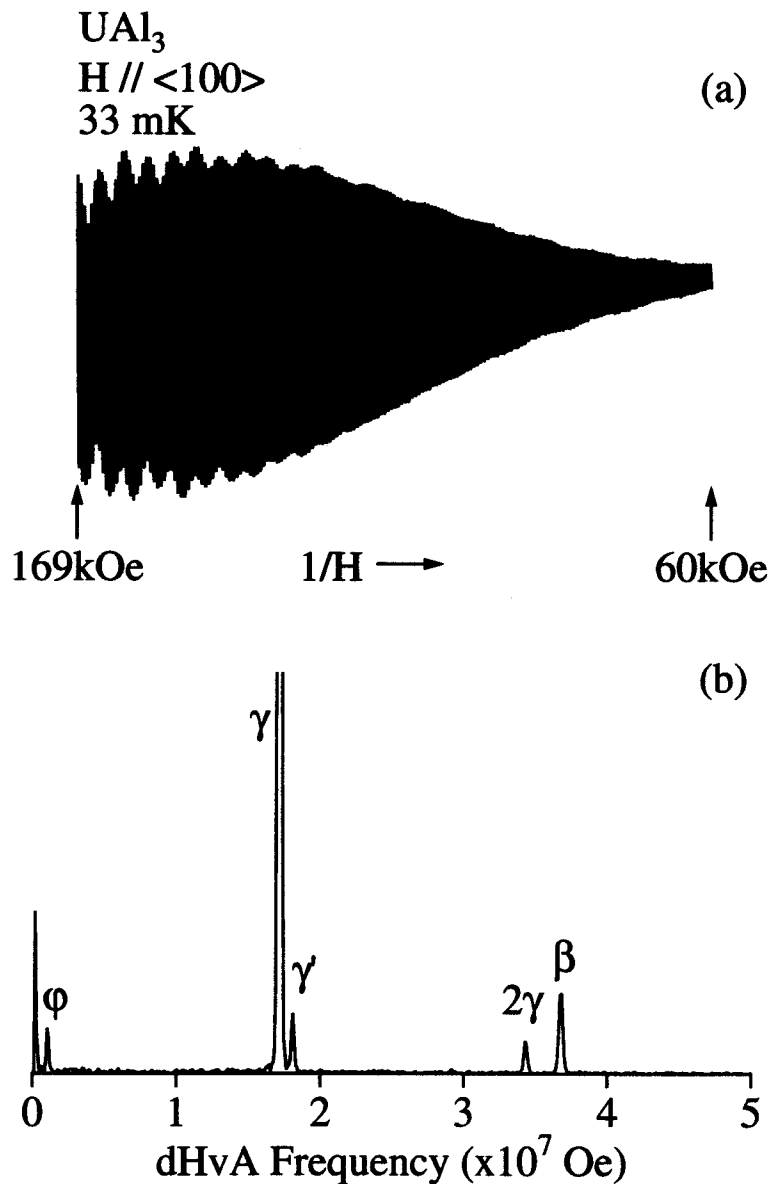
Fig. 5.46 (a) Typical dHvA oscillation and (b) its FFT spectrum for the field along $\langle 100 \rangle$ direction in UAl_3.

We determined the cyclotron mass m_c^* from the temperature dependence of the dHvA amplitude A, namely from the slope of a mass plot of $\ln[A\{1 - \exp(-2\alpha m_c^* T/H)\}]$ vs T by using eq. (4.29), as shown in Fig. 5.49. From this slope, the cyclotron mass was determined as $5.8\,m_0$ for branch β, $3.2\,m_0$ for branch γ and $3.0\,m_0$ for branch φ for the

UAl₃
H // 18°
55 mK   (a)

169kOe   1/H ⟶   155kOe

(b)

γ   β

2β   α

0   1   2   3
dHvA Frequency (x10⁸ Oe)
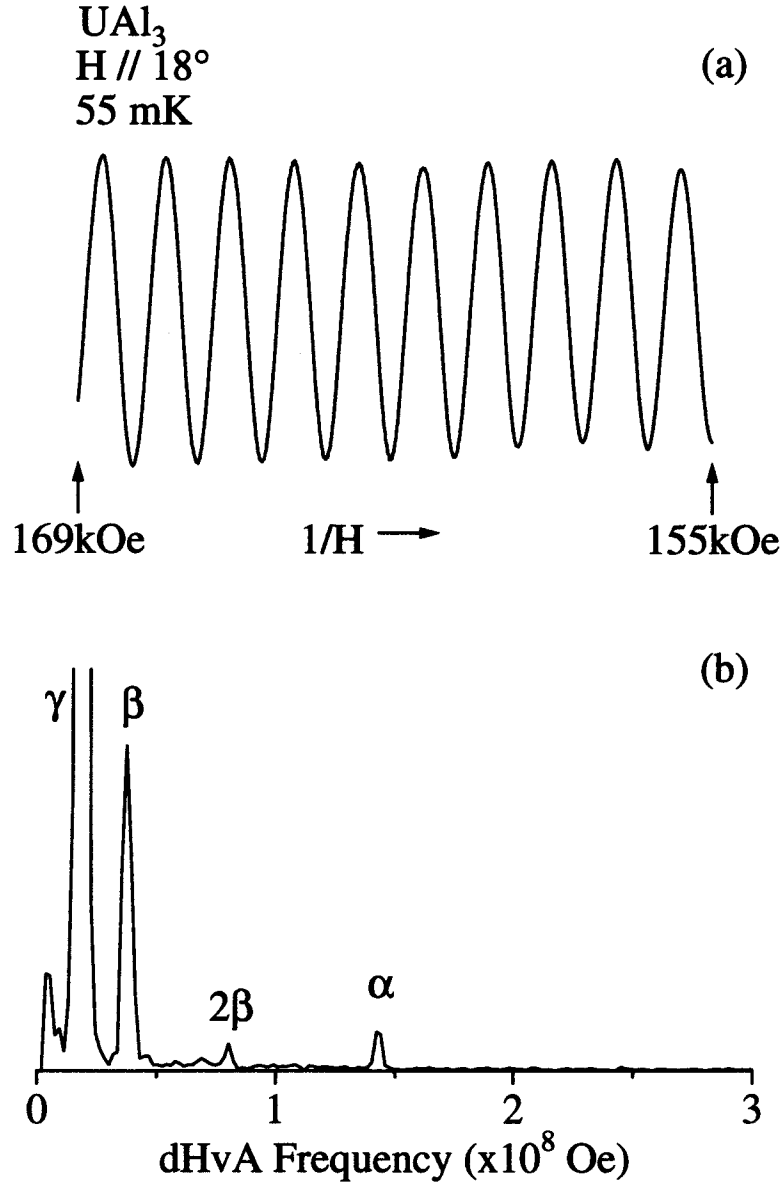
Fig. 5.47 (a) dHvA oscillation and (b) its FFT spectrum at high magnetic field in UAl₃.
The field angle is tilted 18° from ⟨100⟩ to ⟨110⟩.

field along ⟨100⟩ direction. The mass of branch α is determined as $17\,m_0$ for the field angle of 18° from ⟨100⟩ to ⟨110⟩. The present large mass is consistent with the electronic specific heat coefficient $43\,\mathrm{mJ/K^2 mol}$ in the previous report.[61]

We also determined the Dingle temperature T_D from the field dependence of the dHvA amplitude A, namely from the slope of $\ln[AH^{1/2}\sinh(\alpha m_\mathrm{c}^* T/H)/J_2(x)]$ vs H^{-1}, by using eq. (4.37). Figure 5.50 shows the so-called Dingle plot. The determined Dingle temperature for branches α, β and γ is the same value of 1.1 K. We can estimate the mean free path l by using the following formulae: $S_\mathrm{F} = \pi k_\mathrm{F}^2$, $\hbar k_\mathrm{F} = m_\mathrm{c}^* v_\mathrm{F}$ and $l = v_\mathrm{F}\tau$. Here, k_F is
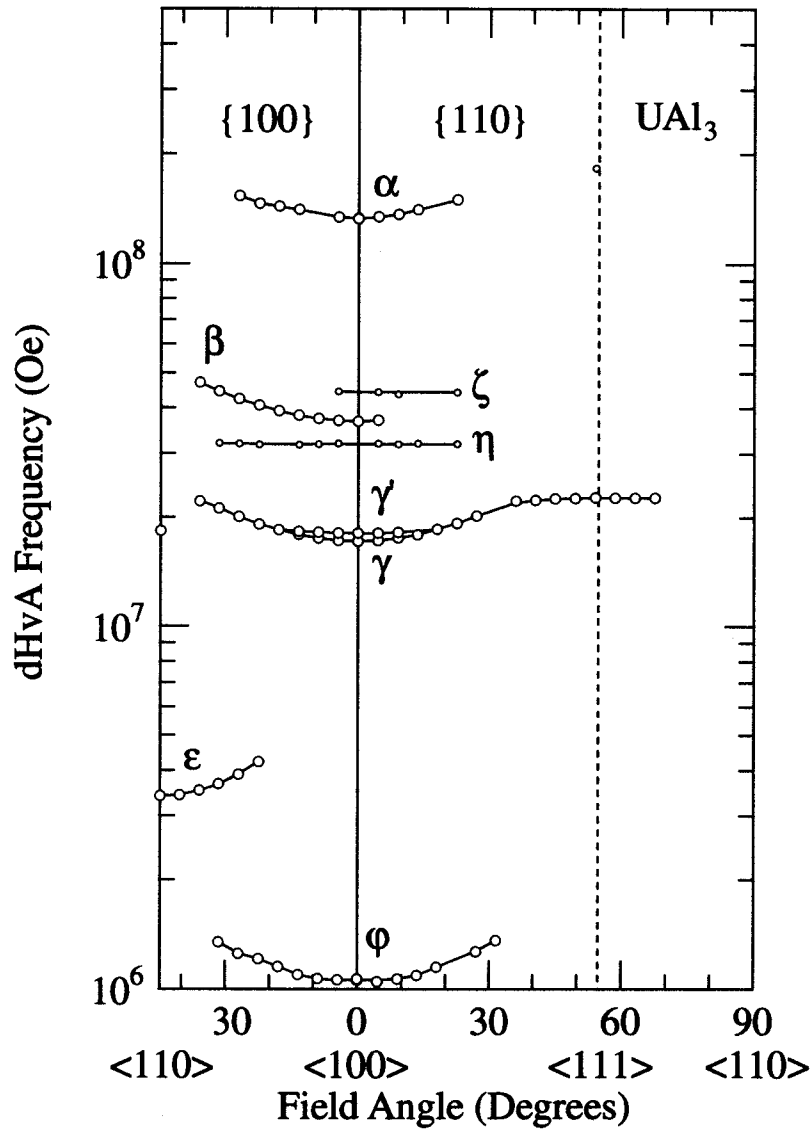
Fig. 5.48 Angular dependence of the dHvA frequency in UAl₃.

half of the caliper dimension of the spherical cross-section of the Fermi surface and v_F is Fermi velocity. The mean free path l is 410 Å for branch α, 730 Å for branch β and 940 Å for branch γ.

All determined cyclotron mass, Dingle temperature and mean free path are summarized Table 5.8

These results are compared to those of the FLAPW band calculation on the basis of the 5f-itinerant band model. Figure 5.51 shows the theoretical angular dependence of the dHvA frequency. The corresponding Fermi surfaces are shown in Fig. 5.52. These Fermi surfaces are two in number. One is a band 8-hole Fermi surface centered at Γ point. The another is also a band 8-hole Fermi surface centered at R point. Both of them are closed
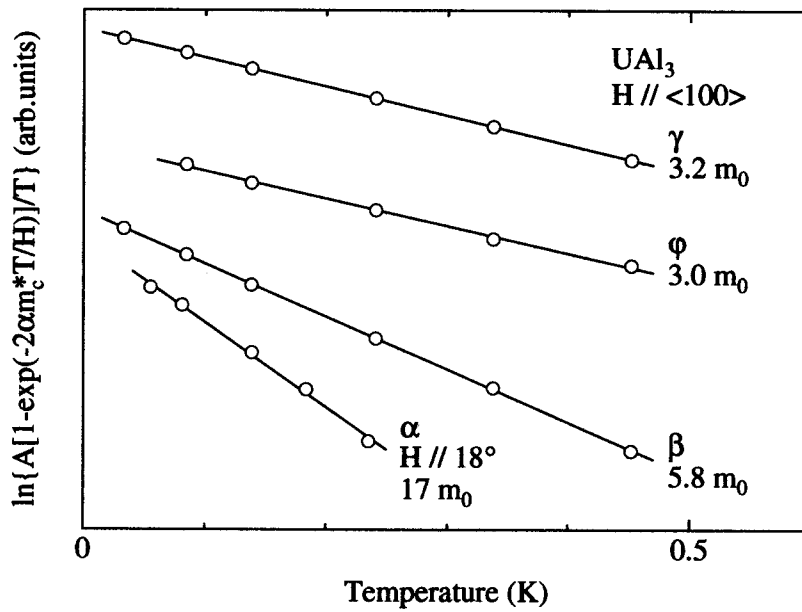
Fig. 5.49 Mass plot for UAl₃.
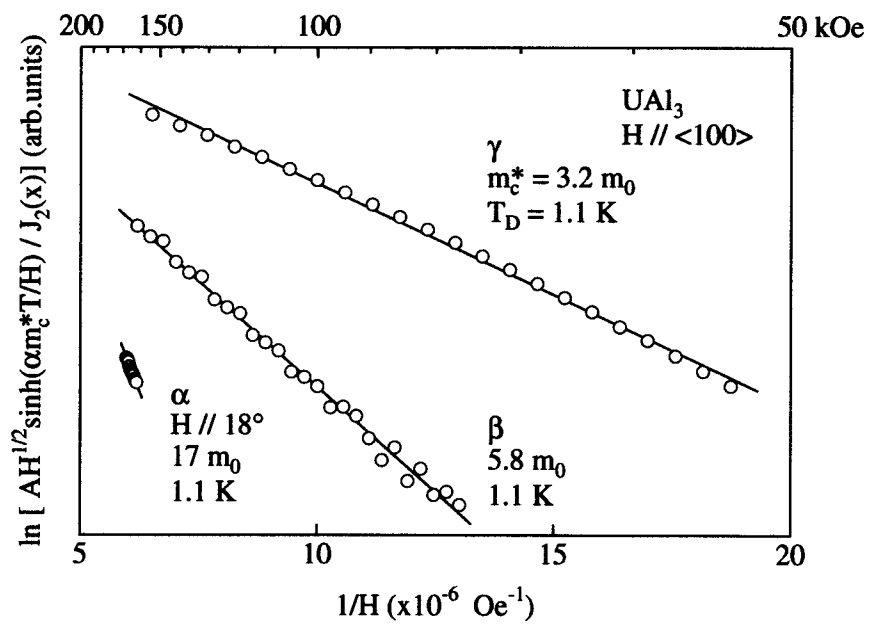
Fig. 5.50 Dingle plot for UAl₃.

Table 5.8 dHvA frequency F, cyclotron mass m_c^*, Dingle temperature T_D and mean free path l for UAl$_3$.

| | $H \parallel \langle 100 \rangle$ | | | | $H \parallel \langle 111 \rangle$ | | | |
	F (×10^7 Oe)	m_c^* (m_0)	T_D (K)	l (Å)	F (×10^7 Oe)	m_c^* (m_0)	T_D (K)	l (Å)
α	14.3†	17†	1.1†	490†				
β	3.67	5.8	1.1	730				
γ'	1.81	3.6						
γ	1.72	3.2	1.1	940	γ 2.27	4.8	1.0	750
φ	0.11	3.0						

†The data were obtained for the field along 18° tilted from ⟨100⟩ to ⟨110⟩.

Fermi surfaces. Branches α and γ in experiments are in good agreement with the results of band calculation, although neither branch is observed around ⟨110⟩. This is most likely due to the curvature factor, which is apparent in Fig. 5.52. Therefore we conclude that branches α and γ originate from the hole Fermi surfaces centered at R and Γ point, respectively. In the previous paper, the "dogs bone" Fermi surfaces connecting the above two Fermi surfaces at Λ axes are predicted by the band calculations. We believe that there are not present, because branch γ in Fig. 5.48 forms approximately a closed Fermi surface. If the "dogs bone" Fermi surface exists, the cylindrical Fermi surface with a small frequency must be detected around ⟨111⟩. We observed, however, no such a branch around ⟨111⟩. Therefore the "dogs bone" surface does not exist. Branches β, ε, φ, ζ and η are not predicted in the present band calculation. The modification of the calculations is required to explain these experimental results. For example, in a Pauli paramagnet of YbAl$_3$, the experimental dHvA data are well explained by the band calculations where the $4f$ energy levels which are sited far below the Fermi level are slightly shifted.[108] This modification affects the Fermi surface because the $4f$ electrons become a substantial component of the conduction band. The detected cyclotron masses are also large, reflecting a many-body Kondo effect. The band calculation for UAl$_3$ also requires the same consideration because the UAl$_3$ is a paramagnet possessing a large γ-value and cyclotron masses.

The calculated γ-value of 14.8 mJ/K^{2}mol is a factor of 2.9 smaller than the experimental value in ref. (61). On the other hand, the calculated band masses are $6\,m_0$ for branch α and $2\,m_0$ for branch γ. The experimental cyclotron masses are 2.8 and 1.6 times larger than the calculated ones. This enhancement of the cyclotron mass is consistent with that of the γ-value.
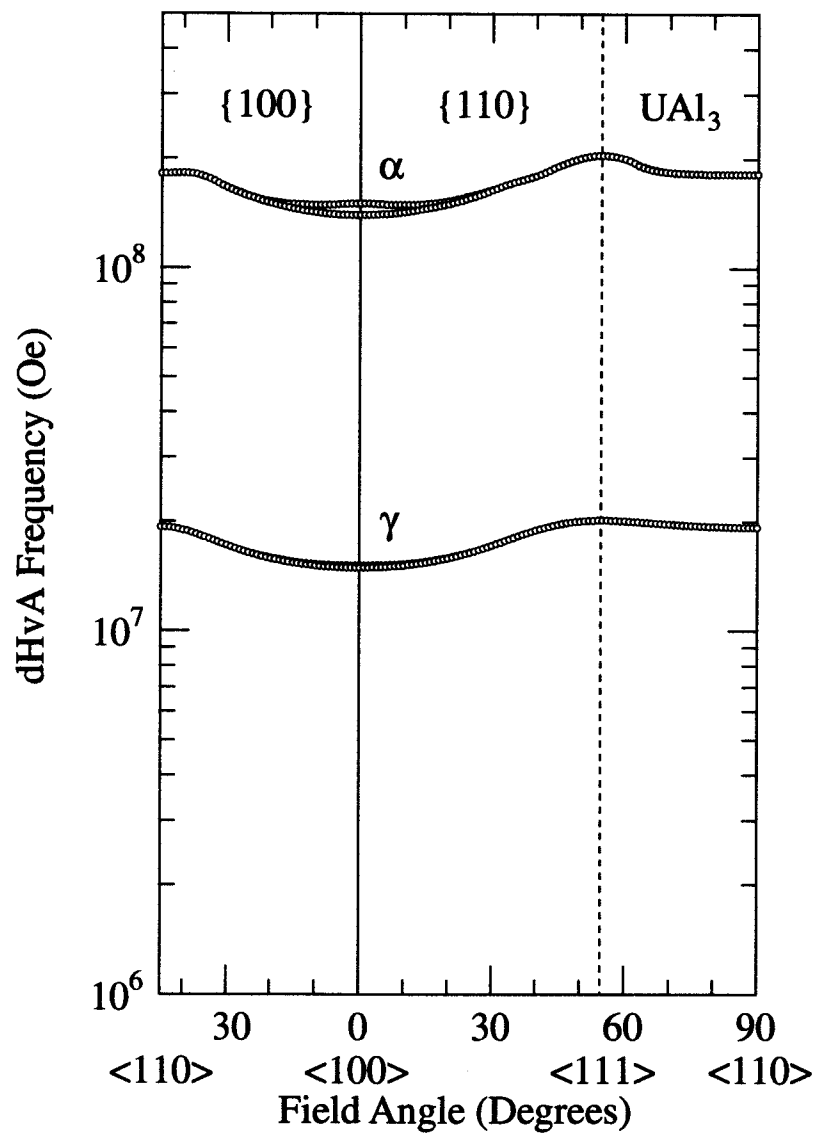
Fig. 5.51 Theoretical angular dependence of the dHvA frequency in UAl₃.

UAl3
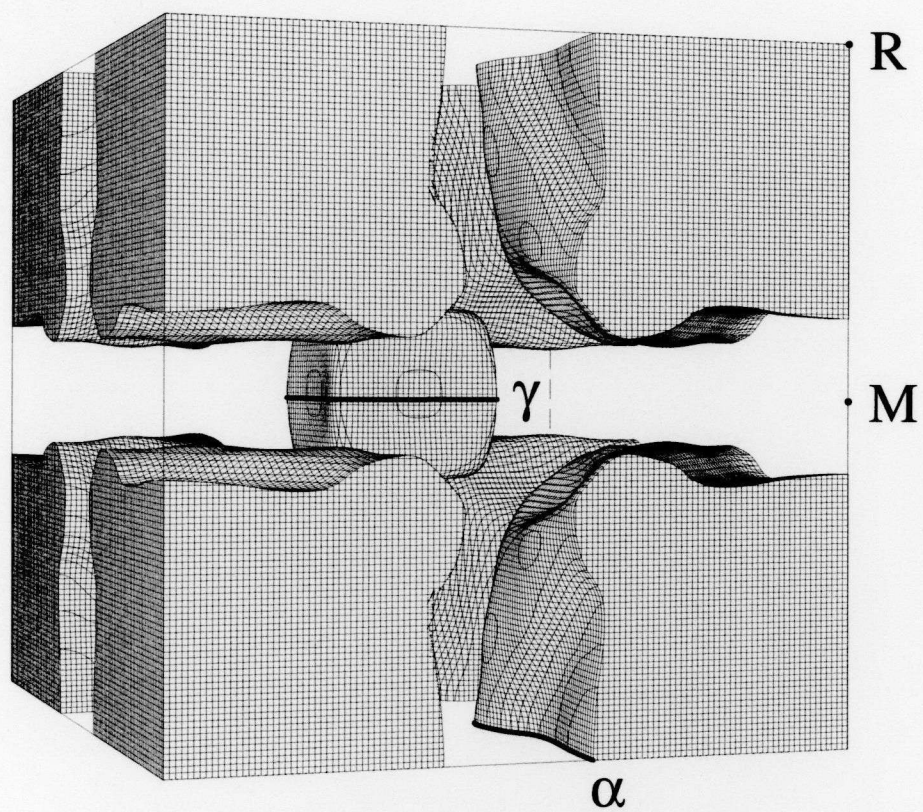
Band 8-hole Fermi surface

Fig. 5.52 Calculated Fermi surface centered at Γ point for UAl3.

5.6 UGa₃

5.6.1 Electrical resistivity

Figure 5.53 shows the temperature dependence of the electrical resistivity ρ.[109,110] There is found a very small hump at $T_N = 67\,\mathrm{K}$, and the resistivity decreases with decreasing the temperature, following a T^2-dependence below about $20\,\mathrm{K}$: $\rho = \rho_0 + AT^2$ ($A = 8.79 \times 10^{-3}\,\mu\Omega \cdot \mathrm{cm/K^2}$), as shown in an inset of Fig. 5.53. The residual resistivity ρ_0 and the residual resistivity ratio ρ_{RT}/ρ_0 are $1.20\,\mu\Omega \cdot \mathrm{cm}$ and 81, respectively. The previous ρ_{RT}/ρ_0 values were 1.7 in ref. (64) and 38 in ref. (61). The present single-crystal sample indicates the highest quality as far as we know, although there is a report on a polycrystal sample with $\rho_{RT}/\rho_0 = 100$.[69] The overall temperature dependence of the resistivity is the same as the previous one.[61,69,71]
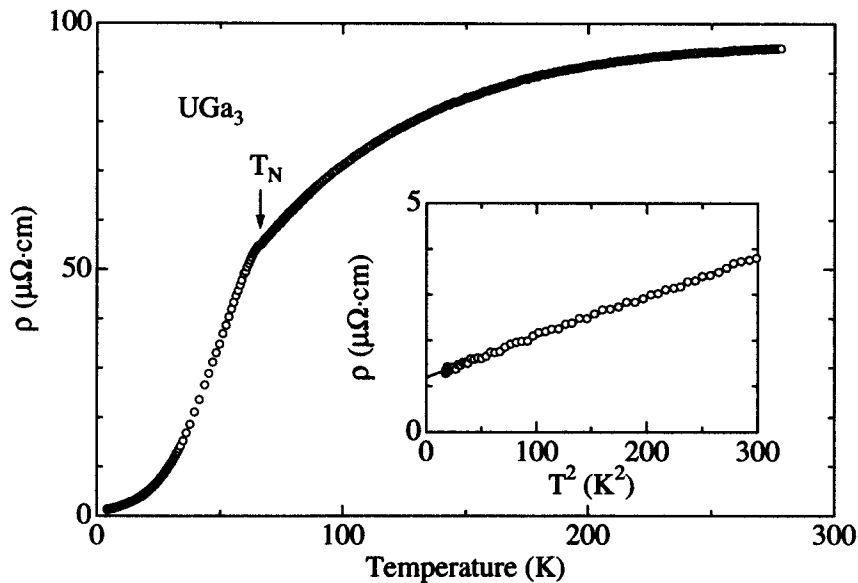
Fig. 5.53 Temperature dependence of the electrical resistivity in UGa₃.

5.6.2 Magnetic susceptibility

Next we measured the magnetic susceptibility χ, as shown in Fig. 5.54. The susceptibility exhibits a very weak temperature dependence in the paramagnetic region. This temperature dependence does not follow the Curie–Weiss law, as mentioned in Sec. 3.3. A steep decrease of the susceptibility is found below $T_N = 67\,\mathrm{K}$, as shown by an arrow in an inset of Fig. 5.54, and furthermore two anomalies are observed at $T_1 \simeq 40\,\mathrm{K}$ and $T_2 \simeq 8\,\mathrm{K}$. These data are the same as the previous result,[73] although the previous experiment was done only for the field along the ⟨100⟩ direction. We measured it for three typical field
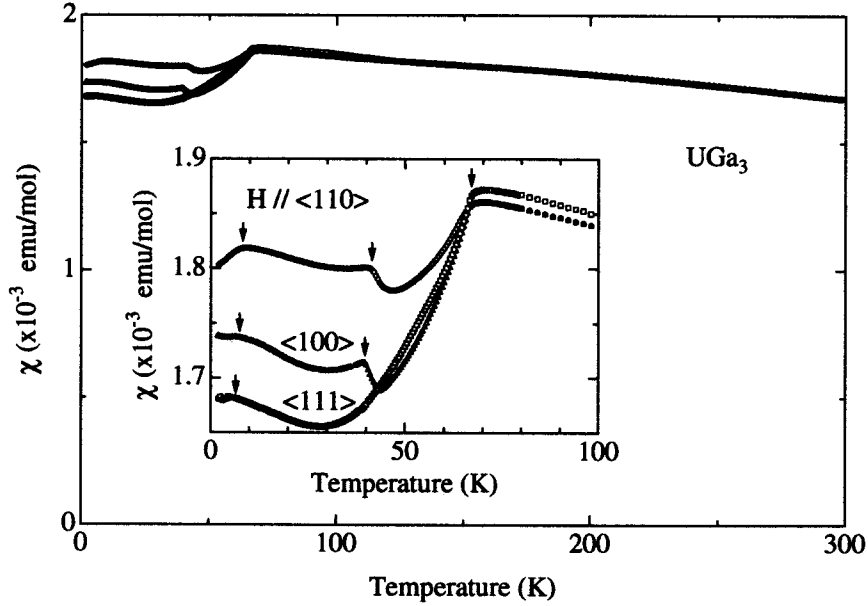
Fig. 5.54 Temperature dependence of the magnetic susceptibility in UGa_3.

directions. The anomaly at T_1 is, however, not observed for $H \parallel \langle 111 \rangle$, and furthermore the susceptibility for $H \parallel \langle 111 \rangle$ has the smallest value among the three field directions.

These data simply suggest that the direction of the moments is $\langle 111 \rangle$. According to the powder neutron diffraction study, uranium moments are aligned ferromagnetically in $\{111\}$ planes which are coupled antiferromagnetically to the adjacent $\{111\}$ planes.[74,75] From the recent study of the neutron diffraction on a UGa_3 single crystal,[76] it is proposed that the moments are along $\langle 111 \rangle$, which is consistent with our susceptibility data. The direction of the moments is, however, not conclusively determined at present.

In the temperature range between $T_1 \simeq 40\,K$ and $T_N = 67\,K$, the value of the susceptibility along $\langle 100 \rangle$ is slightly smaller than that along $\langle 111 \rangle$. Thus it seems that the moments in this temperature region are along $\langle 100 \rangle$ and change to be along $\langle 111 \rangle$ below $40\,K$. The moment reorientation is supported by the rapid increase of the intensities at $40\,K$ on the neutron experiment, as shown in Fig. 3.16.[76]

5.6.3 Hall coefficient and thermoelectric power

There are no reports on the Hall coefficient R_H and thermoelectric power S. We measured them to understand the electronic state and scattering mechanism of conduction electrons. Figure 5.55 shows the temperature dependence of the Hall coefficient. In f-electron systems, the Hall coefficient R_H in the paramagnetic state is represented as follows:

$$R_H = R_0 + 4\pi R_S \chi \tag{5.10}$$
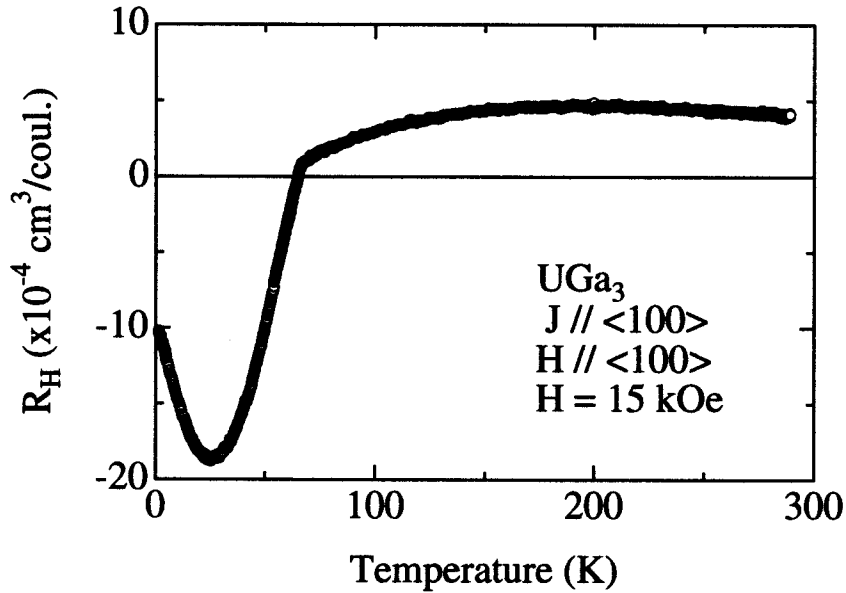
Fig. 5.55 Temperature dependence of the Hall coefficient in UGa$_3$.

or

$$= R_0 + 4\pi R_S \rho \chi, \tag{5.11}$$

where R_0 is the normal Hall coefficient related to the carrier concentration and mobility, R_S is the anomalous Hall coefficient, χ is the magnetic susceptibility and ρ is the resistivity. Note that the normal Hall coefficient is approximately temperature-independent and the anomalous part of $\rho\chi$ is temperature-dependent.

When we compare the result of the Hall coefficient to those of the susceptibility and resistivity, eq. (5.10) is not applied to the temperature dependence of the Hall coefficient for UGa$_3$ because R_H shows a broad maximum around 200 K. We suppose that eq. (5.11) might explain the temperature dependence of the Hall coefficient. Figure 5.56 shows the $\rho\chi$ vs R_H relation. In the paramagnetic region, the Hall coefficient is found to be proportional to $\rho\chi$. From this relation, we can get the normal Hall coefficient $R_0 = -6.0 \times 10^{-4}$ cm^3/coul., extrapolated to 0 K, as shown by a broken line in Fig. 5.56. As shown in Figs. 5.55 and 5.56, the Hall coefficient is drastically changed below T_N. The sign is changed from positive to negative and a R_H-value of -1.0×10^{-3} cm^3/coul. at 1.3 K is different from the value of $R_0 = -6.0 \times 10^{-4}$ cm^3/coul. estimated above. These results indicate that the electronic states are changed and/or the scattering mechanism is drastically changed below T_N.

The 4f-electronic properties can be well explained by the localized 4f-electron model. In some case, the 4f-electrons hybridize significantly with conduction electrons, forming a heavy electron system at low temperatures. On the other hand, the 3d-electrons are
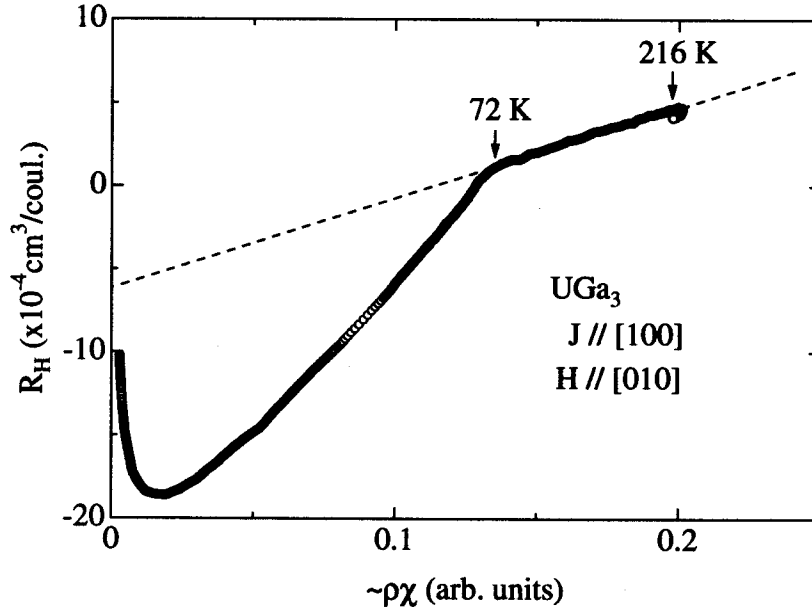
Fig. 5.56 $\rho\chi$ vs R_H relation in UGa₃.

responsible for ferromagnetism in such transition metals as Ni and Fe, which can be described on the basis of the itinerant $3d$-electron model. Equation (5.10) is applied to the localized $4f$-electron system. On the other hand, the eq. (5.11), which is based on the skew scattering, is often applied to the itinerant $3d$-electron system. The present Hall coefficient might be qualitatively close to the itinerant $3d$-electron system.

Next we show in Fig. 5.57 the temperature dependence of the thermoelectric power S. A value of the thermoelectric power itself is large at room temperature as in the heavy electron system. The thermoelectric power is represented by an energy derivative of the density of states. A positive thermoelectric power is consistent with the recent result of the theoretical density of states based on the energy band structure calculations.[61] As shown in Fig. 5.57, the thermoelectric power decreases steeply below $T_N = 67$ K. The anomalies at T_1 and T_2 are also reflected in the thermoelectric power as in the susceptibility data, as shown in an inset of Fig. 5.57.

5.6.4 Specific heat

Figure 5.58 shows the temperature dependence of the specific heat. A solid line in Fig. 5.58 is a guide line. A small increase at 67 K is due to the antiferromagnetic ordering, although the data points are scattered above 40 K. Moreover, the magnetic contribution to the specific heat appears to be considerably small. This is consistent with the previous results which shows the reduced magnetic entropy.[69] An inset indicates the T^2-dependence of the specific heat in the form of C/T. The specific heat C is well explained by the simple form of $\gamma T + \beta^* T^3$, where the second term consists of phonon and antiferromagnetic
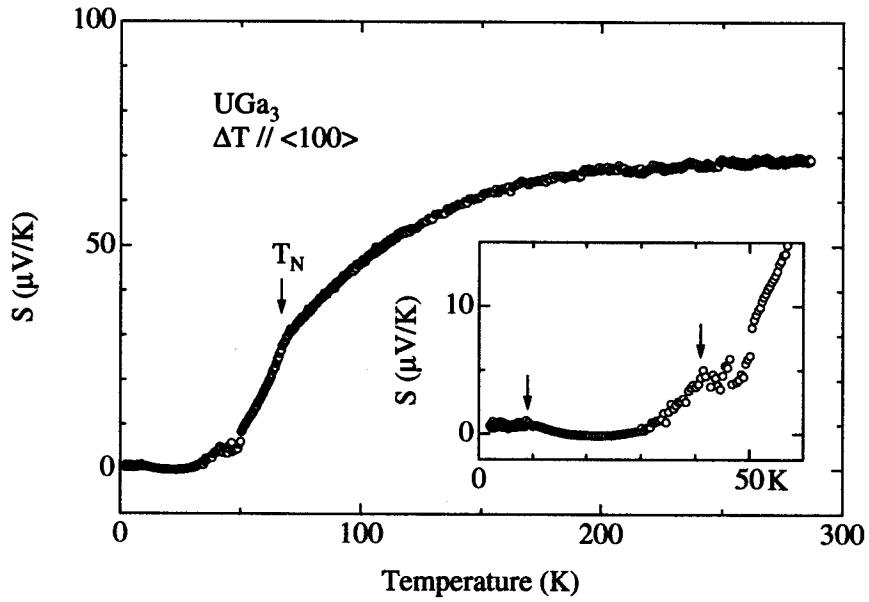
Fig. 5.57 Temperature dependence of the thermoelectric power in UGa$_3$.

contributions. A γ-value is obtained as $52\,\mathrm{mJ/K^2 \cdot mol}$, which is in good agreement with the previous result.[69] The present A and γ values are approximately consistent with the well-known Kadowaki-Woods relation,[32,111] as shown in Fig. 5.59.
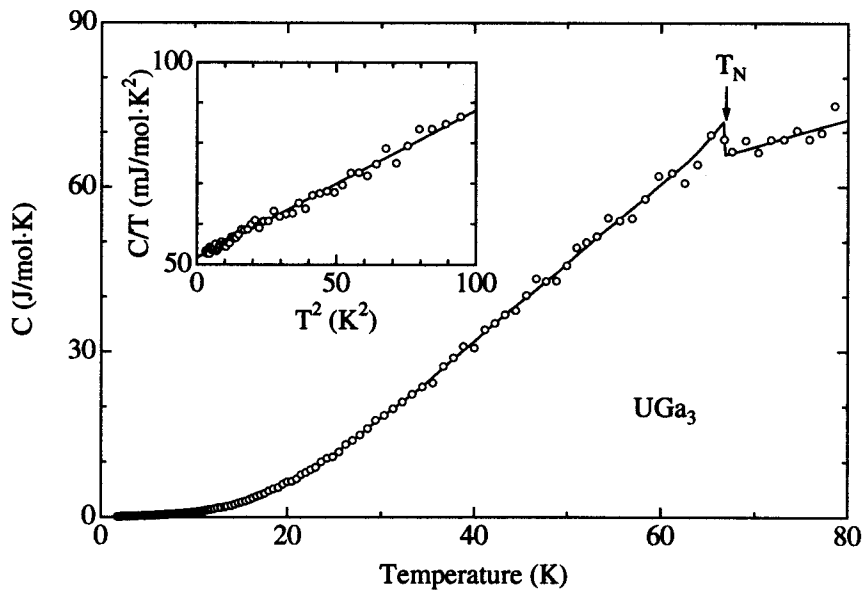
Fig. 5.58 Temperature dependence of the specific heat in UGa$_3$.
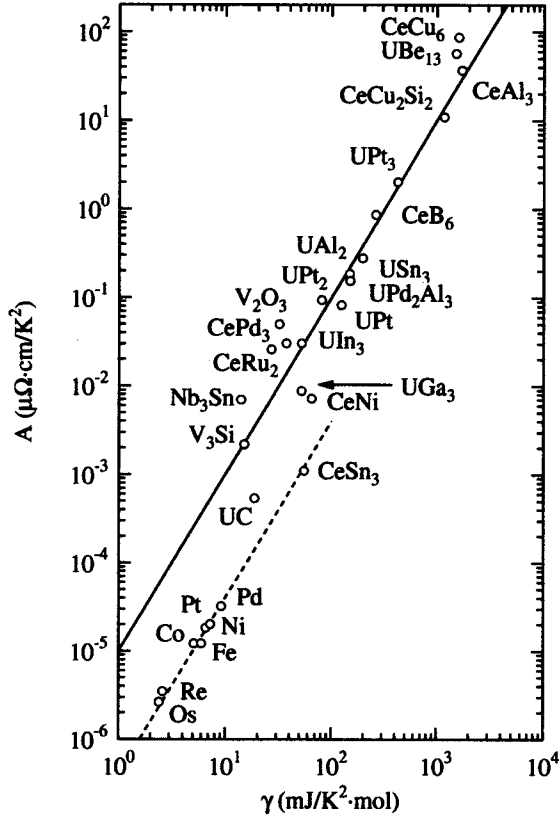
Fig. 5.59 Kadowaki-Woods plot including our results of UGa₃.

5.6.5 Magnetoresistance

To investigate the Fermi surfaces of UGa₃, we measured the transverse magnetoresistance. We show in Figs. 5.60 and 5.61 the angular dependence of the transverse magnetoresistance $\Delta\rho/\rho \equiv \{\rho(H) - \rho(0)\}/\rho(0)$ and the field dependence of $\Delta\rho/\rho$ for the typical three directions, respectively. The magnetoresistance increases as H^n ($n = 1.6$–1.7) for any field direction, where solid lines indicate fitting lines.

The transverse magnetoresistance, in which the directions of magnetic field and current are perpendicular to each other, provides important information on the overall topology of the Fermi surface. For a compensated metal with equal carrier numbers of electrons and holes without open orbits, $\Delta\rho/\rho$ increases as H^n ($1 < n \leq 2$) for a general field direction. Note that the integer n is not equal to 2 because the high-field condition is not fully satisfied in the real sample. In the high-field condition, the magnetoresistance increases quadratically; $\Delta\rho/\rho \sim (\omega_c\tau)^2$, where ω_c ($= eH/m_c^*c$) is the cyclotron frequency, m_c^* is the cyclotron effective mass and τ is the scattering lifetime.

The present results directly indicate that UGa₃ is a compensated metal without open orbits. Namely, Fermi surfaces consist of closed ones. The very recent paper reported the similar field dependence, although the magnetoresistance measurement was carried out
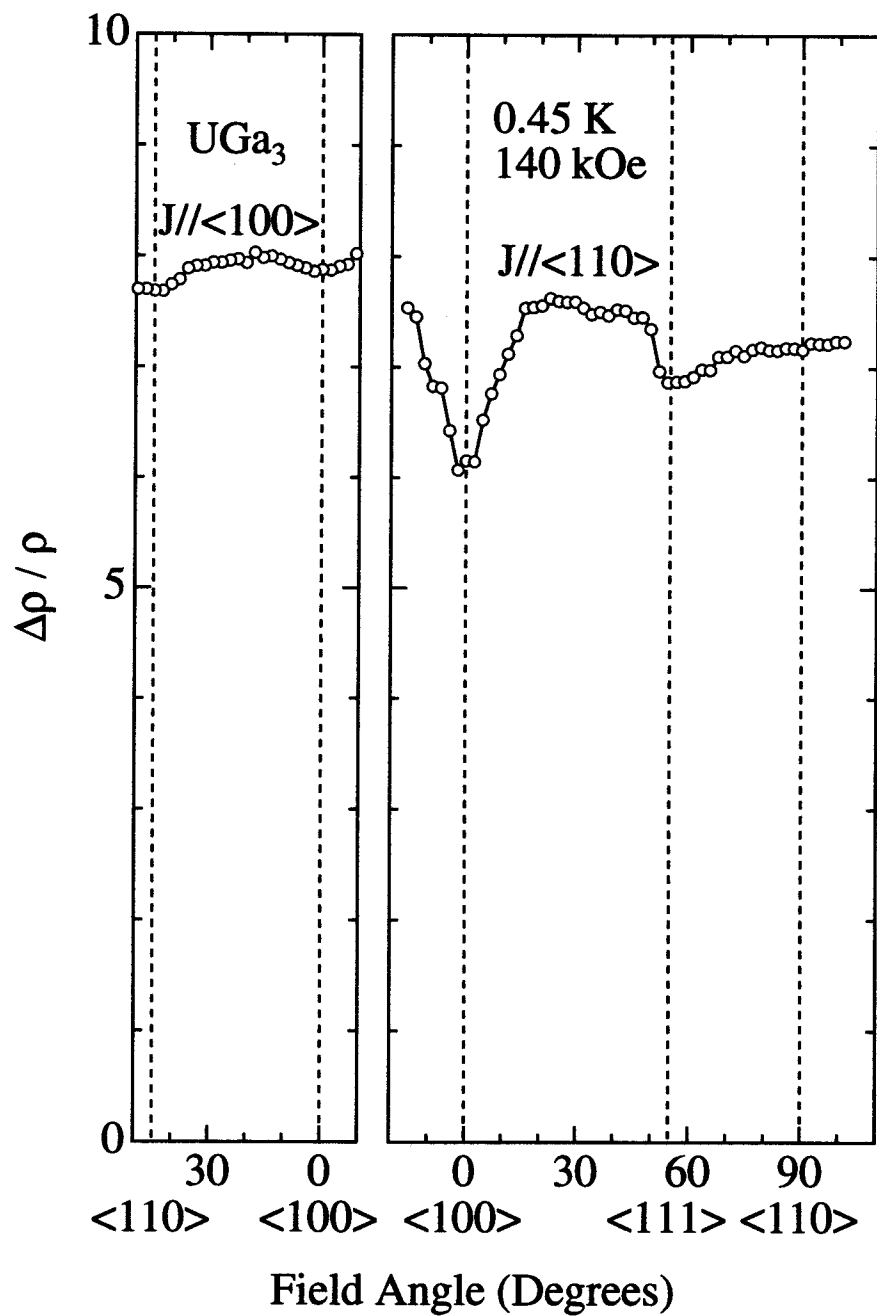
Fig. 5.60 Angular dependence of the transverse magnetoresistance in UGa$_3$.
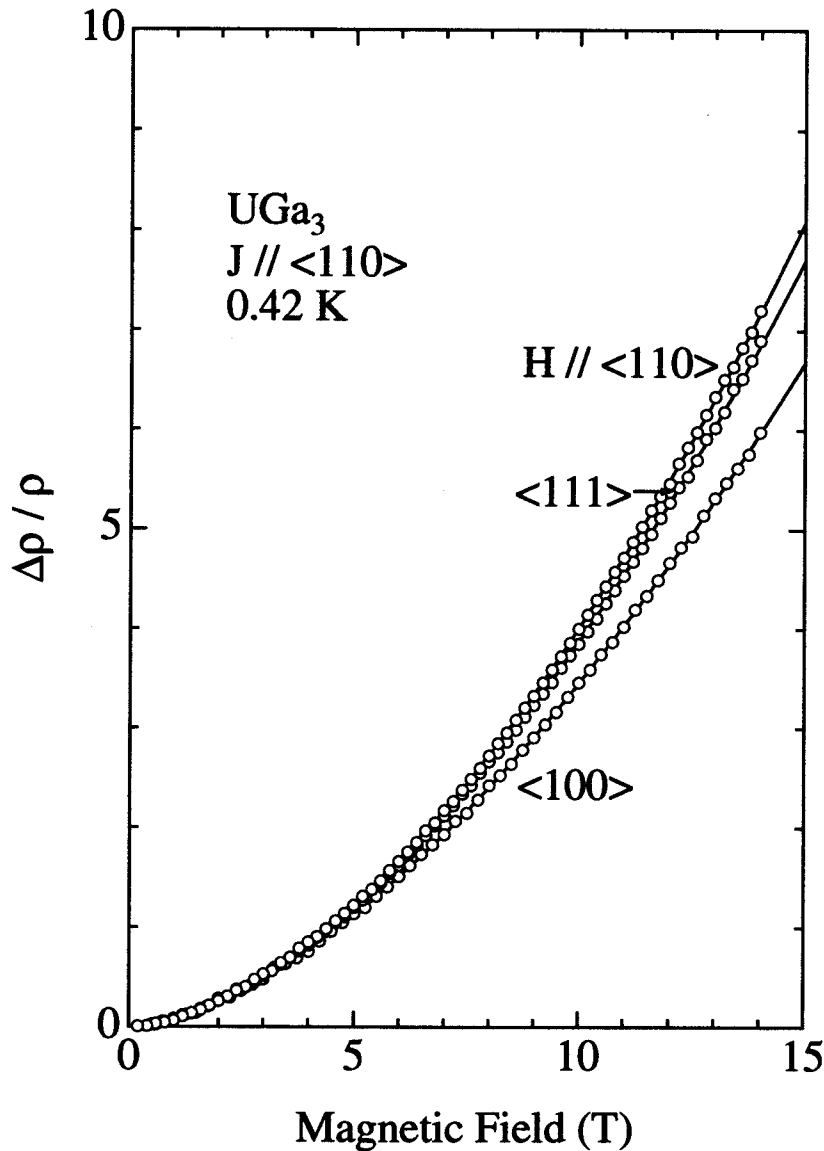
Fig. 5.61 Field dependence of the transverse magnetoresistance in UGa₃.

for one field direction.[61] The $\Delta\rho/\rho$ value at 110 kOe is reported to be 0.7 as shown in Fig. 3.10, which is compared to a present large value of $\Delta\rho/\rho = 4$ at 110 kOe in Fig. 5.61. The sample in ref. (61) has $\rho_{RT}/\rho_0 = 38$, which is compared to our high-quality sample with $\rho_{RT}/\rho_0 = 81$.

5.6.6 dHvA effect

Next we measured the dHvA oscillation. Figure 5.62 shows the typical dHvA oscillation for the field along $\langle 100 \rangle$ at 40 mK and the corresponding fast Fourier transformation (FFT) spectrum. There are detected three dHvA branches named α, γ and δ as well as
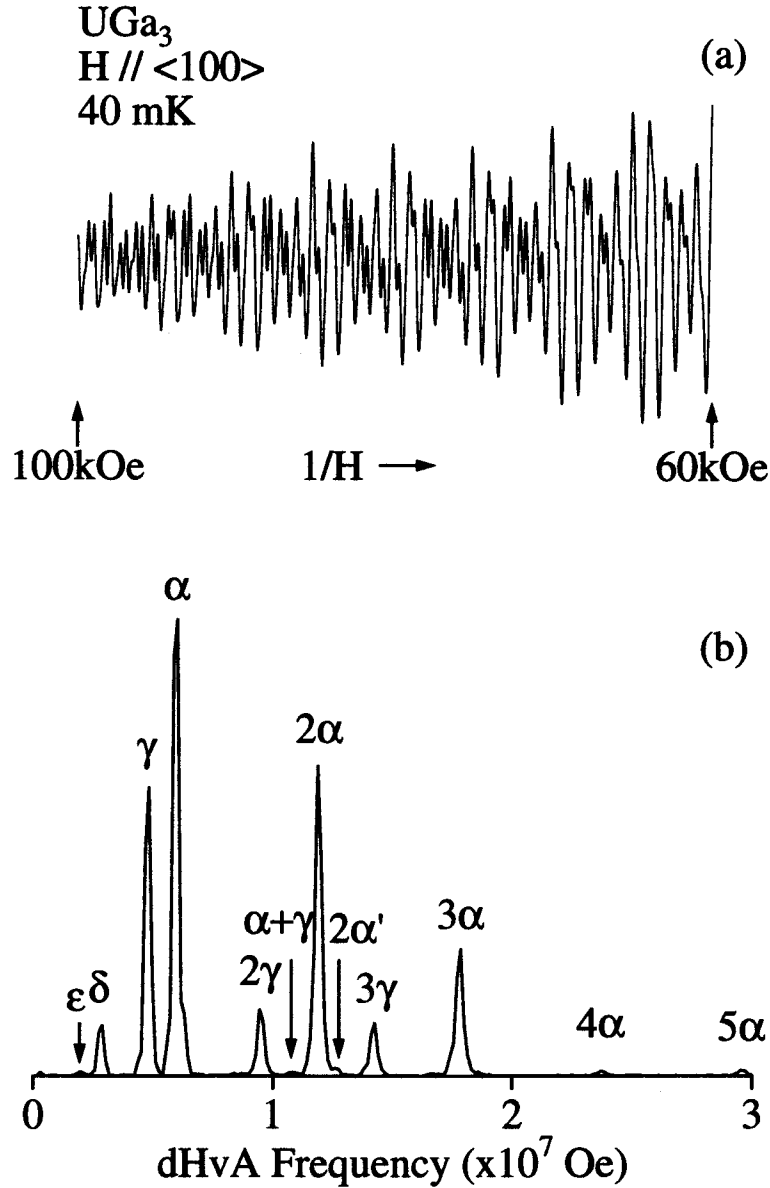
Fig. 5.62 (a) Typical dHvA oscillation and (b) the corresponding FFT spectrum in UGa₃.

their harmonics. When the field is reduced and/or the field direction is tilted from ⟨100⟩, branches β and ε are detected clearly. These branches are shown in Fig. 5.63 by large circles.

By using eq. (4.29), we determined the cyclotron effective mass m_c^* from the temperature dependence of the dHvA amplitude A, namely from the slope of a plot of $\ln[A\{1 - \exp(-2\alpha m_c^* T/H)\}]$ vs T on the basis of a method of successive approximations, as shown in Fig. 5.64. From this slope, the cyclotron mass was determined as $3.5\,m_0$ for branch α, $2.5\,m_0$ for branch γ and $2.5\,m_0$ for branch δ for the field along ⟨100⟩ direction. Every branches possess moderately heavy masses although they are small Fermi surfaces.

111
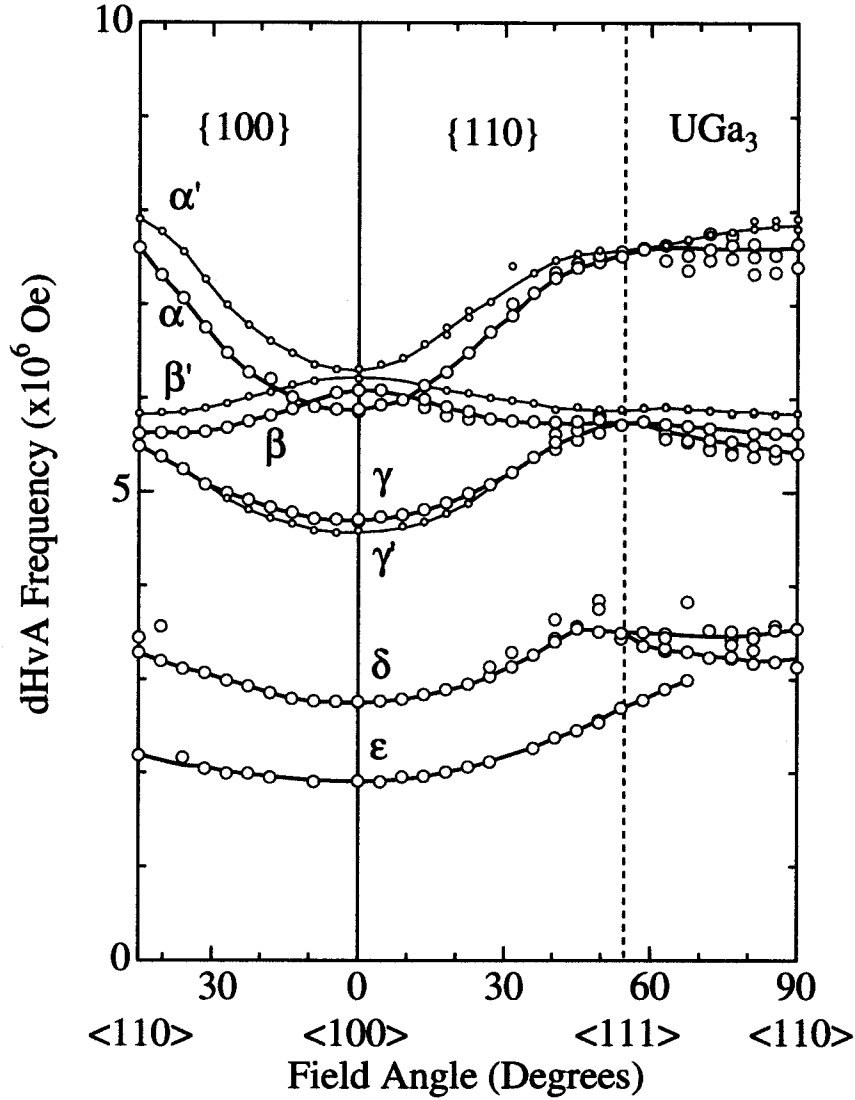
Fig. 5.63 Angular dependence of the dHvA frequency in UGa₃.

The cyclotron masses for the other directions are shown in Table 5.9.

We also determined the Dingle temperature from the field dependence of the dHvA amplitude by using eq. (4.37), namely from the slope of $\ln[AH^{1/2}\sinh(\alpha m_c^* T/H)/J_2(x)]$ vs H^{-1}. Figure 5.65 shows the so-called Dingle plot. From this slope, T_{D} along $\langle 100 \rangle$ is obtained as 0.19 K for branch α, 0.32 K for branch γ and 0.36 K for branch δ. Assuming that the cross sections are circles, we can use the following formulae of $S_{\mathrm{F}} = \pi k_{\mathrm{F}}^2$, $\hbar k_{\mathrm{F}} = m_c^* v_{\mathrm{F}}$ and $l = v_{\mathrm{F}}\tau$. Here, k_{F} is half of the caliper dimension of the spherical cross-section of the Fermi surface and v_{F} is Fermi velocity. From above equations, we can simply obtain the mean free path l. It is 2900 Å for branch α along $\langle 100 \rangle$. The l-value is large, indicating a high-quality sample. All determined Dingle temperatures and mean free

112
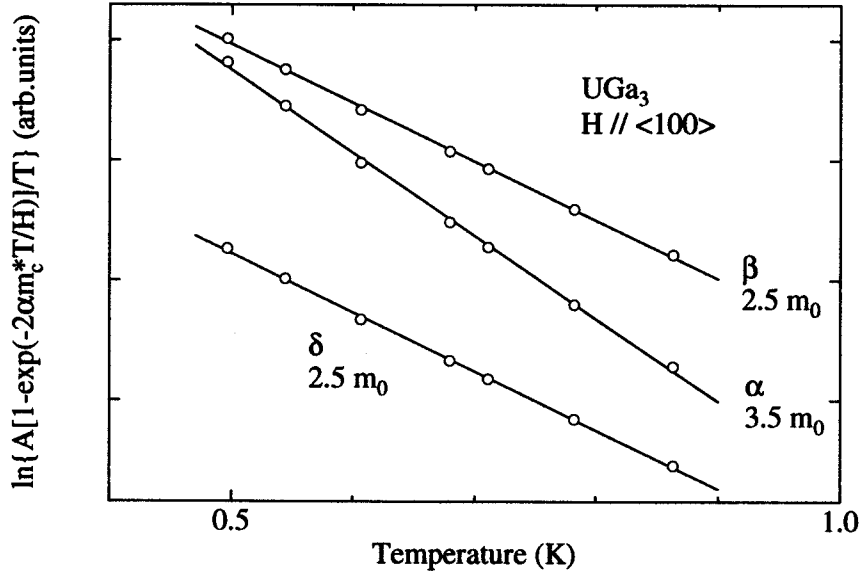
Fig. 5.64 Mass plot for UGa₃.

Table 5.9 dHvA frequency F, cyclotron mass m_c^*, Dingle temperature T_D and mean free path l for UGa₃.

	$H \parallel \langle 100 \rangle$					$H \parallel \langle 110 \rangle$					$H \parallel \langle 111 \rangle$			
	F (×10⁶ Oe)	m_c^* (m_0)	T_D (K)	l (Å)		F (×10⁶ Oe)	m_c^* (m_0)	T_D (K)	l (Å)		F (×10⁶ Oe)	m_c^* (m_0)	T_D (K)	l (Å)
α'	6.31				α'	7.91				α	7.52	3.5	0.29	2100
β'	6.21				α	7.60	5.0			β'	5.88			
β	6.09				β'	5.84				γ	5.83	3.1	0.36	1700
α	5.89	3.5	0.19	2900	β	5.62	2.3	0.52	1500	δ	3.85			
γ	4.71	2.5	0.32	2100	γ	5.49				ε	2.62			
δ	2.76	2.5	0.36	1400	δ	3.29	3.8	0.67	580					
ε	1.91				ε	2.19								

paths are summarized in Table 5.9

Main five branches are closed Fermi surfaces in topology, although branch β corresponds to a nearly spherical one, and a signal of branch ε is not observed around $\langle 110 \rangle$, which might be closely related to the curvature of this Fermi surface. Closed Fermi surfaces are consistent with the result of the magnetoresistance experiments. Anyway, these Fermi surfaces are small in volume. For example, the volume of the branch α is about 0.9 % in the fcc magnetic Brillouin zone. If the Fermi surface of UGa₃ might consist of the present branches, UGa₃ could be a semimetal with a 2.5 % volume of the fcc magnetic Brillouin zone. This speculation is not consistent with the γ-value of 52 mJ/K² · mol because the electronic specific heat coefficient due to branch α, for example, is estimated as 1.8 mJ/K² · mol. The total value due to five branches is about 4–5 mJ/K² · mol, which is by one order smaller than the γ-value. There exist another large Fermi surfaces, not observed by the present dHvA experiments. The large Fermi surfaces are theoretically

ln [$AH^{1/2}\sinh(\alpha m_c^* T/H)$ / $J_2(x)$] (arb.units)

150 100   50 kOe

UGa$_3$
H // <100>

α
$m_c^* = 3.5\,m_0$
$T_D = 0.19$ K

γ
2.5 m_0
0.32 K

δ
2.5 m_0
0.36 K

1   2   3   4
1/H (x10^{-5} Oe)
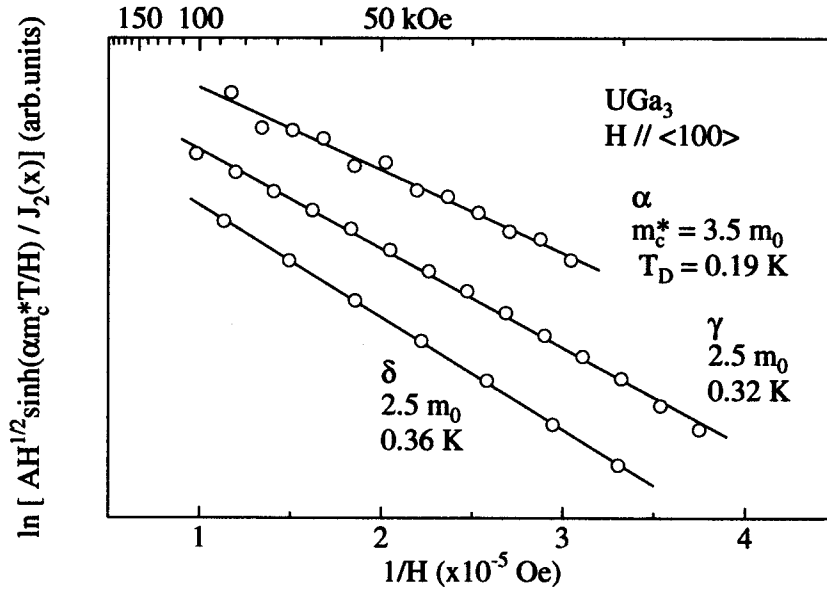
Fig. 5.65 Dingle plot for UGa$_3$.

expected in the recent band calculations.[61]

In Fig. 5.63, we added another branches named α', β' and γ', shown by small circles. Characteristic features are as follows. The dHvA amplitudes of these branches are extremely small, and angular dependencies of the dHvA frequencies are almost the same as the corresponding main branches. For example, branch α' is not clearly observed but the second harmonic $2\alpha'$ is ascertained in Fig. 5.62. The angular dependence of branch α' is almost the same as that of branch α.

There are three possibilities to explain them. One is due to Fermi surfaces with up- and down-spin states. Another is related to a corrugated Fermi surface, possessing a maximum and minimum cross-sections for each Fermi surface. The last is ascribed to subgrains. Namely the present sample might contain a small subgrain whose crystal axes are slightly different from those of a main subgrain. The last is most probable, although it is strange that branch α and α' degenerate at $\langle 111 \rangle$. The origin of these branches is not clear at present.

Lastly we discuss the metamagnetic transition at $H_M \simeq 125\,$kOe and dHvA results noted in ref. (61). As seen in Fig. 5.66 (a), we have no such transition around 120 kOe. Figures 5.66 (b) and (c) show FFT spectra in the field range below and above 120 kOe, respectively. There is no difference between them. As the present sample is much better than that in ref. (61), Existence of the metamagnetic transition on which they insist is less reliable. Their dHvA data are also explained by harmonics of fundamental branches α, γ and δ, which are in principle the same as the present results.
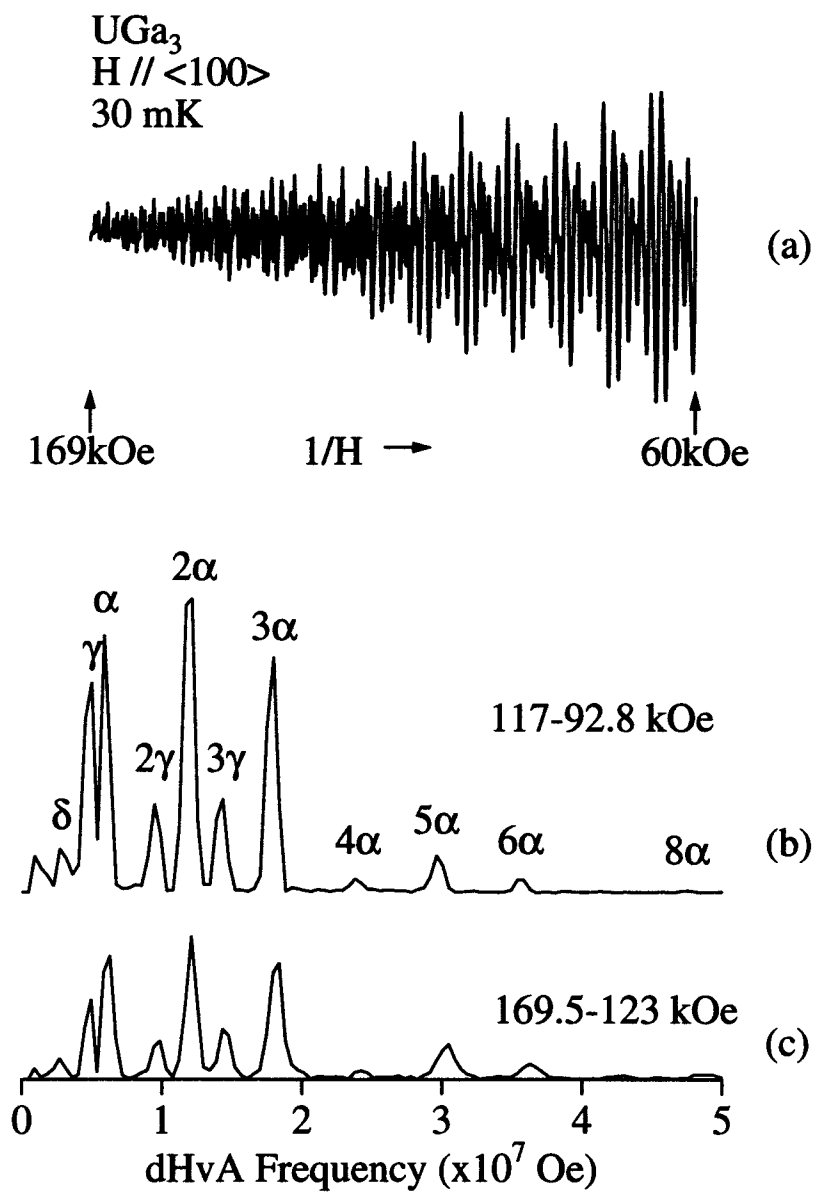
Fig. 5.66 (a) dHvA oscillation, (b) its FFT spectrum in the field range from 92.8 to 117 kOe and (c) that in the field range from 123 to 169.5 kOe in UGa₃.

5.7 UX$_2$ (X = P, As, Sb, Bi)

5.7.1 Electrical resistivity

Figure 5.67 shows the temperature dependence of the electrical resistivity in UX$_2$ (X = P, As, Sb, Bi) for the current along [100].[110,112] The resistivity decreases abruptly below 204 K in UP$_2$, 274 K in UAs$_2$, 203 K in USb$_2$ and 181 K in UBi$_2$. These indicate the antiferromagnetic orderings mentioned in Sec. 3.4. The values of these transition temperatures, namely, the Néel temperatures are in good agreement with those in the previous results.[81,85,113] Overall, the Néel temperatures of UX$_2$ are considerably high. It is worth noting that the Néel temperatures of UX$_2$ decrease with increasing the lattice constant except the case of UP$_2$. This is due to the hybridization of 5f-electrons with the conduction electrons, which is sensitive to U–U distance. UP$_2$ holds on the special position among UX$_2$ series. Similar results are obtained in U$_3$X$_4$ (X = P, As, Sb, Bi).[85] The unique feature on UP$_2$ also appears in the behavior of the resistivity below T_N. The resistivity of UP$_2$ shows the positive curvature in the temperature range from 200 to 100 K, while the resistivities in other UX$_2$ compounds show the negative curvature.

The residual resistivities of UP$_2$, UAs$_2$, USb$_2$ and UBi$_2$ are $\rho_{0.5K} = 0.11\,\mu\Omega \cdot$ cm, $\rho_0 = 0.29\,\mu\Omega \cdot$ cm, $\rho_{1.4K} = 2.97\,\mu\Omega \cdot$ cm and $\rho_{0.5K} = 2.8\,\mu\Omega \cdot$ cm, respectively. The residual resistivity ratios (RRR) of UP$_2$, UAs$_2$, USb$_2$ and UBi$_2$ are $\rho_{RT}/\rho_{0.5K} = 2900$, $\rho_{RT}/\rho_0 = 580$, $\rho_{RT}/\rho_{1.4K} = 80$ and $\rho_{RT}/\rho_{0.5K} = 22$, respectively. Here we note that the samples in UP$_2$ and UAs$_2$, which are grown by the chemical transport method, are whisker-shaped, while the samples in USb$_2$ and UBi$_2$ are bulk grown by the self-flux method. These values of RRR indicate the high quality of the obtained samples and is usually sufficient to detect the dHvA signal. In particular, the value of RRR in UP$_2$ is extremely large, which is largest in all of the uranium compounds as far as we know.

To investigate the two-dimensionality of UX$_2$ compounds, we measured the electrical resistivities in USb$_2$ and UBi$_2$ for the current along [001]. Figure 5.68 (a) shows the temperature dependence of the resistivity along [001] and [100] in USb$_2$. The anisotropy ratio $\rho_{[001]}/\rho_{[100]} \equiv \rho_c/\rho_a$ is shown in Fig 5.68 (b). Experimental results are consistent with the previous results.[85] A large hump below T_N along [001] indicates that the two-dimensionality in USb$_2$ is enhanced due to the antiferromagnetic ordering. This is simply understood as the reconstruction of the Fermi surfaces. As mentioned in Sec. 3.4, the magnetic unit cell of USb$_2$ is doubled along the [001] direction with respect to the chemical unit cell, which brings about a strongly flattened magnetic Brillouin zone. Therefore, it is expected that the slightly isotropic Fermi surfaces in the paramagnetic state are changed into the strong two-dimensional Fermi surfaces in the antiferromagnetic state. However, even in the paramagnetic state, Fermi surfaces possess two-dimensionality, because the Brillouin zone is still flat ($k_c/k_a = 0.49$). The anisotropy ratio ρ_c/ρ_a in USb$_2$ is, however, rather small. It is usually 10^2–10^3. We will discuss this point in Sec. 5.7.3 with the dHvA results.
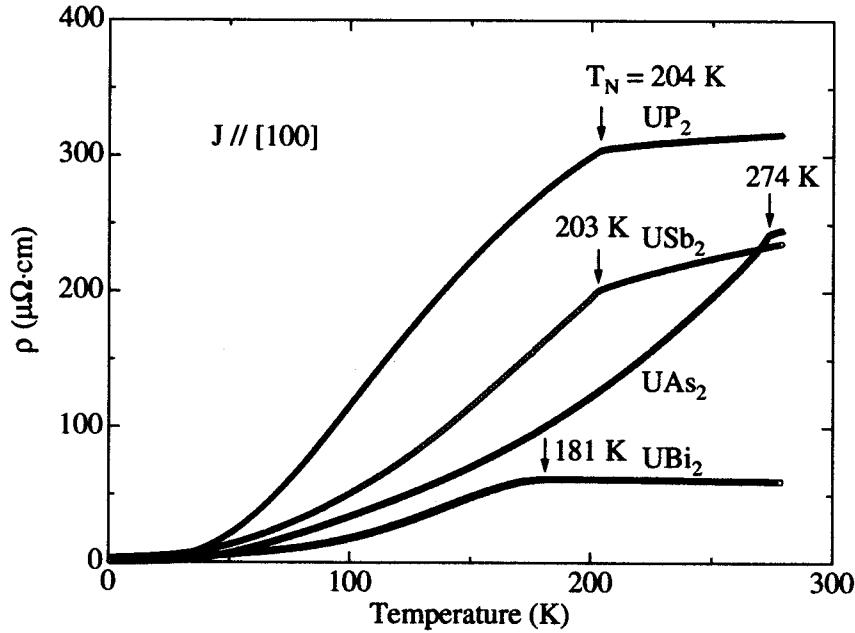
Fig. 5.67 Temperature dependence of the electrical resistivity in UX_2 (X = P, As, Sb, Bi).

On the other hand, the resistivity along [001] in UBi_2 shows no hump below T_N, as shown in Fig. 5.69. This result indicates that Fermi surfaces in UBi_2 are not reconstructed by the antiferromagnetic ordering, since the magnetic unit cell is the same as the chemical one, yielding no flattened magnetic Brillouin zone. The anisotropy ratio ρ_c/ρ_a in UBi_2 is large. It is about 500 at room temperature, indicating the two-dimensional properties on conduction electrons. The residual resistivity ratio along [001] is 180, which displays the high-quality of the sample.

5.7.2 Specific heat

We show in Fig. 5.70 the T^2-dependence of the specific heat in the form of C/T. At low temperatures, the specific heat can be simply expressed as $C/T = \gamma + \beta T^2$. Here we note that the UX_2 (X = P, As, Sb, Bi) compounds are antiferromagnets, possessing relatively high Néel temperatures. Thus the magnetic contribution to the specific heat is proportional to T^3 at low temperatures. The electronic specific heat coefficient γ is determined as $27\,mJ/K^2mol$ for UP_2, $11.7\,mJ/K^2mol$ for UAs_2, $26\,mJ/K^2mol$ for USb_2 and $20\,mJ/K^2mol$ for UBi_2, although the data for UP_2 are scattered. The determined γ-value of UP_2 is different from the previously reported $20\,mJ/K^2mol$.[81] The γ-value of USb_2 is in good agreement with the previous result of $25\,mJ/K^2mol$. On the other hand, in UAs_2 there is a large discrepancy between our result and the previous one of $45\,mJ/K^2mol$.[81]

117
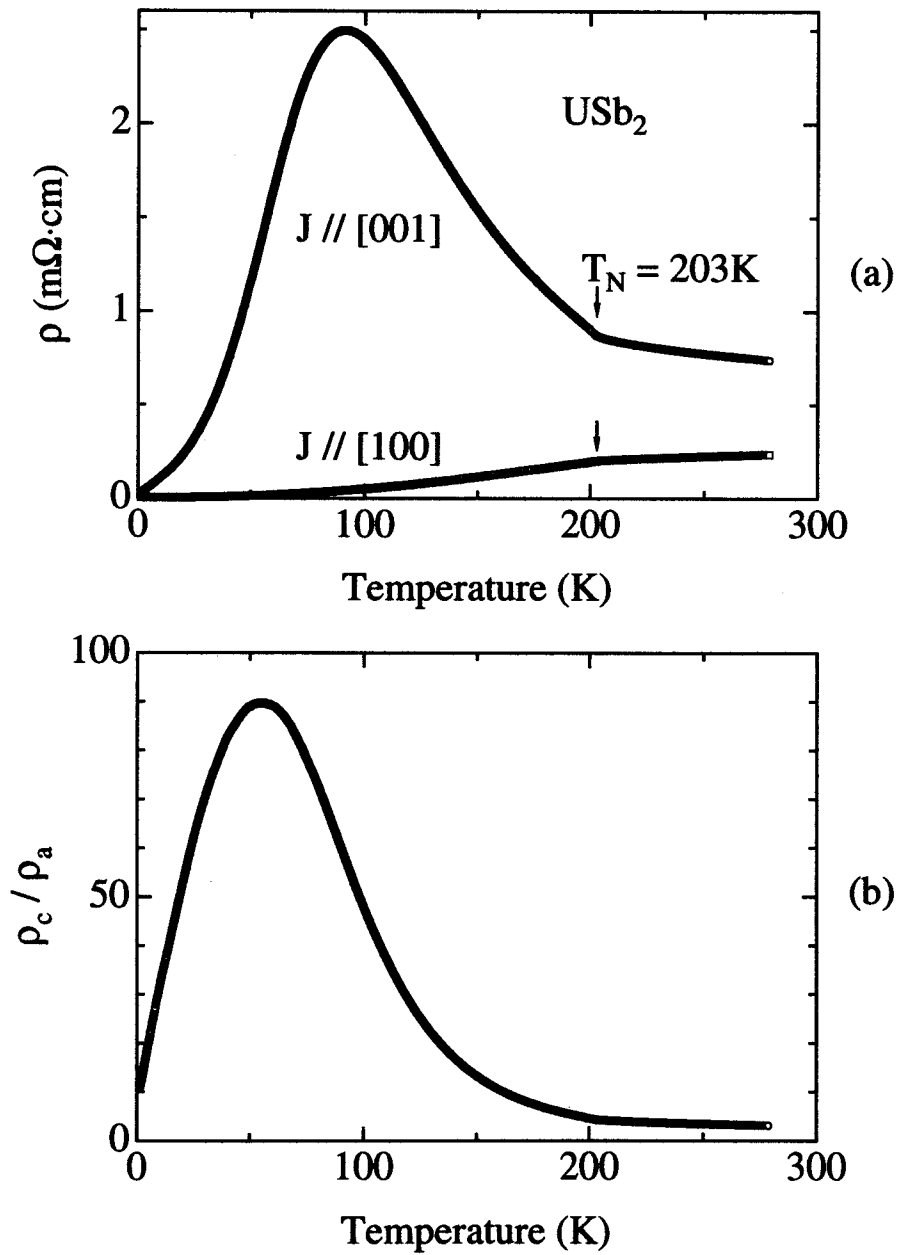
Fig. 5.68 (a) Temperature dependences of the electrical resistivity along [001] and [100] and (b) of the anisotropy ratio $\rho_{[001]}/\rho_{[100]} \equiv \rho_c/\rho_a$ in USb_2.
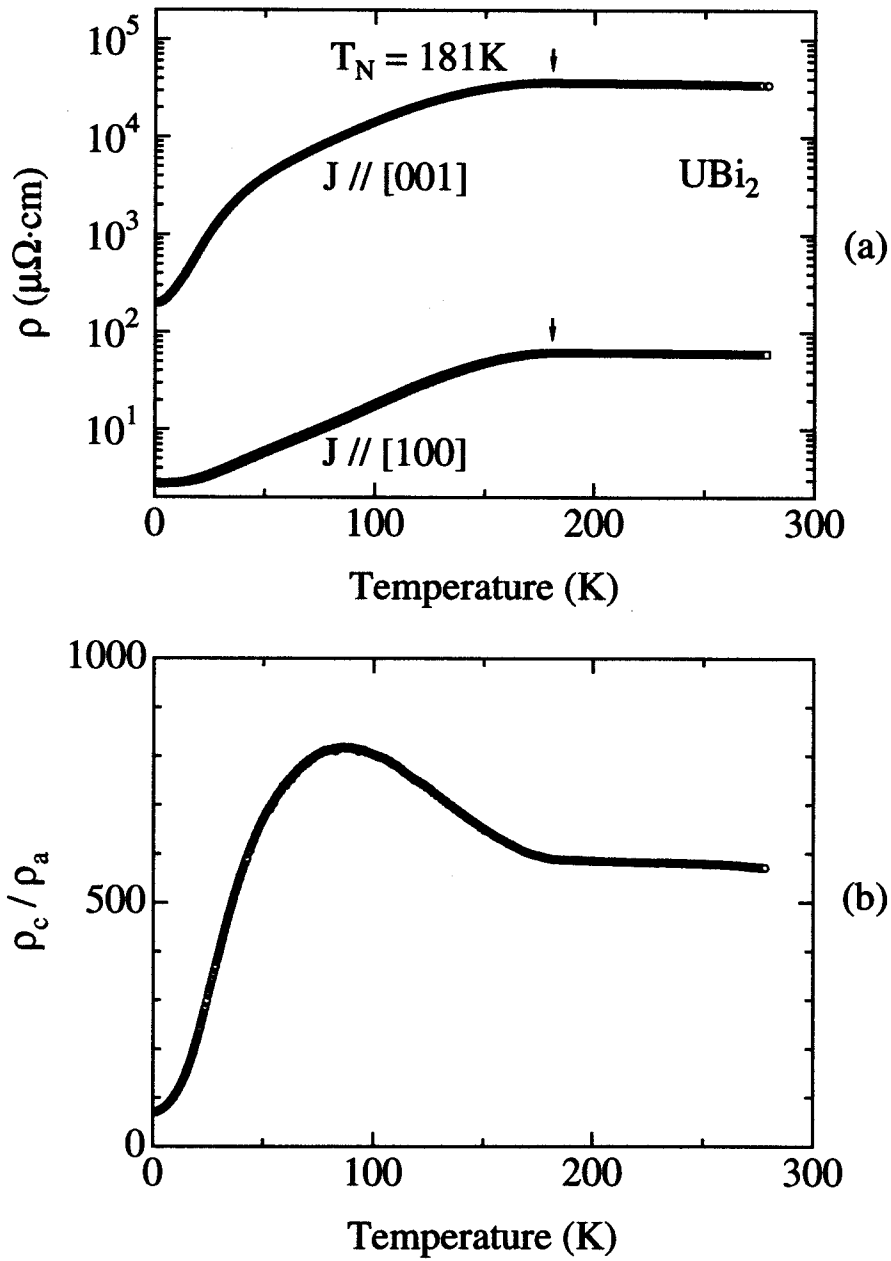
Fig. 5.69 (a) Temperature dependences of the electrical resistivity along [001] and [100] and (b) of the anisotropy ratio $\rho_{[001]}/\rho_{[100]} \equiv \rho_c/\rho_a$ in UBi_2.
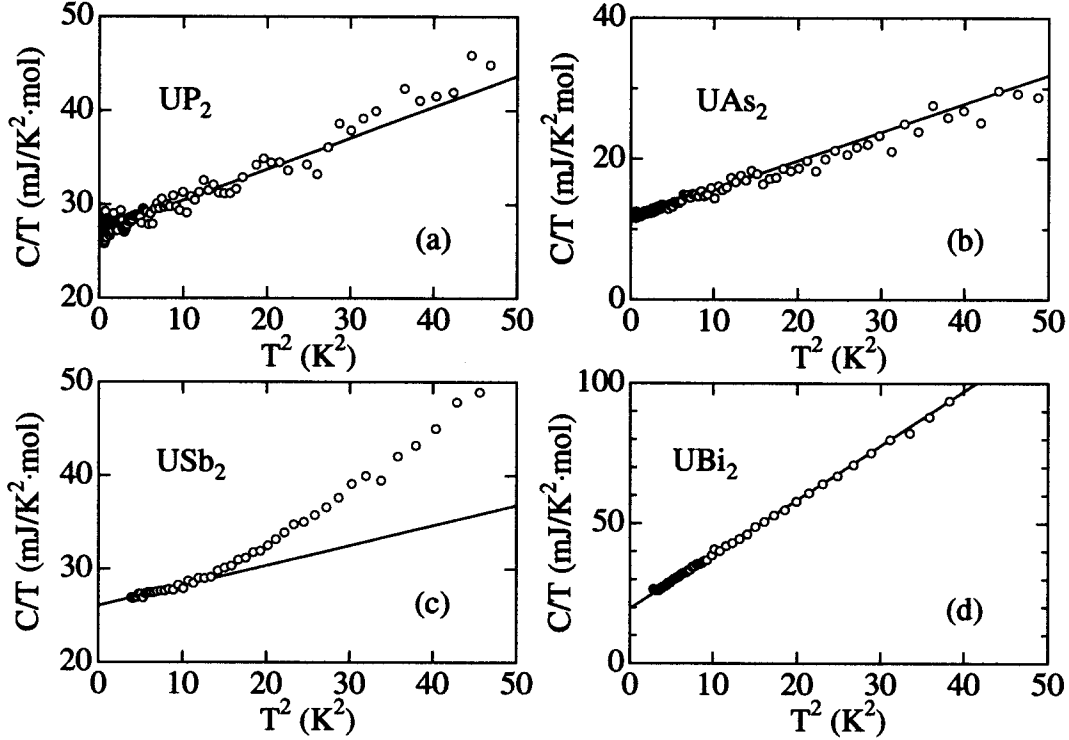
Fig. 5.70 T^2-dependence of the specific heat C in the form of C/T for UX_2 (X = P, As, Sb, Bi).

5.7.3 dHvA effect and SdH effect

We measured the SdH (Shubnikov–de Haas) effect for UAs_2 by using a whisker-shaped sample and the dHvA effect for USb_2 and UBi_2 by using bulk samples.

1) Results of SdH effect in UAs_2

First we show the results of UAs_2.[114] The SdH experiments were performed using both the field-modulation and DC techniques in magnetic fields up to 130 kOe and at temperatures down to 0.4 K. The current is along the [100] direction and its typical value is 3 mA. A typical SdH oscillation for the field along [001] and the corresponding fast Fourier transformation (FFT) spectrum are shown in Fig 5.71. Five dHvA branches named here α, γ, δ, ε and ζ were found in the spectrum, in addition to the harmonics, sums and differences of the branches. All detected SdH branches have relatively small dHvA frequencies F (= $\hbar c S_F / 2\pi e$), ranging from 7.24×10^6 to 4.33×10^7 Oe. These frequencies are proportional to the extremal (maximum or minimum) cross-sectional areas of the Fermi surfaces S_F. We have tilted the field direction from [001] to [100] by rotating the sample. Figure 5.72 shows the angular dependence of the SdH frequency. It follows the $1/\cos\theta$-dependence for all branches except branch ζ, where θ denotes a tilt angle. Solid

lines for branch α, γ, δ and ε in Fig. 5.72 show the $1/\cos\theta$-dependence. For example, branch α follows the $1/\cos\theta$-dependence up to $65°$. These results indicate that branch α, γ, δ and ε originate from cylindrical Fermi surfaces. Branch ζ is observed only around [001]. Thus it is difficult to mention the shape of the Fermi surface originated from branch ζ.

Fig. 5.71 (a) Typical SdH oscillation and (b) the corresponding FFT spectrum in UAs$_2$.

Next we determined the cyclotron effective mass m_c^*, from the temperature dependence of the SdH amplitude by using eq. (4.29). Figure 5.73 shows the so-called mass plot. From its slope, the cyclotron mass was determined as $2.4\,m_0$ for branch α, $3.1\,m_0$ for γ, $2.1\,m_0$
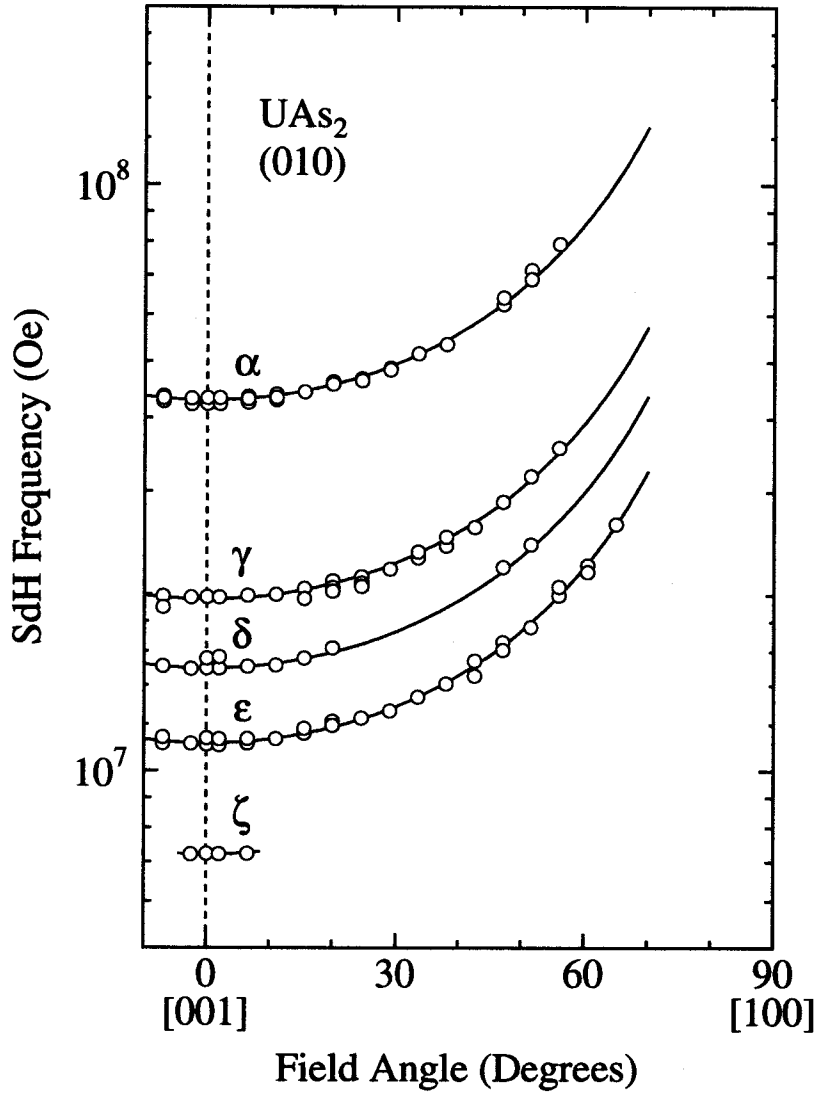
Fig. 5.72 Angular dependence of the SdH frequencies in UAs$_2$.

for δ, 1.2 m_0 for ε and 0.34 m_0 for ζ, where m_0 is the rest mass of an electron. The masses are rather large because the corresponding Fermi surface sheets are not large.

We also determined the Dingle temperature T_D ($= \hbar/2\pi k_B \tau$) from the field dependence of the dHvA amplitude by using eq. (4.37), where T_D is inversely proportional to the scattering lifetime of the conduction electrons τ. Figure 5.74 shows the so-called Dingle plot. From its slope, the Dingle temperature was determined as 3.2 K for branch α, 1.5 K for γ, 1.4 K for δ, 2.3 K for ε and 8.6 K for ζ. From the simple relations:

$$S_F = \pi k_F{}^2, \tag{5.12}$$

$$\hbar k_F = m_c^* v_F \tag{5.13}$$
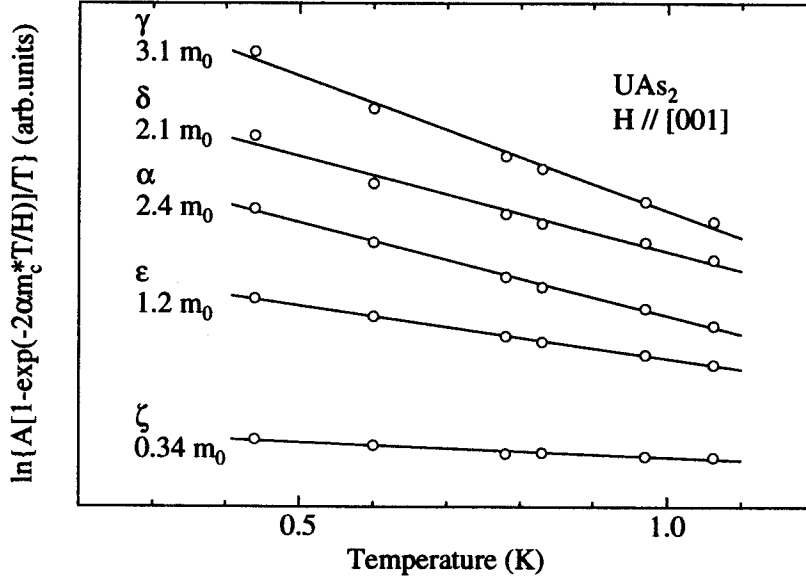
Fig. 5.73 Mass plot for UAs_2.

Table 5.10 SdH frequency F and the cyclotron mass m_c^*, the Dingle temperature T_D and the mean free path l at $H \parallel [001]$ for UAs_2.

branch	F ($\times 10^6$ Oe)	m_c^* (m_0)	T_D (K)	l (Å)
α	42.3	2.4	3.2	660
γ	19.8	3.1	1.5	730
δ	15.0	2.1	1.4	1000
ε	11.1	1.2	2.3	910
ζ	7.2	0.34	8.6	720

and

$$l = v_F \tau, \tag{5.14}$$

where k_F is a half of the caliper dimension of S_F and v_F is Fermi velocity, we can estimate the mean free path l. It is 660 Å for branch α, 730 Å for γ, 1000 Å for δ, 910 Å for ε and 720 Å for ζ.

Fermi surface properties in UAs_2 are summarized in Table 5.10.

2) Results of dHvA effect in USb_2

Next we show the results of the dHvA effect in USb_2.[112] The dHvA experiments were carried out by a conventional field modulation method, in magnetic fields up to 170 kOe and at temperatures down to 30 mK. A typical dHvA oscillation for the field along [001] direction and its fast Fourier transformation (FFT) spectrum are shown in Fig 5.75. Four
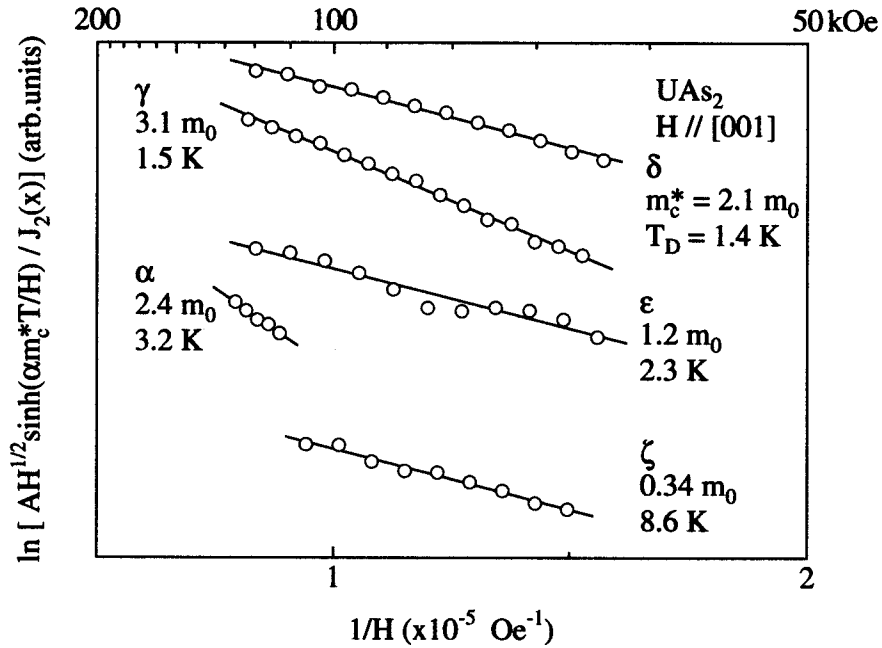
Fig. 5.74 Dingle plot for UAs$_2$.

dHvA branches named here α, γ, δ and ε were found in the spectrum, in addition to the harmonics, sums and differences of the branches. All branches in USb$_2$ are roughly consistent with those in UAs$_2$, although branch ζ observed in UAs$_2$ does not appears in USb$_2$. The detected dHvA frequencies in USb$_2$ are slightly smaller than the corresponding SdH frequency in UAs$_2$. For example, the value of frequency, which is proportional to cross sectional-area of Fermi surface, for branch α in USb$_2$ is 88 % for that in UAs$_2$. This is due to the smaller Brillouin zone in USb$_2$, whose area, perpendicular to [001] direction, is $k_a{}^2 = 2.163 \times 10^{16}\,\mathrm{cm}^{-2}$, while the area in UAs$_2$ is $k_a{}^2 = 2.525 \times 10^{16}\,\mathrm{cm}^{-2}$. Thus the area of Brillouin zone in USb$_2$ is 88 % smaller than that in UAs$_2$, which is in good agreement with the reduction of the frequency in USb$_2$.

We tilted the field direction from [001] to [100] by rotating the sample. Figure 5.76 shows the angular dependence of the dHvA frequency in USb$_2$. It follows the $1/\cos\theta$-dependence for branch α, γ, δ and ε. Solid lines for these branches in Fig. 5.76 show the $1/\cos\theta$-dependence. These results indicate that branch α, γ, δ and ε originate from cylindrical Fermi surfaces. Surprisingly, branch ε follows the $1/\cos\theta$-dependence up to 83.5°, showing a nearly complete cylindrical Fermi surface. From this result, we can conclude that the Fermi surfaces in USb$_2$ are almost the same as those in UAs$_2$. It is interesting that the branch at about 2.5×10^7 Oe appears around [100] and [110] direction in Fig. 5.76. Figure 5.77 shows the typical dHvA oscillation and its FFT spectrum around [100] direction. The dHvA amplitude abruptly increases from 100 kOe with increasing the magnetic field.
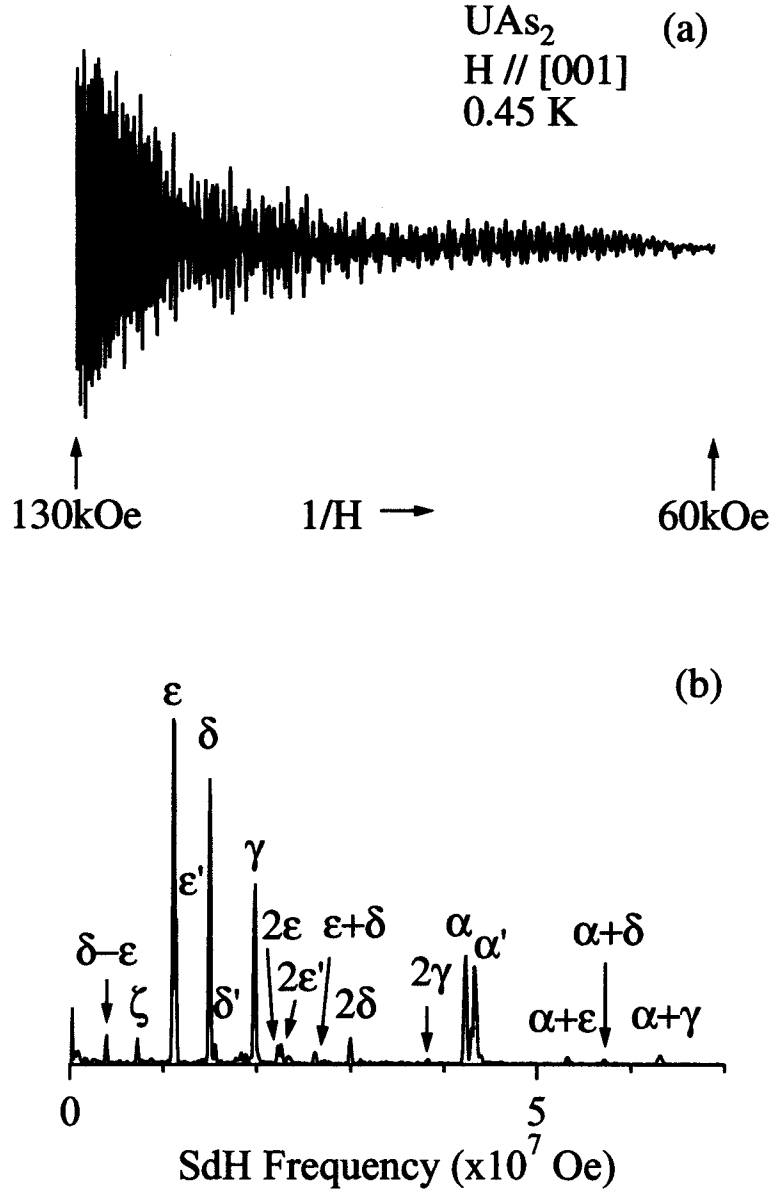
124
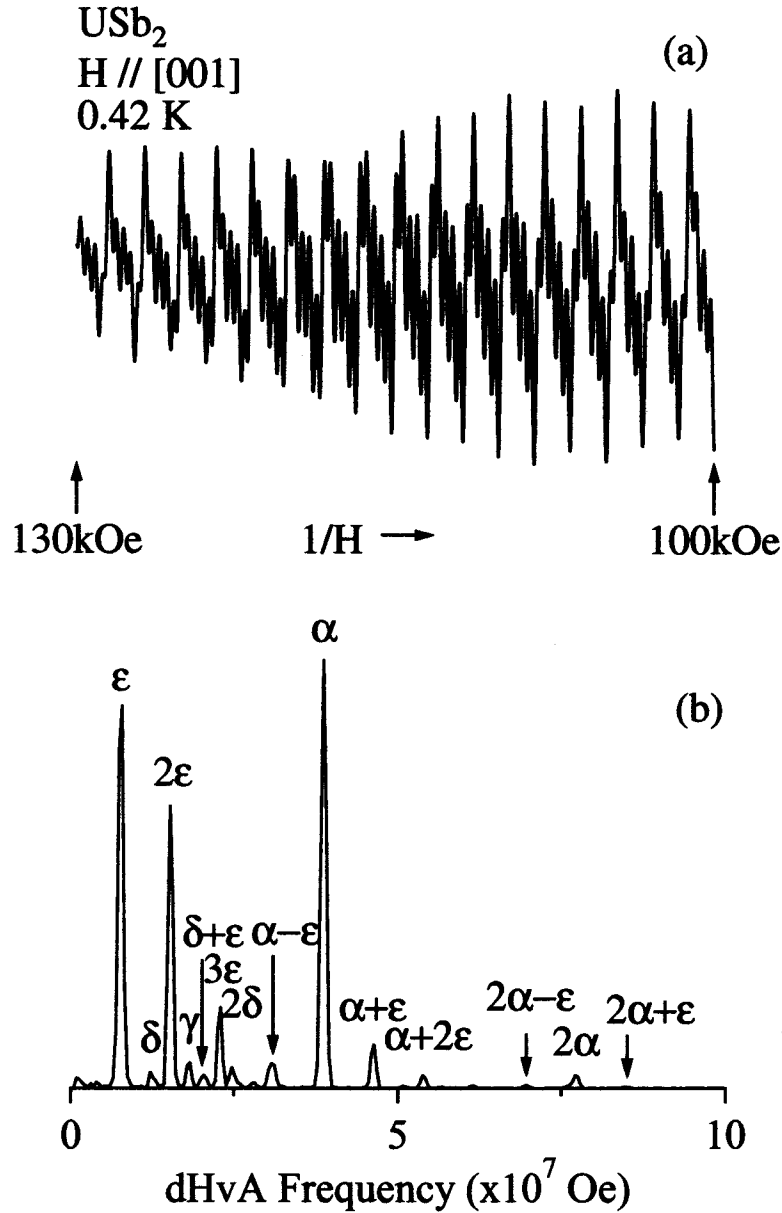
Fig. 5.75 (a) Typical dHvA oscillation and (b) the corresponding FFT spectrum in USb_2.

Next we determined the cyclotron effective mass m_c^*, from the temperature dependence of the dHvA amplitude by using eq. (4.29). Figure 5.78 shows the so-called mass plot for the field along [001]. From its slope, the cyclotron mass was determined as $3.78\,m_0$ for branch α, $6.01\,m_0$ for γ, $3.83\,m_0$ for δ and $1.96\,m_0$ for ε. The masses are rather large because the corresponding Fermi surface sheets are not large. Here we note that the mass of branch α is almost the same as that of branch δ. We also determined the cyclotron mass for the branch of 2.3×10^7 Oe along [100]. The detected cyclotron mass is $31\,m_0$, which is exceptionally large compared to the cyclotron mass along [001].
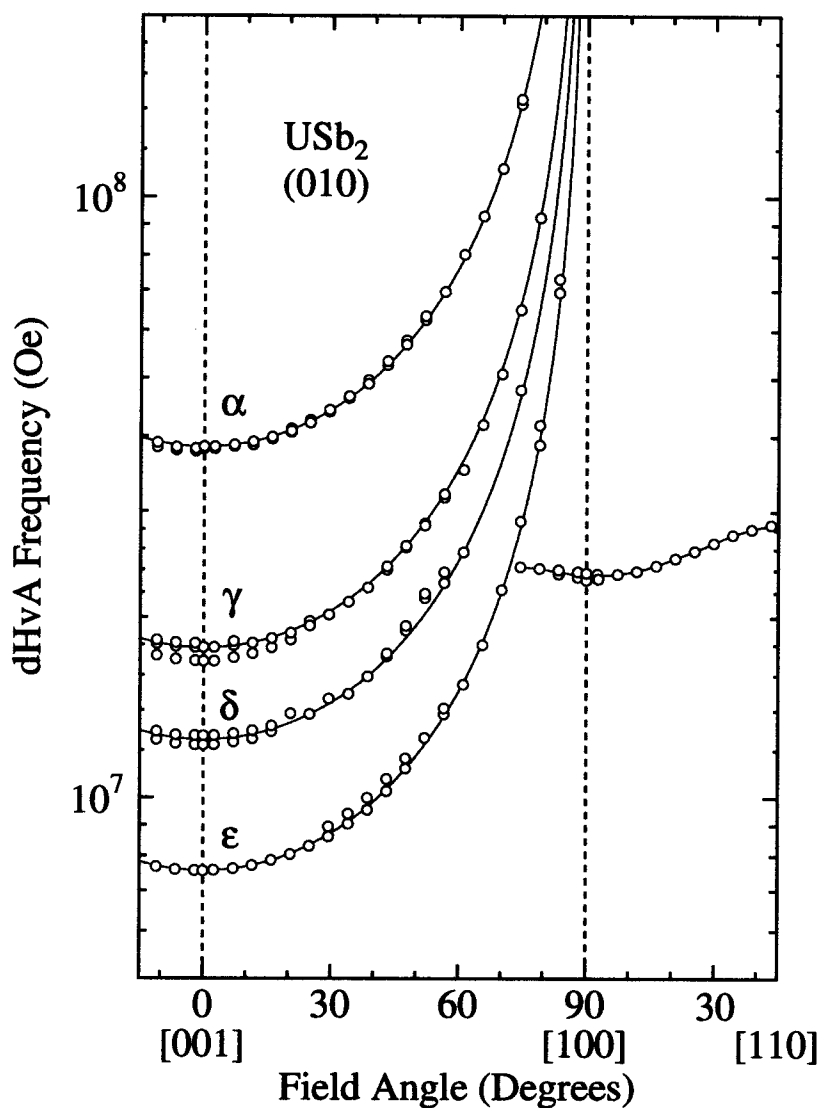
Fig. 5.76 Angular dependence of the dHvA frequencies in USb₂.

Next we determined the Dingle temperature T_D ($= \hbar/2\pi k_B \tau$) from the field dependence of the dHvA amplitude, by using eq. (4.37). Figure 5.79 shows the so-called Dingle plot. From its slope, the Dingle temperature was determined as 0.45 K for branch α, 0.24 K for γ, 0.35 K for δ and 0.54 K for ε. From the simple relations mentioned in eqs. (5.12)–(5.14), we can estimate the mean free path l. It is 2900 Å for branch α, 2300 Å for γ, 2000 Å for δ and 2000 Å for ε. These indicate the high quality of the sample.

Fermi surface properties in USb₂ are summarized in Table 5.11.

126

USb$_2$
H // 7 °
30 mK

(a)

169kOe 1/H ——→ 100kOe

(b)

0   1   2   3   4   5
dHvA Frequency (x10^7 Oe)
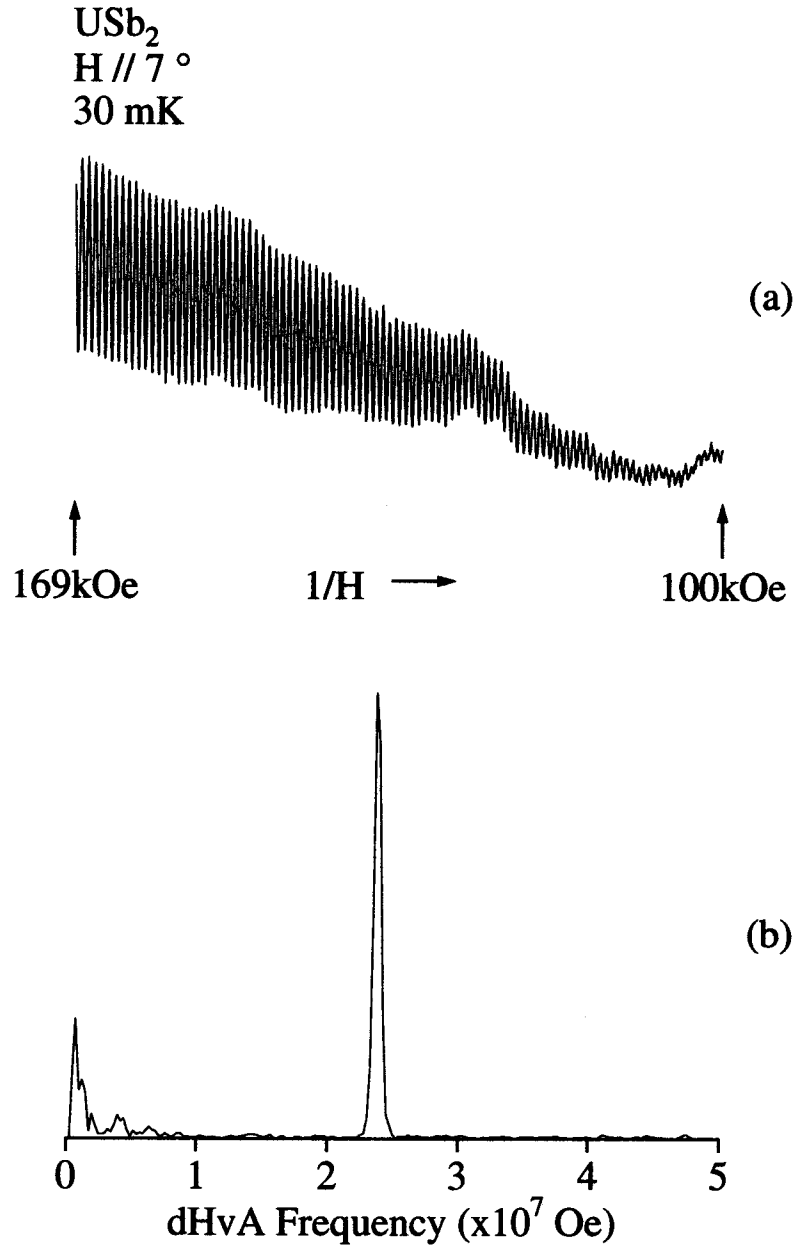
Fig. 5.77 (a) Typical dHvA oscillation and (b) the corresponding FFT spectrum around [100] direction in USb$_2$.

3) Results of dHvA effect in UBi$_2$

We show the results of the dHvA effect in UBi$_2$. The dHvA experiments in UBi$_2$ were carried out under the same condition as in USb$_2$. A typical dHvA oscillation for the field along [001] direction and its fast Fourier transformation (FFT) spectrum are shown in Fig 5.80. Two fundamental dHvA branches named here α and β were found in the spectrum, in addition to the harmonics, sums and differences of the branches. Branch β' originates from the same Fermi surface as in branch β, as mentioned below. We also
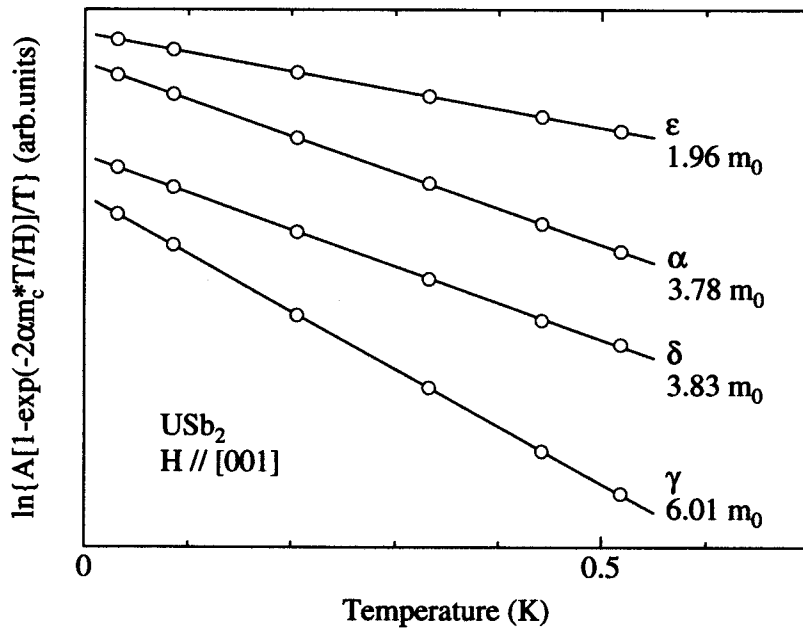
Fig. 5.78 Mass plot for USb2.
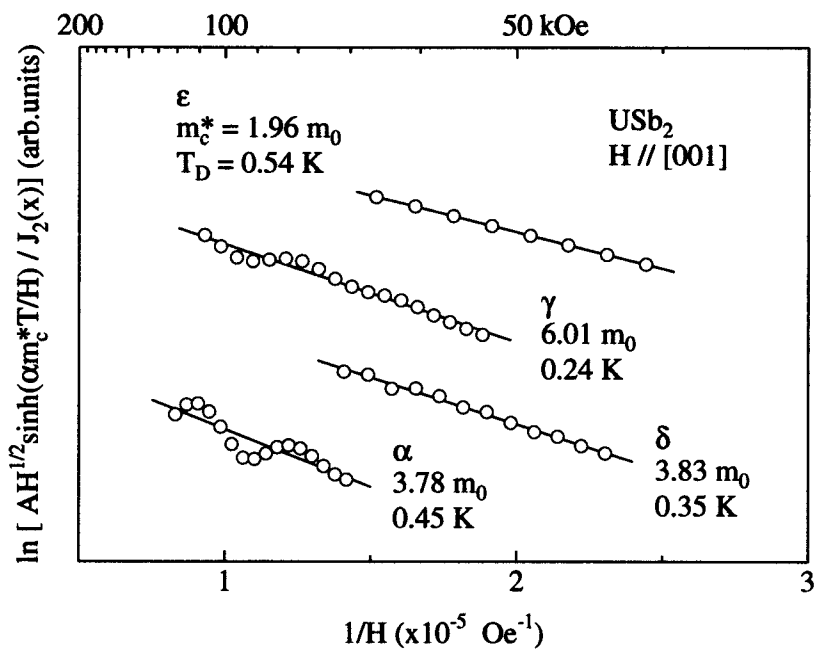
Fig. 5.79 Dingle plot for USb2.

Table 5.11 dHvA frequency F and the cyclotron mass m_c^*, the Dingle temperature T_D and the mean free path l for USb$_2$.

branch	F ($\times 10^6$ Oe)	m_c^* (m_0)	T_D (K)	l (Å)
$H \parallel$ [001]				
α	38.2	3.78	0.45	2900
γ	17.8	6.01	0.24	2300
δ	12.2	3.83	0.35	2000
ε	7.56	1.96	0.54	2000
$H \parallel$ [100]				
	23.3	31		

show in Fig. 5.81 the dHvA oscillation and its FFT spectrum for the field along [100]. Although branch β is not observed, branch α clearly appears together with its harmonics.

We tilted the field direction from [001] to [100] by rotating the sample. Figure 5.82 shows the angular dependence of the dHvA frequency in UBi$_2$. It follows the $1/\cos\theta$-dependence for branch β or β' up to 81°. A Solid line for these branches in Fig. 5.82 shows the $1/\cos\theta$-dependence. These results indicate that branch β or β' originates from cylindrical Fermi surfaces. Split branches β and β' along [001] degenerate around 23°. Therefore branches β and β' correspond to the minimum and maximum cross-sectional area of the cylindrical Fermi surface, respectively. These branches above 30° split again into three or four in number. Two reasons can be considered to explain this. One is due to the maximum and minimum cross-sectional area as mentioned above. Another is due to a possibility of the sample containing a small tilted subgrain. The effect of this subgrain is negligible around [001] where the dHvA frequencies are almost constant. However, when the frequencies change drastically with increasing the field angle, the branch from the small subgrain is clearly observed. In contrast to the behavior of branches β and β', branch α is almost constant against the field angle. This indicates that branch α originates from a spherical Fermi surface. Anyway, the results of angular dependence in UBi$_2$ is highly different from those in USb$_2$ and UAs$_2$, although branch β in UBi$_2$ corresponds to the cylindrical Fermi surfaces. It is interesting that the cylindrical Fermi surface is formed in the non-flattened magnetic Brillouin zone of UBi$_2$.

Next we determined the cyclotron effective mass m_c^*, from the temperature dependence of the dHvA amplitude by using eq. (4.29) Figure 5.83 shows the so-called mass plot for the field along [001]. From its slope, the cyclotron mass was determined as $9.2\,m_0$ for branch α, $6.3\,m_0$ for β' and $4.4\,m_0$ for β. The masses are rather large because the corresponding Fermi surface sheets are not large in volume.

Next we determined the Dingle temperature T_D ($= \hbar/2\pi k_B\tau$) from the field dependence of the dHvA amplitude, by using eq. (4.37). Figure 5.79 shows the so-called Dingle plot. From its slope, the Dingle temperature was determined as 0.11 K for branch α and 0.17 K for β. From the simple relations mentioned in eqs. (5.12)–(5.14), we can estimate the
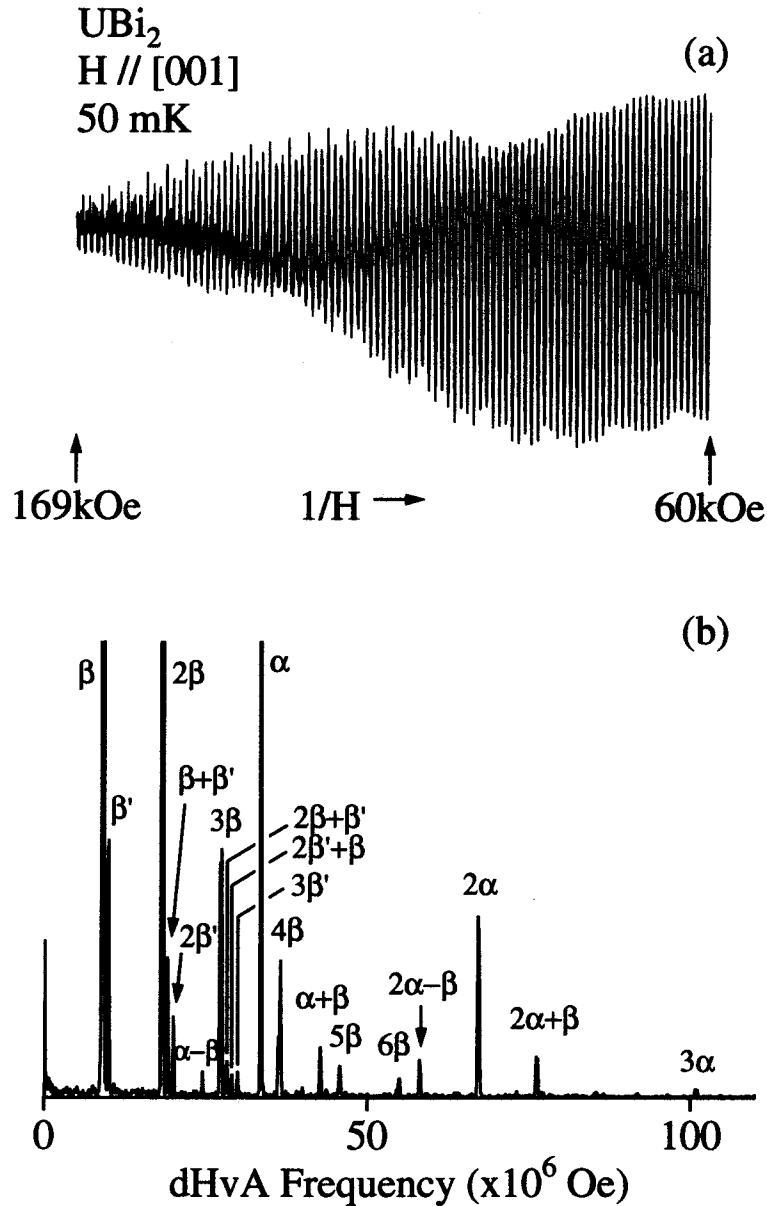
Fig. 5.80 (a) Typical dHvA oscillation and (b) the corresponding FFT spectrum for the field along [001] in UBi$_2$.

mean free path l. It is 4600 Å for branch α and 3100 Å for β. These indicate the high quality of the sample.

Fermi surface properties in UBi$_2$ are summarized in Table 5.11.

## 5.7.4 Magnetoresistance

To study the two-dimensional Fermi surface in USb$_2$, we measured the magnetoresistance in magnetic fields up to 170 kOe and at temperatures down to 40 mK. The current

UBi$_2$

H // [100]

60 mK

(a)

↑
169kOe   1/H →   ↑
                              60kOe

α

(b)

3α
2α   ↓

0   50   100   150

dHvA Frequency (x10^6 Oe)
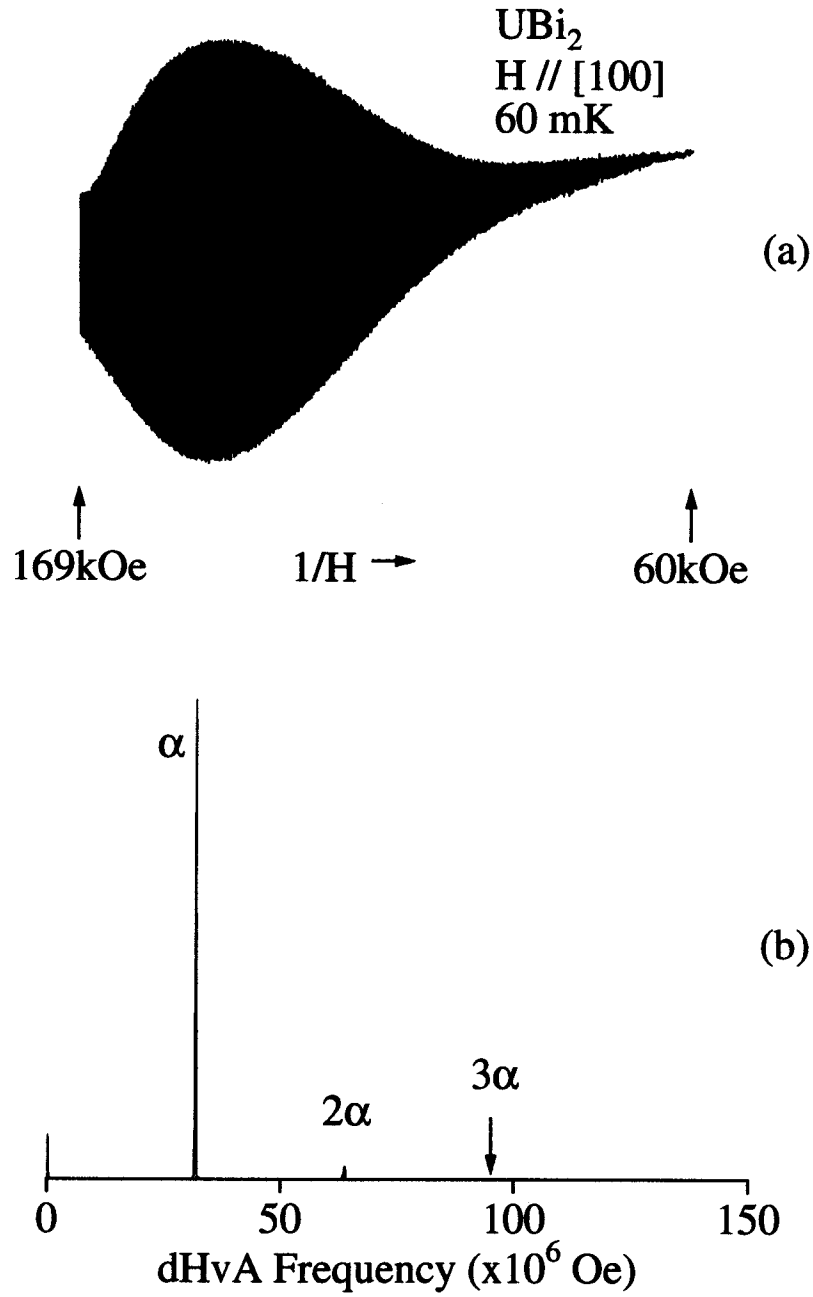
Fig. 5.81 (a) Typical dHvA oscillation and (b) the corresponding FFT spectrum for the field along [100] in UBi$_2$.

Table 5.12 dHvA frequency F and the cyclotron mass m_c^*, the Dingle temperature T_D and the mean free path l at $H \parallel$ [001] for UBi$_2$.

branch	F (×10^6 Oe)	m_c^* (m_0)	T_D (K)	l (Å)
α	33.6	9.2	0.11	4600
β'	10.0	6.3		
β	9.10	4.4	0.17	3100
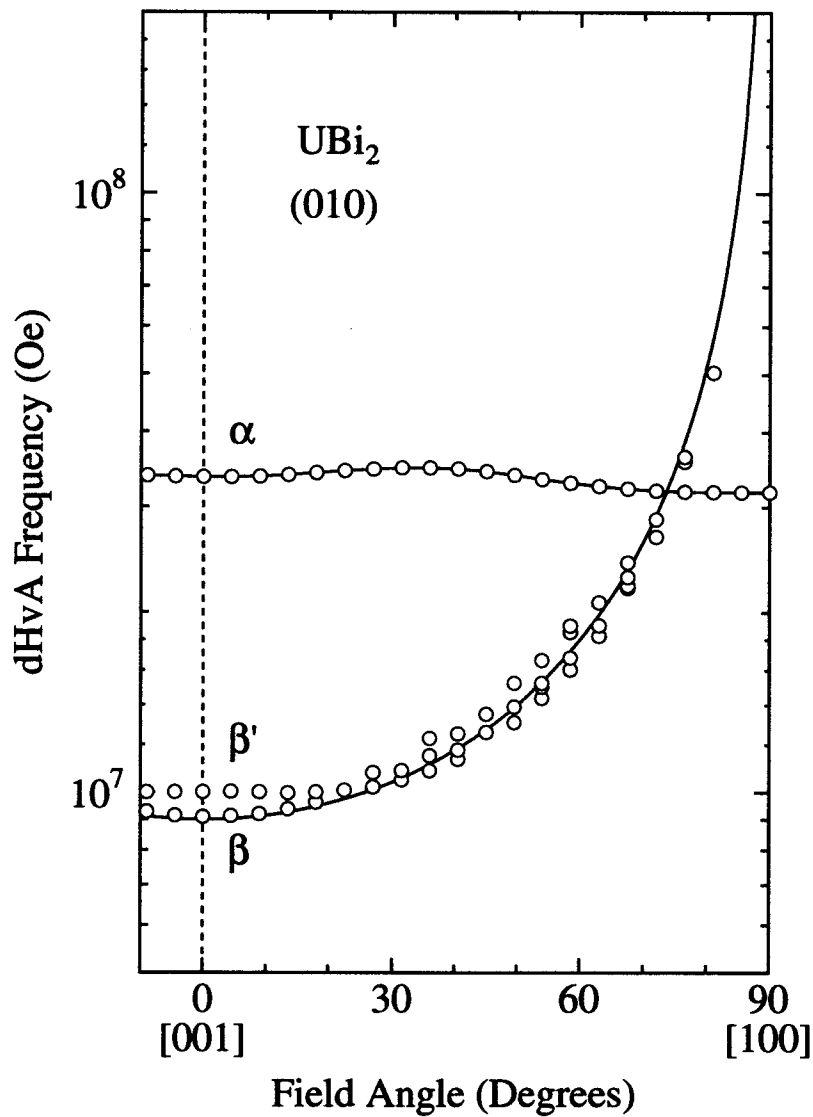
Fig. 5.82 Angular dependence of the dHvA frequencies in UBi$_2$.

was directed along the [001] direction and the sample was rotated from $H \parallel$ [001] to $H \parallel$ [100], as shown in an inset of Fig. 5.87.

First we show in Fig. 5.85 (a) the field dependence of the magnetoresistance for the field along [001] and [100] directions. Here we note that the $\Delta\rho/\rho$ is defined as $\Delta\rho/\rho \equiv (\rho(H) - \rho(0))/\rho(0)$. The magnetoresistance along [100] increases with increasing the field, showing no saturation, although it seems to oscillate at high fields. On the other hand, the magnetoresistance along [001] is saturated and also shows the oscillatory behavior at high fields. Thus the open orbit is expected along the [001] direction. This result is consistent with that of the dHvA effect indicating the existence of the cylindrical Fermi surfaces.
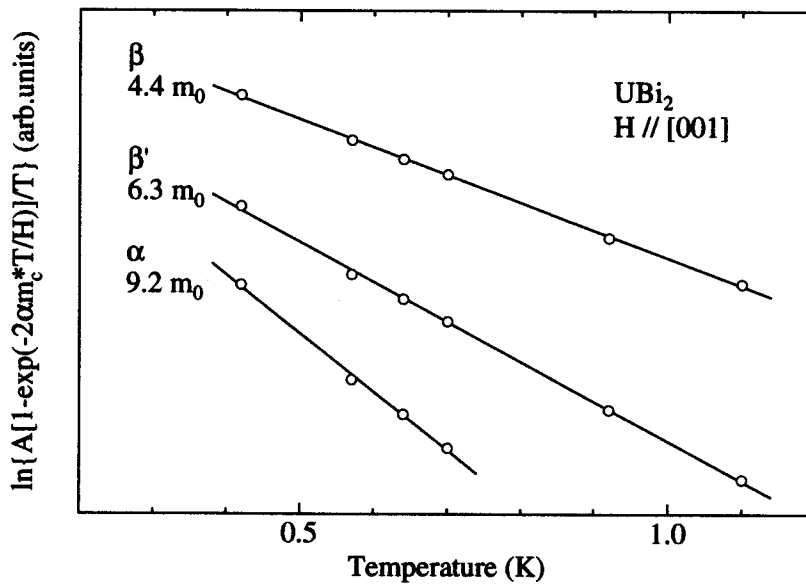
Fig. 5.83 Mass plot for UBi_2.
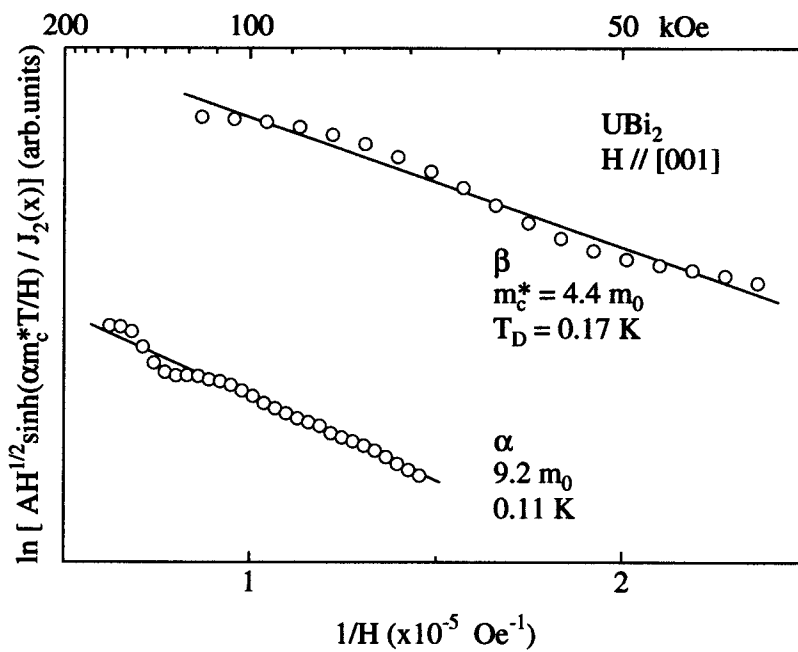
Fig. 5.84 Dingle plot for UBi_2.

Furthermore, we measured the magnetoresistance with very small step fields in order to investigate the oscillatory behavior, as shown in Fig 5.85 (b). This measurements were done by sweeping the magnetic field continuously and under the constant current without changing polarity, as if to measure the SdH effect by the DC method. Therefore, the absolute value of the magnetoresistance is less reliable than that in Fig. 5.85 (a), although the overall behavior is almost the same. The oscillations were clearly detected and confirmed as the SdH effect. Figure 5.86 shows the corresponding FFT spectra derived from the magnetoresistance in Fig. 5.85 (b). Fundamental branches α, γ, δ and ε along [001] appear in Fig. 5.86 (a), in good agreement with the results of the dHvA effect. The branch along [100] in Fig. 5.86 (b) is also in good agreement with the dHvA results. It is worth noting that the SdH amplitude along [100] increases abruptly from 110 kOe, as in the case of dHvA effect.

Next we show in Fig. 5.87 the angular dependence of the magnetoresistance at 170 kOe in USb_2. The $\Delta\rho/\rho$ is equal to 0.47 along [001], whereas 4.87 along [100], showing large anisotropy. This also indicates that there are open orbits along [001]. In particular, the sharp peak is observed at [100]. Incidentally, it is expected that an angle-dependent magnetoresistance oscillation (AMRO), so-called Yamaji effect, is observed in USb_2, because the all Fermi surfaces are cylindrical. However, as it is apparent in Fig. 5.87, the Yamaji effect is not observed.
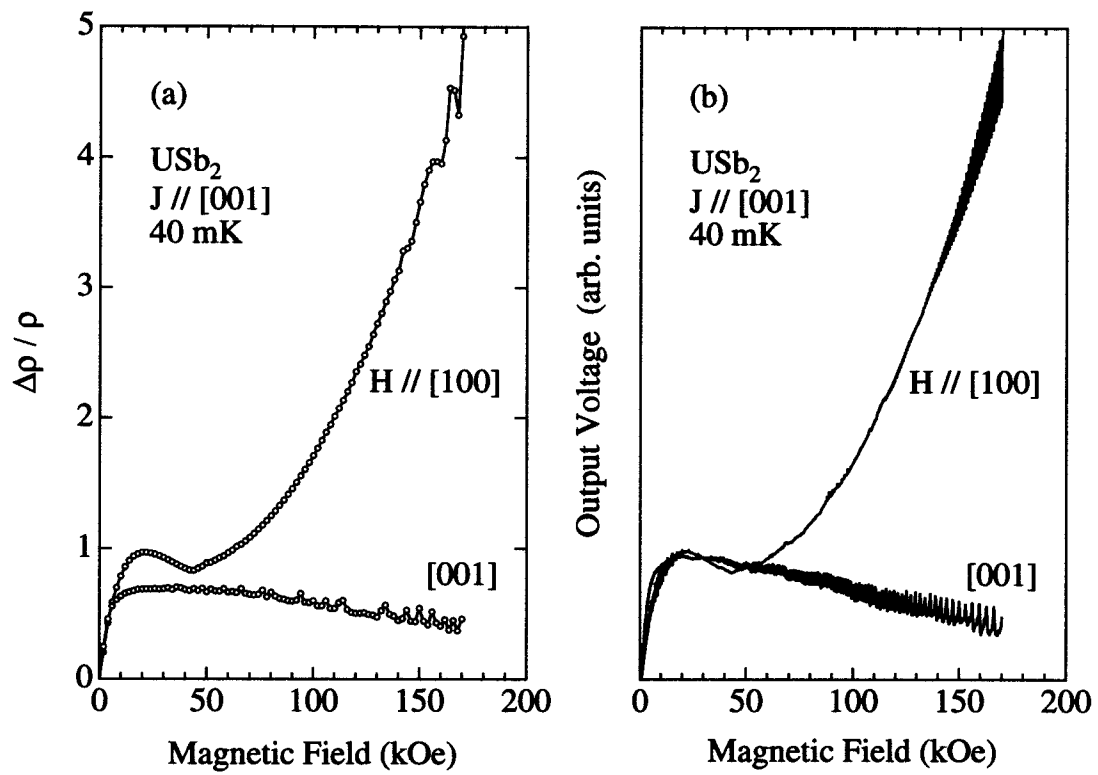
Fig. 5.85 Field dependence of the magnetoresistance for the principal field direction in USb₂. Measurements (a) by the usual DC method and (b) by sweeping the field continuously under constant current.
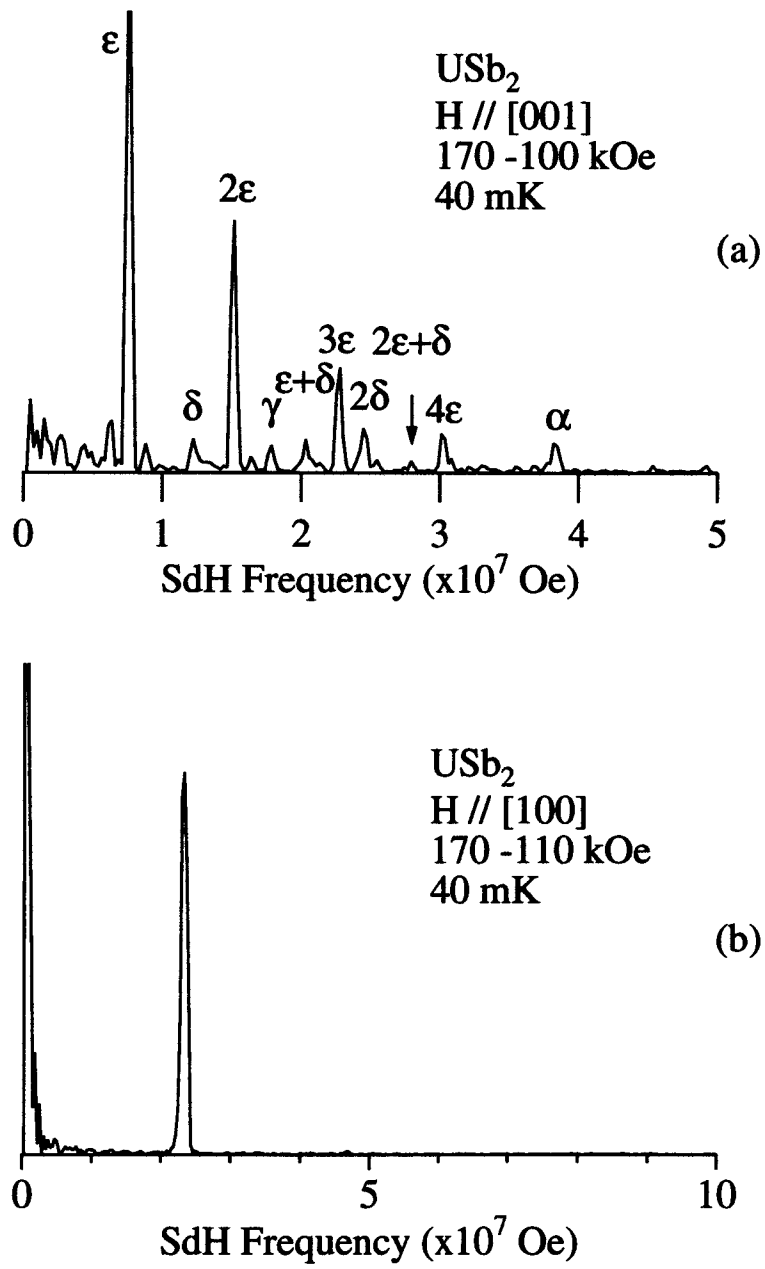
Fig. 5.86 FFT spectra derived from the SdH oscillations in USb$_2$

136
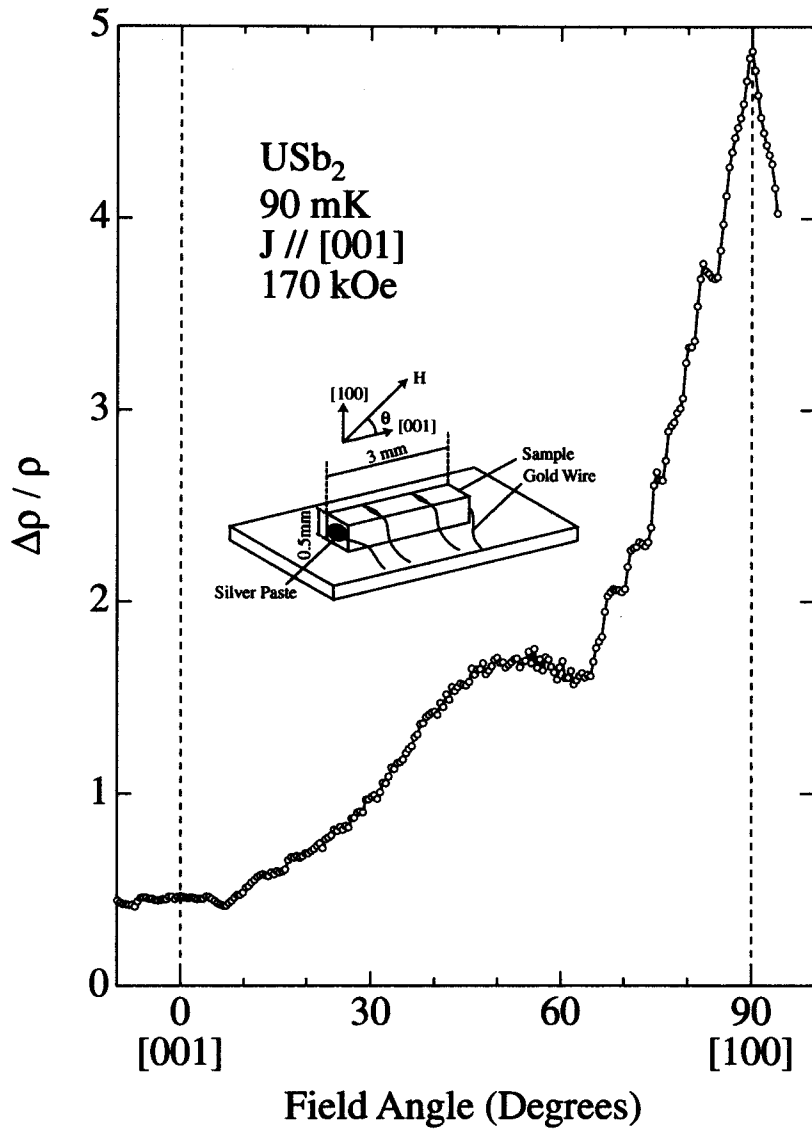
Fig. 5.87 Angular dependence of the magnetoresistance in USb₂.

5.7.5 Discussion on Fermi surface properties

Before discussing the electronic nature of $5f$ electrons in UX_2, we will first describe the general properties of $3d$ or $4f$ electron system.

The $3d$-electrons are responsible for ferromagnetism in such transition metals as Ni and Fe, which can be described on the basis of the itinerant $3d$-electron model. On the other hand, the $4f$-electron properties can be well explained by the localized $4f$-electron model. In some cases, the $4f$-electrons hybridize significantly with the conduction electrons, forming a heavy electron system at low temperatures. Namely, the $4f$-levels of the Ce^{3+} ion at high temperatures are generally split into three doublets because the $4f$-electrons are almost localized and the magnetic susceptibility follows the Curie–Weiss law, as mentioned in Chap. 2. At low temperatures, the magnetic entropy of the ground-state doublet in the $4f$-levels or the magnetic specific heat C_m is changed into the electronic specific heat γT via the many-body Kondo effect as follows:

$$R \ln 2 = \int_0^{T_K} \frac{C_m}{T} \, dT, \tag{5.15}$$

$$C_m = \gamma T. \tag{5.16}$$

The value of γ can be obtained as

$$\gamma = \frac{R \ln 2}{T_K} \simeq \frac{10^4}{T_K} \ \text{(mJ/K}^2\text{mol)}. \tag{5.17}$$

In fact, this value is $1600 \, \text{mJ/K}^2\text{mol}$ for $T_K = 5 \, \text{K}$ in $CeCu_6$ and $350 \, \text{mJ/K}^2\text{mol}$ for $T_K = 20 \, \text{K}$ in $CeRu_2Si_2$.

In many aspects, however, the f-electron nature in the uranium compounds is different from that in the rare earth compounds. For example, the magnetic susceptibility of USb_2 follows the Curie-Weiss law with the effective magnetic moment of $\mu_{eff} = 3.04 \, \mu_B/U$ in the temperature range from 220 to $400 \, \text{K}$.[115] The ordered moment is, however, $1.88 \, \mu_B/U$. This value can be compared to $3 \, \mu_B/U$ in a ferromagnetic compound UGa_2, where the $5f$ electrons are considered to be localized. The $5f$ electrons have an intermediate character between the $3d$ and $4f$ electrons, and their nature is dual: partially itinerant and partially localized. The determined γ-value of UAs_2, USb_2 and UBi_2 are $11.7 \, \text{mJ/K}^2\text{mol}$, $26 \, \text{mJ/K}^2\text{mol}$ and $20 \, \text{mJ/K}^2\text{mol}$, respectively, which is not small because the detected Fermi surfaces have small volume. In fact, the cyclotron mass along [001] in UAs_2, USb_2 and UBi_2 is in the range from 2.0 to $9.2 \, m_0$. This large cyclotron mass thus originates from the contribution of $5f$-electrons.

UBi_2

Next we discuss the Fermi surfaces of UBi_2. UBi_2 could be a good reference to consider the Fermi surface properties of USb_2 or UAs_2, because the magnetic Brillouin zone in UBi_2 is not flattened but the same as the chemical one in the antiferromagnetic state.

Actually, the detected dHvA branches are two in number, showing a relatively simple angular dependence. As described previously, the Fermi surfaces consist of a cylindrical Fermi surface named branch β and a spherical one named branch α. The volume of the cylindrical Fermi surface occupies 4.8 % of the magnetic Brillouin zone, whereas the spherical Fermi surface occupies 9.9 %. As the magnetic unit cell contains two molecules of UBi_2, UBi_2 is a compensated metal with equal carrier numbers of electrons and holes. Thus if we assume that there are one spherical Fermi surface from electrons and two cylindrical Fermi surfaces from holes in the magnetic Brillouin zone, the number of carrier is well compensated, where the electron and the hole occupy 9.9 % and 9.6 %. We show in Fig. 5.88 (a) the schematic magnetic Brillouin zone and the Fermi surfaces in UBi_2 on the basis of this speculation. Here we note the Brillouin zone where the spherical Fermi surface exists is different from that where the cylindrical Fermi surfaces exist, although in Fig. 5.88 (a) these Fermi surfaces are shown all together in the same magnetic Brillouin zone.

Furthermore we calculated the γ-value from these Fermi surfaces, using eqs. (4.32) and (4.36). The estimated γ-values from branches α and β are $\gamma_\alpha = 8.1\,\mathrm{mJ/K^2mol}$ and $\gamma_\beta = 4.9\,\mathrm{mJ/K^2mol}$, respectively. Thus the total γ-value is $\gamma_{total} = \gamma_\alpha + 2\gamma_\beta = 17.9\,\mathrm{mJ/K^2mol}$, which is in good agreement with $20\,\mathrm{mJ/K^2mol}$ determined from the specific heat measurements.

Let us now consider the two-dimensionality of the Fermi surface in UBi_2. As is apparent from the electrical resistivity shown in Fig. 5.69, two-dimensionality of the conduction electron is strong. This is confirmed by our dHvA experiments indicating the cylinder Fermi surface. The reason of this two-dimensionality is due to the characteristic crystal structure where the Bi and U planes are stacked along [001], as shown in Fig. 3.20 (b). Recently, cylindrical Fermi surfaces were observed in CePtAs and CePtP, where the hexagonal crystal structure has the similar sequence of the Ce- and (Pt-As)-basal planes.[116] The Pt and As atoms are in the same basal plane. The strong hybridization between the $5d$ electrons of Pt and the $4p$ electrons of As in the Pt-As plane causes the quasi two dimensional character of the electronic band structure. The cyclotron mass is thus small, ranging from 0.47 to $0.84\,m_0$ in CePtAs and 0.34 to $0.80\,m_0$ in CePtP, for the similar magnitude of dHvA frequencies as in UBi_2. The cyclotron mass in USb_2 is, however, large. It is thus concluded that the $5f$ electrons become itinerant, contributing to the conduction band. The conduction electrons are thus due to $5f$, $6d$ and $7s$ electrons in the U-plane. It is expected that these conductive U-planes are separated by the non-conductive Bi-planes, bringing about the two-dimensional character. It is interesting that the cylindrical Fermi surface exists in UBi_2, although the antiferromagnetic ordering in UBi_2 does not induce the flattened magnetic Brillouin zone as in USb_2, It is also worth noting that the spherical Fermi surface is very close to the Brillouin zone boundary, as shown in Fig. 5.88 (a).
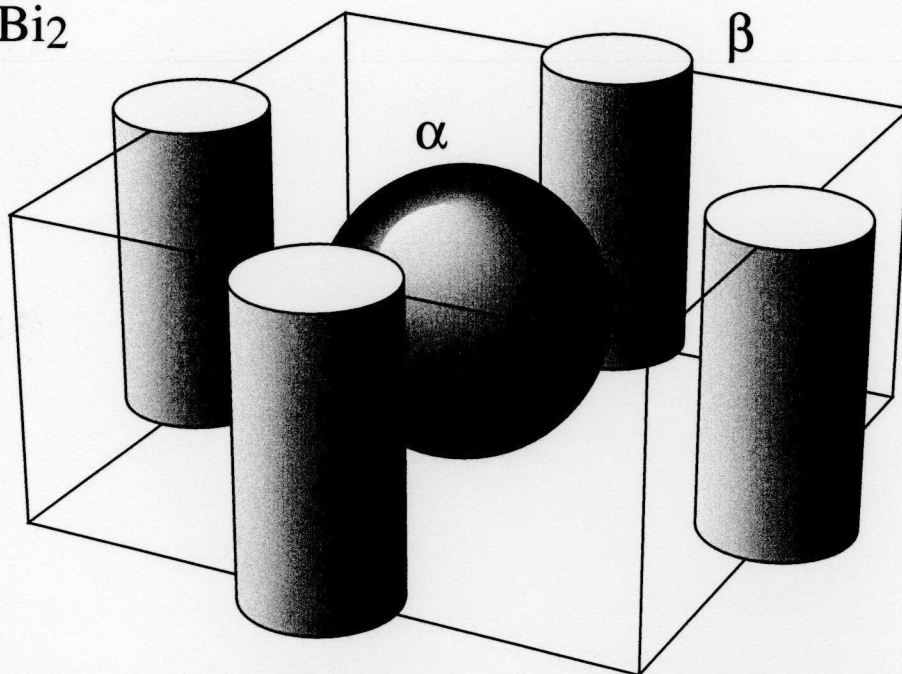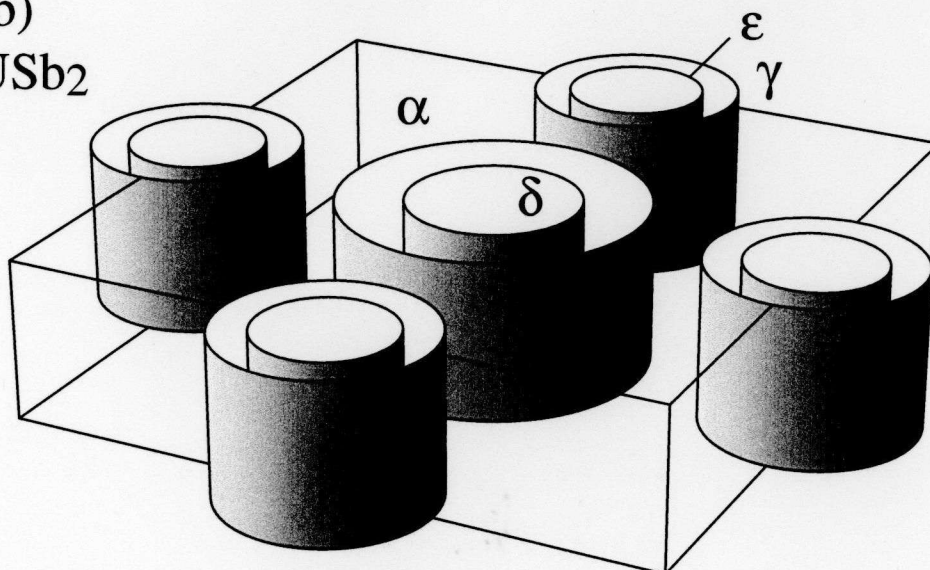
Fig. 5.88 Schematic magnetic Brillouin zone and the Fermi surfaces (a) for branches α and β in UBi$_2$ (b) for branches α, γ, δ and ε in USb$_2$.

USb$_2$

On the contrary to UBi$_2$, the flattened magnetic Brillouin zone is realized in the antiferromagnetic state on USb$_2$, while the Brillouin zone in the paramagnetic state is the same as that in UBi$_2$. Hence, it is expected that the base of the Fermi surface in USb$_2$ is the same as that in UBi$_2$ in the paramagnetic state, althoguh it is modified due to the magnetic Brillouin zone. From the angular dependence of the dHvA frequency in Fig. 5.76, it is clarified that all Fermi surfaces consist of cylinder ones in USb$_2$. The detected cylinder Fermi surfaces occupy in the magnetic Brillouin zone 16.84 % for branch α, 7.85 % for branch γ, 5.40 % for branch δ and 3.33 % for branch ε. As the magnetic unit cell contains the four molecules of USb$_2$, shown in Fig. 3.20 (a), USb$_2$ is a compensated metal with equal carrier numbers of the electrons and holes. To compensate the number of carrier, therefore we can assume as follows:

> one electron-Fermi surface from branch α,
> one electron-Fermi surface from branch δ,
> two hole-Fermi surfaces from branch γ and
> two hole-Fermi surfaces from branch ε.

On this assumption, electron-Fermi surfaces occupy 22.24, % and hole-Fermi surfaces occupy 22.36 %, showing well compensated. Figure 5.88 (b) shows the schematic magnetic Brillouin zone and the Fermi surfaces in USb$_2$ from this speculation. Here we note that in Fig. 5.88 (a) the detected Fermi surfaces are shown all together in the same magnetic Brillouin zone.

Furthermore we calculated the electronic specific coefficient γ from these Fermi surfaces, using eq. (4.36). The estimated γ-values are $\gamma_\alpha = 3.4\,\mathrm{mJ/K^2mol}$, $\gamma_\gamma = 5.4\,\mathrm{mJ/K^2mol}$, $\gamma_\delta = 3.4\,\mathrm{mJ/K^2mol}$ and $\gamma_\varepsilon = 1.8\,\mathrm{mJ/K^2mol}$. Thus the total γ-value is $\gamma_{\mathrm{total}} = \gamma_\alpha + \gamma_\delta + 2\gamma_\gamma + 2\gamma_\varepsilon = 21.2\,\mathrm{mJ/K^2mol}$, which is roughly in good agreement with $26\,\mathrm{mJ/K^2mol}$ determined from the specific heat measurements.

Next we will discuss the two-dimensionality of the Fermi surface in USb$_2$. Two reasons can be considered for this two-dimensionality in USb$_2$. One of the reasons is ascribed to the characteristic crystal structure where the Sb and U planes are stacked along [001], as shown in Fig. 3.20 (a). This reason is the same as that of UBi$_2$ as discussed above. Moreover, the 5f electrons in USb$_2$ also become itinerant, contributing to the conduction band because of the large cyclotron masses. Therefore it is expected that these conductive U-planes are separated by the non-conductive Sb-planes, bringing about the two-dimensional character. Second reason for two-dimensionality is ascribed to the form of magnetic unit cell which is doubled in the [001] direction; this elongated magnetic unit cell is due to the ($\uparrow\downarrow\downarrow\uparrow$) sequence of uranium magnetic moments. The corresponding magnetic Brillouin zone is small and flat, as shown in Fig. 5.88. Hence, the spherical Fermi surfaces cannot exist, but the cylindrical ones appear. This second reason is the difference between USb$_2$ and UBi$_2$.

Let us now consider changes of Fermi surfaces systematically from UBi_2 to USb_2 in the antiferromagnetic state. Figure 5.89 shows the scheme of these Fermi surfaces, when viewed from the [100] direction.

The Fermi surfaces of UBi_2 in the paramagnetic or antiferromagnetic state are the spherical one named α as shown in Fig. 5.89 (a), and the cylindrical one named β as shown in Fig. 5.89 (b).

In the paramagnetic state, the Fermi surfaces of USb_2 are fundamentally the same as those of UBi_2, because the Brillouin zone in USb_2 is not flattened but almost the same as that in UBi_2. Figure 5.89 (c), (e) and (f) show the Fermi surfaces of USb_2 in the paramagnetic state. It is worth noting that the Fermi surface in Fig. 5.89 (c), which originates from the spherical Fermi surface α in UBi_2, is a cylindrical Fermi surface, although it is strongly corrugated. This is because the spherical Fermi surface α in UBi_2 nearly touches the Brillouin zone boundary. We assume that the cylindrical Fermi surface in Fig. 5.89 (e) originates from the long ellipsoidal Fermi surface (Fig. 5.89 (d)), which crosses over the Brillouin zone boundary. This long ellipsoidal Fermi surface yields the cylindrical Fermi surface in Fig. 5.89 (e) and small pocket Fermi surfaces shown in Fig. 5.89 (f). Actually, the small pocket Fermi surface is not observed, due to the extremely small dHvA frequency and/or the large curvature factor. Moreover, it is easily expected that the dHvA frequency for the pocket Fermi surface is small, because the number of carriers is almost compensated only from the cylindrical Fermi surfaces α, δ, γ and ε. We note that these Fermi surfaces in the paramagnetic state are not observed experimentally due to the high Néel temperature of 203 K.

When USb_2 undergoes antiferromagnetic ordering, it enhances a two-dimensional character due to the flattened magnetic Brillouin zone. Figure 5.89 (g) and (h) show the Fermi surfaces of USb_2 in the antiferromagnetic state. The dashed lines in these figures show the induced magnetic Brillouin zone boundary. The corrugated Fermi surface in Fig. 5.89 (c) splits into two Fermi surfaces, named α and δ, forming cylindrical Fermi surfaces. Simultaneously the Fermi surface in Fig. 5.89 (e) also splits into two Fermi surfaces, named γ and ε, forming cylindrical Fermi surfaces. The difference of the dHvA frequencies between α and δ is large, reflecting the strongly corrugated Fermi surface in Fig. 5.89 (e). On the other hand, the difference between γ and ε is small. This small difference causes the magnetic breakthrough as described below. As discussed above, the reconstruction of the Fermi surfaces results in the enhancement of the two-dimensionality on the conduction electrons. This is supported by the fact that the electrical resistivity along [001] in USb_2 displays a large hump below the Néel temperature, as shown in Fig. 5.68 (a), while the resistivity along [001] in UBi_2 shows no hump, as shown in Fig. 5.69 (a).

Finally we will give an interpretation on the magnetoresistance in USb_2. In Fig. 5.87, a spike-like peak is observed in the field along [100]. When the field is directed along [100], the cylotron orbit circulating along a belly part of the Fermi surface drifts along the field direction, as illustrated in Fig. 5.90. This direction is perpendicular to the current

direction. The present phenomenon brings about the large positive magnetoresistance, showing a peak. Moreover, the open orbit, which is directed along the current direction in k-space, is directed to the $k \times H$ direction. These cause the positive magnetoresistance for the field along [100]. Acually, Similar results are observed in CePtAs and Sr_2RuO_4, which possess the cylindrical Fermi surfaces.[116,117]
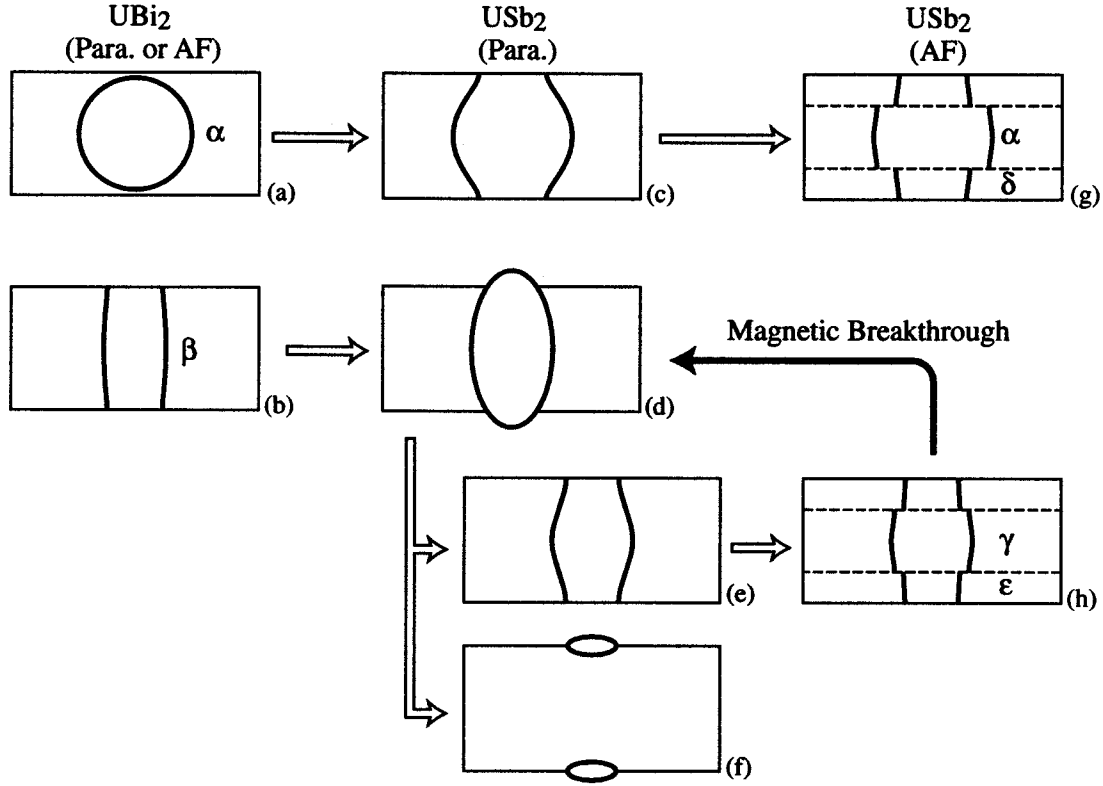
Fig. 5.89 Scheme of the Fermi surfaces in UBi_2 and USb_2 viewed from [100] direction. Figures (a) and (b) show the Fermi surfaces of UBi_2 in the paramagnetic and/or antiferromagnetic state. Figures (c), (d), (e) and (f) show the Fermi surfaces of USb_2 in the paramagnetic state. Figures (g) and (h) show the Fermi surfaces of USb_2 in the antiferromagnetic state.

Magnetic breakthrough in USb_2

Next we discuss the dHvA branch observed between [100] and [110] directions, as shown in Fig. 5.76. This branch originates from the magnetic breakthrough (breakdown) effect. The reason is as follows. The dHvA or SdH amplitude for this branch increases abruptly with increasing the field from 100 kOe, as shown in Fig. 5.77 and 5.85 (b). This drastic increase of the amplitude cannot be explained by the normal Lifshitz–Kosevich formula. In general, magnetic breakthrough occurs when the separation $\hbar\omega_c$ between Landau levels becomes comparable to or greater than the energy gap ε_g.[118] Namely,

$$\frac{e\hbar H_0}{m_c^* c} = \hbar\omega_c \gtrsim \varepsilon_g. \tag{5.18}$$

143

(a) k-space   (b) r-space
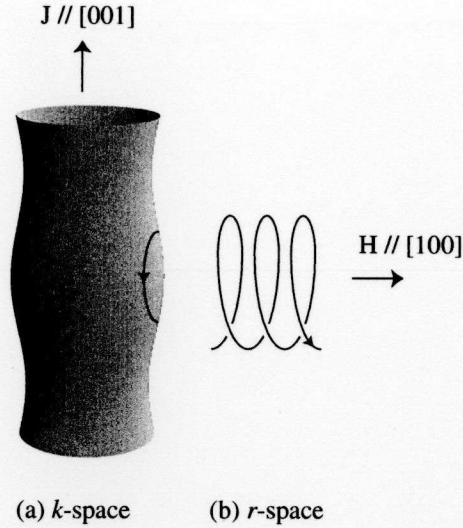
Fig. 5.90 Orbit circulating along a belly part of the Fermi surface

In reality, the criterion for magnetic breakthrough is much milder as

$$\frac{e\hbar H_0}{m_c^* c} = \hbar\omega_c \gtrsim \varepsilon_g^2/\varepsilon_F, \tag{5.19}$$

where ε_F is the Fermi energy.[119] Furthermore, The probability P of the magnetic breakthrough can be expressed as[95]

$$P = \exp(-H_0/H), \tag{5.20}$$

where H_0 is the breakthrough field obtained by eq. (5.19). Therefore, the dHvA amplitude from magnetic breakthrough will simply increase exponentially with increasing the field, although in reality the field dependence of the amplitude is much complicated to describe it and requires the special consideration such as a shape of the orbit and so on.

Returning to our results, the detected branch is certainly from the magnetic breakthrough effect because of the abrupt increase of the amplitude.

Next, we would like to confirm which orbit brings about the magnetic breakthrough. We have concluded that the magnetic breakthrough effect originates from the cylinder Fermi surfaces γ and ε. The area encircled by the magnetic breakthrough orbit is $2.24 \times 10^{15}\,\mathrm{cm}^{-2}$ along the [100] direction, which is obtained from the simple relation of $S = 2\pi e F/\hbar c$. On the other hand, the area in the magnetic Brillouin zone, encircled by cylinder orbits and zone boundaries, is nearly a rectangle, when viewed from [100] (see Fig. 5.89 (g) or (h)). This area is obtained from $2k_F k_c$, where k_F is a radius of the cylinder Fermi surface, and k_c is the length of the magnetic Brillouin zone along [001], namely, equal to $(2\pi/c)/2$ (c: lattice constant). The sum of the areas from branches γ and ε is $2.76 \times 10^{15}\,\mathrm{cm}^{-2}$. This value is nearly equal to the area of detected magnetic

breakthruough. Thus we conclude that the magnetic breakthrough comes from branches γ and ε.

To explain the magnetic breakthrough orbit from γ and ε, we consider that the breakthrough effect occurs at two steps. The first step is the breakthrough from the antiferromagnetic state to the paramagnetic state, namely, Fig. 5.89 (h) $\rightarrow$ (e). In this scheme the breakthrough arises from γ orbit to ε orbit. As a result, the orbit in the paramagnetic state is realized as shown in Fig. 5.89 (e), while this orbit is still open one which cannot be observed along [100] in the dHvA experiments.

The second step is the breakthrough between the cylindrical Fermi surface and the pocket Fermi surfaces, namely, Fig. 5.89 (e) or (f) $\rightarrow$ (d). As discussed above, the existence of the small pocket Fermi surface is easily expected in USb_2. These small pocket Fermi surfaces originate from the long ellipsoidal Fermi surface in Fig. 5.89 (d). Thus the breakthrough easily occurs between cylindrical Fermi surface and pocket Fermi surface. Therefore long ellipsoidal Fermi surface is realized. In other words, the original Fermi surface in USb_2 is formed, as shown in Fig. 5.89 (d).

In reality, these two steps for the magnetic breakthrough occur simultaneously. Consequently, the cylinder Fermi surfaces γ and ε in Fig. 5.89 (h) form the closed orbit in Fig. 5.89 (d) through the magnetic breakthrough.

Next we will discuss an extremely large cyclotron mass of $31\,m_0$ for the magnetic breakthrough. We consider that this is a characteristic feature of breaking through the magnetic Brillouin zone boundary and the large value of the cyclotron mass does not reflect the real value for the conduction electrons, but an apparent or dressed one.

To simulate this cyclotron mass, we applied the effective mass model to our results. This model is the simple assumption that there is an ellipsoidal Fermi surface as a virtual image, from the confirmed closed orbit at a certain direction. Generally, in an ellipsoidal Fermi surface, the cyclotron mass is proportional to the extremal cross sectional area. Then, we assume to exist the ellipsoidal Fermi surface from the magnetic breakthrough orbit. The radius of the cylinder Fermi surface γ is $2.33 \times 10^7\,\mathrm{cm}^{-1}$ ($\equiv a$), which corresponds to the radius of the ellipsoid cross sectional area. The area of the magnetic breakthrough is $2.24 \times 10^{15}\,\mathrm{cm}^{-2}$. Thus the another radius of the ellipsoid cross sectional area is obtained as $3.07 \times 10^7\,\mathrm{cm}^{-1}$ ($\equiv c$). Since the detected cyclotron mass for branch γ along [001] is $6.01\,m_0$ ($\equiv m^*_{c\gamma}$), the cyclotron mass along [100] is estimated as $m^*_{c\gamma} \times \pi a c / \pi a^2 = 7.9\,m_0$. This value is different far from the detected cyclotron mass of $31\,m_0$. Therefore we should consider another mass enhancement reason.

Next we noticed an abrupt increase of the dHvA amplitude with increasing the field, as shown in Fig. 5.77. To explain this, we should add the another reduction factor of the magnetic breakthrough R_b to the Lifshitz–Kosevich formulae in eqs. (4.22)–(4.26). If we assume that the probability of the magnetic breakthrough is proportional to the dHvA

145

amplitude, from eq. (5.20) we can describe the reduction factor R_b as

$$R_b \propto \exp(-H_0/H),$$ (5.21)

where H_0 is the breakthrough field, defined in eq. (5.18) or (5.19). To simplify the discussion, we use the eq. (5.18). Therefore, the reduction factor R_b can be rewritten as

$$R_b \propto \exp\left(-\beta \frac{m_c^*}{H}\right),$$ (5.22)

$$\beta = \frac{c}{e\hbar}\varepsilon_g.$$ (5.23)

We add this reduction factor R_b to the Lifshitz–Kosevich formulae in eqs. (4.22)–(4.26). Thus the dHvA amplitude A is simply described as

$$A \propto R_T R_D R_b$$ (5.24)

$$\sim \exp\left[-\frac{m_c^*}{H}(\alpha T + \beta + \alpha T_D)\right],$$ (5.25)

$$\alpha = \frac{2\pi^2 c k_B}{e\hbar}.$$ (5.26)

In the above equations, the temperature T is not included except the reduction factor R_T, so that the mass enhancement is not caused by the magnetic breakthrough effect. Actually, on the normal magnetic breakthrough, the factor R_b is independent of temperature, as pointed out by Shoenberg.[95] Our detected magnetic breakthrough, however, originates from passing through the antiferromagnetic gap ε_g. Therefore, it is natural to consider that this antiferromagnetic gap possesses the field- and temperature-dependence. Hence, we assume the effective antiferromagnetic gap ε_g^* as

$$\varepsilon_g^* = \varepsilon_{g0} + \Delta\varepsilon(T, H),$$ (5.27)

where $\Delta\varepsilon(T, H)$ is an additional energy gap dependent on temperature and field. This additional energy gap is expected to become smaller with increasing the field, because the antiferromagnetic state at high fields is close to the field-induced paramagnetic state. Furthermore, when the temperature is lower, the additional gap becomes smaller, because the scattering of carriers caused by the temperature is suppressed. Therefore, the additional energy gap is simply written as $\Delta\varepsilon_g(T, H) = \gamma T/H$. The effective antiferromagnetic gap ε_g^* is

$$\varepsilon_g^* = \varepsilon_{g0} + \gamma\frac{T}{H}.$$ (5.28)

Here we note that the constant γ is extremely small. At the sufficiently high field, namely H_0, the effective antiferromagnetic gap ε_g^* is almost the same as the original one ε_{g0}. Then, eq. (5.23) is modified as

$$\beta^* = \frac{c}{e\hbar}\left(\varepsilon_{g0} + \gamma\frac{T}{H}\right)$$ (5.29)

$$= \beta_0 + \gamma_\beta\frac{T}{H}$$ (5.30)

146

Therefore, the dHvA amplitude A is given by

$$A \sim \exp\left[-\frac{m_c^*}{H}(\alpha T + \beta^* + \alpha T_D)\right] \tag{5.31}$$

$$= \exp\left\{-\frac{m_c^*}{H}\left[\left(\alpha + \frac{\gamma_\beta}{H}\right)T + \beta_0 + \alpha T_D\right]\right\} \tag{5.32}$$

The mass is generally determined from the temperature dependence of the dHvA amplitude, namely the slope $-\alpha m_c^*/H$ of a mass plot. In the above equation of the magnetic breakthrough effect, $-(\alpha + \gamma_\beta/H)m_c^*/H$ is substituted for $-\alpha m_c^*/H$ as the slope of a mass plot. Therefore, the cyclotron mass of the magnetic breakthrough m_{cb}^* is

$$m_{cb}^* = \left(1 + \frac{\gamma_\beta}{2\pi^2 k_B}\frac{1}{H}\right)m_c^*. \tag{5.33}$$

Here we note that m_{cb}^* does not reflect the real cyclotron mass m_c^* but the dressed one.

Let us now return to our detected cyclotron mass of the breakthrough. As mentioned above, the detected mass $31\,m_0$ for the breakthrough is not the real cyclotron mass but the apparent one. This is supported by the field dependence of the cyclotron mass. Figure 5.91 shows the dHvA oscillation for the magnetic breakthrough and the corresponding field dependence of the cyclotron mass. Each mass was determined in the small field range. Interestingly, the cyclotron mass of $38\,m_0$ at $110\,\mathrm{kOe}$ decreases with increasing the field and reaches $30\,m_0$ at $160\,\mathrm{kOe}$. This indicates that the enhancement of the cyclotron mass is dependent on the magnetic field and the mass returns to the normal value at the sufficiently high magnetic field, namely at the vicinity of the critical field H_c. Although there is no report of H_c in USb$_2$, we can roughly estimate H_c to be $3000\,\mathrm{kOe}$ from the Néel temperature of $203\,\mathrm{K}$. Therefore, at about $3000\,\mathrm{kOe}$, the cyclotron mass is expected to be a normal value of $7.9\,m_0$ obtained by the effective mass model, as mentioned above. We show in Fig. 5.92 the field dependence of the cyclotron mass expanded from Fig. 5.91 (b). The straight line is a guide to eye. If we assume that the cyclotron mass decreases linearly with decreasing the inverse field, the mass becomes $13\,m_0$ at $3000\,\mathrm{kOe}$. This value is fairly comparable to $7.9\,m_0$ obtained by the effective mass model.

We summarize that the interpretation of the detected large mass is as follows:

(1) The detected large mass of $31\,m_0$ is not the real value but the apparent one due to breaking through the antiferromagnetic gap; this gap is dependent on the temperature and magnetic field.

(2) The apparent enhancement of the cyclotron mass is proportional to the inverse field. At sufficiently high fields, the mass returns to the proper value expected from the ellipsoidal Fermi surface.
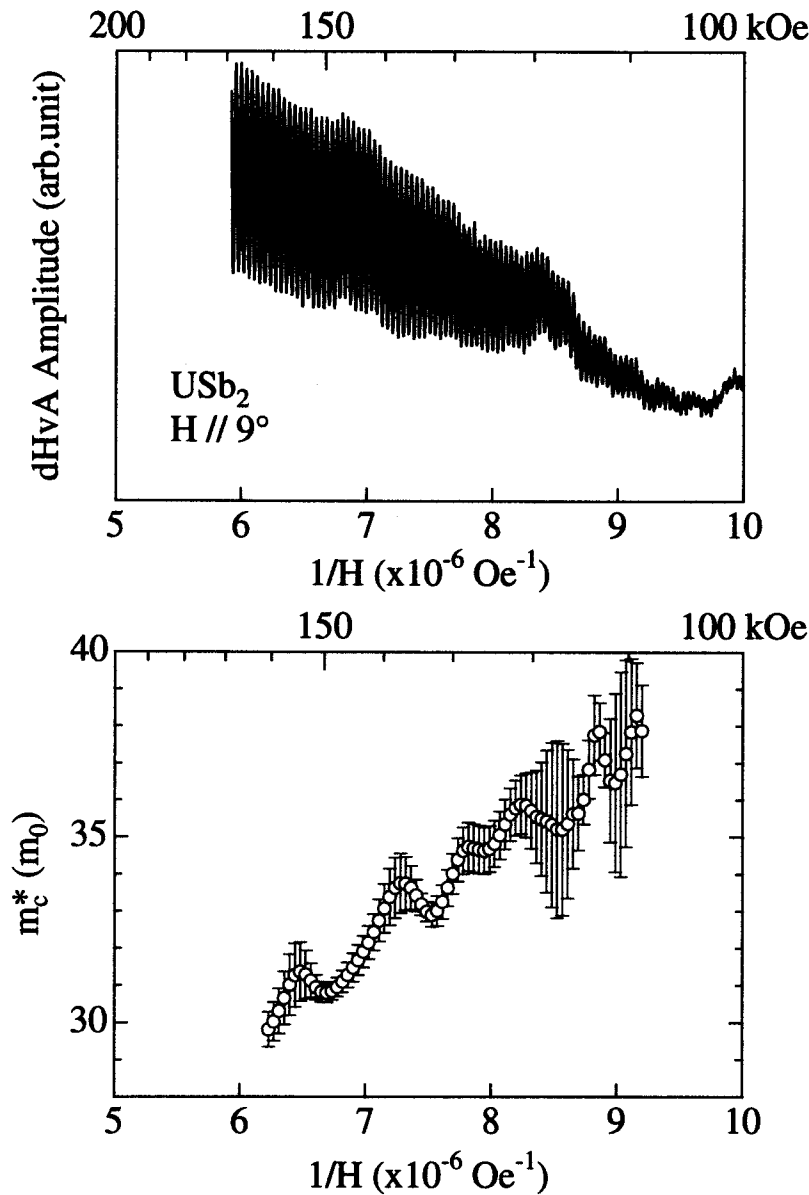
Fig. 5.91 (a) dHvA oscillation for the magnetic breakthrough and (b) the corresponding field dependence of the cyclotron mass. The field direction is tilted 9° from [100] to [110]. The error bar is statistical one from the fitting of the mass plot.

UAs$_2$

It is very easy to understand the results of UAs$_2$, because the obtained results and the magnetic unit cell in UAs$_2$ is similar to or the same as those in USb$_2$ except the magnetic breakthrough in USb$_2$.

From the angular dependence of the dHvA frequency in Fig. 5.72, it is clarified that all Fermi surfaces consist of cylindrical Fermi surfaces in UAs$_2$ except branch ζ. The detected cylinder Fermi surfaces occupy in the magnetic Brillouin zone 16.0 % for branch
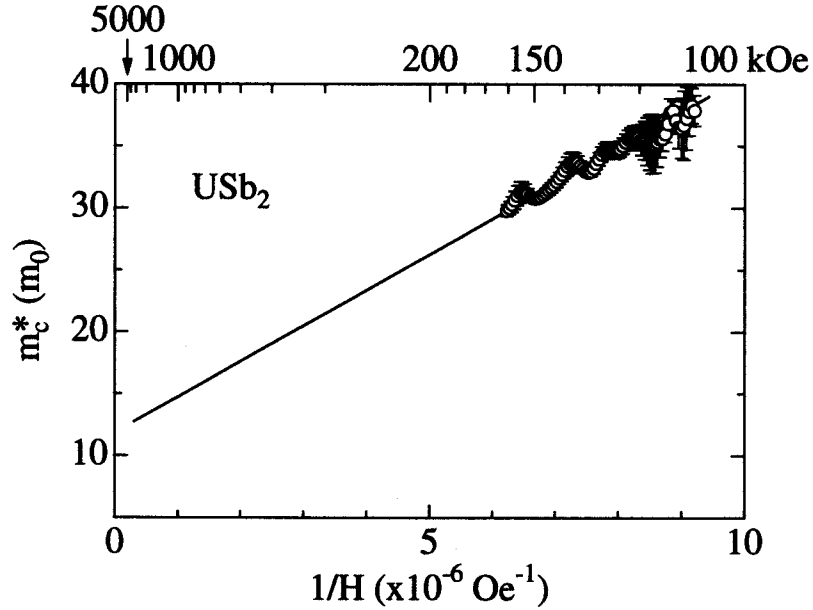
Fig. 5.92 Field dependence of the cyclotron mass expanded from Fig. 5.92 (b). The straight line is a guide to eye.

α, 7.48 % for branch γ, 5.65 % for branch δ and 4.57 % for branch ε. As the magnetic unit cell contains four molecules of UAs_2, shown in Fig. 3.20 (a), UAs_2 is a compensated metal with equal carrier numbers of the electrons and holes. To compensate the number of carrier, therefore we can assume as follows:

one electron-Fermi surface from branch α,

one electron-Fermi surface from branch δ,

two hole-Fermi surfaces from branch γ and

two hole-Fermi surfaces from branch ε.

On this assumption, electron-Fermi surfaces occupy 22.5, % and hole-Fermi surfaces occupy 24.1 %, showing well compensated. The magnetic Brillouin zone and the Fermi surfaces in UAs_2 from this speculation is almost the same as that in USb_2, as shown in Fig. 5.88 (b). Here we note that in Fig. 5.88 (b) the detected Fermi surfaces are shown all together in the same magnetic Brillouin zone. The cross sectional area occupied by branch ζ is a negligibly small value. Thus branch ζ most likely forms a small pocket Fermi surface, which causes the magnetic breakthrough in USb_2, as shown in Fig. 5.89

Furthermore we calculated the electronic specific coefficient γ from these Fermi surfaces, using eq. (4.36). The estimated γ-values are $\gamma_\alpha = 1.9\,\mathrm{mJ/K^2mol}$, $\gamma_\gamma = 2.4\,\mathrm{mJ/K^2mol}$, $\gamma_\delta = 1.6\,\mathrm{mJ/K^2mol}$ and $\gamma_\varepsilon = 0.9\,\mathrm{mJ/K^2mol}$. Thus the total γ-value is $\gamma_{total} = \gamma_\alpha + \gamma_\delta + 2\gamma_\gamma + 2\gamma_\varepsilon = 10.1\,\mathrm{mJ/K^2mol}$, which is in good agreement with $11.7\,\mathrm{mJ/K^2mol}$ determined from the specific heat measurements.

149

5.8 UCd₁₁

Figure 5.93 shows the temperature dependence of the electrical resistivity ρ, magnetic susceptibility χ and specific heat C at low temperatures.[120] The resistivity decreases rather steeply below 5.5 K and has a shoulder around 2 K, as shown in Fig. 5.93 (a). The former transition corresponds to the antiferromagnetic ordering mentioned above, which is also reflected as a peak in the susceptibility of Fig. 5.93 (b). The antiferromagnetic ordering is clearly found in the specific heat at 5.5 K, and furthermore the second phase transition is also observed at 1.7 K, as shown in Fig. 5.93 (c). The latter transition corresponds to the broad shoulder at 3–4 K reported previously.[89] We note that the resistivities at 1.3 K and room temperature are 7.6 and 70 $\mu\Omega \cdot$ cm. The value of $\rho_{\mathrm{RT}}/\rho_0$ is about 9, which is larger than 2.6 in the previous report, indicating a higher-quality sample.[91] This might be reflected as a sharp peak at 1.7 K in the specific heat.

Next the high-field magnetization measurements were carried out. Figure 5.94 shows typical magnetization curves at 1.4, 6 and 20 K. A small step-like metamagnetic transition at 1.4 K occurs at 9 T and a slope of the magnetization curve changes around 20 T. These transitions are more clearly reflected in the corresponding dM/dH curve, as shown in an inset. The first metamagnetic transition at 9 T is unchanged with increasing the temperature and disappears above 4.2 K. The high-field anomaly at 20 T shifts to a lower field with increasing the temperature. Two metamagnetic transitions are qualitatively the same as the recent result, which occurs at 6 and 16 T as mentioned in Sec. 3.5[61]

We show in Fig. 5.95 the temperature dependence of a capacitance, which corresponds to the thermal expansion. A jump corresponding to the second phase transition is clearly observed at 1.7 K in zero field. The transition temperature is almost unchanged in magnetic fields less than 7 T but is slightly shifted to lower temperatures with increasing the fields.

We summarize our experimental results in Fig. 5.96. The results of the high-field magnetization measurements are shown by open circles in the magnetic phase diagram. The data shown by solid circles, open squares, solid squares and open triangles in Fig. 5.96 are the results of low-field commercial SQUID-magnetization, capacitance, specific heat and AC susceptibility measurements. The antiferromagnetic phase diagram is very complicated, although UCd₁₁ is cubic in the crystal structure.

The change of the slope at about 20 T in the magnetization curve is interesting. The magnetization at 20 T is 1.1 μ_{B}/U at 1.4 K, but increases monotonously with increasing the field. This result suggests that the magnetic moment is about 1 μ_{B}/U in the antiferromagnetic state.

We note that the value of magnetization at the first metamagnetic transition, 0.5 μ_{B}/U, is half of the magnetic moment. If we neglect a gradual increase of the magnetization at higher fields than 20 T, a simple speculation for the metamagnetic transition at 9 T in Fig. 5.94 is as follows. One local 5f-electron moment parallel to the magnetic field,
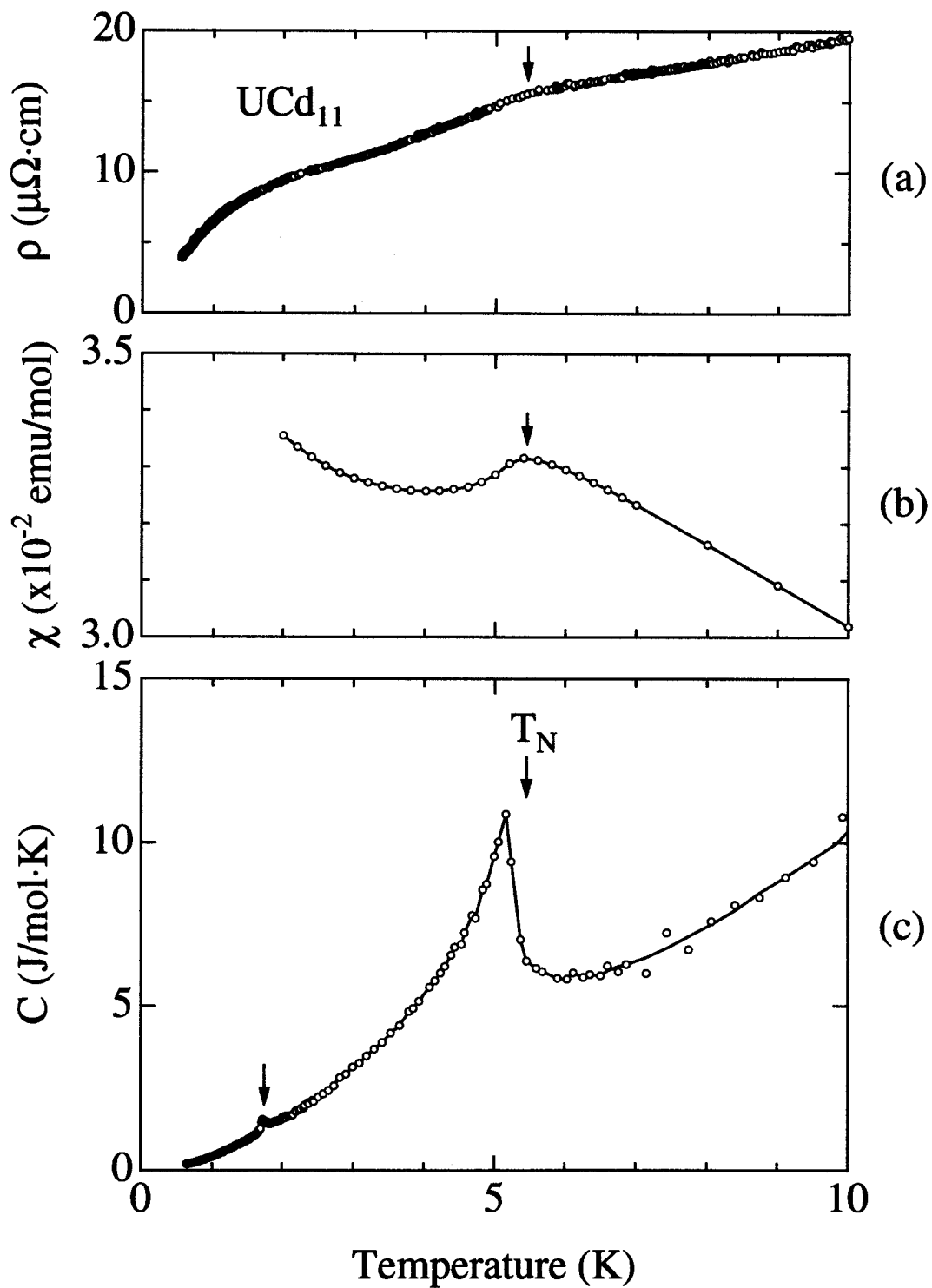
Fig. 5.93 Temperature dependence of (a) the electrical resistivity, (b) magnetic susceptibility and (c) specific heat in UCd$_{11}$.
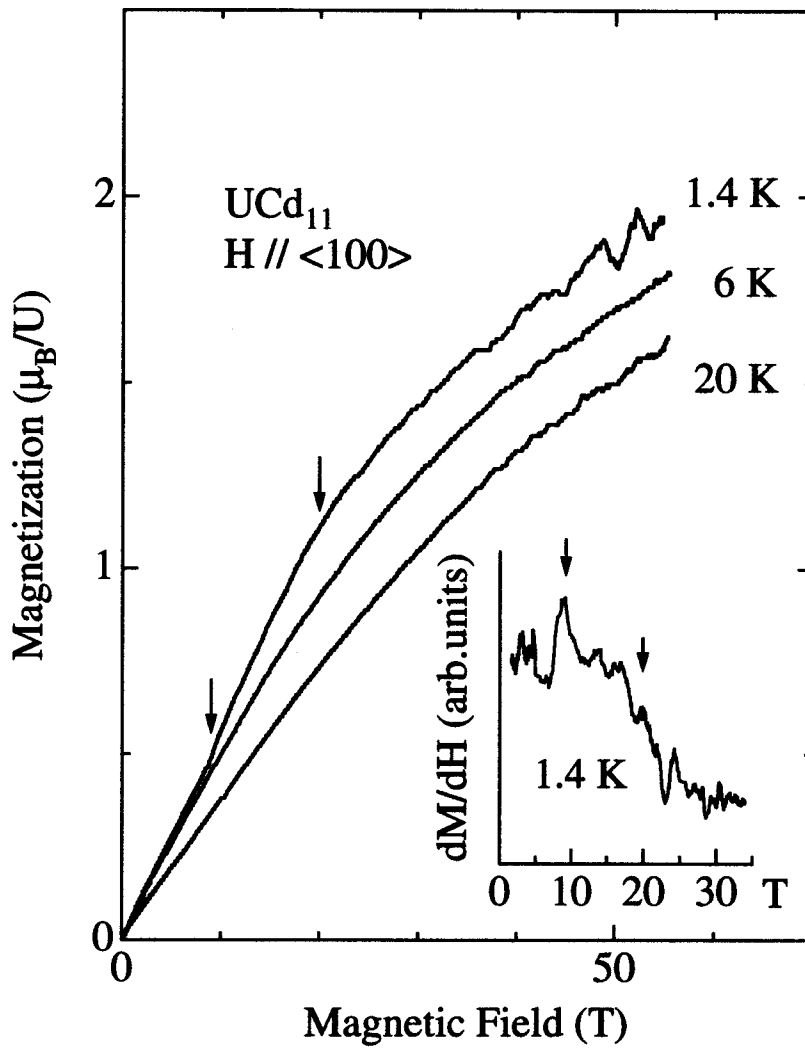
Fig. 5.94 Magnetization curves in UCd_{11}. The inset shows the dM/dH curve at 1.4 K.

namely along $\langle 100 \rangle$ is flopped by 45° and the corresponding antiferromagnetic moment by 135°. Both local moments are directed gradually for the field direction with increasing the magnetic field and saturates around 20 T.
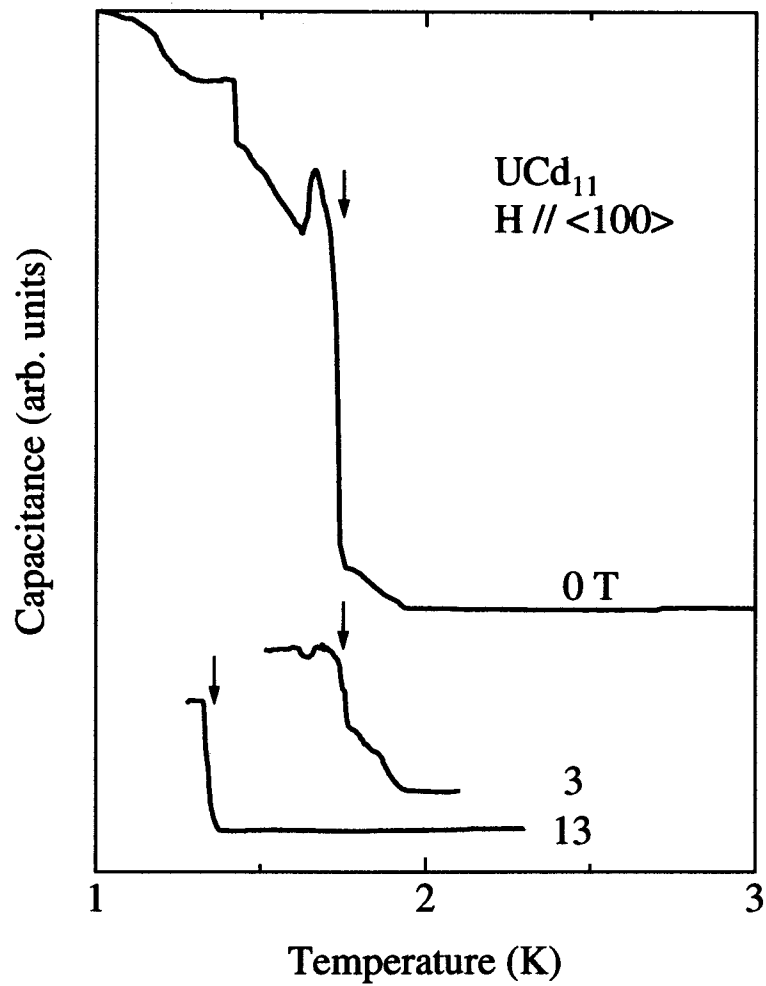
Fig. 5.95 Temperature dependence of the capacitance under the constant magnetic field in UCd₁₁.
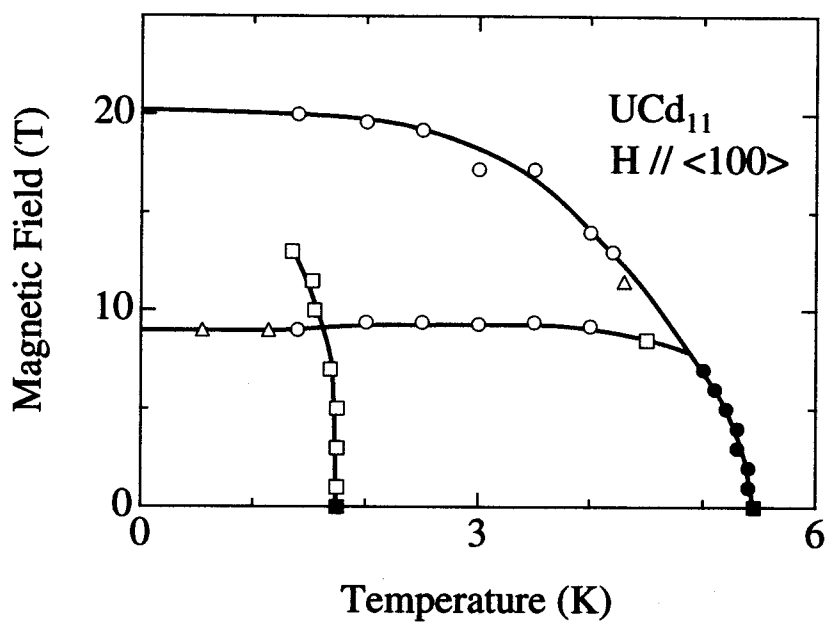
Fig. 5.96 Antiferromagnetic phase diagram in UCd$_{11}$. The data shown by open circles, solid circles, open squares, solid squares and open triangles are results of the high-field magnetization, SQUID-magnetization, capacitance, specific heat and AC susceptibility measurements.

Chapter 6 Summary

We grew high-quality single crystals of RPb_3 (R = Pr, Sm, Eu, Gd, Yb), $YbIn_3$, UAl_3, UGa_3, UX_2 (X = P, As, Sb, Bi) and UCd_{11}. The Fermi surface properties, magnetic and transport properties were studied for these compounds. Our experimental results are summarized as follows:

PrPb$_3$

(1) The detected main Fermi surfaces are four in number and nearly spherical in topology.

(2) They are well explained by the results of FLAPW band calculations for the non-f reference compound of $LaPb_3$.

(3) The cyclotron effective mass of branch γ increases with decreasing the temperature below 1 K, while the mass of branch δ has no appreciable temperature dependence.

(4) Metamagnetic transition occurs at about 70 kOe below 0.6 K. The critical field is almost constant against the temperature.

(5) This transition and mass enhancement are closely related to the antiferroquadrupolar ordering which occurs below 0.4 K.

YbPb$_3$ and EuPb$_3$

(1) The detected Fermi surfaces of $YbPb_3$ are three in number. These are highly different from those of $LaPb_3$ due to Yb divalent.

(2) The detected Fermi surfaces of $YbPb_3$ are explained by the results of FLAPW band calculations. $YbPb_3$ is a compensated metal with equal carrier numbers of electrons and holes. The cyclotron mass is light, ranging from 0.21 to 0.61 m_0.

(3) Branch α of an antiferromagnetic compound $EuPb_3$ is in good agreement with that of $YbPb_3$, which can be seen by the magnetic breakthrough effect. The other branches with lower dHvA frequencies are antiferromagnetic Fermi surfaces, most likely produced by the band folding procedure in a small magnetic Brillouin zone.

(4) $EuPb_3$ is a divalent compounds, which was confirmed from the magnetic entropy, the effective Bohr magneton and the saturated moment. We also estimated the magnetic exchange interaction on the basis of the two-sublattice model from the high-field magnetization.

SmPb$_3$ and GdPb$_3$

(1) Branches α of both compounds are in fairly good agreement with that of LaPb$_3$. These are observed by the magnetic breakthrough effect. The other branches are different from those of LaPb$_3$, due the small antiferromagnetic Brillouin zone.

(2) The cyclotron mass is in the range from 0.23 to $1.4\,m_0$ for SmPb$_3$, indicating no mass enhancement. The mass for GdPb$_3$ is in the range from 0.61 to $1.6\,m_0$.

YbIn$_3$

(1) The detected Fermi surfaces are six in number. All Fermi surfaces are closed ones. The cyclotron mass is light, ranging from 0.22 to $1.3\,m_0$.

(2) The experimental results are in excellent agreement with the result of FLAPW band calculations.

(3) YbIn$_3$ is a divalent metal and the $4f$ levels are far below the Fermi level.

UAl$_3$

(1) Three main dHvA branches and other small branches are detected. Among them, main branches α and γ correspond to the closed Fermi surfaces and are well explained by the results of FLAPW band calculations under the assumption that $5f$ electrons in the U atom are itinerant.

(2) The cyclotron mass is in the range from 3 to $17\,m_0$, suggesting the strong $5f$ hybridization with the conduction electrons

UGa$_3$

(1) Electronic states and/or the scattering mechanism are drastically changed below $T_N = 67\,\mathrm{K}$, which are reflected in the Hall coefficient and thermoelectric power as well as the electrical resistivity and magnetic susceptibility.

(2) Two anomalies at $T_1 \simeq 40\,\mathrm{K}$ and $T_2 \simeq 8\,\mathrm{K}$, which were observed in the susceptibility, are also ascertained in the thermoelectric power measurement.

(3) The transverse magnetoresistance increases nearly quadratically for any field directions. This result indicates that UGa$_3$ is a compensated metal with equal carrier numbers of electrons and holes and Fermi surfaces consist of closed ones.

(4) We detected five dHvA branches with small closed Fermi surfaces. For example, branch α, which is the largest Fermi surface among them, occupies 0.9 % of the volume in the magnetic fcc Brillouin zone. The cyclotron mass is moderately large $3.5\,m_0$ for $\langle 100 \rangle$ $5.0\,m_0$ for $\langle 111 \rangle$. The mean free path is long, 2900 Å, indicating a

high-quality sample. Besides five Fermi surfaces mentioned above, another larger closed Fermi surfaces with much larger masses should exist to explain the γ-value of $52\,mJ/K^2mol$.

(5) All detected mass is relatively large, ranging from 2.3 to $5.0\,m_0$.

UX_2 (X = P, As, Sb, Bi)

(1) High-quality single crystals were grown by the self-flux method for USb_2 and UBi_2, and by the chemical transport method for UP_2 and UAs_2. In particular, the residual resistivity ratio of UP_2 is 2900, which is the highest value in the uranium compounds as far as we know.

(2) The Fermi surfaces of UBi_2 consist of a spherical one and a cylindrical one.

(3) The Fermi surfaces of USb_2 are four cylindrical ones. Two Fermi surfaces originate from the spherical Fermi surfaces in UBi_2 and another two Fermi surfaces from the cylindrical ones in UBi_2. The Fermi surfaces of UAs_2 are the same as those of USb_2.

(4) The two-dimensional character of Fermi surfaces on these compounds is due to the conduction electrons in the U-plane, including the $5f$ electrons. The itinerant nature of $5f$-electrons is reflected to the large cyclotron masses.

(5) Another reason for the two-dimensionality on USb_2 and UAs_2 is a flattened magnetic Brillouin zone caused by the antiferromagnetic ($\uparrow\downarrow\downarrow\uparrow$) sequence.

(6) The dHvA branch was observed between [100] and [110] in USb_2, which is due to the magnetic breakthrough effect. This branch originates from branches δ and ε.

(7) The detected large mass in USb_2 is the apparent or dressed one, which is based on breaking through the antiferromagnetic gap. At sufficiently high fields, the mass is close to the proper value expected from the effective mass model.

(8) UAs_2, USb_2 and UBi_2 are compensated metals with equal carrier numbers of electrons and holes. This is confirmed from the volume of the detected Fermi surfaces.

(9) The cyclotron masses in UAs_2, USb_2 and UBi_2 are consistent with the corresponding specific heats.

UCd_{11}

(1) The another transition at $1.7\,K$ was found below the Néel temperature of $5.5\,K$.

(2) The magnetic phase diagram was determined from the magnetization, AC/DC susceptibility, magnetostriction and specific heat.

157

Acknowledgements

References

1) Y. Ōnuki and A. Hasegawa, "Fermi Surfaces of Intermetallic Compounds," in *Handbook on the Physics and Chemistry of Rare Earths*, eds. by K. A. Gschneidner Jr. and L. Eyring (North-Holland, Amsterdam, 1995), Vol. 20, Chap. 135, p. 1.

2) T. Kasuya, O. Sakai, H. Harima and M. Ikeda: J. Magn. Magn. Mater. **76&77** (1988) 46.

3) M. Ruderman and C. Kittel: Phys. Rev. **96** (1954) 99.

4) T. Kasuya: Prog. Theor. Phys. **16** (1956) 45.

5) K. Yosida: Phys. Rev. **106** (1957) 893.

6) A. Sumiyama, Y. Oda, H. Nagano, Y. Ōnuki, K. Shibutani and T. Komatsubara: J. Phys. Soc. Jpn. **55** (1986) 1294.

7) A. J. Arko, J. J. Koelling and J. E. Schirber, "Energy Band Structure and Fermi Surface of the Actinide Materials," in *Handbook on the Physics and Chemistry of Actinides*, eds. by A. J. Freeman and G. H. Lander (North-Holland, Amsterdam, 1985), Vol. 2, Chap. 3, pp. 175–238.

8) T. Moriya: J. Magn. Magn. Mater. **31–34** (1983) 10.

9) N. Kimura, Ph.D. thesis, Osaka University, 1997.

10) Y. Ōnuki, K. Ueda and T. Komatsubara, "Heavy Electron System," in *Slected Paper in Physics IV* (Physical Society of Japan, 1994), (in Japanese).

11) R. Settai, S. Araki, P. Ahmet, M. Abliz, K. Sugiyama, Y. Ōnuki, T. Goto, H. Mitamura, T. Goto and S. Takayanagi: J. Phys. Soc. Jpn. **67** (1998) 636.

12) P. Morin and D. Schmitt, "Quadrupolar Interactions and Magneto-Elastic Effects in Rare Earth Intermetallic Compounds," in *Ferromagnetic Materials*, eds. by K. H. J. Buschow and E. P. Wohlfarth (North-Holland, Amsterdam, 1990), Vol. 5, p. 1.

13) J. M. Effantin, J. Rossat-Mignod, P. Burlet, H. Bartholin, S. Kunii and T. Kasuya: J. Magn. Magn. Mater. **47&48** (1985) 145.

14) T. Matsumura, S. Nakamura, T. Goto, H. Amitsuka, K. M. T. Sakakibara and T. Suzuki: J. Phys. Soc. Jpn. **67** (1998) 612.

15) T. Sakakibara, T. Tayama, K. Tenya, H. Amitsuka, D. Aoki, Y. Ōnuki and Z. Kletowski: Physica B **259–261** (1999) 340.

16) F. J. Ohkawa: J. Phys. Soc. Jpn. **54** (1985) 3909.

17) R. Shiina, H. Shiba and P. Thalmeier: J. Phys. Soc. Jpn. **66** (1997) 1741.

18) R. Shiina, O. Sakai, H. Shiba and P. Thalmeier: J. Phys. Soc. Jpn. **67** (1998) 941.

19) K. Hanzawa and T. Kasuya: J. Phys. Soc. Jpn. **53** (1984) 1809.

20) T. Kasuya: J. Phys. Soc. Jpn. **66** (1997) 2950.

21) G. Uimin, Y. Kuramoto and N. Fukushima: Solid State Commun. **97** (1996) 595.

22) N. Fukushima and Y. Kuramoto: J. Phys. Soc. Jpn. **67** (1998) 2460.

23) D. D. Koelling, B. D. Dunlap and G. W. Crabtree: Phys. Rev. B **31** (1985) 4966.

24) K. H. J. Buschow, H. J. van Daal, F. E. Maranzana and P. B. van Aken: Phys. Rev. **3** (1971) 1662.

25) R. D. Parks: *Valence Instabilities and Related Narrow-Band* (Plenum Press, New York, 1977).

26) L. M. Falicov, W. Hanke and M. P. Maple: *Valence Fluctuations in Solids* (North-Holland, Amsterdam, 1981).

27) K. Yamada, K. Yosida and K. Hanzawa: Prog. Theor. Phys. **71** (1984) 450.

28) K. Yamada and K. Yosida: Prog. Theor. Phys. **76** (1986) 621.

29) K. A. Gschneidner Jr., S. K. Dhar, R. J. Stierman, T. -W. E. Tsang and O. D. McMasters: J. Magn. Magn. Mater. **47&48** (1985) 51.

30) A. de Visser, A. Menovsky and J. J. M. Franse: Physica B **147** (1987) 81.

31) G. R. Stewart: Rev. Mod. Phys. **56** (1984) 755.

32) K. Kadowaki and S. B. Woods: Solid State Commun. **58** (1986) 507.

33) P. A. Lee, T. M. Rice, J. W. Serene, L. J. Sham and J. W. Wilkins: Condensed Matter Phys. **12** (1986) 99.

34) Y. Ōnuki, T. Goto and T. Kasuya, in *Materials Science and Technology*, ed. by K. H. Buschow (VCH Weinheim, 1992), Vol. 3A, p. 545.

35) M. R. Norman and D. D. Koelling, in *Handbook on the Physics and Chemistry of Rare Earths*, eds. by K. A. Gschneidner Jr., L. Eyring, G. H. Lander and G. R. Choppin (North-Holland, Amsterdam, 1993), Vol. 17, p. 1.

36) D. Aoki, Y. Katayama, R. Settai, Y. Inada, Y. Ōnuki, H. Harima and Z. Kletowski: J. Phys. Soc. Jpn. **66** (1997) 3988.

37) P. Lethuillier and J. Chaussy: J. Phys. (Paris) **37** (1976) 123.

38) E. Bucher, K. Andres, A. C. Gossard and J. P. Maita: J. Low Temp. **2** (1972) 322.

39) W. Gross, K. Knorr, A. P. Murani and K. H. J. Buschow: Z. Phys. B **37** (1980) 123.

40) P. Morin, D. Schmitt and E. du Trémolet de Lacheisserie: J. Magn. Magn. Mater. **30** (1982) 257.

41) J. Kitagawa, N. Takeda, M. Ishikawa, T. Yoshida, A. Ishiguro and T. Komatsubara: Physica B **230-232** (1997) 139.

42) A. Czopnik, N. Iliew, B. Stalinski, H. Madge, C. Bazan and R. Pott: Physica B **130** (1985) 262.

43) J. McDonough and S. R. Julian: Phys. Rev. B **53** (1996) 14411.

44) P. Lethuillier, J. Pierre, K. Knorr and W. Drexel: J. Phys. **36** (1975) 329.

45) T. Ebihara, R. Settai, N. Kimura, H. Toshima, K. Motoki, H. Ikezawa, Y. Ōnuki, H. Harima, P. Sławiński and Z. Kletowski: J. Phys. Soc. Jpn. **64** (1995) 3416.

46) B. Liu, M. Kasaya and T. Kasuya: J. Physique **49** (1988) C.

47) D. Endoh, T. Goto, A. Tamaki, B. Liu, M. Kasaya, T. Fujimura and T. Kasuya: J. Phys. Soc. Jpn. **58** (1989) 940.

48) P. Sławiński: Phys. Stat. Sol. (b) **175** (1993) K17.

49) R. D. Hutchens and W. E. Wallace: J. Solid State Chem. **3** (1971) 564.

50) D. Aoki, Y. Katayama, R. Settai, N. S. K. Sugiyama, K. Kindo, H. Harima and Y. Ōnuki: J. Phys. Soc. Jpn. **67** (1998) 4251.

51) T. Ebihara, Y. Haga, E. Yamamoto, Y. Aoki, H. Sato, S. K. Dhar and Y. Ōnuki: J. Phys. Soc. Jpn. **66** (1997) 1842.

52) M. J. Steiner, I. R. Walker, F. M. Grosche, D. M. Freye and G. G. Lonzarich, "Low Temperature Resistivity of CeIn$_3$ near the Border of Magnetic and Superconducting Order at High Pressure," In *SCES 99*, (Nagano, Japan, 1999).

53) Y. Kurosawa, I. Umehara, M. Kikuchi, N. Nagai, K. Satoh and Y. Ōnuki: J. Phys. Soc. Jpn. **59** (1990) 1545.

54) K. Satoh, I. Umehara, N. Nagai, Y. Ōnuki I. Sakamoto, M. Hunt, P. Meeson, P. A. Probst and M. Springford: J. Magn. Magn. Mater. **104-107** (1992) 1411.

55) T. Ebihara, I. Umehara, A. K. A. K. Satoh and Y. Ōnuki: Physica B **186–188** (1993) 123.

56) I. Umehara, N. Nagai and Y. Ōnuki: J. Phys. Soc. Jpn. **60** (1991) 591.

57) Z. Kletowski, M. Glinski and A. Hasegawa: J. Phys. F **17** (1987) 993.

58) H. Kitazawa, Q. Z. Gao, H. Shiba, T. Suzuki, A. Hasegawa and T. Kasuya: J. Magn. Magn. Mater. **76&77** (1985) 40.

59) A. Hasegawa: in *Crystalline Electric Field Effects in f-Electron Magnetism*, eds. by W. Suski and Z. Zolnierek (Plenum, 1982), p. 201.

60) A. Percheron-Guegan, O. Gorochov and F. Gonzalez-Jimenes: J. Less-Common. Met. **37** (1974) 1.

61) A. L. Cornelius, A. J. Arko, J. L. Sarrao, J. D. Thompson, M. F. Hundley, C. H. Booth, N. Harrison and P. M. Oppeneer: Phys. Rev. B **59** (1999) 14473.

62) J. M. Fournier and R. Troć, in *Handbook on the Physics and Chemistry of the Actinides* (North-Holland, Amsterdam, 1985), Vol. 2, Chap. 2, p. 29.

63) H. H. Hill, in *Plutonium and Other Actinides*, ed. by W. N. Miner (AIME, New York, 1970), p. 2.

64) H. R. Ott, F. Hulliger, H. Rudigier and Z. Fisk: Phys. Rev. B **31** (1985) 4966.

65) M. H. van Maaren, H. J. van Daal, K. H. J. Buschow and G. J. Schinkel: Solid State Commnun. **14** (1974) 145.

66) A. Blaise: J. Phys. (France) **40** (1979) 49.

67) T. Takimoto and T. Moriya: Solid State Commun. **99** (1996) 457.

68) I. Lupsa, E. Burzo and P. Lucaci: J. Magn. Magn. Mater. **157 & 158** (1996) 696.

69) D. Kaczorowski, R. Troć, D. Badurski, A. Böhm, L. Shlyk and F. Steglich: Phys. Rev. B **48** (1993) 16425.

70) A. Misiuk, J. Mulak and A. Czopnik: Bull. Acad. Pol. Sci. Ser. Sci. Chim. **20** (1972) 459.

71) D. Kaczorowski, R. Hauser and A. Czopnik: Physica B **230-232** (1997) 35.

72) G. E. Grechnev, A. Delin, O. Eriksson, B. Johansson, A. S. Panfilov, I. V. Svechkarev and D. Kaczorowski: Acta. Phys. Pol. A **92** (1997) 331.

73) D. Kaczorowski, P. W. Klamut, A. Czopnik and A. Jeżowski: J. Magn. Magn. Mater. **171–181** (1998) 41.

74) A. Murasik, J. Leciejewicz, S. Ligenza and A. Zygmunt: Phys. Stat. Sol. (a) **23** (1974) K147.

75) A. C. Lawson, A. Williams, J. L. Smith, P. A. Seeger, J. A. Goldstone, J. A. O'Rourke and Z. Fisk: J. Magn. Magn. Mater. **50** (1985) 83.

76) P. Dervenagas, D. Kaczorowski, F. Bourdarot, P. Burlet, A. Czopnik and G. H. Lander: Physica B **269** (1999) 368.

77) L. W. Zhou, C. S. Jee, C. L. Lin, J. E. Crow, S. Bloom and R. P. Guertin: J. Appl. Phys. **61** (1987) 3377.

78) C. Jee, T. Yuen, C. L. Lin and J. E. Crow: Bull. Am. Phys. Soc. **61** (1987) 3377.

79) Z. Henkie and W. Trzebiatowski: Phys. Stat. Sol. **35** (1969) 827.

80) Z. Henkie and Z. Kletowski: Acta. Phys. Polon. **A42** (1972) 405.

81) A. Blaise, J. M. Fournier, R. Langnier, M. J. Mortimer, R. Schenkel, Z. Henkie and A. Wojakowski: Inst. Phys. Conf. Ser. **37** (1978) 184.

82) R. Troć, J. Leciejewicz and R. Ciszewski: Phys. Stat. Sol. **15** (1966) 515.

83) A. Oleś: J. de Phys. **26** (1965) 561.

84) J. Leciejewicz, R. Troć, A. Murasik and A. Zygmunt: Phys. Stat. Sol. **22** (1967) 517.

85) Z. Henkie, R. Maślanka, P. Wiśniewski, R. Fabrowski and P. J. Markowski: J. Alloys Compds. **181** (1992) 267.

86) H. C. Montgomery: J. Appl. Phys. **42** (1971) 2971.

87) G. Amoretti, A. Blaise and J. Mulak: J. Magn. Magn. Mater. **42** (1984) 65.

88) F. Grønvold, M. R. Zaki, E. F. Westrum Jr., J. A. Sommers and D. B. Downie: J. Inorg. Nucl. Chem. **40** (1978) 635.

89) Z. Fisk, G. R. Stewart, J. O. Willis, H. R. Ott and F. Hulliger: Phys. Rev. B **30** (1984) 6360.

90) B. Andraka, G. R. Stewart and Z. Fisk: Phys. Rev. B **44** (1991) 10346.

91) J. D. Thompson, Z. Fisk, M. W. McElfresh, H. R. Ott and M. B. Maple: Phys. Rev. B **39** (1989) 2578.

92) J. D. Thompson, A. C. Lawson, M. W. McElfresh, A. P. Sattelberger and Z. Fisk: J. Magn. Magn. Mater. **76&77** (1988) 437.

93) Z. Fisk and J. P. Remeika, "Growth of Single Crystals From Molten Metal Fluxes," in *Handbook on the Physics and Chemistry of Rare Earths*, eds. by K. A. Gschneidner Jr. and L. Eyring (North-Holland, Amsterdam, 1995), Vol. 12, Chap. 81, p. 53.

94) Z. Kletowski, N. Iliev, Z. Henkie and B. Staliński: J. Less-Common Met. **110** (1985) 235.

95) D. Shoenberg: *Magnetic oscillations in metals* (Cambridge University Press, 1984).

96) E. N. Adams and T. D. Holstein: J. Phys. Chem. Sol. **10** (1959) 254.

97) A. B. Pippard: *The dynamics of Conduction Electrons* (Blackie & Son, 1965).

98) D. Aoki, Y. Katayama, R. Settai, Y. Inada, Y. Ōnuki, H. Harima, Z. Kletowski, T. Tayama and T. Sakakibara: JJAP Series **11** (1998) 188.

99) D. Aoki, Y. Katayama, R. Settai, Y. Inada, Y. Ōnuki, H. Harima and Z. Kletowski: J. Magn. Magn. Mater. **177-181** (1998) 365.

100) M. Takashita, H. Aoki, T. Terashima, S. Uji, K. Maezawa, R. Settai and Y. Ōnuki: J. Phys. Soc. Jpn. **65** (1996) 515.

101) I. Umehara, N. Nagai and Y. Ōnuki: J. Phys. Soc. Jpn. **60** (1991) 3150.

102) H. H. Teitelbaum and P. M. Levy: Phys. Rev. B **14** (1976) 3058.

103) T. Tayama, Ph.D. thesis, Hokkaido University, 1998.

104) T. Sakakibara, T. Tayama, K. Kitami, M. Yokoyama, K. Tenya, H. Amitsuka, D. Aoki, Y. Ōnuki, Z. Kletowski, T. Matsumura and T. Suzuki (unpublished).

105) I. Sakamoto, S. Ohhara, I. Oguro and S. Marumo: Physica B **230–232** (1997) 286.

106) K. Sugiyama, Y. Koyohi, S. Kunii, T. Kasuya and M. Date: J. Phys. Soc. Jpn. **57** (1988) 1762.

107) D. Aoki, Y. Katayama, S. Nojiri, R. Settai, Y. Inada, K. Sugiyama, Y. Ōnuki, H. Harima and Z. Kletowski: Physica B **259-261** (1999) 1083.

108) T. Ebihara, Y. Inada, M. Murakawa, S. Uji, C. Terakura, T. Terashima, E. Yamamoto, Y. Haga, Y. Ōnuki and H. Harima (unpublished).

109) D. Aoki, N. Suzuki, K. Miyake, Y. Inada, R. Settai, K. Sugiyama, E. Yamamoto, Y. Haga, Y. Ōnuki, H. Sugawara and H. Sato (unpublished).

110) D. Aoki, P. Wiśniewski, K. Miyake, R. Settai, Y. Inada, K. Sugiyama, E. Yamamoto, Y. Haga and Y. Ōnuki (unpublished).

111) K. Miyake, T. Matsuura and C. M. Varma: Solid State Commun. **71** (1989) 1149.

112) D. Aoki, P. Wiśniewski, K. Miyake, N. Watanabe, Y. Inada, R. Settai, E. Yamamoto, Y. Haga and Y. Ōnuki: J. Phys. Soc. Jpn. **68** (1999) 2182.

113) W. Trzebiatowski and A. Zygmunt: Bull. Acad. Polon. Sci. Ser. Sci. Chem. **14** (1966) 495.

114) P. Wiśniewski, D. Aoki, N. Watanabe, K. Miyake, R. Settai, Y. Ōnuki, Y. Haga, E. Yamamoto and Z. Henkie (unpublished).

115) W. Trzebiatowski, A. Sepichowska and A. Zygmunt: Bull. Acad. Polon. Sci. Ser. Sci. Chem. **12** (1964) 687.

116) R. Settai, Y. Yoshida, A. Yamaguchi, Y. Ōnuki, S. Yoshii, M. Kasaya, H. Harima and K. Takegahara: J. Phys. Soc. Jpn. **68** 3615.

117) Y. Yoshida, A. Mukai, R. Settai, K. Miyake, Y. Inada, Y. Ōnuki, K. Betsuyaku, H. Harima, T. D. Matsuda, Y. Aoki and H. Sato: J. Phys. Soc. Jpn. **68** (1999) 3041.

118) M. H. Cohen and J. M. Falicov: Phys. Rev. Lett. **7** (1961) 231.

119) E. I. Blount: Phys. Rev. **126** (1962) 1636.

120) D. Aoki, T. Inoue, N. Suzuki, K. Miyake, Y. Inada, R. Settai, K. Sugiyama, E. Yamamoto, Y. Haga, K. Kindo and Y. Ōnuki: J. Phys. Soc. Jpn. **68** (1999) 3117.

Appendix

The conditions of the single crystal growth by the self-flux method are as follows.

UAl₃

Ratio of starting materials

U : Al	=	4 : 96	(at %)
	≃	2.6567 : 7.2569	(g)

Growing process

	Rate (°C/h)	Target (°C)
1.	153	640
2.	34	1050
3.	0 (keep for 24 h)	1050
4.	0.4	900
5.	0.5	750

Total time = 715 h ≃ 30 days

*To prevent growth of UAl₄, the power was cut at 750 °K.

Results

Cubic shape $(5 \times 7 \times 7\,\text{mm}^3)$

$\rho_{RT}/\rho_0 = 88$

UGa₃

Ratio of starting materials

U : Ga	=	6.8 : 93.2	(at %)
	≃	3.4068 : 13.6415	(g)

Growing process

	Rate (°C/h)	Target (°C)
1.	28	1040
2.	0 (keep for 72 h)	1040
3.	0.4	950
4.	0.6	850
5.	0.8	750
6.	1.0	650
7.	1.5	550
8.	5.0	450
9.	15	100

Total time = 835 h ≃ 35 days

Results

Cubic shape $(5 \times 6 \times 6\,\text{mm}^3)$

$\rho_{RT}/\rho_0 = 80$
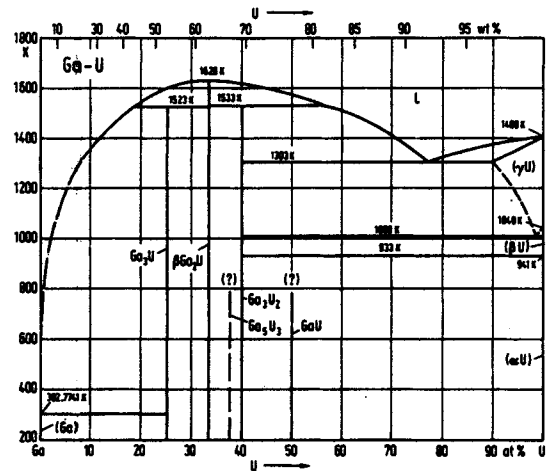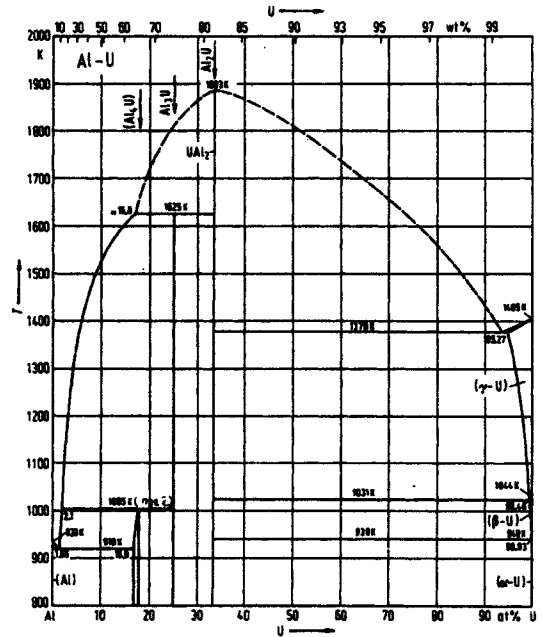
UIn$_3$

Ratio of starting materials

U : In = 10 : 90 (at %)

≃ 2.5845 : 11.2208 (g)

Growing process

	Rate (°C/h)	Target (°C)
1.	40	150
2.	30	1050
3.	0 (keep for 48 h)	1050
4.	0.8	800
5.	1.2	700
6.	2.0	600
7.	5.0	500
8.	10	400
9.	15	140

Total time = 574 h ≃ 24 days

Results

Cubic shape ($1 \times 1 \times 1\,\text{mm}^3$)

$\rho_{RT}/\rho_0 = 130$

Phase diagram is unknown.
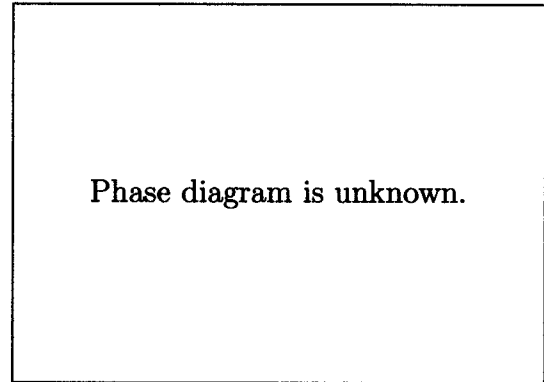
USn$_3$

Ratio of starting materials

U : Sn = 6.8 : 93.2 (at %)

≃ 1.0191 : 13.5400 (g)

Growing process

	Rate (°C/h)	Target (°C)
1.	28	1020
2.	0 (keep for 72 h)	1020
3.	0.4	910
4.	0.5	860
5.	0.7	800
6.	1.5	700
7.	2.5	600
8.	10	300
9.	20	200

Total time = 680 h ≃ 28 days

Results

Cubic shape ($2 \times 2 \times 2\,\text{mm}^3$)

$\rho_{RT}/\rho_0 = 49$ (no superconducting of Sn)

167
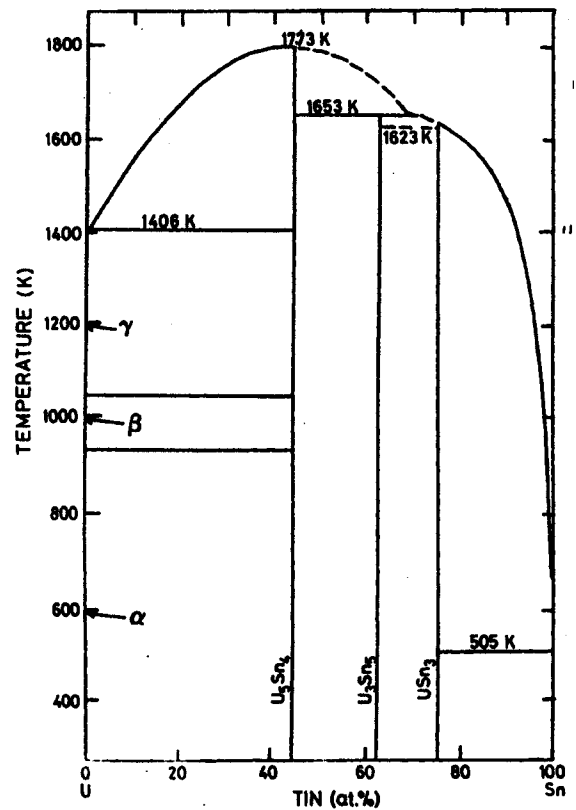
UPb$_3$

Ratio of starting materials

U : Pb = 2.4 : 97.6   (at %)

    $\simeq$ 0.7759 : 27.5000   (g)

Growing process

	Rate (°C/h)	Target (°C)
1.	90	300
2.	32	1070
3.	0 (keep for 72 h)	1070
4.	0.3	900
5.	0.4	800
6.	0.6	700
7.	0.9	600
8.	2.0	400
9.	5.0	300

Total time = 1314 h $\simeq$ 55 days

Results

Cubic shape (1 × 1 × 1 mm^3)

ρ_{RT}/ρ_{7K} = 43
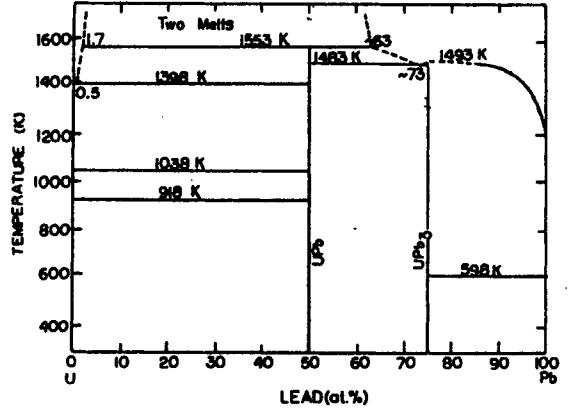
USb$_2$

Ratio of starting materials

U : Sb = 6.5 : 93.5   (at %)

    $\simeq$ 2.2900 : 16.8382   (g)

Growing process

	Rate (°C/h)	Target (°C)
1.	30	600
2.	9.8	1070
3.	0 (keep for 48 h)	1070
4.	0.4	950
5.	0.6	850
6.	0.8	750
7.	1.0	600
8.	10	100

Total time = 907 h $\simeq$ 38 days

Results

Plate shape (10 × 10 × 5 mm^3)

ρ_{RT}/ρ_0 = 80   ($J \parallel [100]$)

168

UBi₂

UBi$_2$

Ratio of starting materials

U : Bi = 11.9 : 88.1   (at %)

$\simeq$ 3.1222 : 20.2925 (g)

Growing process

	Rate (°C/h)	Target (°C)
1.	110	360
2.	13	980
3.	0 (keep for 72 h)	980
4.	0.5	950
5.	0.4	850
6.	0.5	700
7.	0.7	600
8.	1.0	500
9.	1.5	400
10.	10	250

Total time = 1058 h $\simeq$ 44 days

Results

Plate shape (6 × 6 × 2 mm^3)

$\rho_{RT}/\rho_0 = 180$ ($J \parallel [001]$)

UCd₁₁

UCd$_{11}$

Ratio of starting materials

U : Cd = 0.8 : 99.2   (at %)

$\simeq$ 1.68 : 98.32 (g)

Growing process

	Rate (°C/h)	Target (°C)
1.	90	300
2.	2.4	470
3.	0 (keep for 240 h)	470
3.	0.3	370
4.	0.4	310
5.	10	100

Total time = 786 h $\simeq$ 33 days

Results

Cubic shape (10 × 10 × 10 mm^3)

$\rho_{RT}/\rho_{0.6K} = 16$

UZn$_{12}$

Ratio of starting materials

U : Zn = 1.0 : 99.0   (at %)

  $\simeq$ 0.6253 : 16.9676 (g)

Growing process

	Rate (°C/h)	Target (°C)
1.	100	400
2.	5.0	760
3.	0 (keep for 120 h)	760
3.	0.3	630
4.	0.5	550
5.	1.0	450
6.	2.0	400
7.	5.0	300
8.	10	100

Total time = 954 h $\simeq$ 40 days

Results

Hexagonal shape (4 $\times$ 1.4 $\times$ 1.4 mm^3)

$\rho_{RT}/\rho_{1.3K} = 4.3$
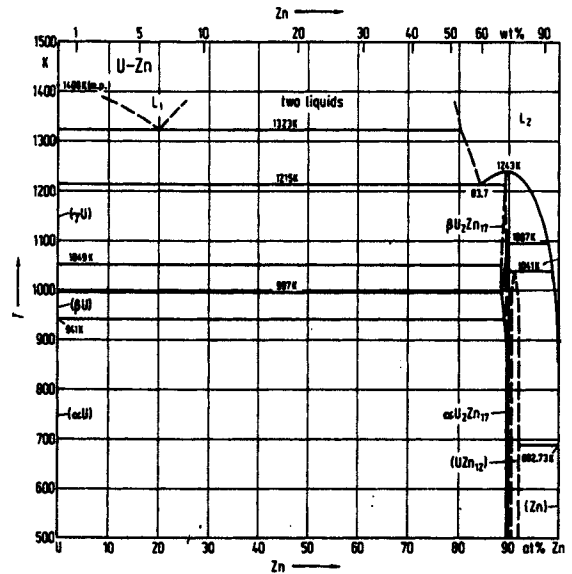
PrPb$_3$

Ratio of starting materials

Pr : Pb = 7.0 : 93.0   (at %)

  $\simeq$ 0.7542 : 14.7370 (g)

Growing process

	Rate (°C/h)	Target (°C)
1.	54	300
2.	25	900
3.	0 (keep for 48 h)	900
3.	1.0	860
4.	0.3	800
5.	0.4	700
6.	0.5	650
7.	0.6	600
8.	1.0	550
9.	2.0	500
10.	5.0	400
11.	15	250

Total time = 855 h $\simeq$ 36 days

Results

Cubic shape (1.4 $\times$ 1.4 $\times$ 1.4 mm^3)

$\rho_{RT}/\rho_{8K} = 9.9$
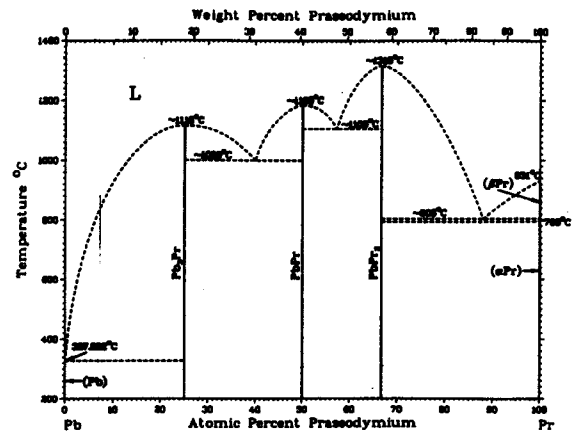
EuPb₃

Ratio of starting materials

Eu : Pb   =   19.4 : 80.6   (at %)

          ≃   2.0093 : 11.3795   (g)

Growing process

	Rate (°C/h)	Target (°C)
1.	50	300
2.	20	790
3.	0 (keep for 24 h)	790
3.	2.0	750
4.	0.4	600
5.	0.6	550
6.	0.8	500
7.	2.5	320
8.	10	200

Total time = 678 h ≃ 28 days

Results

Cubic shape $(1.4 \times 1.4 \times 1.4\,\mathrm{mm}^3)$

$\rho_{\mathrm{RT}}/\rho_{7\mathrm{K}} = 21$
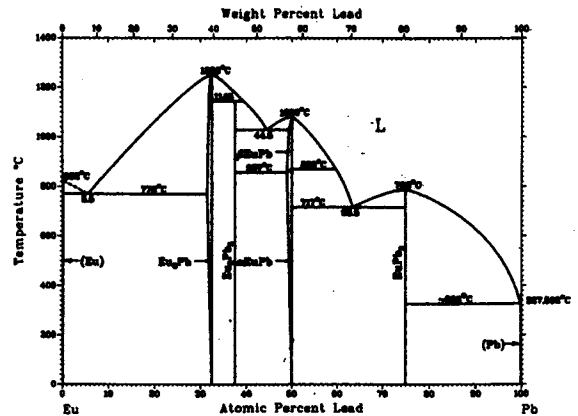
GdPb₃

Ratio of starting materials

Gd : Pb   =   6.5 : 93.5   (at %)

          ≃   1.0279 : 19.5860   (g)

Growing process

	Rate (°C/h)	Target (°C)
1.	135	300
2.	26	920
3.	0 (keep for 48 h)	920
3.	1.0	880
4.	0.4	750
5.	0.6	700
6.	0.7	600
7.	2.0	500
8.	20	300

Total time = 725 h ≃ 30 days

Results

Cubic shape $(1.2 \times 1.2 \times 1.2\,\mathrm{mm}^3)$

$\rho_{\mathrm{RT}}/\rho_{7\mathrm{K}} = 19$
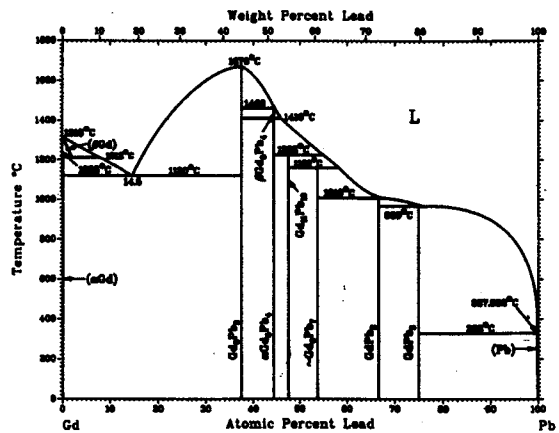
Publication List

1. *D. Aoki*, T. Inoue, N. Suzuki, K. Miyake, Y. Inada, R. Settai, K. Sugiyama, E. Yamamoto, Y. Haga, K. Kindo and Y. Ōnuki
   Magnetic phase diagram in UCd_{11}
   J. Phys. Soc. Jpn. **68** (1999) 3117

2. K. Sugiyama, N. Nakashima, *D. Aoki*, K. Kindo, N. Kimura, H. Aoki, T. Komatsubara, S. Uji, Y. Haga, E. Yamamoto, H. Harima and Y. Ōnuki
   Metamagnetic transition in UPt_3 studied by high-field magnetization and de Haas–van Alphen experiments
   Phys. Rev. B **60** (1999) 9248.

3. *D. Aoki*, P. Wiśniewski, K. Miyake, N. Watanabe, Y. Inada, R. Settai, E. Yamamoto, Y. Haga and Y. Ōnuki
   Crystal growth and cylindrical Fermi surfaces of USb_2
   J. Phys. Soc. Jpn. **68** (1999) 2182.

4. T. Sakakibara, T. Tayama, K. Tenya, H. Amitsuka, *D. Aoki*, Y. Ōnuki and Z. Kletowski
   Magnetization study on the antiferro-quadrupolar ordering in $PrPb_3$
   Physica B **259-261** (1999) 340.

5. E. Yamamoto, T. Honma, Y. Haga, Y. Inada, *D. Aoki*, M. Hedo, Y. Yoshida, H. Yamagami and Y. Ōnuki
   Fermi surface of UB_2 studied by the de Haas–van Alphen oscillation
   Physica B **259-261** (1999) 1085.

6. *D. Aoki*, Y. Katayama, S. Nojiri, R. Settai, Y. Inada, K. Sugiyama, Y. Ōnuki, H. Harima and Z. Kletowski
   Fermi surfaces of RPb_3
   Physica B **259-261** (1999) 1083.

7. *D. Aoki*, Y. Katayama, R. Settai, Y. Inada, Y. Ōnuki, H. Harima, Z. Kletowski, T. Tayama and T. Sakakibara
   Antiferroquadrupolar ordering and Fermi surface property in $PrPb_3$
   Phys. of Strongly Correlated Electron Systems eds. T. Komatsubara, H. Fujii, Y. Ōnuki, H. Shiba,
   Jpn. J. Appl. Phys. Series **11** (1998) 188.

8. E. Yamamoto, T. Honma, Y. Haga, *D. Aoki*, M. Hedo, Y. Inada, R. Settai, H. Yamagami and Y. Ōnuki
   De Haas-van Alphen effect of UB_2, UB_4 and UGa_3

Phys. of Strongly Correlated Electron Systems eds. T. Komatsubara, H. Fujii, Y. Ōnuki, H. Shiba,
Jpn. J. Appl. Phys. Series **11** (1998) 209.

9. *D. Aoki*, Y. Katayama, R. Settai, N. Suzuki, K. Sugiyama, K. Kindo, H. Harima and Y. Ōnuki
de Haas–van Alphen oscillations and magnetic properties of $YbPb_3$ and $EuPb_3$
J. Phys. Soc. Jpn. **67** (1998) 4251.

10. E. Yamamoto, Y. Haga, T. Honma, Y. Inada, *D. Aoki*, M. Hedo, Y. Yoshida, H. Yamagami and Y. Ōnuki
De Haas-van Alphen effect and energy band structure in UB_2
J. Phys. Soc. Jpn. **67** (1998) 3171.

11. N. Kimura, T. Komatsubara, *D. Aoki*, Y. Ōnuki, Y. Haga, E. Yamamoto, H. Aoki and H. Harima
Observation of a main Fermi surface in UPt_3
J. Phys. Soc. Jpn. **67** (1998) 2185.

12. Y. Yoshida, K. Sugiyama, T. Takeuchi, Y. Kimura, *D. Aoki*, M. Kouzaki, R. Settai, K. Kindo and Y. Ōnuki
Metamagnetic transition based on the quadrupole moment in $DyCu_2$
J. Phys. Soc. Jpn. **67** (1998) 1421.

13. *D. Aoki*, Y. Katayama, R. Settai, Y. Inada, Y. Ōnuki, H. Harima and Z. Kletowski
De Haas-van Alphen effect and the antiferroquadrupolar ordering of $PrPb_3$
J. Magn. Magn. Mater. **177-181** (1998) 365.

14. *D. Aoki*, Y. Katayama, R. Settal, Y. Inada, Y. Ōnuki, H. Harima and Z. Kletowski
Fermi surface properties and metamagnetism in the antiferroquadrupolar compound $PrPb_3$
J. Phys. Soc. Jpn. **66** (1997) 3988.

15. K. Sugiyama, Y. Yoshida, *D. Aoki*, R. Settai, T. Takeuchi, K. Kindo and Y. Ōnuki
Metamagnetic magnetization in $DyCu_2$
Physica B **230-232** (1997) 748.

16. Y. Inada, T. Ishida, H. Azuma, *D. Aoki*, R. Settai, Y. Ōnuki, K. Kobayashi, T. Takabatake, G. Nakamoto, H. Fujii and K. Maezawa
Anisotropic magnetoresistance of CeNiSn
Physica B **230-232** (1997) 690.

17. Y. Haga, E. Yamamoto, Y. Inada, *D. Aoki*, K. Tenya, M. Ikeda, T. Sakakibara and Y. Ōnuki Single crystal growth and superconducting properties of UPd_2Al_3
Physica B **230-232** (1997) 357.

18. M. Abliz, R. Settai, P. Ahmet, *D. Aoki*, K. Sugiyama and Y. Ōnuki
    de Haas–van Alphen effect and the metamagnetic transition based on the quadrupole moment in $PrCu_2$
    Philos. Mag. B **75** (1997) 443.

19. M. Abliz, P. Ahmet, *D. Aoki*, Y. Kimura, S. K. Dahr, R. Settai, Y. Ōnuki and H. Harima
    Magnetoresistance, de Haas–van Alphen effect and Fermi surface of $LaCu_2$
    J. Phys. Soc. Jpn. **66** (1997) 194.

20. Y. Haga, E. Yamamoto, Y. Inada, *D. Aoki*, K. Tenya, M. Ikeda, T. Sakakibara and Y. Ōnuki
    Single crystal growth, normal and superconducting properties of UPd_2Al_3
    J. Phys. Soc. Jpn. **65** (1996) 3646.

21. Y. Inada, H. Azuma, R. Settai, *D. Aoki*, Y. Ōnuki, K. Kobayashi, T. Takabatake, G. Nakamoto, H. Fujii and K. Maezawa
    Magnetoresistance and the anisotropic hybridization gap in CeNiSn
    J. Phys. Soc. Jpn. **65** (1996) 1158.

22. R. Settai, M. Abliz, P. Ahmet, H. Azuma, *D. Aoki*, Y. Yoshida, K. Sugiyama and Y. Ōnuki
    Metamagnetic transition in $PrCu_2$ studied by the de Haas–van Alphen effect
    Physica B 216 (1996) 326.

23. 青木大
    簡便で安価なフラックス法電気炉の作製
    強相関伝導系の物理 ニュースレター Vol. 5, No. 1 (1997) 94.
    D. Aoki
    Making a simple and inexpensive electronic furnace for flux method
    News Letter in Physics of Strongly Correlated Electron System, Vol. 5, No. 1 (1997) 94. (in Japanese)

24. *D. Aoki*, N. Suzuki, K. Miyake, Y. Inada, R. Settai, K. Sugiyama, E. Yamamoto, Y. Haga, Y. Ōnuki, H. Sugawara and H. Sato
    Electronic Property of An Antiferromagnet UGa_3
    J. Phys. Soc. Jpn. (to be published)

25. *D. Aoki*, P. Wiśniewski, K. Miyake, R. Settai, Y. Inada, K. Sugiyama, E. Yamamoto, Y. Haga and Y. Ōnuki
    Single crystal growth by flux method and Fermi surface of uranium compounds
    Physica B (in press)

26. P. Wiśniewski, *D. Aoki*, N. Watanabe, K. Miyake, R. Settai, Y. Ōnuki, Y. Haga,
    E. Yamamoto and Z. Henkie
    Shubnikov-de Haas effect study of cylindrical Fermi surfaces in UAs_2
    J. Phys. Condens. Matt. (in press)